Coarsening and percolation in 2d kinetic Ising models, and quench dynamics of the isolated p=2 spherical spin glass model

Alessandro Tartaglia

SORBONNE UNIVERSITÉ

LPTHE
LABORATOIRE DE PHYSIQUE THEORIQUE ET HAUTES ENERGIES

THÈSE DE DOCTORAT
DE SORBONNE UNIVERSITÉ

Spécialité : Physique

École doctorale n.564: Physique en Île-de-France

réalisée

au Laboratoire de Physique Théorique et Hautes Energies

sous la direction de Marco PICCO et Leticia F. CUGLIANDOLO

présentée par

Alessandro TARTAGLIA

pour obtenir le grade de :

DOCTEUR DE SORBONNE UNIVERSITÉ

Sujet de la thèse :

Coarsening and percolation in $2d$ kinetic Ising models

&

Quench dynamics of the isolated $p = 2$ spherical spin glass model

soutenue le 27 septembre 2018

devant le jury composé de :

M.	Marco PICCO	Directeur de thèse
Mme	Leticia F. CUGLIANDOLO	Codirectrice de thèse
M.	Dragi KAREVSKI	Rapporteur
M.	Federico RICCI-TERSENGHI	Rapporteur
M.	Marco TARZIA	Examinateur
Mme	Cécile APPERT-ROLLAND	Examinatrice
M.	Ludovic JAUBERT	Examinateur

Acknowledgments

First and foremost, I would like to thank my thesis supervisors Marco Picco and Leticia Cugliandolo. I am profoundly grateful to them for having provided me an opportunity to join their research team as an intern during my last year of master degree and then for having accepted me as their PhD student. They have constantly inspired me throughout the last few years, with their ideas, advises, and their devoted commitment to research, all aspects that contributed to make my PhD experience productive and stimulating. Without their guidance and encouragement this work would not have been possible.

I would like to express particular thanks to Professors Dragi Karevski and Federico Ricci-Tersenghi for having accepted to review the present manuscript and for having provided their useful comments. I also want to thank the other members of the committee, Professors Cécile Appert-Rolland, Ludovic Jaubert and Marco Tarzia, for having participated in the examination of my thesis by providing insightful critique.

A part of this thesis issued from the collaboration with Professor Gustavo Lozano and Nicolás Nessi from University of Buenos Aires. I am deeply grateful to them for their precious work and support and for having welcomed me in Argentina during the first stage of the collaboration.

I also want to express my thanks to Ferdinando Insalata and Marco Esposito for very useful discussions on topics related to the subject of my thesis.

I thank all the members of the LPTHE, especially the director of the lab Benoit Douçot and the secretaries Françoise Got and Isabelle Nicolai for their kindness and availability. Special mention goes to all the fellow PhD students I shared my workplace with during these three years: Charles, Chrysoula, Constantin, Enrico, Gaëtan, Hugo, Johannes, Matthieu, Oscar, Ruben, Sophie, Thomas, Yifan and Yoan. They all contributed, in one way or an other, in making my PhD experience a stimulating and enriching journey.

Last but not least, I wish to express my deepest gratitude to my family for their support. They gave me faith and strength to cope with difficulties and inspired me with confidence.

Abstract

This Thesis is divided into two independent parts.

In the first part, we study the early time dynamics of some $2d$ kinetic Ising models subject to istantaneous quench from the disordered to the ordered, low temperature, phase. The post-quench relaxation dynamics is realised by means of stochastic spin update rules, of various types, which are simulated numerically through Monte Carlo methods. Measurements of different observables related to the statistical and geometrical properties of ordered domains suggest that the relaxation dynamics approaches a dynamical scaling regime with features ascribed to $2d$ critical percolation. We study the scaling properties of the evolution towards this regime and we identify an associated growing length, different from the usual one that is responsible for coarsening. We find that this characteristic length depends on the particular microscopic dynamics and the lattice geometry. In particular, we treat three different cases: ferromagnetic Ising Model evolving with Glauber single spin-flip dynamics, ferromagnetic Ising Model evolving with Kawasaki spin-exchange dynamics and the special stochastic dynamics represented by the voter model spin update rules. In all the cases in which the stochastic dynamics satisfies detailed balance, the critical percolation state persists over a very long period of time before usual coarsening of domains takes over and leads the system to equilibrium. After having attained this critical-percolation-like state, the system continues to evolve by means of the usual curvature-driven motion of domain walls, or by more complicated microscopic dynamics. In the case of the voter model, we observe that the system briefly passes through a critical percolation state, to later approach a dynamical regime in which the scaling behaviour of the domain pattern can be ascribed to a different criticality.

In the second part, we study the Hamiltonian dynamics of the 2-spin spherical spin glass model, following a uniform quench of the strength of the disorder. The dynamics is studied both in $N \to \infty$ limit, through the Schwinger-Dyson equations describing the time-evolution of the two-time autocorrelation and linear response functions, and in the case of N finite, with N the number of spin degrees of freedom, by directly integrating their equations of motion. In each case, we consider initial conditions from Gibbs-Boltzmann equilibrium at a given temperature, and subsequently evolve the configurations with Newton dynamics dictated by a new Hamiltonian, obtained from the initial one by a uniform quench of the interaction couplings. From the numerical solutions, we can identify three dynamical phases (in the limit $N \to \infty$) depending on the parameters that characterise the initial state and the post-quench Hamiltonian. We argue that, in the $N \to \infty$ limit, the modes decouple at long times. We evaluate the mode temperatures and we relate them to the frequency-dependent effective temperatures measured with the fluctuation-dissipation relation in the frequency domain, similarly to what was recently proposed for quantum integrable cases. Finally, we notice

that the post-quench dynamics of this model is equivalent to that of the Neumann integrable model, and thus we analyse the integrals of motion, notably, their scaling with N, and we use them to show that the system is out of equilibrium in all phases, even for parameters that show an apparent Gibbs-Boltzmann behaviour of the global observables.

Résumé

Cette thèse est divisée en deux parties indépendantes.

Dans la première partie, on étudie la dynamique aux temps très courts d'un modèle cinétique d'Ising en $2d$ qui est soumis à une trempe instantanée de la température (quench). Cette trempe pousse le système d'un état initial désordonné à un état final ordonné ferromagnétiquement qui est atteint grâce à la croissance des domaines de spin ordonnés. La dynamique de relaxation post-trempe du système est modélisée par un processus stochastique, qui est realisé numériquement à travers des simulations de type Monte Carlo sur des réseaux de taille finie. Les mesures des différentes observables reliées aux propriétés statistiques et géométriques des domaines ordonnés suggèrent que la dynamique de relaxation approche un régime de "scaling" dynamique dans lequel les domaines présentent les caractéristiques du modèle de la percolation critique en $2d$. À travers l'étude des propriétés de scaling pendant l'évolution du système, on peut identifier une longueur critique $\ell_p(t)$ liée à la percolation qui est différente de la longueur usuelle associée au processus de croissance. Cette longueur sépare deux échelles différentes: à chaque instant de temps t après la trempe, les propriétés typiques de la percolation critique peuvent être observées sur des distances $R < \ell_p(t)$, tandis que sur des distances plus grandes, le système ressemble encore à l'état desordonné initial. Au contraire, sur des distances très petites, $R < \ell_d(t)$, les domaines sont equilibrés à la température finale du refroidissement. Par conséquence, pour un système de taille finie L, on observe qu'au temps t_p tel que $\ell_p(t_p) = L$, la percolation critique s'étend sur tout les longueurs, avec une taille effective $\ell_d(t)$. Ce phénomène a été observé pour des différents types de dynamique microscopique stochastique. En particulier, pour des modèles d'Ising en $2d$ évoluant avec une dynamique de Glauber (single spin-flip dynamics) et une dynamique de Kawasaki ou "spin-exchange dynamics". Dans ces cas, des gros domaines ordonnés qui percolent s'établissent au temps t_p et deviennent stable, par leur topologies, par rapport à la dynamique microscopique jusqu'au moment à lequel tout le système est equilibré, c'est-à-dire jusqu'au temps $t_{\rm eq} \sim L^{z_d}$ approximativement. Un phénomène similaire est aussi observé dans le cas du "voter model" sur un réseau de taille finie. Mais dans ce dernier modèle, le système évolue vers un état qui est caractérisé par une criticalité différente de celle de la percolation.

Dans la deuxième partie, on étudie la dynamique hamiltonienne du modèle de Sherrington-Kirkpatrick (SK) spherique dans le cas $p = 2$ (2-spin spherical spin glass model), suivant une trempe uniforme de l'intensité du désordre. Plus précisément, on considère un état initial prélevé dans la distribution d'équilibre à la Gibbs-Boltzmann, à une certaine température et avec une certaine intensité du désordre (qui est Gaussien), et puis on fait évoluer cet état sous une dynamique hamiltonienne par rapport à un nouveau Hamiltonien, obtenu de l'Hamiltonien initial par une dilatation uniforme de la matrice des couplages. La dynamique a été etudiée tant dans le cas d'un système infini, à travers les équations de type Schwinger-Dyson qui relient la fonction d'autocorrelation avec la réponse linéaire, que dans le cas d'un

système avec un nombre N fini de degrés de liberté. À partir des solutions numériques, on peut identifier trois phases dynamiques différentes (dans la limite thermodynamique) selon la température initiale du système et le paramètre qui quantifie l'intensité du désordre dans l'Hamiltonien post-trempe. On observe que le système ne réussit pas à thermaliser dans aucune de ces phases. En fait on peut vérifier que le modèle SK sphérique avec $p = 2$, avec une dynamique hamiltonienne, est équivalent au modèle de Neumann, un modèle intégrable de la mécanique classique. C'est la raison pour laquelle la distribution d'équilibre canonique (à la Gibbs-Boltzmann) n'est pas correcte pour décrire le régime stationnaire qui va finalement s'établir aux temps très longs après la trempe. Finalement, on analyse aussi les intégrales premières des équations du mouvement associées au modèle de Neumann et on peut vérifier qu'il n'y a pas aucune condition particulière pour laquelle les modes normaux du système peuvent thermaliser à la même température.

Motivations

In the following I present briefly the main motivations and interests that guided the work I have done during my PhD.

First of all, my work with Marco Picco and Leticia Cugliandolo started with my master's internship. The subject of this internship was the study of the coarsening phenomena appearing in the $2d$ voter model, a purely dynamical stochastic system that is commonly used as a prototype of opinion dynamics and as a toy model to describe many issues in population genetics. We were interested in this model because it displays the same kind of nonequilibrium dynamics, and in particular the same kind of ordering process, as in the most common cases of kinetic spin models where, usually, the domain growth is prompted by a quench from the high-temperature phase to the low-temperature one. In particular, the focus of the project was put on the characterization of the geometrical and statistical properties of the domain pattern produced by the coarsening dynamics, with the aim of relating these properties with known results of $2d$ critical percolation.

In fact, M. P. and L. C. and other researchers, at that time, had already observed that percolation has an important role in the coarsening dynamics of magnetic systems. The initial interest was sparked by the observation of the so-called "striped" states in the late stages of the evolution of the spin configuration of a $2d$ ferromagnetic Ising model, following an istantaneous quench from infinite temperature to zero or very small finite temperature, for systems of finite size. Surprisingly, the probabilities of occurence of such metastable states (that effectively prevent the system from reaching the full equilibration) were found to be coincident with the probabilities of having percolating clusters with the same topology in $2d$ critical percolation. Moreover, analytical and numerical results already showed that the probability distribution of the size of the spin clusters in an Ising model quenched to the low-temperature phase, after a sufficiently long time, acquired a power-law decay, with the same exponent as in $2d$ critical percolation, that persisted throughout the rest of the evolution of the system. These observations motivated us to search the same kind of phenomenology in the $2d$ voter model. The stochastic spin update rules defining the voter model are, in fact, very similar to those that define the Glauber dynamics, which is the standard stochastic process used to simulate a quench for the Ising model. And indeed, by means of numerical simulations, we found that a spin configuration, initiated in a fully disordered state and then let evolve under voter model dynamics, was approaching, at late times, a state in which the domains had geometrical and statistical properties similar to those of $2d$ critical percolation. The results of this work became the subject of a publication in Physical Review [1].

During my PhD, we continued to investigate the percolation phenomena emerging in the coarsening dynamics of various kinetic Ising models, considering also the influence of the particular lattice geometry and finite-temperature effects. A study of the typical time required for a finite system to reach the so-called critical percolation state, t_p, had already been developed by M. P. and L. C., but many aspects still needed to be clarified. In particular, how

to characterize the transient between the initial disordered state and the critical percolation regime, and the scaling behaviour of many observables related to the geometrical properties of the ordered domains like, for example, the size of the largest cluster, the length of the percolating domain walls, the pair-connectivity function and so on, once the system has fully entered in the critical percolation regime. The analysis was pursued mainly by means of numerical simulations, since to our knowledge there were no analytical methods, and still there is any, apart from some approximate scaling arguments, that could be used to predict the existence of such critical percolation state in a dynamical model. We came to the conclusion that a better description of the transient between the initial state and the critical percolation regime could be achieved by considering not the typical time t_p, that was supposed to scale as $t_p \sim L^{z_p}$ with the system size L (and z_p an exponent to be determined by finite-size scaling), but a dynamical characteristic length $\ell_p(t)$ that separates two scales. At time t, the properties of the domain pattern are those of critical percolation over lengths shorter than $\ell_p(t)$, while over lengths longer than $\ell_p(t)$ the system still looks as in the initial fully disordered state. The assumption here is that the dynamical characteristic length $\ell_p(t)$ grows faster than the usual dynamical length $\ell_d(t)$ associated to coarsening, so that a state in which the critical percolation features have "extended" over the entire system can be observed before equilibrium is reached. Results of this work were published in [2].

After refining our study of the percolation phenomena appearing in the Ising model evolving with Glauber dynamics, we were interested in other type of stochastic spin update rules. We decided to focus on kinetic Ising models evolving under conserved order parameter (COP) dynamics, and in particular, the Kawasaki spin-exchange dynamics. This was motivated by looking at some experimental and numerical observations on the phase separation process occuring in $2d$ Bose-Einstein condensates, in which evidence of the existence of states with domain walls having the fractal behaviour of critical percolation was found. It was clear, at that point, that the presence of a dynamical regime in which the domain pattern properties have critical percolation scaling behaviour, in the coarsening dynamics of KIMs, was independent of the particular microscopic stochastic update rules. Indeed, we found that also in the case of Kawasaki dynamics the system reaches a critical-percolation-like dynamical scaling regime. In general the approach to this dynamical regime is controlled by the characteristic length $\ell_p(t)$, whose form depends on the microscopic dynamics and the lattice geometry. Accounts of these results have been published in [3, 4]. Along this line, we also revisited the $2d$ voter model in order to include it in this general framework. However, through a more accurate analysis than the one done in the early stages of my PhD, we determined that the voter model dynamics brings the system to a different kind of criticality. By performing longer numerical simulations on very large systems, we were able to find that, in the case of the voter model, the system indeed passes through a $2d$ critical percolation state, but very soon it departs from it and approaches a dynamical scaling regime in which the fractal properties of the ordered domains belongs to a different universality class, which unfortunately we were unable to fully characterize.

A second part of my PhD was dedicated instead to the study of the quench dynamics of classical isolated systems with (quenched) disorder. In particular, we considered the (classical) p-spin spherical spin glass model and analysed the evolution of the system under Hamiltonian dynamics after the strength of the couplings is quenched. The interest was originally sparked by an analogy with quantum many-body models that are subject to a quench, a problem for which many aspects have been already thouroghly explored both thoretically and experimentally. In this context, the most natural question that one may ask is wether the (isolated) system is able to provide a bath for itself, allowing it to reach an equilibrium state

thanks to the interactions between the different degrees of freedom. In other words, the main issue is to determine wheter the system is able to attain, in the long time limit, a stationary state which is characterized by a Gibbs-Boltzmann probability measure. In the case of quantum systems, one finds that at least two classes of models, integrable models and models that display the so-called many-body localization, fail to reach equilibrium in the quench dynamics. The p-spin spherical spin model is a classical model whose Hamiltonian quench dynamics poses similar questions. At the time that I started approaching this problem, the case $p > 3$ was already under study by Leticia Cugliandolo and collaborators Gustavo Lozano and Nicolás Nessi from University of Buenos Aires. They found that, under certain quenching conditions, the isolated dynamics of these non-integrable interacting systems approached a non-stationary ageing regime, which was reminding of the glassy behaviour observed in the case of purely dissipative relaxation dynamics. The lack of relaxation to thermal equilibrium was explained in terms of a complex free-energy landscape that include fully trapping regions. Motivated by these results, we decided to see if the same kind of phenomena could be observed in the $p = 2$ spherical spin glass model, a case which is particularly interesting since the energy conserving dynamics is almost equivalent to that of the Neuman integrable model. We investigated the isolated quench dynamics of this model both numerically and analytically and found that indeed, given the similarity with an integrable model, the system fails to relax to an equilibrium state for almost every choice of the quenching conditions. We published the results of this study in [5].

In the following sections of this Dissertation, I am going to expose in full detail each one of the topics that have been briefly described here.

Contents

Part I

Coarsening and percolation in $2d$ kinetic Ising models

Chapter 1

Percolation in the $2d$ KIM evolving under Glauber dynamics.

1.1 Introduction

In this Chapter, we are going to discuss the existence of a critical-percolation-like scaling regime in the coarsening process arising in a $2d$ Kinetic Ising Model (KIM) evolving with single spin-flip dynamics. Observations made from numerical simulations suggest that the relaxation dynamics of the IM ensued by such nonconserved order parameter dynamics (which mimics an instantaneous quench from infinite temperature to a subcritical temperature) is characterized by at least two different stages. In particular, in the early stage of the dynamics, we observe the system evolving from the initial disordered state to a state in which growing ordered domains have the statistical and geometrical properties of clusters of connected sites in critical percolation, after proper rescaling. After having attained this "percolation" state, the system continues to evolve by means of the usual curvature-driven motion of domain walls.

In the context of coarsening phenomena in the KIM, most of the analyses were based on investigations of the space-time correlation function or, equivalently, the dynamic structure factor. The time-evolving domain structure, that has not been as much studied so far, should contain additional information and be of interest from both practical and theoretical viewpoints. From the existence of a *single* growing length ℓ_d implied by the dynamic scaling hypothesis one may conclude that, on the one side, the instantaneous distribution of domain sizes is peaked at the value $\ell_d^d(t)$ with the power d being the space dimension and, on the other side, the systems attain equilibrium when this growing length ℓ_d reaches the systems size L, *i.e.*, after times of the order of $t_{\rm eq}(L) \simeq L^{z_d}$. None of these conclusions are totally valid, as was recently shown in a series of works [6, 7, 8, 9].

As an example, the dynamical number density of domain areas in the $2d$ Ising model evolving with nonconserved order parameter dynamics and quenched from infinite to a subcritical temperature was studied in [10, 11]. It was shown in these papers that after a short time scale the number density takes a form with two distinct regimes separated by $\ell_d^2(t)$: at short length scales the behaviour is determined purely by the coarsening mechanism while at long length scales the number density decays algebraically, with a power law that is numerically equal to that of $2d$ random critical percolation. The geometric properties of clusters of aligned spins and their interfaces of various kinds also show this crossover. Similar results were found under weak quenched disorder [12] and for conserved order parameter dynam-

ics [13]. Very generally and quite surprisingly, the systems first approach the morphology of critical percolation, with one (or more) percolating cluster(s), to later evolve following usual coarsening. The number density of domain areas (also interfaces) satisfies dynamic scaling and the "typical" area $\ell_d^2(t)$ appears as a shoulder in the number density for curvature-driven coarsening [10, 11, 12] and as a maximum for phase separation dynamics [13].

The determination of the typical time scale, t_p, over which the critical-percolation-like scaling regime for spin clusters establishes during the coarsening process, is the main subject that is going to be discussed in this Chapter. In particular, since we are always dealing with finite systems, we are interested in the way this time scale depends on L, the linear size of the system. Numerically, an algebraic dependence was already found [14]

$$t_p \sim L^{z_p} \tag{1.1}$$

with an exponent z_p that depends on the coordination number of the lattice, n_c, and the microscopic dynamics.

More precisely, in [14] it was conjectured that, for the Kinetic Ising Model evolving with the zero-temperature Glauber dynamics, the exponent z_p is given by

$$z_p = z_d/n_c \tag{1.2}$$

where $z_d = 2$ is the conventional dynamical exponent for nonconserved order parameter dynamics. This dependence was verified with relatively good numerical accuracy for the KIM on the triangular ($n_c = 6$), bow-tie (on average $n_c = 5$), square ($n_c = 4$), and Kagomé ($n_c = 4$) lattices.

However, the method used in [14] to determine the L-dependence of the time scale t_p might not be the best one and, in fact, we are here proposing a different approach which produces slightly different results. At this stage the definition of t_p itself, based on the appearance of the so-called critical-percolation-like regime, might no be very clear. Indeed, one must be very careful to not confuse the first appearance of a percolating spin cluster in the course of the relaxation dynamics, with the onset of a scaling regime characterised by critical percolation features. Depending on the particular lattice on which the model is defined and on the way one chooses the initial condition, clusters of aligned spins can percolate through the system at very early times, or they can even be present right at the beginning. For example, a spin configuration in which each lattice site takes either spin $+1$ or -1 with probability $1/2$, independently of all other sites (that is to say, Ising model at equilibrium at $T \to +\infty$) is right at the critical point of random site percolation for the triangular lattice, but not for other types of $2d$ lattices, like the square or honeycomb lattices.

Nevertheless, percolating cluster are subject to the spin-flip stochastic dynamics and thus they often break in smaller pieces and can reform later with a different topology. Roughly speaking, t_p corresponds to the typical time at which the large percolating structures become "stable" with respect to the spin microscopic dynamics, in the sense that their number and topology remain fixed and, from a macroscopic point of view, the only effect of coarsening is the motion of their walls.

In practice, however, this definition is still pretty vague, so that the estimation of the L-dependence of the time scale t_p is done by looking at the scaling of properties of other observables. More details about the methods and observables used are given in the next Sections. If a time scale t_p related to the emergence of percolation features exists, different from the usual time scale associated to the coarsening process, $t_{\rm eq} \sim L^{z_d}$, it must be evident

in the time evolution of observables that capture the statistical and geometrical properties of spin clusters, such as the domain area number density, or the largest cluster size.

One can associate a time-dependent characteristic length ℓ_p with this time scale, in the same way as the dynamical length $\ell_d(t) \sim t^{1/z_d}$, describing the law of growth of ordered domains due to the usual coarsening process, is associateed to the time scale $t_{\rm eq} \sim L^{z_d}$. We demonstrate that the dynamical regime in which the system approaches the "stable" percolation pattern is controlled by the dynamical length $\ell_p(t)$, for which we propose the following form

$$\ell_p(t) \simeq \ell_d(t)\ t^{1/\zeta}\ , \tag{1.3}$$

with the exponent ζ to be determined. In order to give strong support to this claim we show a thorough analysis of the size distribution of spin clusters for the model on $2d$ finite lattices. We observe the presence of two different dynamical scaling regimes: on length scales shorter than $\ell_d(t)$, domains (spin clusters) display the typical properties of thermal equilibrium at the target temperature of the quench dynamics; on the other hand, on length scales longer than $\ell_d(t)$ and up to the "new" characteristic length $\ell_p(t)$, domain statistical and geometrical properties are the ones of critical percolation (after proper rescaling of all lengths by $\ell_d(t)$). An additional large-size regime is present, for length scales longer than $\ell_p(t)$, and we show how the size distribution of domains in this regime (whose main contribution comes from large percolating domains) satisfy a similar dynamical scaling but with $\ell_p(t)$ as the correct dynamical length.

The analysis of the statistical and geometrical properties of the percolating structures that emerge in the zero-temperature nonconserved ordered parameter dynamics of the $2d$ Ising model (but also for IM in more dimensions) is also very useful for understanding the problem of metastability. Indeed, the existence of metastable states in the KIM evolving with single spin-flip dynamics at $T = 0$ was first signalled in [6, 7] and the passage through a critical percolation state was exploited in [8, 9] to predict their probability of occurrence. These states are, typically, configurations with stripes and flat interfaces that are stable with respect to the zero-temperature dynamics. At finite though sub-critical temperature, these states trap the dynamics for very long time scales, indeed longer than the naively expected equilibration time scale $t_{\rm eq} \sim L^{z_d}$. A brief analysis of the effects of these long-lived states on the equilibration of the KIM will be given in App. A.1.

1.2 Definition of the KIM equipped with Glauber dynamics

The model we consider is a classical spin system on a regular lattice with finite size. To each lattice site i we associate a spin, $s_i = \pm 1$, and the Hamiltonian of the system is that of the nearest-neighbour ferromagnetic Ising Model,

$$\mathcal{H}_J[\{s_i\}] = -J \sum_{\langle ij \rangle} s_i s_j \tag{1.4}$$

with $J > 0$ and the sum running over the pairs of nearest-neighbour lattice sites (each pair counted once).

The equilibrium properties of this model are well-known. In particular, it is known that this model undergoes a second order phase transition, in the thermodynamic limit, at a positive critical temperature T_c in dimensions $d \geq 2$. For example, in the case of the IM on a square lattice, a second order phase transition occurs at a critical temperature $T_c^{\rm sq}$ satisfying the relation $J/(k_B T_c^{\rm sq}) = \frac{1}{2} \ln(1 + \sqrt{2})$.

The *kinetic* part of the model comes from considering a continuous-time Markov chain on the space of spin configurations, $\{s(t) : t \in [0, +\infty)\}$ with $s(t) \in \{-1, 1\}^{\Lambda}$ (where Λ denotes the lattice), with given transition rates $W(s', s)$. $W(s, s')$ is defined as the probability per unit time for the stochastic process to make a transition from configuration s to configuration s'. If the system is in configuration s_0 at time $t = 0$, one can associate a probability $P(s, t|s_0)$ with the stochastic process $\{s(t)\}$, that is the probability that the configuration of the system is s at time t given that the initial configuration is s_0.

In order to let the time-dependent probability measure for the spin configuration, $P(s, t|s_0)$, converge towards the canonical equilibrium probability distribution at a given temperature T, $P_{\rm eq}(s; T) = \frac{1}{Z(T)} \exp\left[-\frac{\mathcal{H}_J(\{s_i\})}{k_B T}\right]$, as $t \to +\infty$, the transition rates $W(s', s)$ are chosen so that they satisfy the detailed balance condition

$$W(s, s')\, P_{\rm eq}(s; T) \;=\; W(s', s)\, P_{\rm eq}(s'; T) \quad . \tag{1.5}$$

The above condition ensures that the stochastic dynamics enforced by the transition rates $W(s, s')$ bring the system towards a stationary state with the desired probability distribution $P_{\rm eq}$ of canonical equilibrium at a given temperature T, for any given initial configuration s_0, provided that the Markov process ruled by the transition rates W is ergodic.

Eq. (2.2) gives a lot of freedom on the choice of the transitions that can be allowed in the stochastic process. In principle, one can decide to have a nonzero transition rate for any two spin configurations s and s', but since the goal is to study in detail the relaxation dynamics towards an equilibrium state in the low-temperature phase or exactly at $T = 0$, and, for $T \ll T_c$, the spatial extent of correlations between lattice sites is much smaller than the typical size of the system, one must allow only those transitions that produce a change in the spin configuration which is localized in space. A procedure that allows the system to make a "jump" from a given spin configuration to an other one by changing the spin of large clusters of sites, in one move (or, in an infinitesimal time window), would not mimic the coarsening dynamics observed experimentally in magnetic systems when quenching the temperature below the critical one.

The standard choice, and the simplest one, is to allow only transitions that change at most the value of the spin on one lattice site. In this case, the resulting stochastic dynamics is called single spin-flip dynamics. In practice, the only transitions that are allowed are those that do not change the spin configuration and those of the following form

$$s \to s^{(i)}, \quad \text{with} \quad s_j^{(i)} = \begin{cases} s_j & , \text{ for } j \neq i \\ -s_i & , \text{ for } j = i \end{cases} \tag{1.6}$$

for any given lattice site $i \in \Lambda$, with transition rates $w_i(s) \equiv W(s, s^{(i)})$ and $w_i(s^{(i)}) \equiv W(s^{(i)}, s)$ satisfying the relation

$$\frac{w_i(s; \beta)}{w_i(s^{(i)}; \beta)} = \frac{P_{\rm eq}(s^{(i)}; \beta)}{P_{\rm eq}(s; \beta)} = \exp\left\{-2\beta J\, s_i \sum_{k \in \mathcal{N}(i)} s_k\right\} \tag{1.7}$$

where the quantity $\Delta E_i(s) = \mathcal{H}_J[\{s_j^{(i)}\}] - \mathcal{H}_J[\{s_j\}] = 2J\, s_i \left(\sum_{k \in \mathcal{N}(i)} s_k\right)$ is the cost in energy for the system to flip the spin at site i, the summation running over $\mathcal{N}(i)$, the set of lattice sites that are nearest neighbours to site i, and $\beta = \frac{1}{k_B T}$ being the inverse temperature. Notice that the single spin-flip transition rate $w_i(s; \beta)$ depends on the spin configuration s only through the value of the spin on a very small number of lattice sites, precisely the

spin a the site i to be flipped and at its nearest neighbours. In particular, the quantity $h_i = \sum_{k\in\mathcal{N}(i)} s_k$ can be seen as an effective magnetic field produced by neighboring sites and acting on the site i. If the majority of the sites that are nearest neighbours to site i have antiparallel spin (in the configuration s), that is, $s_i h_i < 0$, than Eq. (1.7) states that, for $\beta < +\infty$ ($T > 0$), $w_i(s) > w_i(s^{(i)})$, which means that the transition $s \to s^{(i)}$ is favoured with respect to the inverse one. On the other hand, if $s_i h_i > 0$, that is, the majority of the nearest neighbour sites have parallel spin (in the configuration s), then $w_i(s) < w_i(s^{(i)})$, which means that the transition $s \to s^{(i)}$ is less favoured than the inverse one. Thus, the net result is that the stochastic dynamic ruled by the transition rates satisfying Eq. (1.7), on average, makes the spin at each lattice site align with the effective spin produced by the neighbouring sites.

Eq. (1.7) still leaves a lot of freedom on the choice of the particular form of the single spin-flip rates $w_i(s)$. A pretty common choice is given by

$$w_i(s;\beta) = \frac{C}{2}\ \left(\ 1 - \tanh\left[\beta \Delta E_i(s)\right]\ \right) \tag{1.8}$$

where again $\Delta E_i(s) = 2J\, s_i \left(\sum_{k\in\mathcal{N}(i)} s_k\right)$, while C is a constant which has the dimension of an inverse time. The stochastic dynamics that is produced by the above rates is called Glauber dynamics in literature [15]. Note that, in this form, the function $w_i(s) = W(s, s^{(i)})$ depends on the "depart" spin configuration, $s = \{s_j\}$, and on the "arrival" one, $s^{(i)} = \{s_j^{(i)}\}$, only through the energy cost $\Delta E_i(s)$ for the system to go from s to $s^{(i)}$. An other common choice is given by

$$w_i(s;\beta) = C\ \min\left(1,\ \frac{P_{\rm eq}(s^{(i)};\beta)}{P_{\rm eq}(s;\beta)}\right) = C\ \min\left(1,\ \exp\left\{-2\beta J\, s_i \sum_{k\in\mathcal{N}(i)} s_k\right\}\right) \tag{1.9}$$

which is just the Monte Carlo Metropolis-Hastings rule [16, 17] applied to single spin-flip transitions. In the case of $T = 0$ ($\beta \to +\infty$), the rates given by Eq. (1.8) reduce to

$$w_i(s) = \ C \times \left\{ \begin{array}{ll} 1 & ,\ \text{if } \Delta E_i(s) < 0 \\ \frac{1}{2} & ,\ \text{if } \Delta E_i(s) = 0 \\ 0 & ,\ \text{if } \Delta E_i(s) > 0 \end{array} \right. . \tag{1.10}$$

In Fig. 1.1 we show a schematic representation of the possible single spin-flip transitions that can occur in the case of an Ising model on a square lattice. Notice that, because of the simmetries of the model and the geometry of the lattice, and since the transition rates W depend on the particular spin configuration s only through the change in the energy ΔE due to the flip of one spin, there are only five different cases. In general, for a lattice of coordination number n_c there are $n_c + 1$ different "classes" of spin-flip transition.

In order to complete the construction of the stochastic process $\{s(t) : t \in [0, +\infty)\}$ resulting from the transition rates $W(s, s')$, it is necessary to specify the way in which the time t is increased between two consecutive transitions. One must take into account that, in the context of single spin flip dynamics, a possible transition could be either one in which the spin configuration remains unchanged or one in which the spin at one single lattice site is flipped. Then, one possibility is to increase the time by a fixed amount τ every time that an attempt at changing the spin configuration is made, independently of the outcome. In this case, the time evolution of the spin configuration can be seen as a sequence of spin flip events that are separated by a time which is a multiple of τ. This is the approach adopted in the

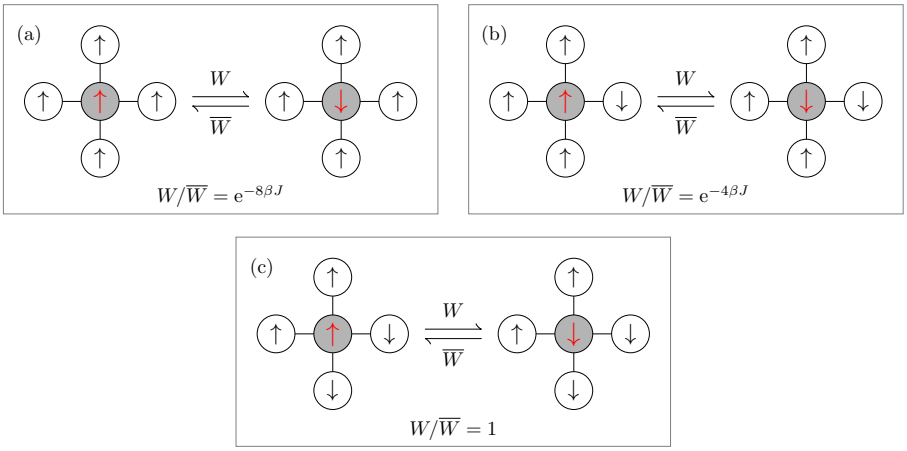

Figure 1.1: The possible spin-flip transitions on a square lattice. In each case, the central site (gray circle) represents the lattice site whose spin is chosen to be flipped. The spins on the four nearest-neighbours are shown as well. W is the transition rate from the configuration on the left to that on the right, while $\overline{W}$ is the rate associated with the inverse transition. They satisfy the detailed balance condition with respect to the canonical equilibrium distribution, that is to say, $W/\overline{W} = \exp(-\beta\Delta E)$, with ΔE the change in energy due to the transition, and β the inverse temperature.

discrete time Monte Carlo method. In our case we used a slightly different procedure, called continuous time Monte Carlo method [16]. This method is rejection-free, which means that, at each step of the algorithm, a spin is always flipped, independently of the change in energy ΔE. However, the time between two consecutive spin flip events is not constant, but drawn at random from an exponential distribution. One can easily show that the two versions of the method, discrete and continuous, are equivalent if one chooses the average time increment (for the continuous time method) of the form

$$\overline{\Delta t} = \left(\sum_i w_i(s) \right)^{-1} . \tag{1.11}$$

Note that $\overline{\Delta t}$ depends on the configuration of the system s at the time at which the spin flip is made.

The initial state is always taken to be a random spin configuration with no correlations, obtained by choosing $s_i = +1$ or $s_i = -1$ with probability $1/2$ on each lattice site (long-range correlated initial conditions, as the ones of the critical Ising point, fall in a different class [10, 18, 19, 20]). This initial condition corresponds to equilibrium at infinite temperature. Thus, with this choice, the stochastic dynamics that ensues from the spin flip rates $w_i(s;\beta)$ described above, simulates the relaxation of the spin system with Hamiltonian given by Eq. (1.4), from an initial state equilibrated at infinite temperature towards a state in equilibrium at a finite temperature $T \propto 1/\beta$. In other words, the evolution in time of the spin configuration produced by these transitions rates is a realization of a (classical) quench in temperature: the system is initially prepared in equilibrium at $T_0 \to +\infty$, and then the temperature is *instantaneously* changed to a finite value T.

Every case of numerical simulations of the KIM that is presented in this Chapter is relative to a sub-critical quench, that is, the "arrival" temperature T entering in the transition rates

is below the critical one, T_c. In fact, as stated in the introductory section of this Chapter, the goal is to study the domain growth that emerges in the $2d$ Kinetic Ising Model when it is relaxing towards the low-temperature ordered phase. In particular, coarsening is especially studied in the case of $T = 0$ Glauber dynamics, since the absence of thermal fluctuations allows the domain growth to be driven purely by a domain-wall-curvature mechanism [10, 21] after a sufficiently long time. Since the KIM equipped with Glauber dynamics at a temperature $T < T_c$ is an example of nonconserved order parameter dynamics [22], in the thermodynamic limit the typical relaxation time τ_{rel} scales with the equilibrium correlation length at the "arrival" temperature T, $\xi_{\text{eq}}(T)$, as

$$\tau_{\text{rel}}(T) \sim \xi_{\text{eq}}(T)^{z_d} \tag{1.12}$$

with $z_d = 2$ being the dynamical critical exponent. In the case of a finite system of linear size L, a simple finite-size scaling argument tells us that equilibration is reached in a typical time

$$\tau_{\text{rel}}^{(f)} \sim L^{z_d} \quad . \tag{1.13}$$

In dimensions $d = 2$, then, the relaxation time scales as the volume of the system, $N = L^2$.

When dealing with the zero-temperature Glauber dynamics, defined by the spin flip rates given by Eq. (1.10), one observes that, for a finite system, depending on the geometry of the lattice and on the boundary conditions, there are certain spin configurations that act as *absorbing* states. Once the system gets into one of these configurations it can not escape and thus the dynamics is over. The completely magnetized states, that is, the two spin configurations in which all sites have the same spin, are trivial examples of these absorbing states. Other less trivial absorbing states exist and correspond to local minima of the free energy of the Ising Model on the finite lattice.

Consider, for example, the zero-temperature Glauber dynamics, defined by the spin flip rates in Eq. (1.10), on the square lattice with periodic boundary conditions. Non-trival examples of absorbing states are spin configurations in which spin clusters of opposite phase are separated by straight walls: each one of the spins that are in the bulk of a domain are clearly frozen, but also the ones sitting on lattice sites at the border of a domain, since they are surrounded by three nearest neighbours with the same spins and just one with the opposite spin. In both cases the cost in energy for flipping the spin is positive and, by Eq. (1.10), $w = 0$. More complex absorbing spin configurations are possible in the case of a lattice with odd coordination number, as the honeycomb lattice, see App. A.2. Often they will be called *frozen* states in the rest of this work.

In summary, in the case of the Glauber dynamics at exactly $T = 0$, the system will eventually get trapped in one of these absorbing states and thus, the resulting stochastic process is not ergodic. Moreover, in the case of sub-critical Glauber dynamics at a positive but very small temperature ($T \ll T_c$), the absorbing states of the $T = 0$ dynamics have an important effect on the time required for equilibration. The system can spend a lot of time wandering in the basin of attraction of these local minima, and, effectively, for very large system sizes, numerical simulations could not be able to reach the final equilibrium state in the time scale predicted by the finite-size scaling in Eq. (1.13), but a longer time would be needed.

Since the main interest of this work is to study the appearance and influence of percolation phenomena in the coarsening dynamics of the kinetic Ising model, the choice of the particular lattice on which the KIM is placed represents an important specification of the model. In fact, the value of the threshold probability for percolation depends on the particular lattice

geometry, and, because of the finiteness of the system, having a cluster of connected aligned spins that percolates already in the initial state can have a great effect on the evolution of the system under the stochastic dynamics. As an example, consider a completely random spin configuration with no spatial correlation, where the probability for a site to have spin $+1$ or -1 is equivalently $1/2$. In other words, a state taken from equilibrium at $T \to +\infty$. For the triangular lattice, this state is critical in the context of percolation, that is, there is a nonvanishing probability (in the thermodynamic limit) of having a cluster of connected aligned spins that percolates through the system. This is not the case for the square lattice, since its threshold probability for percolation is larger than $\frac{1}{2}$.

Throughout this Chapter, we consider the KIM with Glauber dynamics on the square and triangular lattices. App. A.2 is dedicated to the analysis of the dynamics on the honeycomb lattice, a case which deserves a particular attention. The differences caused by the particular lattice geometry on the behaviour of the coarsening dynamics will be highlighted as much as possible.

1.3 Observables

In this Section we give an exhaustive list of the observables that we are going to study in order to characterize the coarsening process that the system is subjected to, and the geometrical and statistical properties of ordered domains that help us identify the onset of the critical-percolation-like scaling regime we have been mentioning before.

A crucial observable in our analysis is the characteristic dynamical length, denoted by ℓ_d. According to the dynamical scaling hypothesis, at sufficiently late times, a coarsening system develops a domain mosaic whose morphology is (statistically) scale-invariant with respect to a spatial characteristic scale given by ℓ_d. This means that the typical domain structure is statistically independent of time if all lengths are rescaled by ℓ_d. In this sense, $\ell_d(t)$ can be seen as the typical domain size at time t since the relaxation dynamics has begun, or as the average separation between ordered domains of the same phase.

The way by which the scaling hypothesis is usually probed is by means of the two-point dynamical correlation function, $C(\boldsymbol{r},t) = \langle s(\boldsymbol{x}+\boldsymbol{r},t)\, s(\boldsymbol{x},t)\rangle$, which should have the scaling form

$$C(\boldsymbol{r},t) \sim f\left(\frac{r}{\ell_d(t)}\right) \tag{1.14}$$

at late times t and for distances r much longer than the lattice spacing. Here we have denoted the value of the spin on the site $\boldsymbol{x}$ of the lattice, at time t, by $s(\boldsymbol{x},t)$ and the brackets $\langle\,\cdot\,\rangle$ denote the average over the initial conditions and the stochastic dynamics.

In the context of numerical simulations, the characteristic length $\ell_d(t)$ is usually estimated as the distance r over which the correlation C falls to a selected portion of its maximum value, or as the square root of the quantity

$$R^2(t) = \frac{\int_0^{+\infty} \mathrm{d}\boldsymbol{r}\, r^2\, C(\boldsymbol{r},t)}{\int_0^{+\infty} \mathrm{d}\boldsymbol{r}\, C(\boldsymbol{r},t)}\,. \tag{1.15}$$

A more practical way of measuring it is by means of the excess-energy associated to the domain walls, which is given by

$$\epsilon(t) = \frac{E_{\mathrm{eq}} - E(t)}{E_{\mathrm{eq}}}\,, \tag{1.16}$$

with $E(t) = \langle \mathcal{H}(\{s_i(t)\}) \rangle$ the average energy of the system at time t (where $\mathcal{H}$ is given by Eq. (1.4) and $\langle \cdot \rangle$ again represents the average over many independent realizations of the stochastic dynamics and the initial spin configuration) and $E_{\rm eq}$ the energy of the equilibrium state or stationary state that the system is approaching to (eventually in the limit $t \to +\infty$). The excess-energy ϵ is proportional to the density of defects which, in our case, are the domain walls. In the case of the ferromagnetic Ising model, one can easily see that $\epsilon(t)$ coincides with the average fraction of *unsatisfied* lattice bonds in excess with respect to the reference equilibrium state, where an unsatisfied lattice bond, for a given spin configuration, is a bond between two sites having opposite spin values. The typical domain radius, which is proportional to ℓ_d, is roughly given by the inverse of this quantity [23]. In particular we introduce an *excess-energy growing length*, $\ell_G(t)$, which is given by $\ell_G(t) = 1/\epsilon(t) = E_{\rm eq}/(E_{\rm eq} - E(t))$.

In the paramagnetic initial state, $E(0) \simeq 0$ and $\ell_G(0) \simeq 1$. As the system approaches thermal equilibrium at temperature T below the critical temperature T_c, the growing length increases, reflecting the fact that the density of defects (domain walls) decreases. As $t \to +\infty$ one expects that $\ell_G(t) \to +\infty$, since the time-dependent energy of the system, $E(t)$, reaches the equilibrium value and thus $\epsilon(t) \to 0$. In the case of the Glauber dynamics at $T < T_c$, this essentially amounts to the disappearance of large scale defects that can not be produced by thermal fluctuations alone, that is, most of the system is covered by a large cluster of aligned spins of a given sign and there can not exist ordered domains of the minority phase with size larger than the equilibrium correlation length at the target temperature T.

However, for the dynamics at $T = 0$ (and on a finite lattice), the system does not always reach full equilibration since it can get trapped forever in one of the frozen configuration we have mentioned in the previous Section. For this reason, $\ell_G(t)$ saturates at a finite value. Moreover, even in the case of Glauber dynamics at nonvanishing, but very low, temperature, the system can wander a lot of time around these metastable states before reaching true equilibrium. Thus, the characteristic length $\ell_G(t)$ first grows up to the saturation value for the zero-temperature dynamics and remains blocked approximately around it for a given period of time, after which it begins to increase again and eventually diverges. The duration of the plateau increases as the "arrival" temperature decreases, diverging to $+\infty$ as $T \to 0$. The presence of this intermediate regime slows down the relaxation dynamics and as a result, for finite systems, the typical equilibration time can be much larger than the one predicted theoretically for the nonconserved order parameter universality class, that is $t_{\rm eq} \sim L^2$.

Since, for times t such that $r_0 \ll \ell_G(t) \ll L$, with r_0 the lattice spacing and L the lattice linear size, we expect $\ell_G(t)$ to be a measure of the typical domain radius (or to be proportional to it), then in the thermodynamic limit we should have $\ell_G(t) \sim \ell_d(t) \sim t^{1/z_d}$, with $z_d = 2$. However, in the case of the KIM evolving with Glauber dynamics on a finite lattice, $\ell_G(t)$ can have a much richer structure. Therefore, throughout this dissertation we will use the numerically estimated $\ell_G(t)$ as an effective measure of $\ell_d(t)$ and we will not care much about its particular time dependence. Whenever the theroetical $\ell_d(t) \sim t^{1/z_d}$ is involved in the scaling of some measured length, $\ell_G(t)$ will be used instead.

Throughout this dissertation we are going to discuss about the geometrical and statistical properties of the spin clusters and relate them to those of clusters of occupied sites in the context of $2d$ random percolation. It is then necessary to provide the reader with a clear definition of spin cluster and features associated with it in the context of the Kinetic Ising Model. A *spin cluster* or *domain* is a set of connected lattice sites that have all the same spin. We call the *area* (or volume) A of a spin cluster the number of sites that belong to it. An important geometric feature of a spin cluster is its *interface*. The interface of a spin

cluster is essentially the boundary that separates it from neighboring spin clusters (which have obviously opposite spin). In order to give a clear representation of what this boundary consists of, we must first define what a domain wall is, also sometimes called "hull" in the following. A *domain wall* or *hull* is a non-self-intersecting path on the *dual* lattice (graphically, the dual lattice is constructed from the original one by connecting the centers of the original lattice plaquettes) which is constructed by joining bonds (on the dual lattice) that intersect unsatisfied bonds on the original lattice. If one imposes periodic boundary conditions on the system, such paths on the dual lattice are always closed (in $d = 2$ dimensions this can be easily depicted by imagining that the finite lattice folds onto itself to form a torus). The interface between a certain spin cluster and the neighbouring sites can be composed of many hulls. In particular, one can make a distinction between the different domain walls (or hulls) making up the whole interface: there is always one which encloses all the sites belonging to the spin cluster, which will be often referred to as *external hull*, and then there are, eventually, other hulls that are embedded inside the cluster itself, which we call *internal hulls*. Actually, in the case in which a spin cluster is percolating across the system, there can be a third possibility, namely hulls that can be considered neither external nor internal to any spin cluster.

In fact, we must now give a proper definition of *percolating spin cluster* on a finite-size system and distinguish different possibilities. Let us first focus on the case of a $2d$ system with PBC, *i.e.*, a model defined on a torus, with toroidal and poloidal directions represented as horizontal and vertical directions when picturing the torus as a $2d$ sheet, see Fig. 1.2. A closed curve on a torus can be homotopic to a point or it can wind around the torus so that it can not be shrinked down to a point by a continuous deformation of the torus itself. In the second case, we call it a *wrapping* hull. A spin cluster is said to percolate if it *wraps* around the system, that is to say, if there exists a path composed of connected sites belonging to the cluster that winds around at least one of the two directions of the torus. A wrapping cluster is separated by one or more hulls from one or more clusters of the opposite phase. Schematic examples of the different topologies of a wrapping cluster are depicted in Fig. 1.2.

We can have four distinct situations:

- a spin configuration with no wrapping cluster;
- a spin configuration that contains at least one cluster wrapping only along one direction (that is to say, horizontal or vertical stripes), see Fig. 1.2-(a) and 1.2-(b);
- a spin configuration that contains at least one cluster wrapping in both directions, with wrapping cluster walls (also called diagonal stripe configuration), see Fig. 1.2-(d);
- a spin configuration that contains a unique cluster wrapping in both directions, but without any wrapping walls (we refer to this case as a "cross" topology configuration), see Fig. 1.2-(c).

These are the only possible cases in two dimensions and are mutually exclusive.

To each one of the wrapping configurations described above we can associate a probability: the probability of having a cluster wrapping in both directions with a cross topology, π_{hv}, the probabilities of having a cluster wrapping only horizontally or only vertically, π_{h} and π_{v} respectively, and the probability of having a cluster wrapping in both directions in what we call a diagonal stripe configuration, π_{diag}. The probability that the spin configuration has no wrapping cluster is then given by $\pi_0 = 1 - \pi_{\mathrm{hv}} - \pi_{\mathrm{h}} - \pi_{\mathrm{v}} - \pi_{\mathrm{diag}}$.

We expect that, at a sufficiently long time after the quench, the system spends a very long period of time in a regime in which geometrical and statistical properties of spin clusters have

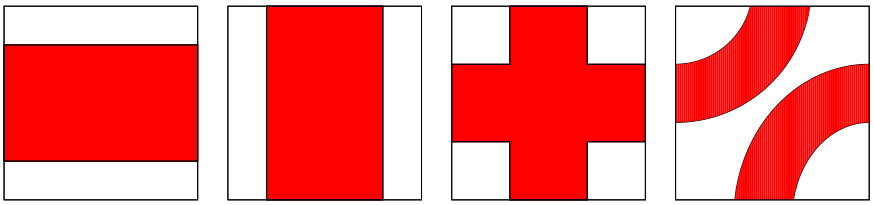

Figure 1.2: Sketches of wrapping clusters on a lattice with unit aspect ratio and PBC (*i.e.*, on a torus). The panels show in red clusters spanning the system horizontally (a), vertically (b), both horizontally and vertically (c), and diagonally (d). In the first, second and fourth cases, the topology of the red clusters implies the existence of a white percolating cluster next to them. On the contrary, in the third case the red cluster percolating in both directions forbids the existence of other spanning clusters.

the same scaling behaviour of clusters of occupied sites in critical site percolation on the same lattice. As the system approaches this regime, the time-dependent wrapping probabilities should become equal to corresponding ones in $2d$ critical percolation. Actually, one must take care of the fact that in a percolation problem one considers just the cluster of occupied sites, while in the spin models that we study here we have to consider clusters of both spin signs at an equal footing. With this consideration in mind, one can compare the values that the probabilities $\pi_{\rm hv}$, $\pi_{\rm h}$, $\pi_{\rm v}$ and $\pi_{\rm diag}$ reach in the late stages of the coarsening dynamics with the corresponding ones of $2d$ critical percolation, $\pi^{(p)}_{\rm hv}$, $\pi^{(p)}_{\rm h}$, $\pi^{(p)}_{\rm v}$ and $\pi^{(p)}_{\rm diag}$. In the case of a lattice of unit aspect ratio with periodic boundary conditions $\pi^{(p)}_{\rm hv} \simeq 0.6190$, $\pi^{(p)}_{\rm h} = \pi^{(p)}_{\rm v} \simeq 0.1694$ and $\pi^{(p)}_{\rm diag} \simeq 0.0418$ [24].

One can introduce similar probabilities in the case of a system with free boundary conditions (FBC). In this case, a spin cluster is said to percolate if there is a path of connected sites, belonging to the cluster, that crosses the system from one border to the opposite one. The distinction between the different percolating cluster geometries still applies. The "crossing" probabilities have been computed by Cardy [25] and Watts [26]. In particular, in the case of critical percolation on a square lattice with unit aspect ratio: $\pi^{\rm FBC}_{\rm hv} = 1/2 + \sqrt{3}/(2\,\pi)\,\ln(27/16) \simeq 0.6442$.

An other interesting geometrical object whose time evolution we are going to study is the largest spin cluster. In fact, in the problem of percolation, the fraction of occupied sites belonging to the largest cluster represents, in the thermodynamical limit, the order parameter of the system. In the limit $L \to +\infty$ and as $p \to p_c^-$ (with p_c the threshold site occupation probability) the largest cluster becomes the incipient infinite cluster present at the critical point, and thus a fractal object. In particular, its size (or area), that we denote by A_c, and the length of its interface, denoted by l_c, are related to its linear size l by

$$A_c \sim l^{D_A} \ , \qquad\qquad l_c \sim l^{D_\ell} \ , \tag{1.17}$$

as $l \to +\infty$, with D_A the area fractal dimension and D_ℓ the interface fractal dimension. These dimensions can be exactly computed for the critical points of the q-state Potts model in two dimensions for $0 < q \leq 4$ (where $q = 2$ for the Ising model and $q \to 1$ for percolation) through a Coulomb gas formulation [27]. The parameter κ, related to q through $\sqrt{q} = -2\cos(4\pi/\kappa)$, determines the universality class of the model near criticality. The above-mentioned fractal

dimensions are then expressed in the following form

$$D_A = 2 - \frac{\beta}{\nu} = 1 + \frac{3\kappa}{32} + \frac{2}{\kappa} , \qquad D_\ell = 1 + \frac{\kappa}{8} , \tag{1.18}$$

where β is the critical exponent of the order parameter and ν that of the equilibrium correlation length. For $2d$ critical percolation $\kappa = 6$ [28] and thus

$$D_A = \frac{91}{48} \simeq 1.8958 , \qquad D_\ell = \frac{14}{8} = 1.75 . \tag{1.19}$$

We will show the time evolution of the observables A_c and l_c for the KIM evolving with Glauber dynamics and study their finite-size scaling properties. However, a clarification on the definition of l_c as the length of the interface of the largest spin cluster is in order. As we have explained above the interface of a spin cluster can be composed of many mutually disjoint hulls. For the calculation of l_c we are going to consider only the contribution deriving from the external hull, in the case in which the largest cluster is not percolating, or the one from the two wrapping hulls, in the case the largest cluster is percolating, since they are the longest ones and thus their scaling properties are expected to suffer less from the effects of the discreteness of the lattice.

A quantity which plays a central role in percolation problems is the *number density of domain areas*, $N(A)$, which is defined as the number of clusters of occupied sites of size A per unit area of the system. At the critical percolation point, $N(A)$ is given by a power law

$$N(A) \sim A^{-\tau_A} , \tag{1.20}$$

with τ_A a characteristic exponent (also called Fisher exponent) related to D_A, the fractal dimension of the incipient percolating cluster at the percolation critical point, by [29]

$$\tau_A = 1 + \frac{d}{D_A} = \frac{187}{91} \approx 2.0549 , \tag{1.21}$$

where d is the dimensionality of the lattice, $d = 2$ in our case.

In order to study the statistics of domains in the coarsening process appearing in the kinetic spin models (on finite systems), we introduce a dynamical number density of *spin cluster* areas, tha we denote by $\mathcal{N}(A, t, L)$. In the KIM scenario, $\mathcal{N}(A, t, L)$ is the number of spin clusters of area A being present at time t in the dynamics after the quench, for a system of linear size L, per unit area of the system. In general, $\mathcal{N}(A, t, L)$ is given by the sum of two contributions

$$\mathcal{N}(A, t, L) \simeq N(A, t) + N_p(A, t, L) , \tag{1.22}$$

with the first term being the contribution to the number density due to domains with linear size much smaller than that of the system, and the second one being instead the contribution from domains with size that is comparable to that of the whole system, including percolating spin clusters. The first contribution, $N(A, t)$, is, in fact, the one that would be present alone in the case of $L \to +\infty$, while the contribution $N_p(A, t, L)$ is explicitly included in order to take into account finite-size effects (hence the dependence on L). N_p weighs mostly spin clusters that are percolating, but also spin clusters that, although not percolating, have a linear size which is comparable to L and thus are highly subjected to boundary effects.

Our conjecture is that, as the system approaches the critical-percolation-like scaling regime, which would occur in a typical time t_p, the term N_p becomes dependent on A and L only through A/L^{D_A} reflecting the scaling behavior of the incipient percolating cluster at

critical percolation, while the contribution $N(A,t)$ given by non-percolating clusters gets an algebraic decay similar to the one at critical percolation, namely $N(A,t) \sim C(t)\, A^{-\tau_A}$, with $C(t)$ a particular time-dependent prefactor to be determined, and τ_A the Fisher exponent of $2d$ critical percolation, namely $\tau_A = 187/91$.

An approximate expression for the time-dependence of the number density of non-percolating domains, $N(A,t)$, was derived in [10, 11] for the $2d$ NCOP dynamics by assuming that, after a sufficiently long time, the domain growth can be reduced to the motion of independent domain walls governed by a curvature-driven mechanism. Essentially this argument leads to

$$N(A,t) \simeq \frac{2c_d\,[\lambda_d(t-t_p+t_0)]^{\tau_A-2}}{[A+\lambda_d(t-t_p+t_0)]^{\tau_A}} \qquad t \geq t_p\ , \tag{1.23}$$

where $\tau_A = 187/91$ is the Fisher exponent of $2d$ critical percolation, $c_d \simeq (\tau_A-2)(\tau_A-1)/2 \approx 0.0289$ [11], λ_d is a parameter related to the diffusion coefficient of the domain walls, and t_0 is a characteristic cutoff time such that $\lambda_d t_0 = 1$. In order to obtain this expression it was assumed that, at a certain time t_p, the system has reached a critical percolation state and that, for $t \geq t_p$, the curvature-driven motion of domain walls is the only mechanism governing the domain growth.

Similar arguments were used in [13] to derive an approximate expression for $N(A,t)$ in the case of locally conserved order parameter (LCOP) coarsening, yielding

$$N(A,t) \simeq \ell_d(t)^{-4}\, \frac{2c_d\,\left(\frac{A}{\ell_d(t)^2}\right)^{\frac{1}{2}}}{\left[1+\left(\frac{A}{\ell_d(t)^2}\right)^{\frac{3}{2}}\right]^{\frac{2\tau_A+1}{3}}}\quad , \tag{1.24}$$

where $\ell_d(t)$ is the characteristic length associated to coarsening (or typical domain radius), which, for LCOP dynamics, should behave asymptotically as $\ell_d(t) \sim t^{\frac{1}{3}}$. Again this result is supposed to hold for times t after the system has already reached a critical percolation state. Note that both Eq. (1.24) and Eq. (1.23) can be rewritten as

$$N(A,t) \simeq \ell_d^{-4}(t)\, f\left(\frac{A}{\ell_d(t)^2}\right)\quad , \tag{1.25}$$

with the scaling function

$$f(x) = \begin{cases} 2c_d\ (1+x)^{-\tau_A} & \text{for NCOP dynamics} \\ 2c_d\ x^{\frac{1}{2}}\ (1+x^{\frac{3}{2}})^{-\frac{2\tau_A+1}{3}} & \text{for LCOP dynamics} \end{cases} \tag{1.26}$$

assuming also that $\ell_d(t) \simeq [\lambda_d(t-t_p+t_0)]^{1/z_d}$ and $t-t_p \gg t_0$. Note that, in the limit $x \to \infty$, both versions behave as $f(x) \sim 2c_d\ x^{-\tau_A}$, and thus we can use the approximation $N(A,t) \simeq 2c_d\ [\ell_d(t)]^{2(\tau_A-2)}\ A^{-\tau_A}$ for $A \gg \ell_d^2(t)$.

The scaling behaviour, in the continuum limit, of many $2d$ stochastic processes, as critical percolation, the critical Ising model, self-avoiding random walks, *etc.*, can be described by the Schramm-Loewner evolution (known also as stochastic Loewner evolution or SLE). An SLE with parameter κ, or SLE$_\kappa$, is essentially a family of conformally invariant random planar curves [30, 31, 32], with the parameter κ controlling how much the curve "turns". It has been shown [28, 33, 34] that the parameter κ is the same as the one in the aforementioned Coulomb gas formulation of the q-state Potts model, and it is linked to the central charge c

of the associated conformal field theory: for example, SLE_3 reproduces the domain walls in $2d$ critical Ising model, SLE_6 those of $2d$ critical percolation, etc.

The fractal dimension of the random curves in SLE_κ is given by $D_\ell(\kappa) = 1 + \kappa/8$. Thus, by measuring D_ℓ it is possible to obtain κ and, consequently, the type of criticality of the model. Our approach will be then to study the fractality of the percolating hulls (or domain walls) by analysing their scaling with L. This is done, for example, by studying the scaling behaviour of the interface of the largest spin cluster.

Another method that we will use is the analysis of the *winding angle* of the cluster hulls. The winding angle $\theta(x)$ between two points P and P' on a planar curve, such that the arc with extremes P and P' has length x, is defined as the incremental angle that the tangent to the curve is rotated by when moving from one point to the other one. For conformally invariant stochastic planar curves belonging to SLE_κ, $\theta(x)$ as a function of the arc length x behaves as [35, 27]

$$\langle \theta^2(x) \rangle = \mathrm{cst} + \frac{4\kappa}{8+\kappa} \ln x \ , \tag{1.27}$$

with the brackets $\langle \cdot \rangle$ denoting the average over all possible realisations of the stochastic process. In the dynamic problem we will deal with the time-dependent winding angle $\theta(x,t)$ measured for the hulls of the spin clusters. If the system were to attain a critical-percolation-like state or another type of $2d$ criticality (in general, any Potts model criticality) during the relaxation dynamics, we would then be able to observe $\langle \theta^2(x,t) \rangle$ satisfying the law expressed by Eq. (1.27) after having rescaled the curvilinear distance x by a proper dynamical length. In this way it is possible to distinguish between different types of criticalities.

However, Eq. (1.27) is satisfied in the continuum space limit, while the models are defined on a lattice. In Fig. 1.3 we show a schematic representation of the definition of θ on a lattice. To compute the winding angle for an arc of domain wall of length n (with n a positive integer), we start from one of the two extrema and we walk along the interface of the spin cluster (defined on the dual lattice) incrementing the tangent angle θ by a quantity $\Delta\theta$ each time the curve turns. Notice that on the square lattice $\Delta\theta$ can only take the values 0, $\pi/2$ or $-\pi/2$. The winding angle is then given by

$$\theta(n) = \sum_{k=1}^{n} \Delta\theta_k \tag{1.28}$$

with $\Delta\theta_k$ the increment corresponding to the k-th step of the walk. We always use the convention that the domain wall is travelled in the direction such that the interior of the domain is on the right side of the walker, and that right turns corresponds to $\Delta\theta > 0$, while left turns to $\Delta\theta < 0$. With these convention, one clearly sees that the external hull of a domain has total winding angle (that is to say, the winding angle from one point to itself) equal to 2π, while hulls that are in the interior have total winding angle equal to -2π. There might also be hulls that have zero total winding angle. These are hulls that wrap around the system. For this reason, the total winding angle can also be used to determine whether a domain wall wraps or not. Notice also that the quantity in Eq. (1.27) must not depend on the starting point P on the arc. Hence, for a given domain wall, we average $\theta^2(n)$ over all possible arcs of length n that are part of it.

In the framework of percolation theory, a useful tool to study the geometrical properties of clusters of occupied sites is the *pair connectedness function*, $g(r)$. This quantity is defined as the probability that two lattice sites separated by a distance r belong to the same cluster. At critical percolation in two dimensions, the behaviour of $g(r)$ for large r ($r \gg r_0$, with r_0

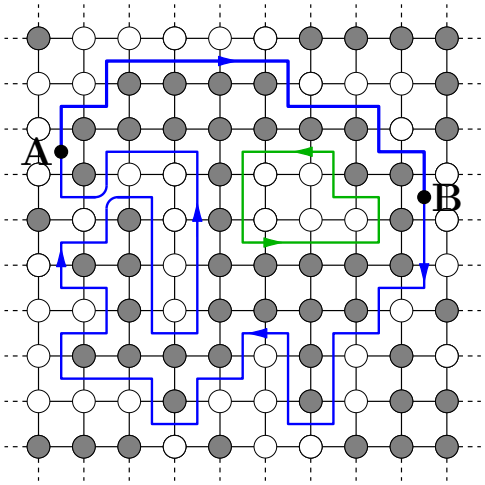

Figure 1.3: A schematic representation of the way we measure the winding angle for domain walls of spin clusters on a square lattice. The figure presents a 10×10 square lattice mesh, where circles represent lattice sites. Gray circles correspond to $+1$ spins, while white ones to -1 spins. We highlight two domain walls forming the interface of a "gray" spin cluster: the blue one is the *external* hull, *i.e.* the hull that encloses the spin cluster; the green one is an *internal* hull. The arrows drawn on the hulls indicate the direction along which they are travelled in order to compute the winding angle, clockwise for external hulls, anti-clockwise for internal ones. As an example, the winding angle corresponding to the arc $\widehat{AB}$ of length 13 (number of unsatisfied lattice bonds traversed by the wall) on the blue domain wall is $\Delta\theta_{\widehat{AB}} = +\pi$. The total winding angle for the external domain wall is 2π, while it is -2π for the internal one.

the lattice spacing) is known [29, 36, 37]

$$g(r) \sim r^{-2\Delta}\,, \tag{1.29}$$

where $\Delta = 2 - D_A$, D_A being the fractal dimension of critical percolation clusters.

In order to assess the presence of a critical-percolation-like regime in the coarsening process occurrying in the quench dynamics of the Ising model, we introduce an analogous quantity for a spin system. On a square lattice:

$$g(r,t) = \frac{1}{4L^2} \sum_i \sum_{i_r} \langle \gamma_{i,i_r}(t) \rangle \tag{1.30}$$

where the first summation is taken over all the lattice sites, the second over the four sites i_r that are located at distance r from site i along the horizontal and vertical directions, and $\gamma_{i,j}(t) = 1$ if the sites i and j belong to the same spin cluster at time t, and equals 0 otherwise.

1.4 Percolation phenomena

In this Section we illustrate the argument that supports our claim of the presence of a critical-percolation-like scaling regime in the $2d$ KIM evolving with Glauber dynamics at a subcritical temperature. First, we show some snapshots of of an Ising model initially prepared in a fully disordered configuration ($T_0 = \infty$), evolving under zero-temperature

Glauber dynamics, and we highlight the fact that, at a sufficiently long time after the quench, the spin configuration consists essentially of one or more large spin clusters, percolating along a certain direction, that are "stable" with respect to the microscopic stochastic dynamics. Second, we show the time evolution of the size of the largest spin cluster and propose a scaling argument that we use to explain how the system approaches a critical-percolation-like scaling regime. In particular we introduce the new time-dependent characteristic length $\ell_p(t)$ that grows faster than $\ell_d(t)$ and represents the length scale up to which the geometrical and statistical properties of the spin clusters resemble those of critical percolation. Finally, we give evidence of the presence of critical percolation features by showing the time evolution and scaling behaviour of the pair connectedness function defined by Eq. (1.30).

The overall conclusion is that there exists a separation of length scales: on lengths smaller than $\ell_d(t)$, that is, the usual dynamical length associated to coarsening, the system behaves as it were already relaxed to the target equilibrium state; on length scales larger than $\ell_d(t)$ and up to $\ell_p(t)$, the system instead has the characteristic features of critical percolation (by looking at the fractal properties of large spin clusters and connectedness). For a system of linear size L, the typical time $t_p(L)$ corresponds approximately to the point at which the percolation criticality extends over the entire length L, that is $\ell_p(t_p) \sim L$.

1.4.1 Snapshots

The istantaneous domain pattern of a kinetic Ising model undergoing stochastic dynamics, be it the Glauber dynamics described in Sec. 1.2 or any other type of dynamics defined by some spin update rules, can help understand what are the mechanisms controlling the domain growth and the type of coarsening phenomena arising.

In Fig. 1.4 we show a series of snapshots of the spin configuration of an Ising model on a square lattice with periodic boundary conditions (PBC) and size $L = 128$, evolving under Glauber dynamics at $T = 0$. The initial spin configuration is drawn at random from equilibrium at infinite temperature, that is to say, by choosing the value of the spin at each site to be $+1$ or -1, independently site by site, with equal probability $1/2$.

Let us denote the time of first appearance of a percolating spin cluster by τ_p, for a given realisation of the stochastic dynamics: τ_p naturally depends on the initial condition and on the sequence of spin-flip events occurring up to the point when one of the spin cluster is percolating. For example, in the case of the Ising model on a triangular lattice, the initial condition corresponding to equilibrium at infinite temperature coincides with the critical percolation point, in the thermodynamic limit. For large system size, one would observe that a percolating spin cluster is almost always present in the initial spin configuration, hence one would have $\tau_p \simeq 0$. Instead, in the case of the square lattice, the initial condition is not critical, and indeed we observe that *typically* $\tau_p > 0$ for a finite system. In the particular case shown in Fig. 1.4, a spin cluster wrapping horizontally first appears at a time $\tau_p \leq 0.59$ (panel (b)).

One may be interested in the time evolution of this first percolating cluster appearing at the time $t = \tau_p$. In particular, one interesting question one may ask is whether this spin cluster is able to "survive" for all $t > \tau_p$ while preserving its topology, that is to say, whether the domain walls that enclose this cluster continue to percolate in the same direction for the rest of the evolution of the system, or if instead, at some point, they collide and break in smaller non-wrapping pieces. As demonstrated by the series of snapshots, the first wrapping cluster does not survive for long. In fact, it disappears after a relatively short time (panel (c)) and later is replaced by a new spin cluster that is wrapping in both directions (panel (d)).

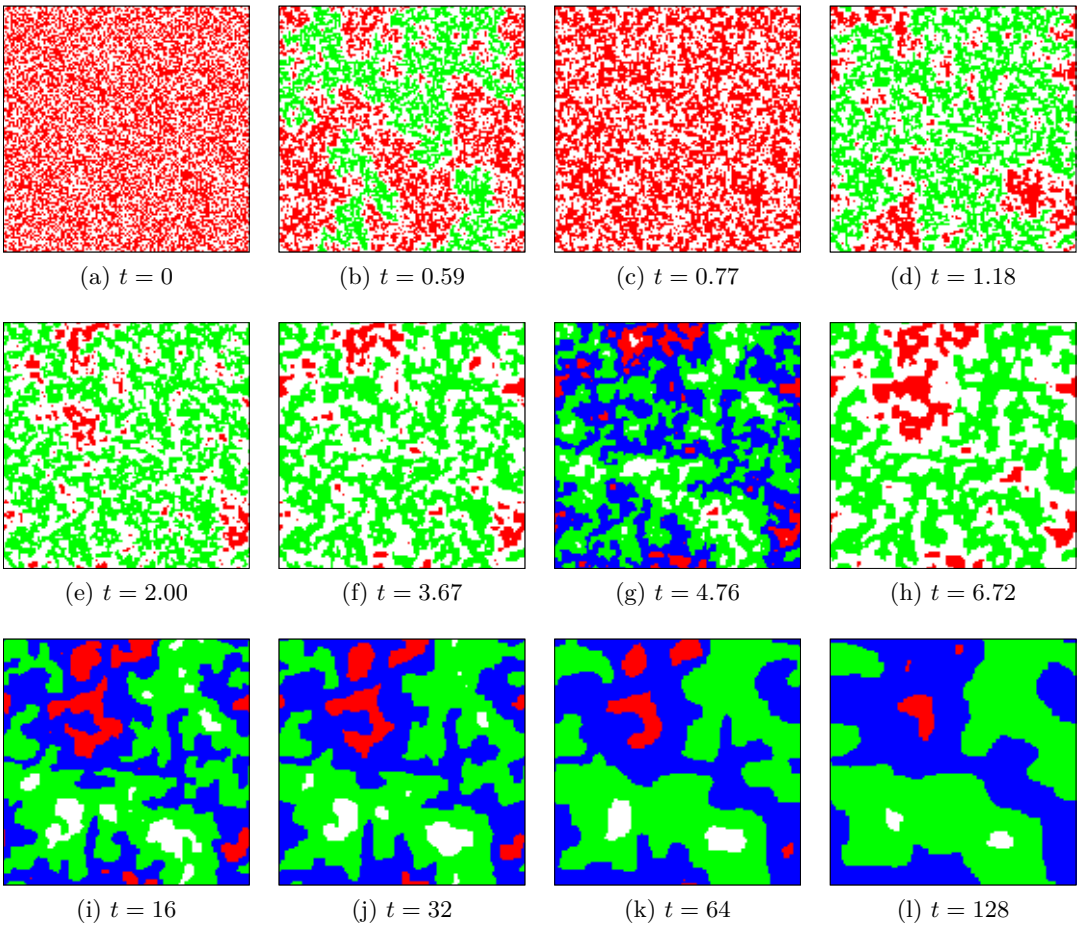

(a) $t = 0$ (b) $t = 0.59$ (c) $t = 0.77$ (d) $t = 1.18$

(e) $t = 2.00$ (f) $t = 3.67$ (g) $t = 4.76$ (h) $t = 6.72$

(i) $t = 16$ (j) $t = 32$ (k) $t = 64$ (l) $t = 128$

Figure 1.4: Some snapshots of an Ising model evolving under Glauber dynamics at temperature $T = 0$, on a square lattice with PBC and linear size $L = 128$. The initial state is a completely random spin configuration in which each site takes spin either $+1$ or -1 with equal probability (equilibrium at $T \to +\infty$). Red cells and white cells represent $+1$ and -1 spins, respectively. Spin clusters that wrap around the system are highlighted in different colours, green for spin $+1$ wrapping clusters, blue for -1 wrapping clusters. The time at which each snapshot has been taken is also indicated.

More precisely, the number of domain walls percolating across the sample, and the direction along which they are percolating, can change many times before reaching a "stable" state. The time t_p is roughly speaking the typical time at which the domain pattern reaches such stable state. Nonetheless, keep in mind that we use here the term "stable" not with the usual meaning. Indeed, percolating domain walls are not really energetically stable with respect to the relaxation dynamics. Eventually, the system is led, in a typical time $t_{\text{eq}} \sim L^2$, to the equilibrium state at the target temperature T of the quench. For $T < T_c$ this corresponds to a state in which no long domain walls are present, but only small and very rare non-percolating ones caused by thermal fluctuations. The $T = 0$ Glauber dynamics represents an exception since, depending on the particular lattice geometry, flat percolating domain walls can be truly energetically stable.

For the particular case shown in Fig. 1.4, the time t_p corresponds approximately to $t = 16$ (panel (i)) or, more precisely, $t_p \leq 16$. At this time there are two large spin clusters of opposite spin orientation, both wrapping in the so-called "diagonal" topology (see Fig. 1.2), which survive at all subsequent times or, at least, until a time of order $t_{\rm eq} \sim L^2$. Indeed, we checked that the further evolution of the system set by the stochastic microscopic dynamics does not modify the way these large clusters percolate. The only effect of coarsening is to smoothen their walls, that continue to fluctuate independently one from each other. In this sense we say that the system has reached a topologically "stable" percolating pattern. In most cases, this is the situation realised by the dynamics at long times.

1.4.2 Largest cluster

In ordinary percolation, the area of the largest cluster of occupied sites (divided by the size of the system, L^2) is the order parameter of the transition. As we mentioned in Sec 1.3, right at the critical percolation point, the size of the largest cluster, A_c, scales as L^{D_A} with $D_A = 91/48$, where L is the linear size of the system.

In the case of the Ising model evolving under Glauber dynamics at $T < T_c$ and starting from a random initial condition, we know that at a short time τ_p a percolating spin cluster appears for the first time. We know that the percolating spin clusters become "stable", in the sense that was described in the previous Section, after a typical time t_p that scales with the system size as $t_p \simeq L^{z_p}$, with $z_p < z_d$ as observed in Refs. [14, 3, 38]. At this time the system is still far from the equilibrium state. In particular, the average magnetisation density m is very small due to the fact that there are usually two large spin clusters of opposite spin orientation, both with a radius comparable with the system linear size L.

In order to provide a better qualitative understanding of what is happening during the dynamics following a quench to zero temperature, we show in Fig. 1.5-(a) and (b) the time evolution of the largest spin cluster (LC) and second largest (SLC) densities (A_c/L^2) for single and independent realisations of the $T = 0$ Glauber dynamics, on a square lattice with PBC and linear size $L = 4096$. In the case shown in Fig. 1.5-(c), for an other independent realisation of the dynamics, we also show the fraction of sites belonging to the third largest cluster (TLC) and the fourth largest one (FLC). Finally in Fig. 1.5-(d), for yet an other realisation of the stochastic dynamics, we show the time evolution of the fraction of sites belonging to the largest cluster of spin $+1$, and the one for the largest cluster of spin -1. These data have been obtained through Monte Carlo simulations. Note that, for all the cases shown in those panels, we consider at any time t the largest spin cluster, second largest, etc. regardless of their history, that is to say, the spin cluster that is the largest at a given time t has not necessarily evolved from that on a previous time, even though one can argue that, at sufficiently long times, one can keep track of them.

As one can see, the sizes of the LC and SLC grow rapidly in all cases. After a time $t_1 \simeq 10$ they have a size that is comparable to that of a typical percolating cluster in random site percolation on a square lattice of same linear size (indicated as an horizontal dashed line), and, most importantly, they have opposite spin orientation, as it is shown in panel (d). On the contrary, the TLC and the FLC remain very small and are not percolating. The LC and SLC sometimes exchange, with these "exchanges" happening until a time $t_2 \simeq 50$. After this time they evolve separately, in the sense that the largest spin cluster at any subsequent time will be the one evolved from the largest at the time t_2, and analogously for the second largest one.

Approximately, t_1 can be identified with the time of first appearance of a percolating

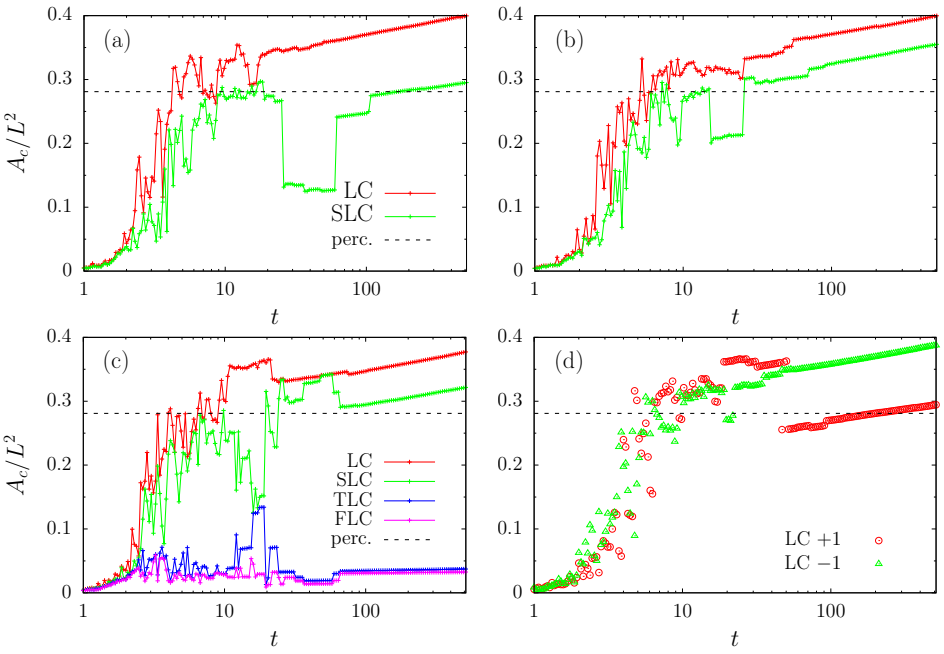

Figure 1.5: The time evolution of the size of the largest spin clusters for the $T = 0$ Glauber dynamics on a square lattice with linear size $L = 4096$, obtained by the numerical simulations. Each panel corresponds to a single realisation of the dynamics. In panels (a) and (b) we show the size of the largest (LC) and second largest (SLC) spin clusters. In panel (c), we also show the third largest (TLC) and fourth one (FLC). Finally, in panel (d) we show the fraction of sites belonging to the largest cluster of spin $+1$ (LC $+1$), indicated with red circles, and the one of the largest cluster of spin -1 (LC -1), indicated with green triangles, for another numerical run. The horizontal dashed line in all plots indicates the fraction of sites belonging to the largest cluster in critical site percolation on a square lattice, $A_c^{(\mathrm{perc})}/L^2$.

spin cluster, that is, $\tau_p \simeq 10$ on average for the particular realisations shown in Fig. 1.5. At this time, however, the domain walls of the largest clusters are still subject to large fluctuations: they can sometimes "collide" thus making one cluster percolate and an other one stop percolating or breaking into two pieces. It is only after a longer time, e.g. $t_2 \simeq 50 > \tau_p$ for the cases shown, that the two largest clusters stop exchanging themselves and become "stable": in this situation the distance between the domain walls become large enough so that they can evolve independently one from each other.

These features are quantified in Fig. 1.6, that shows the time evolution of the size of the two largest spin clusters averaged over many realisations of the dynamics. We observe that after a short time $t \simeq 10$ the largest cluster (LC) occupies already a large fraction of the system, namely $A_c/L^2 \simeq 0.32$. The second largest cluster (SLC) also occupies a sizeable part of the system at this time, say 25%. In the same figure we display the sum of the two (LC + SLC) and their difference (LC − SLC), still normalised by L^2.

Next, we observe that as time elapses, and due to the coarsening process, the areas of both largest spin clusters increase as a power of time. More precisely, a fit of the function $f(t) = C\, t^{\alpha}$ to the data $A_c(t)/L^2$ gives as a result the exponent $\alpha \simeq 0.0502$ (the fit is shown in the plot with a dashed line). As one can see, the second largest cluster grows in the same

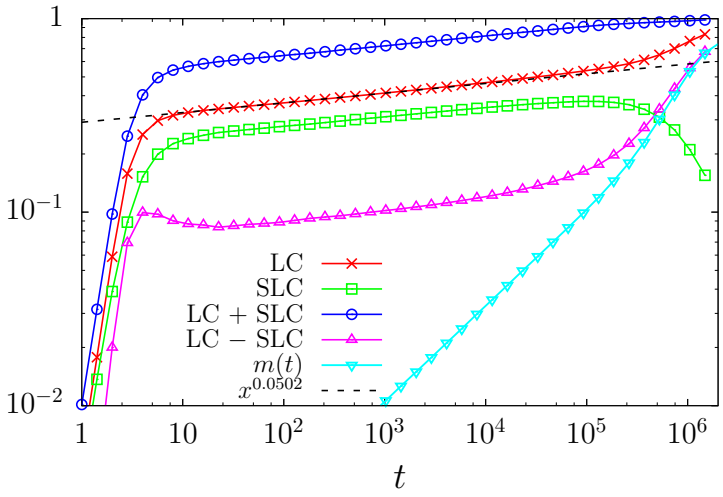

Figure 1.6: Evolution of the (averaged) area of the largest (LC) and second largest (SLC) clusters, their sum (LC + SLC) and their difference (LC − SLC) all normalised by the system area, L^2, and the magnetisation density $m(t)$, for the $T = 0$ Glauber dynamics on a square lattice with linear size $L = 4096$ and PBC. The dashed line is a power law fit to the data for the largest cluster.

way. This power law growth is observed up to a time $t' \simeq 10^5$.

The value of the exponent α can be easily understood using the following arguments. At the static percolation transition, the size of the largest cluster should scale with the system linear size L as $A_c \sim L^{D_A}$, with $D_A = 91/48$ the fractal dimension of the largest cluster of occupied sites in $2d$ critical percolation, see Sec. 1.3. Thus, the fraction of sites belonging to the largest cluster, should scale with the linear size of the system as

$$\chi_c \equiv \frac{A_c}{L^2} \sim L^{D_A-2} = L^{-\frac{\beta}{\nu}} \, , \tag{1.31}$$

where we introduced the exponents β and ν, which are the percolation critical exponents associated to the order-parameter (fraction of sites belonging to the incipient percolating cluster) and the correlation length, respectively.

Because of coarsening, the area of the largest (and second largest) cluster continues to grow at the expense of the smaller clusters that disappear. Therefore, one can think of extending the expression given by Eq. (1.31) to the dynamical case by introducing an effective dynamical lattice size, $\tilde{L}(t) = L/\ell_d(t)$ or, equivalently, an effective dynamical lattice spacing

$$r_0 \to \tilde{r}_0(t) = \ell_d(t) \, , \tag{1.32}$$

where $\ell_d(t)$ is the characteristic length describing the domain growth (that is to say, the typical domain radius, or the typical interwall distance, etc.), which is supposed to behave as $\ell_d(t) \sim t^{1/z_d}$, with $z_d = 2$, for NCOP coarsening. In other words, one can think about the coarsening process set up by the stochastic spin dynamics as a "dynamic" percolation problem, in which all lengths are measured with respect to $\ell_d(t)$. Hence, the natural extension of Eq. (1.31) is given by

$$\chi_c^{\rm dyn}(t, L) \equiv \frac{A_c(t, L)}{L^2} \sim \tilde{L}(t)^{D_A-2} = \left(\frac{L}{\ell_d(t)} \right)^{D_A-2} \, , \tag{1.33}$$

where we denote by $A_c(t, L)$ the average size of the largest spin cluster for the Ising model, on a finite $2d$ lattice with linear size L, evolving under the stochastic dynamics. Assuming $\ell_d(t) \sim t^{1/z_d}$ with $z_d = 2$, one then gets $A_c(t, L) \sim L^{D_A}\ t^{(2-D_A)/z_d} \propto t^{\frac{5}{96}}$, in excellent agreement with the exponent measured from the data obtained through the simulations. The regime of time where this scaling behaviour occurs will be referred to as critical-percolation-like dynamical scaling regime, and the time at which this regime establishes is t_p.

As one can see from Fig. 1.6, for the specific case $L = 4096$, the size of the largest cluster starts to grow faster than that of the second largest, on average, at times $t > t' \simeq 10^5$. However, the latter remains finite until very late times, since, in the case of the zero-temperature Glauber dynamics, there is a nonvanishing probability that the final state of the system is composed of two spin clusters percolating in a so-called *stripe* configuration, that is to say, there is a possibility that the system does not reach the fully magnetised state, but instead a spin configuration with flat interfaces (which are stable against the single-spin flip dynamics at $T = 0$). This situation indeed happens approximately with probability $1/3$ [6, 7]. In any case, at this stage of the relaxation dynamics, the scaling behaviour given by Eq. (1.33) is no more satisfied. We also find that the two largest spin clusters, which have opposite spin orientation, are, most of the times, the only ones surviving. As a consequence, for $t > t'$ the magnetisation density is approximately equal to the difference (indicated by LC − SLC in the plot) between the largest and the second largest spin cluster densities. This last regime of the dynamics corresponds to the final equilibration and we expect that the time t', at which the growth of the largest spin clusters changes behaviour, scales with L as $t_{\rm eq}(L) \sim L^2$.

Summarising, what we observe is that, for a large period of time, namely for t such that $t_p \leq t < t_{\rm eq}$ with $t_p \ll t_{\rm eq} \sim L^2$, the two largest spin clusters grow with the same power law and satisfy dynamical scaling with respect to the coarsening length $\ell_d(t)$. More precisely, $A_c(t) \propto \ell_d(t)^{2-D_A}$, with D_A the fractal dimension of the largest cluster in $2d$ critical percolation. For times $t > t_{\rm eq}$, the system enters in the final equilibration regime, where instead the fractal behaviour ascribed to critical percolation is lost.

We now focus on the scaling properties associated with the *approach to* critical percolation. As we have already stated, a time $t_p > 0$ is needed to reach the "stable" critical percolation state. In Ref. [14] it was conjectured that $t_p(L) \sim L^{z_p}$ with $z_p < 2$. We recall that t_p is not the time at which a percolating cluster first appears in the system. In fact, a percolating cluster first appears at an earlier time, τ_p, that does not necessarily scale with the system size L as t_p does. On the triangular lattice, for example, the critical value of the occupation probability is $p_c = 1/2$ and thus $\tau_p = 0$, since there is already one percolating spin cluster in the initial fully-disordered spin configuration.

With this fact in mind, the most natural finite-size scaling would be given by

$$\frac{A_c(t, L)}{\ell_d(t)^2} \sim \tilde{L}(t)^{D_A}\ f_c\left(\frac{t}{t_p(L)}\right)\ , \tag{1.34}$$

with $t_p(L) \sim L^{z_p}$, and f_c some unknown scaling function that satisfies $f_c(x) \sim$ const. as $x \to +\infty$. The meaning of this scaling is that, for times $t \gg t_p$, the system is in the so-called critical-percolation-like dynamical scaling regime, and thus the largest cluster must have the same fractal dimension as in critical percolation when all lengths are rescaled by $\ell_d(t)$. This is shown in the left panel of Fig. 1.7 where we show the quantity $A_c/L^{D_A}\ell_d(t)^{2-D_A}$ with D_A the fractal dimension of the percolating cluster in $2d$ critical percolation and $\ell_d(t) = \ell_G(t)$ the dynamical length obtained as the inverse of the excess-energy (see Eq. (1.16)), plotted against the rescaled time t/L^{z_p}, for various system sizes. We took $z_p = 1/2$, the value estimated in

Ref. [14] for the zero-temperature Glauber dynamics on a square lattice. The data roughly collapse on a master curve as expected, but there are still some finite-size corrections for $t/L^{z_p} < 1$ to be accounted for.

In the plot we have also included the value of the ratio $A_c^{(\mathrm{perc})}/L^{D_A}$ measured for critical (random) site percolation on a square lattice: $A_c^{(\mathrm{perc})}/L^{D_A} \simeq 0.6683$. Notice that for $t \gg t_p \sim L^{z_p}$, the rescaled A_c matches this constant almost perfectly. However, at sufficiently long times this scaling is broken: A_c starts to grow from the plateau and eventually will approach the equilibrium value (not reached by the numerical simulations).

In order to obtain a better finite-size scaling, the new proposal is to scale the data as a function of $\ell_p(t)/L$, with the "percolation" dynamical length $\ell_p(t)$ having the following meaning. The fractal behaviour that is ascribed to $2d$ critical percolation can be observed over distances r such that $\ell_d(t) \ll r \leq \ell_p(t)$, while for $r > \ell_p(t)$ the geometrical properties of the domain pattern would still be those of the initial state. The time t_p at which the critical percolation properties are extended to the entire system would then be given by $\ell_p(t_p) = L$. Next, we assume the following form for $\ell_p(t)$,

$$\ell_p(t) \simeq \ell_d(t)\, t^{1/\zeta} \ , \tag{1.35}$$

with the exponent ζ to be determined. Notice that, if one assumes $\ell_d(t) \sim t^{1/z_d}$ in the range of times close to t_p, then one gets the following relation between the exponents z_d, ζ and the exponent z_p introduced in Ref. [14],

$$\frac{1}{z_p} = \frac{1}{\zeta} + \frac{1}{z_d} \ . \tag{1.36}$$

However, in the early stages of the coarsening dynamics the dynamical characteristic length $\ell_d(t)$ can be very far from the asymptotic power law $\ell_d(t) \simeq t^{1/z_d}$, while it is exactly at these times that the approach to the critical percolation state occurs. For this reason, we are always going to use the numerical estimate of $\ell_d(t)$ from the simulations, namely, the estimate given by the excess-energy, $\ell_G(t) = \epsilon(t)^{-1}$ with $\epsilon(t)$ defined by Eq. (1.16). In Sec. 1.5.1 we will give an insight on $\ell_G(t)$.

The scaling argument in Eq. (1.34) is then modified to

$$\frac{A_c(t,L)}{\ell_d(t)^2} \sim \tilde{L}(t)^{D_A}\ f_c\left(\frac{\ell_p(t)}{L}\right) \ , \tag{1.37}$$

where again the scaling function f_c is satisfying $f_c(x) \sim$ const. as $x \to +\infty$. This finite-size scaling is done in Fig. 1.7 − right panel, where we plot the rescaled largest cluster size, $(A_c/L^{D_A})\ \ell_d(t)^{2-D_A}$, against the rescaled time $t/\left(L/\ell_d(t)\right)^{\zeta}$, taking $\ell_d(t) = \ell_G(t)$. Note that rescaling time as $t/\left(L/\ell_d(t)\right)^{\zeta}$ is equivalent to using the rescaled length $\ell_p(t)/L$, once one assumes $\ell_p(t) \simeq \ell_d(t) t^{1/\zeta}$. The value of the exponent ζ is found by looking at the best collapse of the rescaled data. In the specific case shown in Fig. 1.7, zero-temperature Glauber dynamics on a square lattice, the value which yields the optimal result is approximately $\zeta = 0.50$.

If one uses Eq. (1.36), $\zeta = 1/2$ implies $z_p = 2/5 = 0.4$, a value which is slightly different from that estimated with other methods in Ref. [14], namely $z_p = 0.5$. We find, however, that in all cases our scaling argument produces a better result and thus we stick to this way of reasoning in the remainder of this Chapter and for all other types of stochastic spin dynamics studied in the rest of this Thesis.

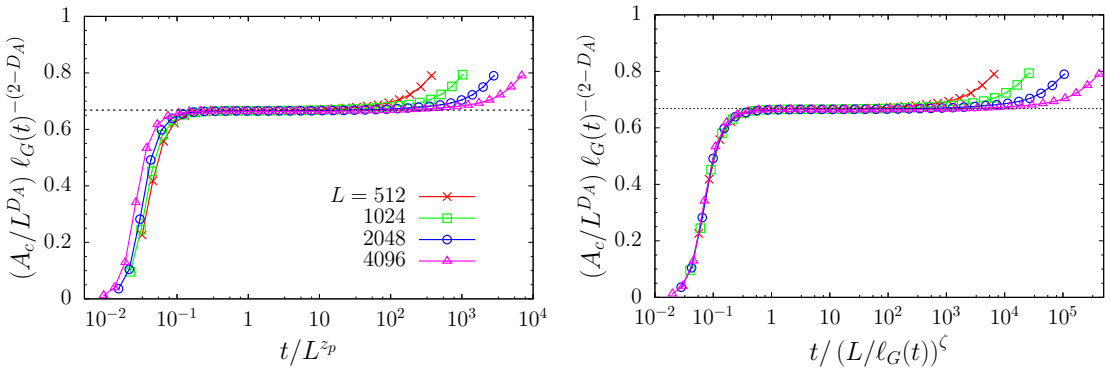

Figure 1.7: Measurement of the (average) size A_c of the largest cluster for the $T = 0$ Glauber dynamics on a square lattice with PBC, for various values of L, the linear size of the system. A_c is scaled as $\ell_G(t)^{-(2-D_A)}A_c/L^{D_A}$, where $\ell_G(t)$ is the characteristic length obtained from the excess energy, taken as a measure of $\ell_d(t)$, and $D_A = 91/48$ is the fractal dimension of largest cluster in $2d$ critical percolation. On the left, the data is plotted against the rescaled time t/L^{z_p}, with $z_p = 0.5$, while against $t/(L/\ell_G(t))^{\zeta}$, with $\zeta = 0.5$, in the right panel. In both panels, the dashed horizontal line corresponds to the value of the ratio A_c/L^{D_A} for critical $2d$ random site percolation on a square lattice, namely $A_c/L^{D_A} \simeq 0.6683$.

Let us stress the fact that the assumption in Eq. (2.1) is purely based on empirical evidence. It is indeed the simplest form that agrees with the scaling analysis. Unfortunately, we were not able to find a rigourous justification from the microscopic dynamics. In general one can think of more complicated forms, while $\ell_p(t)$ retaining the same meaning from a physical point of view.

1.4.3 Pair connectedness function

The correlation function used to characterise percolation is the so-called *pair connectedness* $g(r)$ which measures the probability that two sites at a distance r belong to the same cluster. In the context of percolation clusters are made of connected occupied lattice sites, while, in our problem, we need to consider clusters of connected sites that have same spin. In Sec. 1.3 we introduced the definition of the time-dependent $g(r,t)$ for a spin system undergoing quench dynamics, which is the one that we used for its practical computation in the Monte Carlo simulations.

In Fig. 1.8 we show this "two-point" function at several times, measured for the zero-temperature Glauber dynamics on a square lattice with PBC. This data is compared to the analogous one of critical percolation on a finite square lattice with PBC and same linear size. As one can see, the large distance behaviour, at sufficiently long times, is very close to that of critical percolation. More precisely, for the particular case shown in Fig. 1.8, the large-distance behavior is the same as that of critical percolation, apart from some time-dependent scaling factor, for times $t \geq 8$ approximately. Notice also that as r approaches the maximum distance $L/2$ (the maximum distance that one can probe in the case of a finite lattice with periodic boundary conditions) g, for both the dynamical problem and the static one, tends to become flat. This is due to the boundary conditions that we have chosen, PBC specifically, and it is the reason why one needs to simulate very large systems in order to appreciate the algebraic decay ascribed to critical percolation on a wide range of distances.

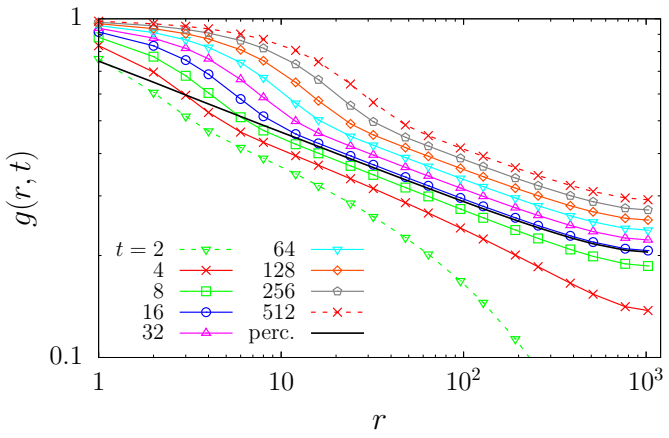

Figure 1.8: Pair connectedness function $g(r,t)$ vs. r for the $T = 0$ Glauber dynamics on a square lattice with $L = 2048$ and PBC, at the times shown in the key. We also indicate with a continuous black line the pair connectedness for critical percolation on a square lattice with same size and boundary conditions.

In Ref. [38] the scaling properties of the pair connectedness function were studied for disordered and clean Ising models evolving with kinetic Monte Carlo dynamics with NCOP spin update rules. It was shown in this article that the data for $g(r,t)$ can be collapsed onto the same master curve by rescaling the distance r by the characteristic length $\ell_G(t)$ obtained from the excess energy. This fact was explained in terms of a random site percolation problem at criticality with an effective lattice spacing $\ell_d(t)$, evaluated with $\ell_G(t)$, similarly to what we explained in the previous Section. Specifically, for a finite system the pair connectedness function is supposed to have the following scaling behaviour,

$$g(r,t,L) \sim \tilde{g}\left(\frac{r}{\ell_d(t)}, \frac{L}{\ell_p(t)}\right) , \tag{1.38}$$

before equilibration effects become important, that is to say, for $\ell_d(t) \ll L$. For times t beyond the characteristic time t_p at which stable percolating clusters appear, or equivalently for t such that $\ell_p(t) \gg L$, the second argument vanishes. In this limit, the short and long distance behaviour with respect to $\ell_d(t)$ can be distinguished. The expectation is then that

$$g(r,t) \sim \left(\frac{r}{\ell_d(t)}\right)^{-2\Delta} \qquad\qquad r \gg \ell_d(t) , \tag{1.39}$$

with $\Delta = 2 - D_A = 5/48$ ($D_A = 91/48$), *i.e.* the same scaling behaviour as in $2d$ critical percolation.

This scaling is shown in Fig. 1.9 – left panel, where we display the quantity $(r/\ell_G(t))^{2\Delta} \cdot g(r,t)$ plotted against r. Again, as explained in the previous section, we take $\ell_G(t)$ as the numerical estimate of $\ell_d(t)$, the usual coarsening length. We also needed to multiply the pair connectedness $g(r,t)$ for the dynamical problem by a factor $\alpha \simeq 0.67$ so that it could be collapsed exactly onto the data relative to critical percolation for large distances. In fact, the two have different normalization, because of the way they are defined. Moreover, $\ell_G(t)$ can also contain a pre-factor, *i.e.* $\ell_d(t) \propto \ell_G(t)$, which is not included in its definition. Notice also that $g_{\rm perc}(r = 1) = p_c^2$ where $p_c \simeq 0.5927$ is the critical occupation probability for percolation on a square lattice.

The behaviour of $g(r,t)$ is very different from that of critical percolation at small distances. Indeed, for distances $r < \ell_d(t)$ the domain pattern has already the properties of the equilibrium state at the target temperature of the relaxation dynamics. This is shown in the right panel of Fig. 1.9, where we plot the quantity $g(r,t) \cdot (r/\ell_G(t))^{2\Delta}$ against the rescaled distance $r/\ell_G(t)$. With this scaling, the short-distance behaviour is correctly collapsed.

Overall, the results presented in this Section confirm that, at sufficiently long times, critical percolation properties can be measured once one rescales all lengths by $\ell_d(t)$, the usual growing length associated with coarsening, or, equivalently, if one considers an effective dynamical lattice spacing $\tilde{r}_0(t) = \ell_d(t)$.

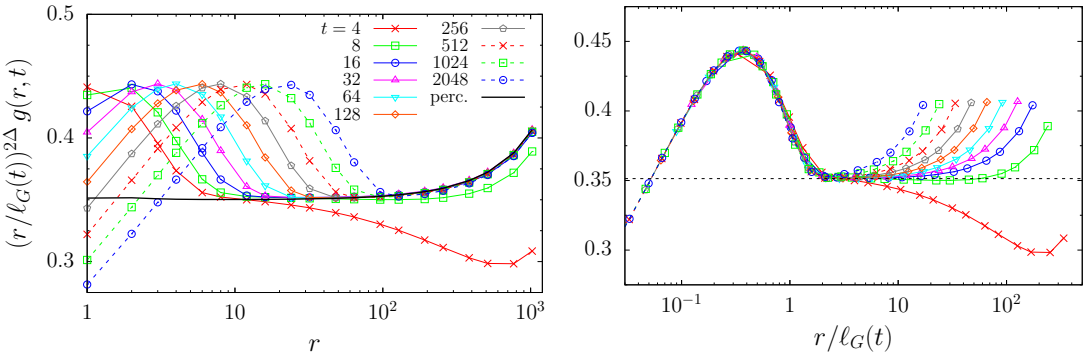

Figure 1.9: Left panel: rescaled pair connectedness $(r/\ell_G(t))^{2\Delta} \cdot g(r,t)$ against r for the $T = 0$ Glauber dynamics on a square lattice with $L = 2048$ and PBC, at the times shown in the key. $\ell_G(t)$ is the characteristic length obtained as the inverse of the excess energy and $\Delta = 2 - D_A$, with $D_A = 91/48$ the fractal dimension of the incipient percolating cluster in $2d$ percolation. We also show the analogous data for critical percolation on a square lattice of same size and boundary condition, $r^{2\Delta} \cdot g_{\rm perc}(r)$ (black solid line). The data for the dynamical problem has also been multiplied by a factor $\alpha \simeq 0.67$ in order to make it collapse onto that of critical percolation, for long distances. Right panel: rescaled pair connectedness $(r/\ell_G(t))^{2\Delta} \cdot g(r,t)$ plotted against the rescaled distance $r/\ell_G(t)$, at the same times as in the left panel. The horizontal dashed line is at p_c^2, with $p_c \simeq 0.5927$ the critical occupation probability for percolation on a square lattice.

1.5 Detailed numerical analysis

Now that we have provided an analysis on some of the main aspects of the coarsening dynamics that support our claim of the presence of a critical-percolation-like scaling regime, we delve further in the study of all the other observables listed in Sec.1.3. The order of presentation in this Section is the following:

- In Subsec. 1.5.1 we show the measurement of the excess energy growing length. This measurement provides the estimate for the usual dynamic growing length $\ell_d(t)$.

- In Subsec. 1.5.2 we analyse the time evolution of the the wrapping probabilities for the dynamics on finite systems, showing that as $t \to t_p(L)$, they approach the values of critical percolation.

- In Subsec. 1.5.3 we show the measurements of the variance of the winding angle along domain walls, which allow us to determine precisely the type of criticality that the fractal behaviour of these wall can be ascribed to.
- In Subsec. 1.5.4 we provide a thorough study of the dynamical scaling behaviour of the size of the largest cluster and the length of its walls, expanding the analysis given in Sec. 1.4.2.
- In Subsec. 1.5.5 we consider the time evolution of the size distribution of the spin clusters highlighting the presence of different scaling regimes. We also show that the size distribution of the largest cluster (or that of the percolating spin clusters) for the KIM can be matched to that of the incipient percolating cluster in $2d$ percolation on a finite lattice, after proper rescaling.

1.5.1 Growing length

The Ising model on a square lattice evolving with single spin flip stochastic dynamics is one of the simplest coarsening systems in dimensions $d = 2$ complying with the dynamic scaling hypothesis. At sufficiently long times, the curvature driven mechanism for scalar NCOP coarsening [39] yields the growing length

$$\ell_d(t) \sim t^{1/z_d} \qquad \text{with} \qquad z_d = 2 \, . \tag{1.40}$$

This growing length is easily recovered in numerical measurements of different observables. For example, the characteristic length $\ell_G(t)$ evaluated as the inverse of the excess energy (see Eq. (1.16)), as explained in Sec. 1.3, represents a good estimate of $\ell_d(t)$, at least in the early stages of the dynamics, when finite size effects do not have great influence over the domain growth. In Fig. 1.10 we show the time evolution of ℓ_G for the zero-temperature Glauber dynamics on a square lattice with PBC with linear size $L = 1280$. The exponent $z_d = 2$ establishes early after the quench, say at $t \simeq 10$, and is found over a wide time-interval, before finite-size effects force saturation. However, the early time dependence of the growing length is especially important for our study of the approach to the critical-percolation-like scaling regime. This is shown in a zoom included as an inset in the figure. In the following, in all the scaling analysis we will use the numerical evaluation of the growing length $\ell_G(t)$ as an estimate of the characteristic length $\ell_d(t)$.

1.5.2 Wrapping probabilities

In Fig. 1.11 (upper panel) we show the wrapping probabilities for the zero-temperature Glauber dynamics on a square lattice (with PBC), for different values of L, the lattice linear size, obtained through numerical simulations. We remind the reader that these probabilities are: $\pi_{\rm h}$, the probability that the spin configuration has at least one spin cluster wrapping in the horizontal direction only, $\pi_{\rm v}$, the probability for at least one spin cluster wrapping in the vertical direction only, $\pi_{\rm diag}$, the probability of having at least one spin cluster wrapping in so-called "diagonal" topology, and finally $\pi_{\rm hv}$, the probability of having a unique spin cluster wrapping along both directions in the so-called "cross" topology (see Sec. 1.3 for a detailed explanation). The first two, $\pi_{\rm h}$ and $\pi_{\rm v}$, are supposed to be identical because of the symmetry of the square lattice and the fact that the system has the same length along both directions, so we only show their sum. Following the scaling argument adopted in Sec. 1.4.2 for the analysis of the time evolution of the size of the largest cluster, data are shown as a

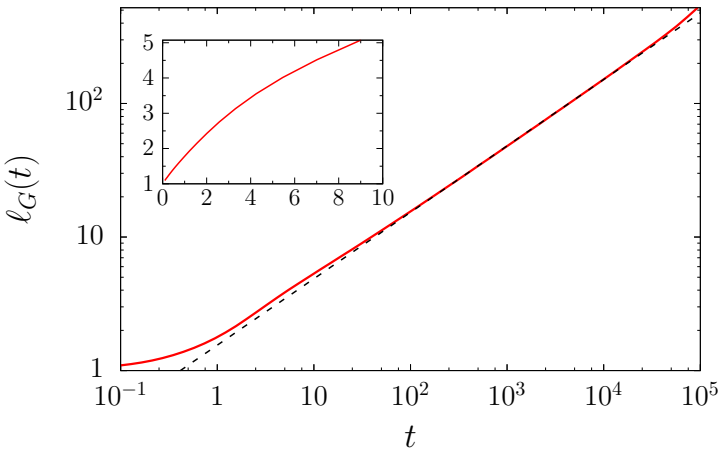

Figure 1.10: Zero temperature Glauber dynamics on a square lattice with linear size $L = 1280$ and PBC. The plot shows the time evolution of the characteristic length ℓ_G (indicated with a red solid line) obtained as the inverse of the excess energy. The black dashed line represents the best fit of the function $f(t) = a\, t^b$ to the data in the interval $[10, 10^4]$, yielding $a \simeq 1.54(1)$ and $b \simeq 0.4974(9)$. In the inset we show (in double linear scale) the same quantity in the time interval $[0, 10]$.

function of the rescaled time $t\,/\,(L/\ell_G(t))^\zeta$, where $\ell_G(t)$, the characteristic length obtained as the inverse of the excess energy, is taken as a measure of $\ell_d(t)$ the usual dynamic length scale associated to coarsening, and $\zeta \simeq 0.50$. The value of the exponent ζ which was chosen is the one that yields the best collapse of the data corresponding to different L. The curves for different system sizes scale relatively well at small values of the scaling variable and until 10^4 for the largest system size.

At a very short time (in terms of the scaling variable $t/(L/\ell_d(t))^\zeta \simeq 1$) after the quench, we observe that there exists always at least one percolating spin cluter, so that $\pi_{\rm hv}(t) + \pi_{\rm h}(t) + \pi_{\rm v}(t) + \pi_{\rm diag}(t) = 1$ for the later dynamics. In particular, at the time t such that $t/(L/\ell_d(t))^\zeta \simeq 1$ the wrapping probabilities get fixed around constant values that are very close to the corresponding critical percolation probabilities (shown with horizontal dotted lines in Fig. 1.11). The period of time during which the πs remain fixed on these plateaus increases with the size of the system. As an example, in the case of the dynamics for $L = 640$ (the largest size simulated) the plateaus corresponding to the critical percolation values last for almost eight decades of the scaling variable $t/(L/\ell_d(t))^\zeta$.

We can use the data shown in Fig. 1.11 to compute an estimate of the time t_p. As an approximate criterion, we assume that t_p corresponds to the time at which the probabilities πs reach the plateaus set by the values of ordinary critical percolation, that is to say, we assume t_p satisfies $t/(L/\ell_d(t_p))^\zeta \simeq 1$. If we use this relation (and using $\ell_G(t)$ as a numerical estimate for $\ell_d(t)$) we get the following estimates: $t_p \simeq 3.7(1)$, $4.9(1)$, $6.4(1)$, $8.5(1)$, $11.3(1)$ for $L = 40$, 80, 160, 320, 640, respectively. These are relatively short times compared to the typical equilibration time for NCOP dynamics, $t_{\rm eq} \sim L^2$, implying that most, if not all, numerical data in the literature lie in a regime in which the percolation structure has already established by a long time and thus is already under the effect of the late stages of coarsening.

If one assumes that $\ell_d(t)$ has already aquired the asymptotic form $\ell_d(t) \sim t^{1/z_d}$ with $z_d = 2$ at the times t of the same order of magnitude of t_p, then the relation $t/(L/\ell_d(t))^\zeta \simeq 1$ implies $t_p \sim L^{\zeta z_d/(\zeta + z_d)}$, so that we can express the explicit dependence of t_p on the system

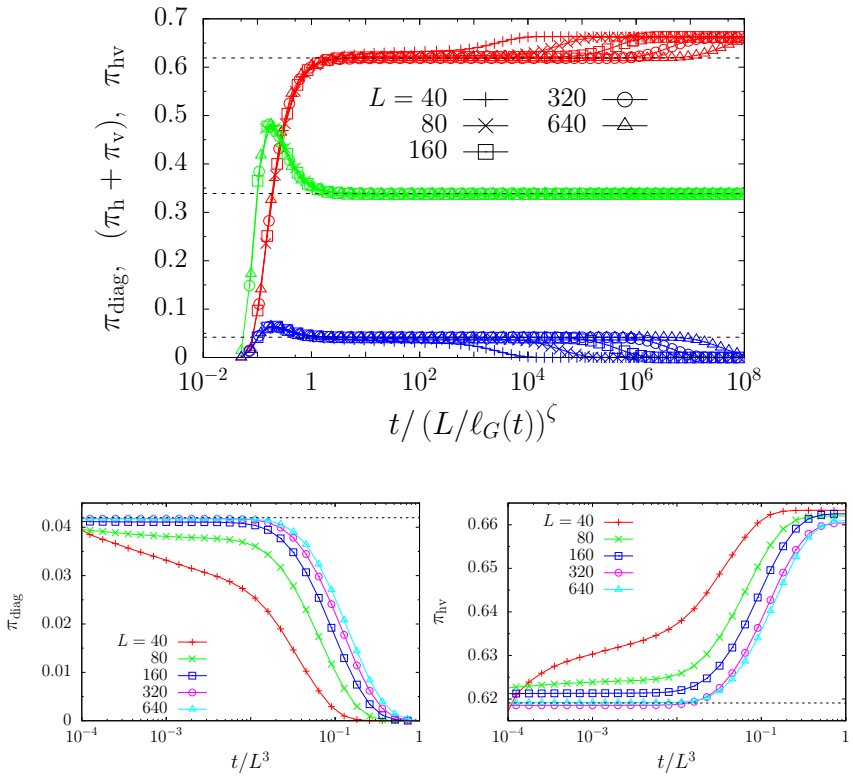

Figure 1.11: Ising model on a square lattice with PBC evolving under Glauber dynamics at $T = 0$, for various system sizes L. In the upper panel we show the probability $\pi_{\rm hv}$ that there exists a (unique) spin cluster wrapping in both directions of the lattice in the so-called "cross" topology (data above); the probability $\pi_{\rm h} + \pi_{\rm v}$ that there exists at least one cluster wrapping either horizontally or vertically (data in the middle); the probability $\pi_{\rm diag}$ that there exists a cluster wrapping diagonally (data below). Data are shown as a function of the rescaled time $t\ (L/\ell_G(t))^{\zeta}$, where $\ell_G(t)$, the characteristic length obtained as the inverse of the excess energy, is taken as a measure of $\ell_d(t)$, and $\zeta = 0.5$. In the lower panels, the probabilities $\pi_{\rm diag}$ (left) and $\pi_{\rm hv}$ (right) as a function of time scaled as t/L^3. The horizontal dashed lines represent the corresponding probabilities in critical percolation.

size, namely $t_p(L) \sim L^{z_p}$, with the exponent z_p related to ζ and z_d through $z_p = \zeta z_d/(\zeta + z_d)$. By using this argument and the fact that our estimate for ζ is $\zeta \simeq 0.50$, we get $z_p \simeq 0.40$.

At very late times, a crossover between the plateau corresponding to the critical-percolation-like scaling regime and the final equilibrium state appears. It corresponds to the disappearance of configurations with spin clusters percolating along a diagonal direction and the consequent increase in probability of clusters that percolate along both lattice principal directions (with the so-called "cross" topology). In fact, hulls winding in a diagonal direction are not stable under zero-temperature Glauber dynamics on the square lattice with PBC, even though they can appear very early and last for very long. This is due to the fact that, once they have established a *ladder* shape (see, for example, [6, 9]), they can move in the perpendicular direction by means of spin flips with no energy cost, and they can thus wander for a very long time before disappearing by annihilating with another "diagonal" hull. On the contrary, hulls that wind only in one direction remain topologically stable with respect to

the late time coarsening. Because of the curvature-driven mechanism, the horizontal (or vertical) wrapping hulls become increasingly smoother as the dynamics progresses until they are completely flat. At that point, they become "blocked" with respect to the zero-temperature Glauber dynamics. This is the reason why the probability $\pi_{\rm h}(t) + \pi_{\rm v}(t)$ remains fixed on the critical percolation value after the time t_p.

For the $T = 0$ Glauber dynamics, there is thus a difference between the late time behaviour of domains wrapping in only one direction and that of domains wrapping in both directions (either in the "cross" topology or the "diagonal" one): domains of the first kind eventually get freezed and lead the system to a so-called "striped" configuration; domains of the second kind, instead, can grow until covering the entire lattice leading to the true ground states. This observation was used in Refs. [8, 9] to compute the probability that a realization of the $T = 0$ Glauber dynamics on a square lattice, starting from an infinite temperature spin configuration, gets freezed in a striped state (or alternatively reaches the full magnetised state). It coincides with the probability $\pi_{\rm h}^{(p)} + \pi_{\rm v}^{(p)}$ (or $\pi_{\rm hv}^{(p)} + \pi_{\rm diag}^{(p)}$ for the full magnetised state) for critical percolation hulls. This fact suggests that around the time t_p the ultimate fate of the system is sealed and can be predicted by simply looking at the presence or not of domain walls wrapping in one direction of the lattice only.

The last regime scales with a different power of L, as shown in the lower panels in the same figure, where we display the probabilities $\pi_{\rm diag}$ (on the left) and $\pi_{\rm hv}$ (on the right). In fact, we can collapse approximately the curves $\pi_{\rm diag}$ and $\pi_{\rm hv}$ corresponding to the two largest L simulated, by plotting them against the rescaled time t/L^3. This result is in contrast with the expectation that the system should equilibrate with a typical time $t_{\rm eq} \sim L^2$ as predicted for NCOP coarsening dynamics.

1.5.3 Averaged squared winding angle

We now consider the time evolution of the variance of the winding angle related to spin cluster hulls, the observable $\langle \theta^2(x,t) \rangle$ defined in Sec. 1.3, for a KIM evolving with zero-temperature Glauber dynamics on a lattice with PBC. The goal of this analysis is to see whether, in a certain period of time and over a certain range of curvilinear lengths, $\langle \theta^2(x,t) \rangle$ reaches the form satisfied by the winding angle for $2d$ hulls in some type of criticality, that is $\langle \theta^2 \rangle \simeq {\rm cst} + \frac{4\kappa}{8+\kappa} \ln x$, with κ the parameter that identifies the associated SLE family of conformally invariant planar curves. We expect that, as the relaxation dynamics enters in the so-called critical-percolation-like scaling regime, that is, as $t \to t_p$, the dependence of $\langle \theta^2(x,t) \rangle$ on the curvilinear distance x takes the above mentioned form with $\kappa = 6$, the value that corresponds to percolation criticality.

In all the cases that are shown here, the winding angle θ has been computed for the hulls that make up the interface of the largest spin cluster. More precisely, θ has been measured for the external hull of the largest spin cluster, or the two wrapping hulls forming its interface in the case in which it is percolating (in only one direction of the lattice or in the so-called "diagonal" topology). The reason behind this choice is that we would like the hulls which we use to measure $\theta(x,t)$ to be as long as possible compared to the lattice unit spacing r_0, in order to probe large curvilinear lengths x over which θ (and in general any other geometrical property of the domain walls) is less affected by the discreteness of the lattice. This is desirable since the relation expressed by Eq. (1.27) is ideally valid in the continuum limit. This requirement is fulfilled by cosidering the external hull of the largest spin cluster, when it does not percolate, or the hulls that wrap around the system, that most of the time are part of the interface of the largest cluster. Note that, at a sufficiently long time after the quench,

even if the largest spin cluster is not percolating it can extend over a distance of order L.

In Fig. A.7, we show $\langle\theta^2(x,t)\rangle$, measured on the wrapping hulls that are part of the interface of the largest spin cluster, plotted against $\ln x$ with x the curvilinear distance along the hull, in the case of the $T=0$ Glauber dynamics on a square lattice with PBC and linear size $L=1280$. We observe that, for sufficiently large values of x, $\langle\theta^2\rangle$ as a function of $\ln x$ has a constant slope. There is, in fact, a crossover length $x_c(t)$ such that, for $x > x_c(t)$ we observe $\langle\theta^2\rangle \simeq a + b\ln x$, while for $x < x_c(t)$ the curve $\langle\theta^2\rangle$ approaches a constant. Moreover, a fit of the function $f(x) = a + \frac{4\kappa}{(8+\kappa)}\ln x$ to the data at $t \simeq 14.84$ for $x > 2$ yields $\kappa \simeq 5.90(1)$, that is rather close to $\kappa = 6$ expected for critical percolation cluster hulls. This means that the domain growth process imposed by the stochastic single spin-flip dynamics is characterised by a separation of length scales (at least at an early stage of the dynamics itself), as already discussed before: on length scales $x < x_c(t)$, wrapping domain walls have already the geometrical properties that are typical of the late stages of NCOP coarsening, that is to say, they are mostly smooth and, in the long time limit, they become eventually flat (think about the "striped" frozen states); instead, on length scales $x > x_c(t)$ these domain walls have the geometrical properties of cluster hulls at critical percolation. We expect $x_c(t) \sim \ell_d(t) \sim t^{1/z_d}$ with $z_d = 2$ since $\ell_d(t)$ is the dynamical length that controls the growth of ordered domains equilibrated at the target temperature of the quench (in this case $T=0$).

To test this argument, we plotted $\langle\theta^2(x,t)\rangle$ against $\ln(x/\ell_G(t))$, taking again the characteristic length $\ell_G(t)$, obtained as the inverse of the excess energy, as a measure of $\ell_d(t)$. The plot is shown in an inset in Fig. A.7 and, as one can see, the measurements corresponding to different times collapse one onto the other when performing this scaling.

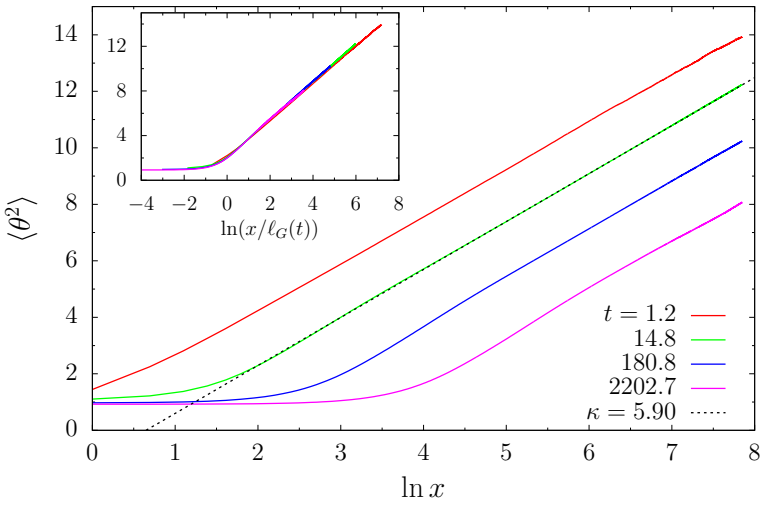

Figure 1.12: KIM evolving with zero-temperature Glauber dynamics on a square lattice. We show the average squared winding angle, $\langle\theta^2(x,t)\rangle$, against $\ln x$ with x being the curvilinear distance along a hull. The data are relative to the dynamics on a square lattice with PBC and $L = 1280$, and $\langle\theta^2\rangle$ was measured on the wrapping hulls that are part of the interface of the largest spin cluster (when it is wrapping). The straight dashed line represents a fit of the function $f(x) = a + 4\kappa/(8+\kappa)\ln x$ to the data in the "linear" region, for which we found $\kappa = 5.90$. The inset contains the same observable plotted against $\ln[x/\ell_G(t)]$ with $\ell_G(t)$ the characteristic length obtained as the inverse of the excess energy.

1.5.4 Largest cluster scaling

In Sec. 1.4 we exposed the main features of the approach to the critical-percolation-like dynamical scaling regime showing the time evolution of the size of the largest spin cluster and its scaling properties. Here we complete the analysis of this observable by taking into account also the same dynamics on the triangular lattice. We also analyse the scaling behaviour of the length of the hulls forming the interface of the largest cluster.

According to the claim expressed in Sec. 1.4.2, at a certain point of the relaxation dynamics, the system should reach a dynamical scaling regime with critical percolation properties. In particular, all the geometrical objects, like the area of the largest spin cluster and the length of the domain walls belonging to its interface, should obey, during this regime, scaling relations with the fractal dimensions of critical percolation, with respect to the effective dynamical system size $\tilde{L}(t) = L/\ell_d(t)$, that is

$$\frac{A_c(t,L)}{\ell_d(t)^2} \sim \text{const.} \times \tilde{L}(t)^{D_A} \ , \quad \frac{l_c(t,L)}{\ell_d(t)} \sim \text{const.} \times \tilde{L}(t)^{D_\ell} \ , \tag{1.41}$$

where A_c is the average size of the largest spin cluster, l_c the average length of the walls (or hulls) forming the largest cluster interface, and D_A and D_ℓ the fractal dimensions relative to the area of the incipient percolating cluster and to the length of its external wall, respectively, in $2d$ critical percolation. Notice that the length l_c and the area A_c must be rescaled by the unit of length $\ell_d(t)$ and the unit of area $\ell_d(t)^2$, respectively.

Let us consider the measurements for the case of a KIM evolving with zero-temperature Glauber dynamics on a finite triangular lattice with PBC and linear size L (with initial spin configuration drawn from equilibrium at infinite temperature, as usual). In Fig. 1.13, we show A_c/L^{D_A} (left panel) and l_c/L^{D_l} (right panel) both plotted against time t. We present the data obtained from numerical simulations for different values of L. In both cases, we also show a convenient power of the growing length $l_G(t)$, which is taken as an estimate of $\ell_d(t)$. Concerning A_c, in the right panel we plot $\ell_G(t)^{2-D_A}$ (multiplied by an arbitrary constant 0.6) and we observe that, up to a constant, it behaves similarly to A_c/L^{D_A}, apart from finite size corrections. The numerical value obtained at the earliest time (it corresponds to $t = 0$ but we show it at $t = 0.1$ in order to remain on a logarithmic scale) is in good agreement with the corresponding value for site percolation on a triangular lattice at the critical point, $A/L^{D_A} \simeq 0.655$, that is shown as a horizontal dashed line.

In regards to the domain wall length, l_c, it is important to clarify that the interface of a spin cluster can be made of multiple hulls (see Sec. 1.3 for the definition of domain wall on a lattice). In the case shown here we are considering separately the two main contributions to the (average) total length of the interface of the largest spin cluster: the contribution coming from the two wrapping hulls (having zero total winding angle), if the largest spin cluster is wrapping across the system, and the one coming from the external hull (having nonzero total winding angle), if the largest spin cluster is not wrapping across the system. We do not take into consideration the so-called internal hulls, that is to say, those ones that separate the spin cluster from the smaller clusters that are embedded inside it. Notice that these two contributions to the total interface may behave very differently. In fact, because of the curvature-driven domain wall motion that characterises the NCOP coarsening in the late stages, non-wrapping hulls are destined to disappear, while wrapping hulls can survive for the whole evolution of the system (since they eventually become flat). In the plot, we also show $\ell_G(t)^{1-D_l}$ which, apart from a proportionality constant and finite size corrections for large times, seems to reproduce very well the behaviour of l_c/L^{D_ℓ} (expecially the contribution

coming from wrapping hulls). The data for non-wrapping hulls is similar but with much stronger finite size corrections appearing in the late times.

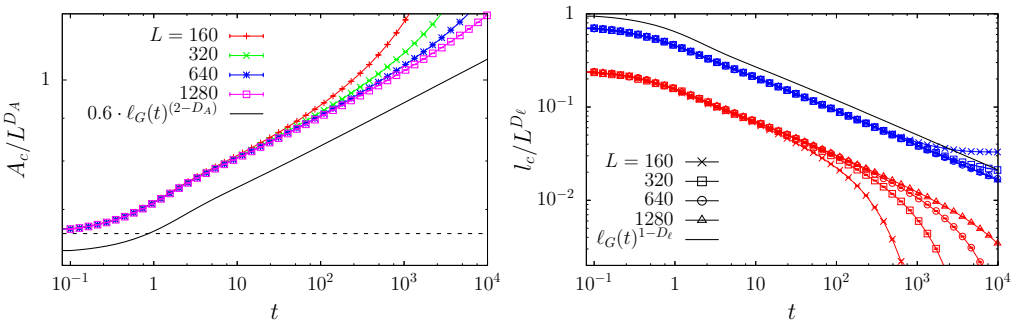

Figure 1.13: Analysis of the geometric properties of the largest cluster in the case of the $T = 0$ Glauber dynamics on a triangular lattice with PBC, for different values of L. On the left A_c/L^{D_A} vs. t, and on the right l_c/L^{D_l} vs. t, with A_c the size of the largest cluster and l_c the average length of its walls. D_A and D_ℓ are the fractal dimensions of the size and the interface of the percolating cluster in $2d$ critical percolation. The interface of the largest cluster has two contributions: one from the wrapping hulls (shown in blue) and the other from non-wrapping hulls (shown in red). The horizontal dashed line in the left panel corresponds to the ratio A_c/L^{D_A} for site percolation on a triangular lattice at the critical occupation probability, that is approximately 0.655.

From the plots in Fig. 1.13 we can conclude that a better analysis of data is achieved by plotting $(A_c/L^{D_A})\ \ell_G(t)^{-(2-D_A)}$ vs. t and $(l_c/L^{D_\ell})\ \ell_G(t)^{D_\ell - 1}$ vs. t. The two cases are shown in Fig. 1.14. If A_c and l_c obeyed the scaling relations expressed by Eq. (1.41) (assuming that $\ell_G(t) \propto \ell_d(t)$), then we should observe the data corresponding to different values of L collapse on the same master curve, and, precisely, on a constant. We note that, for $t \simeq 1$ and for very large L, the rescaled largest cluster size, $(A_c/L^{D_A})\ \ell_G(t)^{-(2-D_A)}$, develops a plateau around the constant 0.675, approximately. This plateau corresponds to the critical-percolation-like scaling regime. However, we also notice strong finite-size effects: after a certain time, which is longer for larger sizes, the curve $(A_c/L^{D_A})\ \ell_G(t)^{-(2-D_A)}$ starts to deviate from this plateau. For example, in the case of $L = 1280$, which is the largest system size simulated in this particular context, this plateau lasts for a period of time of order 10^2. In order to observe more clearly the establishment of the critical-percolation-like scaling regime we should have simulated system with much larger size, but even the data shown in Fig. 1.14 suggests the presence of such a regime. In the same plot we also show the expected value of the ratio A_c/L^{D_A} at the critical point of $2d$ site percolation on the triangular lattice (~ 0.655), indicated by a dashed horizontal line, and on the square lattice (~ 0.668), indicated by a dotted horizontal line. Similar results are obtained for the hull length, see the right panel in Fig. 1.14.: $(l_c/L^{D_\ell})\, \ell_G(t)^{(D_\ell - 1)}$ also develops a plateau after $t \simeq 5$ (notice, however, that the y-range of the plot is larger than that on the left panel). Again, the two contributions to l_c coming from wrapping hulls and non-wrapping ones have been separated, with the former ones being represented by continuous lines, the latter by dashed lines.

We have already shown the time evolution of the largest cluster size and its scaling properties in the case of the zero-temperature Glauber dynamics on the square lattice in Sec. 1.4.2. Here we complete the analysis by showing the scaling properties of the length of its interface, l_c. In the left panel of Fig. 1.15, we show l_c/L^{D_l} vs. t, for systems with

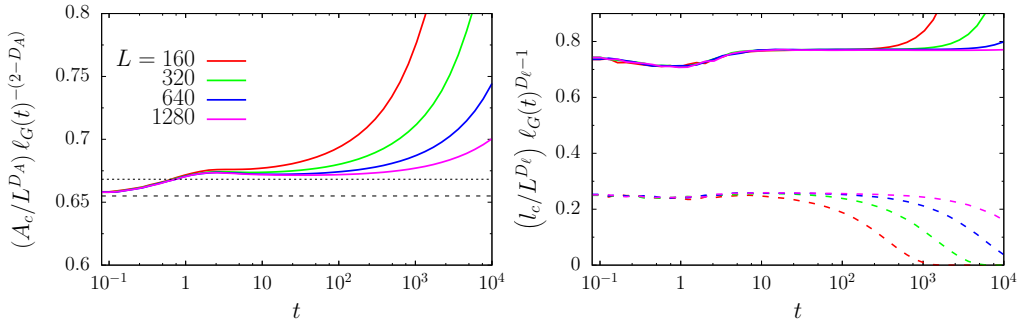

Figure 1.14: Analysis of the geometric properties of the largest cluster in the case of the $T = 0$ Glauber dynamics on a triangular lattice with PBC, for different values of L. On the left $(A_c/L^{D_A})\ \ell_G(t)^{-(2-D_A)}$ vs. t, and on the right $(l_c/L^{D_\ell})\ \ell_G(t)^{(D_\ell-1)}$ vs. t, where $\ell_G(t)$ is the characteristic length obtained as the inverse of the excess energy. As done in Fig. 1.13, the contributions to the largest cluster interface coming from wrapping (continuous lines) and non-wrapping hulls (dashed lines) have been separated. The colour code is the same in both panels.

different linear size. Again, we separate the contribution coming from wrapping domain walls, indicated by continuous lines, from the one coming from non-wrapping ones, indicated by dashed lines. We also show $\ell_G(t)^{1-D_\ell}$ to make a comparison, as was already done in the case of the dynamics on the triangular lattice. After a crossover time that is system size dependent, both types of hulls have a similar behaviour and they seem to be just proportional to $\ell_G(t)^{1-D_\ell}$ up to a second characteristic time (also dependent on L) where deviations caused by finite-size effects occur. As it was done for A_c/L^{D_A} in Sec. 1.4.2, it is possible to collapse the datasets corresponding to different L one onto the other in the small-t region by plotting $(l_c/L^{D_l})\,\ell_G(t)^{-(1-D_\ell)}$ against the rescaled time $t/(L/\ell_G(t))^{\zeta}$. As it was already explained, this rescaling of time is done to take into account the coarsening process occuring during the early-time regime, in which the system is approaching the critical-percolation-like state, with the introduction of the new characteristic length $\ell_p(t) \sim \ell_d(t)t^{\zeta}$, something that is not present instead in the case of the dynamics on the triangular lattice since the system is already at critical percolation at $t = 0$. The value of the exponent ζ that gives us the best collapse is $\zeta \simeq 0.50$ as in the case of the scaling of the largest cluster size, see Fig. 1.7.

1.5.5 Number density of domain areas

In this Section we present the analysis on the number density of domain areas, the observable $\mathcal{N}(A, t, L)$ defined in Sec. 1.3, obtained by numerical simulations of the KIM evolving with zero-temperature Glauber dynamics on a $2d$ finite lattice. Let us first recall some results, obtained both from numerical simulations and approximate analytical argument, that are known so far.

The time-dependent distribution of domain areas was already measured numerically in [10, 11], for the Glauber dynamics on a square lattice, at target temperature $T < T_c$, starting from an infinite temperature initial condition. Three distinct "regions" were identified in the functional form of $\mathcal{N}$. A first region corresponding to small domains or, more precisely, to those domains whose linear size is shorter than $\ell_d(t)$, in which $\mathcal{N}(A, t)$ is almost constant in A , just as in thermal equilibrium at $T < T_c$. A second region corresponding to domains with linear size larger than $\ell_d(t)$, in which $\mathcal{N}(A, t)$ has an algebraic decay in A, namely

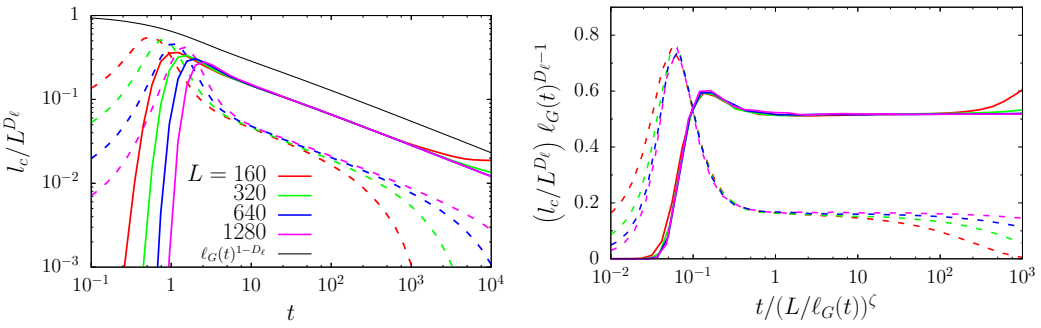

Figure 1.15: Scaling analysis of the length of the largest cluster interface in the case of the $T = 0$ Glauber dynamics on the square lattice, for different values of L, the lattice linear size. On the left we show l_c/L^{D_l} vs. t, while on the right we show $(l_c/L^{D_\ell})\,\ell_d(t)^{(D_\ell-1)}$ against the rescaled time $t/(L/\ell_G(t))^\zeta$, where $\ell_G(t)$ is the characteristic time obtained as the inverse of the excess energy, and $\zeta = 0.5$. As in Figs. 1.13 and 1.14, the contributions from the wrapping and non-wrapping hulls have been separated, with the former indicated by continuous lines and the latter by dashed lines. In the left panel we also show $\ell_G(t)^{1-D_\ell}$ (black solid line). The colour code is the same in both panels.

$\mathcal{N}(A,t) \sim C(t)A^{-\tau_A}$, with $\tau_A = 187/91$ the $2d$ critical percolation Fisher exponent, and $C(t)$ some time-dependent prefactor. Finally, a third region corresponding to very large domains, whose properties are greatly affected by finite-size effects. This last region is, essentially, the size distribution of percolating domains, the contribution tha we denoted by $N_p(A,t,L)$ in Eq. (1.22).

After a sufficiently long time, the fate of the finite size clusters is dictated by curvature-driven coarsening mechanism [39] and an approximate expression for the time-dependence of the finite cluster size distribution was derived [10, 11]

$$N(A,t) \simeq \frac{2c_d\,[\ell_d(t)]^{2(\tau_A-2)}}{[A+\ell_d(t)^2]^{\tau_A}} \quad , \tag{1.42}$$

where ℓ_d is the usual coarsening length. Note that this expression is the same as the one given in Eq. (1.23) by assuming $\ell_d(t) \simeq (\lambda_d(t-t_p)^{\frac{1}{2}})$ and $t \gg t_p$. However, we leave the time dependence of $\ell_d(t)$ unspecified as we have already done for the scaling of other observables, since we are going to use instead the numerical estimate $\ell_G(t)$ given by the inverse of the excess energy. The following two limits can be read from Eq. (1.42)

$$N(A,t) \simeq \begin{cases} 2c_d\,\ell_d(t)^{-4} & A \ll \ell_d(t)^2 \\ \dfrac{2c_d^{\rm eff}(t)}{A^{\tau_A}} & A \gg \ell_d(t)^2 \end{cases} \tag{1.43}$$

where we define

$$c_d^{\rm eff}(t) = c_d\,[\,\ell_d(t)\,]^{2(\tau_A-2)} \,. \tag{1.44}$$

A direct fit of the algebraic decay of $\mathcal{N}$ in the regions of areas $A \gg \ell_d(t)^2$ provides a value of τ_A that is close to the expected one for critical percolation, $\tau_A \simeq 2.0549$, but it is also close to the one for the $2d$ critical Ising model, $\tau_A \simeq 2.0267$. It is therefore difficult to distinguish between these two cases from just the analysis of the algebraic piece. A detailed investigation of $\mathcal{N}(A,t,L)$, expecially its short-time behaviour and the way it approaches the critical-percolation-like scaling regime, is thus in order.

We first present the analysis of the scaling behaviour of $\mathcal{N}(A,t,L)$ for the zero-temperature Glauber dynamics on the triangular lattice, a case which is particularly interesting because the system is already at the critical point of percolation at $t=0$. We then move to the study of the so-called pre-percolation regime for the Glauber dynamics on the square lattice, showing that for domains larger than $\ell_p(t)^{D_A}$, with $\ell_p(t) = \ell_G(t)\, t^{1/\zeta}$ and D_A the fractal dimension of $2d$ critical percolation incipient percolating cluster, we need to introduce a corrective factor to the expression given Eq. (1.42) for $N(A,t)$ in order to obtain a correct scaling. Finally, we present our measurements and scaling analysis for the size distribution of the percolating spin clusters, $N_p(A,t,L)$.

1.5.5.1 The triangular lattice.

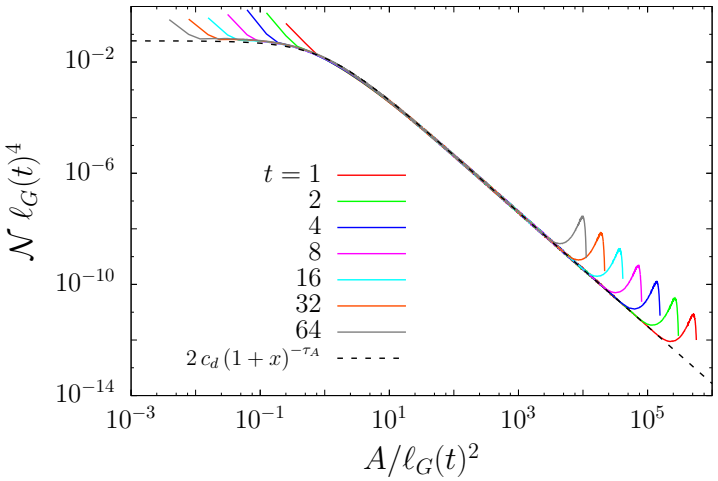

Figure 1.16: Ising model on a triangular lattice with PBC and $L = 2560$ evolving under $T = 0$ Glauber dynamics. We show the scaling of the number density of domain areas $\mathcal{N}(A,t)$ implied by Eq. (1.25). The quantity $\mathcal{N}(A,t)\,\ell_G(t)^4$ is plotted against the rescaled area $A/\ell_G(t)^2$ where $\ell_G(t)$ is the characteristic length scale obtained as the inverse of the excess energy. The datasets corresponding to different times (indicated in the key) collapse on the master curve $f(x) = 2\,c_d\,(1+x)^{-\tau_A}$ (dashed line), which is the expected analytic expression for the scaling function.

In the case in which the model is defined on a triangular lattice, the initial condition is right at the critical percolation point, thus $N(A,0) \simeq 2c_d A^{-\tau_A}$, with $\tau_A = 187/91$ and $2c_d \simeq 0.0579$, if one neglects effects due to the discreteness of the lattice at very small values of A. Added to this there is also the contribution coming from the percolating clusters at very large values of A, $N_p(A,t,L)$. The analytic form expressed by Eq. (1.42) should hold for the time evolution of $\mathcal{N}(A,t,L)$ in the region of areas A where the aforementioned contribution is negligible. In order to highlight this last fact, in Fig. 1.16 we present the rescaled domain area distribution for the $T = 0$ Glauber dynamics on a triangular lattice of linear size $L = 2560$: we plot $\mathcal{N}(A,t)\,\ell_G(t)^4$ against the rescaled area $A/\ell_G(t)^2$. As done before for the scaling of other observables, $\ell_G(t)$ is taken as a measure of $\ell_d(t)$. By so doing, the datasets corresponding to different times should collapse onto the same master curve, which is represented by $f(x) = 2\,c_d\,(1+x)^{-\tau_A}$, see Eq. (1.25). The result of the scaling

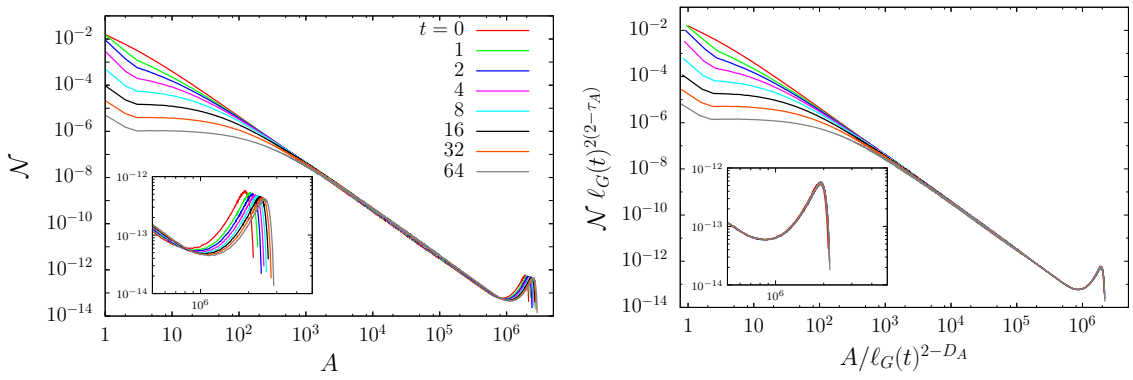

Figure 1.17: Time evolution of the number density of domain areas for the zero-temperature Glauber dynamics on a triangular lattice with linear size $L = 2560$. In the left panel we show the bare domain area distribution $\mathcal{N}(A,t)$ vs. A at various times given in the key. In the right panel we present $\mathcal{N}(A,t)\ \ell_G(t)^{2(2-\tau_A)}$ against the rescaled area $A/\ell_G(t)^{2-D_A}$, with the exponents of critical percolation, $D_A = 91/48$ and $\tau_A = 187/91$, and $\ell_G(t)$ the characteristic length scale obtained as the inverse of the excess energy. In both panels, the insets show a "zoomed" view of the *bump*, to better highlight the difference between the unscaled data and the scaled ones. The colour code is the same in both panels.

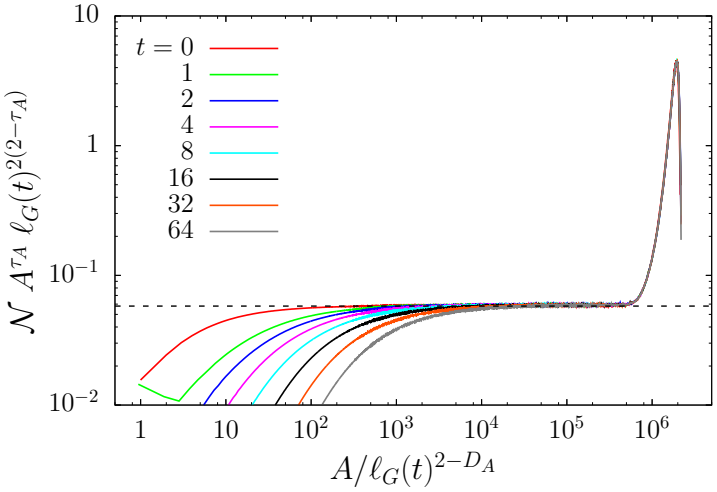

Figure 1.18: Time evolution of the number density of domain areas for the zero-temperature dynamics on a triangular lattice of linear size $L = 2560$. In order to highlight the presence of the algebraic decay $\mathcal{N}(A) \sim N(A) \sim A^{-\tau_A}$ for non-percolating clusters, we show $\mathcal{N}(A,t)\ A^{\tau_A}\ [\ell_G(t)]^{2(2-\tau_A)}$ against the rescaled area $A/\ell_G(t)^{2-D_A}$, where $\ell_G(t)$ is the characteristic length scale obtained as the inverse of the excess energy, $D_A = 91/48$ and $\tau_A = 187/91$ as in Fig. 1.17. The scaling of the area as $A/\ell_G(t)^{2-D_A}$ has been done to collapse the so-called bump, as in the right panel of Fig. 1.17. The rescaled data presents a *plateau* in the interval $[10^4, 5\times10^5]$ of the rescaled area, falling approximately onto the expected value for critical percolation, $2c_d \simeq 0.0579$, indicated by the black horizontal line.

is very good. Deviations from the master curve occur for very small values of the variable $A/\ell_G^2(t)$, where the scaling is supposed to break due to the discreteness of the lattice, and

for very large values corresponding to the appearance of the so-called "bump", which is the contribution N_p given by the percolating spin clusters, as expected.

Let us now turn to the properties of the "bump". Most of the contribution to N_p comes from clusters that are either the largest or the second largest ones in the sample (for $A > L^2/2$, only the largest cluster contributes, and N_p is truly the size distribution of the largest cluster). In Sec. 1.4.2 we argued that the fraction of sites belonging to the largest cluster (or to the second largest one), A_c/L^2, should scale dynamically as $\ell_d(t)^{2-D_A}$, and the results shown in Fig. 1.7 strongly suggests the validity of this argument. Accordingly, in order to collapse the "bumps" at different times t and fixed L, the area A should be rescaled by $\ell_d(t)^{2-D_A}$. At the same time, $\mathcal{N}(A,t)$ must be multiplied by $\ell_d(t)^{2(2-\tau_A)}$ to remove the time-dependence of the pre-factor $2c_d^{\rm eff}(t)$. We present the result of this scaling in the right panel of Fig. 1.17, where we plot $\mathcal{N}\ \ell_G(t)^{2(2-\tau_A)}$ against $A/\ell_G(t)^{2-D_A}$, using the same data as the ones in Fig. 1.16. Again, $\ell_G(t)$ is taken as a measure of the dynamical characteristic length scale $\ell_d(t)$. In the left panel of the same figure we show the unscaled distribution against A to let the reader make a comparison. By looking at the whole distribution one is not able to notice a significant difference between the unscaled and the scaled versions of the data since both D_A and τ_A are close to 2. However, if one focuses only on the region of areas A corresponding to the "bump", as done in the insets, it becomes clear that the scaling makes the data collapse in that specific region.

In order to prove that the contribution to $\mathcal{N}(A,t)$ due to non-percolating spin clusters (with linear size smaller than L) decays as $A^{-\tau_A}$, in Fig. 1.18 we show the quantity $\mathcal{N}\,A^{\tau_A}\,\ell_G(t)^{2(2-\tau_A)}$ against the rescaled area $A/\ell_G(t)^{2-D_A}$. For $A \gg \ell_G(t)^2$, the data corresponding to different times should all collapse onto a *plateau* at the constant $2c_d$ (up to the point where the contribution due to percolating clusters, N_p, starts to be significant). In fact, the rescaled data present a plateau in the interval $[10^4, 5\times10^5]$ of the rescaled area, falling approximately onto the expected value for critical percolation, $2\,c_d \simeq 0.0579$ (indicated by a dashed line). As one can see, the point at which the plateau sets in, that is the point around where there is the crossover between the two different regions described by Eq. (1.43), increases with time. In fact it should grow as $\ell_d(t)^2 \propto \ell_G(t)^2$. At the same time, by scaling the area as $A/\ell_G(t)^{2-D_A}$, as done in the right panel of Fig. 1.17, it is possible to collapse the data in the region corresponding to the "bump".

1.5.5.2 Pre-percolation scaling.

In order to describe the dynamical regime that occurs before the critical percolation properties extend over all length scales (up to the system linear size L) we introduced the characteristic length $\ell_p(t)$ with the following meaning: on length scales shorter than $\ell_p(t)$, the statistical and geometrical features of the spin clusters are those of $2d$ critical percolation (after having rescaled all lengths by $\ell_d(t)$), while on longer scales, the system still retain the features of the initial condition (equilibrium at infinite temperature). Of course, this is true for all cases in which the initial condition is not already critical in the sense of percolation. In the case of the model on the triangular lattice this "pre-percolation" regime is not observed. We have also conjectured that $\ell_p(t) \sim \ell_d(t) t^{1/\zeta}$, with ζ an exponent to be determined and, so far, the scaling analysis on the wrapping probabilities and the largest cluster gives us $\zeta \simeq 0.5$ for the zero-temperature Glauber dynamics on the square lattice.

This separation of scales due to $\ell_p(t)$ is also visible in the time evolution of the number density of domain areas. The argument is the same as the one used in Sec. 1.4. We stated that the largest cluster size should satisfy the scaling relation $A_c(t,L)/\ell_d(t)^2 \sim \text{const.}\times[L/\ell_d(t)]^{D_A}$

for times $t > t_p$, with t_p the typical time at which the system enters in the so-called critical-percolation-like scaling regime, or $\ell_p(t_p) = L$. But at time $t < t_p$, the percolation criticality is present already on length scales shorter than $\ell_p(t)$. In terms of the statistics of the (non-percolating) domains, this means that the algebraic decay $N(A,t) \sim 2c_d^{\rm eff}(t) A^{-\tau_A}$ is already present for $t < t_p$ and $A/\ell_d(t)^2 < [\ell_p(t)/\ell_d(t)]^{D_A}$. We suggest then to add a corrective factor to the expression given in Eq. (1.43),

$$N(A,t) \;\sim\; 2c_d^{\rm eff}(t)\; A^{-\tau_A}\; \Phi\left(\frac{A/\ell_d(t)^2}{[\ell_p(t)/\ell_d(t)]^{D_A}}\right) \tag{1.45}$$

where Φ is a function such that $\Phi(x) \simeq$ const. for $x \ll 1$. In the following we show some data that support this claim.

In Fig. 1.19 we present our numerical measurements of the number density of domain areas in the early stages of a KIM evolving with zero-temperature Glauber dynamics on a square lattice with PBC and $L = 2560$. In the left panel of Fig. 1.19 we show the quantity $A^{\tau_A}\,\ell_G(t)^{2(2-\tau_A)}\,\mathcal{N}(A,t,L)$ plotted against the rescaled area $A/\ell_G(t)^{2-D_A}$. Notice that, apart from the behaviour at very small areas and the very steep increase at late times (due to the appearance of percolating spin clusters), the rescaled data tend to collapse on a plateau as the time increases, as in Fig. 1.18. This plateau corresponds approximately to the constant $2c_d \simeq 0.0579$ (indicated by a horizontal dashed line).

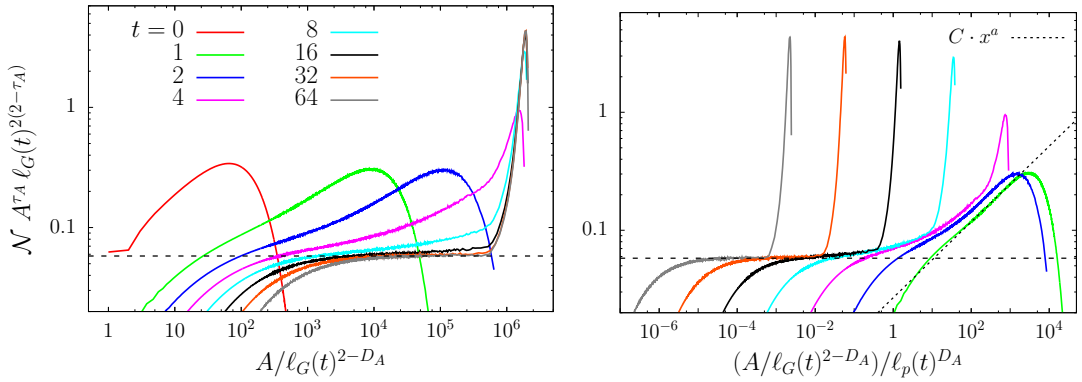

Figure 1.19: Ising model on a square lattice with PBC and $L = 2560$ evolving under $T = 0$ Glauber dynamics. We show the pre-percolation scaling of the number density of domain areas. The quantity $A^{\tau_A}\,\ell_G(t)^{2(2-\tau_A)}\,\mathcal{N}(A,t,L)$, with $\ell_G(t)$ the characteristic length obtained as the inverse of the excess energy, is plotted against $A/\ell_G(t)^{2-D_A}$ in the left panel and against $\left(A/\ell_G(t)^{2-D_A}\right)/\ell_p^{D_A}(t)$ in the right panel, where $\ell_p(t) = \ell_G(t)\,t^{1/\zeta}$, with $\tau_A = 187/91$, $D_A = 91/48$ and $\zeta = 0.5$. The dotted straight line in the right panel corresponds to the power law $\Phi(x) \simeq C\,x^a$, with $a = 0.321(1)$, which is the best fit to the data at time $t = 1$ in the interval $[10, 10^3]$ of the scaling variable. The black dashed horizontal line corresponds to $2c_d = 0.0579$.

In order to highlight the existence of the extra growing length $\ell_p(t)$ through the corrective factor Φ, we plot the same quantity against the rescaled area $(A/\ell_G(t)^{2-D_A})/\ell_p^{D_A}(t)$ where we assume $\ell_p(t) \simeq \ell_G(t)\,t^{1/\zeta}$ with $\zeta = 0.5$. With this choice, we obtain a fairly good collapse, as seen in the right panel in Fig. 1.19. This type of scaling highlights the presence of the two regimes discussed above: the asymptotic one for $A/[\ell_G^{2-D_A}(t)\ell_p^{D_A}(t)] \leq 1$, where the rescaled distribution has a flat region corresponding to the algebraic decay characterising critical percolation, and the "pre-percolation" one for $A/[\ell_G^{2-D_A}(t)\ell_p^{D_A}(t)] \geq 1$. We observe

that the scaling function $\Phi(x)$ is close to a power-law for $x \gg 1$, that is, $\Phi(x) \sim x^a$ for $x \gg 1$ with $a > 0$. By fitting the rescaled data with the function $\Phi(x) = Cx^a$ in the region $x = (A/\ell_G(t)^{2-D_A})/\ell_p^{D_A}(t) > 1$ and for times $t \sim 1$, we obtain $a = 0.321(1)$. (The fitting curve is shown as an inclined dotted line in the same figure.)

We can conclude that, for $A \gg \ell_d(t)^2$, the number density of non-percolating domain areas has the following behaviour,

$$N(A,t) \simeq \begin{cases} 2c_d^{\rm eff}(t)\, A^{-\tau_A} & \text{for } x \ll 1 \\ 2c_d^{\rm eff}(t)\, A^{-\tau_A} \left[\frac{A}{\ell_d(t)^2} \cdot \left(\frac{\ell_d(t)}{\ell_p(t)}\right)^{D_A}\right]^a & \text{for } x \gtrsim 1 \end{cases} , \tag{1.46}$$

where $x = A/[\ell_d^{2-D_A}(t)\ell_p(t)^{D_A}]$, $\ell_p(t) = \ell_d(t)t^{1/\zeta}$ with $\zeta \simeq 0.5$ and $a \simeq 0.321$. The second region is only visible for $t < t_p$, that is to say, $\ell_p(t) < L$.

1.5.5.3 Size distribution of the percolating clusters.

As explained in Sec. 1.4, the very few large spin clusters that survive the coarsening process after a sufficiently long time are those that signal the onset of the critical-percolation-like scaling regime. At the time t_p, these clusters usually span most of the lattice and their geometrical and statistical properties resemble those of the clusters at critical site percolation on the same lattice. Usually, at this time, the two largest spin clusters of opposite spin orientation are both percolating and become "stable" with respect to the coarsening dynamics in the sense explained in Sec. 1.4.2. This is the reason why N_p that constitutes the contribution given by the percolating clusters to $\mathcal{N}$, is mainly due to the two largest clusters. For all practical purposes, we will take N_p as just the size distribution of the two largest clusters in the system.

Let us discuss the scaling of N_p in general. The distribution $N_p(A,t,L)$ satisfies

$$\int dA\, N_p(A,t,L) = \frac{1}{L^2} . \tag{1.47}$$

The result $1/L^2$ is due to the definition of $\mathcal{N}(A,t,L)$ which counts the number of clusters with area A per spin, and to the fact that we have rescaled the distribution by a factor 2 to compare it to the one of percolation for which there is only a single percolating cluster. In site percolation, finite-size scaling implies that, at the critical point, the size distribution of the largest cluster $N_{\rm LC}(A_c,L)$, for a system of linear size L, depends on A_c and L through the ratio A_c/L^{D_A}, with $D_A = 91/48$. The same should be true for $N_p(A,t,L)$ in the dynamical problem for $t \geq t_p$. If we rescale A as $A \to A/L^{D_A}$, we need also to rescale the measure accordingly, *i.e.* $dA \to L^{D_A} dA$. However, in the dynamical problem we need to take into account the effects of coarsening, and we have seen that the largest cluster size (but also the one of the second largest) scale as $\ell_d(t)^{2-D_A}$. Thus, the correct quantity to consider is $L^{D_A}\, \ell_d(t)^{2-D_A} N_p(A,t,L)$ as a function of $A/L^{D_A}\, \ell_d(t)^{2-D_A}$.

We show the data corresponding to the rescaled distribution $N_p(A,t,L)$ in Fig. 1.20 in the case of the zero-temperature Glauber dynamics on the square lattice, for sizes $L = 160$ (a), 320 (b) and 640 (c). Notice that $N_p(A,t,L)$ is multiplied also by a factor L^2 to get rid of the $1/L^2$ present in its definition and make the data fall on a range of values of order $\mathcal{O}(1)$. For each size, we also show the static size distribution of the largest cluster for site percolation at threshold occupation probability on the square lattice of same size, rescaled as $N_p(A,L)\, L^{2+D_A}$ and plotted against the rescaled size A/L^{D_A}. Our goal is to prove that, with this rescaling, the distribution $N_p(A,t,L)$ for the dynamical problem matches the static one for critical

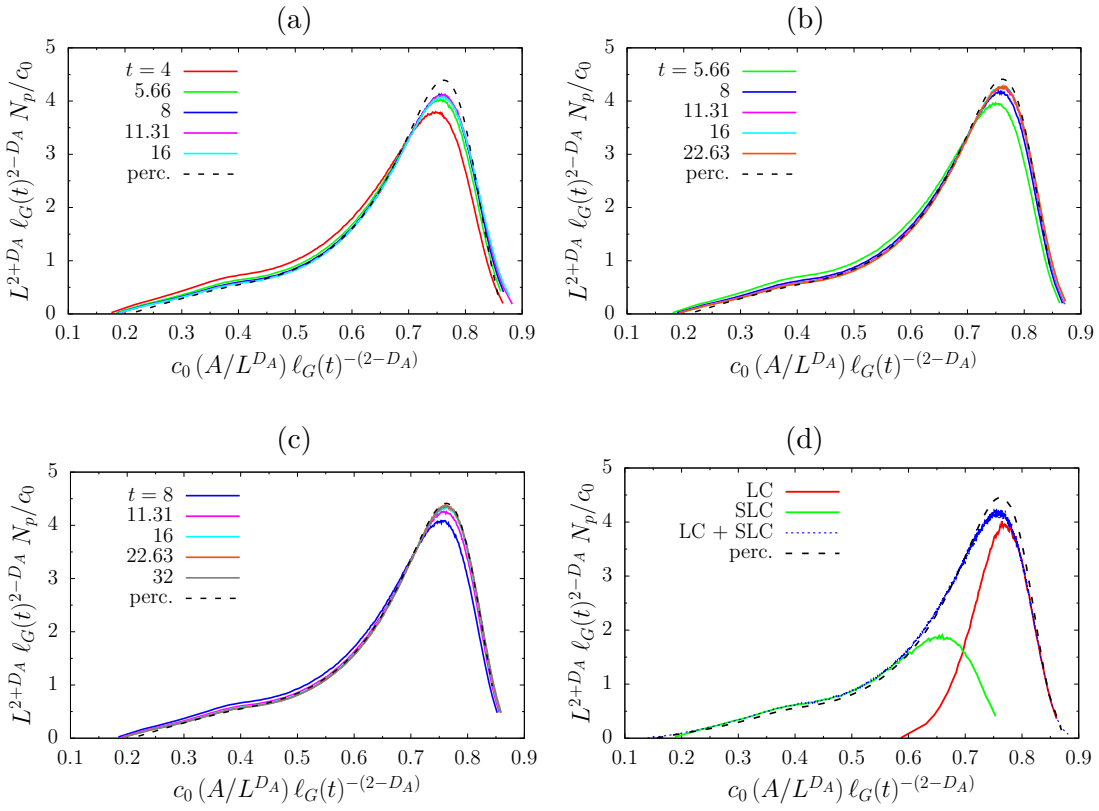

Figure 1.20: The size distribution of the two largest clusters, $N_p(A, t, L)$, for the zero-temperature Glauber dynamics on the square lattice, at different times indicated in the key and for different values of L, $L = 160$ (a), 320 (b) and 640 (c). The distribution is rescaled by the factor $L^{2+D_A}\,\ell_G(t)^{2-D_A}/c_0$ and plotted against the rescaled area $c_0\,(A/L^{D_A})\,\ell_G(t)^{2-D_A}$, where D_A is the fractal dimension of the percolating cluster in $2d$ critical percolation, $\ell_G(t)$ the characteristic length obtained by the excess energy, and $c_0 \simeq 1.165$. In panel (d), instead, we show the contributions to N_p coming from the largest (LC) and the second largest (SLC) clusters, separately, as well as the whole N_p (LC + SLC), at $t = 8$, for the dynamics on a square lattice with $L = 320$. In each panel, the size distribution of the largest cluster for site percolation, at the threshold occupation probability on the square lattice of corresponding size, is also shown with a black dashed line, multiplied by L^{2+D_A} and plotted against A/L^{D_A}. The value of the constant c_0 was chosen so that the rescaled distributions for the dynamical problem coincided with the static one of critical percolation.

percolation. To do so, we need to include an additional scaling factor c_0 for the dynamical problem, that is, we plot $L^{2+D_A}\,\ell_d(t)^{2-D_A}\,N_p(A, t, L)/c_0$ against $c_0\,A/L^{D_A}\,\ell_d(t)^{2-D_A}$. The value which gives the best collapse is $c_0 \simeq 1.165$, independently of the lattice linear size L. Note that the agreement between the data for the quenched system and the critical percolation one becomes much better as we increase the system size.

In panel (d) of Fig. 1.20, we show the contribution to the size distribution N_p coming from the largest cluster (LC) and that from the second largest (SLC) separately, as well as the whole N_p (LC + SLC), at $t = 8$, for the dynamics on a square lattice with $L = 320$. The data is scaled as in the other panels and we have also included the size distribution of the largest cluster at critical percolation (dashed line) on the same lattice (properly rescaled as

in the other panels). The whole distribution N_p is given by $N_p = \frac{1}{2}(N_{\rm LC} + N_{\rm SLC})$.

1.6 Conclusions

In this Chapter we presented a thorough analysis of the critical percolation phenomena emerging in the sub-critical quenches of the $2d$ ferromagnetic Ising model with non-conserved order parameter dynamics, specifically the Glauber dynamics. The measurements obtained through numerical simulations of a KIM evolving with zero-temperature Glauber dynamics on various $2d$ lattices show that, at a particular time τ_p, soon after or right at the quench (depending on the lattice geometry), the system develops typically two large spin clusters of opposite phase that almost always are percolating (or at least have linear size comparable with that of the system). These two large structures are accompanied by smaller non-percolating ones. At τ_p none of these two large domains are stable against the microscopic dynamics: they can break, reconnect and grow by incorporating some smaller domains until a time t_p at which at least one of them percolates and remains percolating (and growing) at all subsequent times. In fact, at a sufficiently long time after the quench, the main mechanism producing the domain growth in the zero-temperature Glauber dynamics is the curvature-driven motion of domain walls, and thus, in the late stages of the dynamics, domain walls that are percolating are "topologically" stable, in the sense that they can not be broken into non-percolating ones or change the direction along which they are percolating.

We observed that, at the typical time t_p, not only the domain pattern acquires features of $2d$ critical percolation, but the system enters in a critical-percolation-like dynamical scaling regime that lasts for a very long period of time, and ideally for the rest of the evolution in the thermodynamic limit. In this regime the geometrical and statistical properties of the spin clusters are those present in $2d$ critical percolation, after having rescaled all lengths by ℓ_d, the usual dynamical length associated to coarsening. More precisely, at time t, on length scales shorter than $\ell_d(t)$, the system behaves as in thermal equilibrium at the target temperature, while on larger length scales critical percolation scaling relations appear. As an example, for the dynamics on a finite lattice of linear size L, the size of the largest spin cluster behaves as

$$\frac{A_c(t,L)}{\ell_d(t)^2} \sim \left(\frac{L}{\ell_d(t)}\right)^{D_A} \quad , \tag{1.48}$$

in this regime, with D_A the fractal dimension of the incipient percolating cluster in $2d$ percolation. We can interpret this dynamic scaling relation as if the system had an effective dynamical lattice spacing $\tilde{r}_0(t) = \ell_d(t)$ and an effective dynamical linear size $\tilde{L}(t) = L/\ell_d(t)$.

In the case in which the initial state of the system, which is always drawn from the equilibrium at infinite temperature, is not already at the percolation critical point, we observed that the time t_p to reach the critical-percolation-like scaling regime scales approximately as

$$t_p(L) \sim L^{z_p} \tag{1.49}$$

with the system linear size L, where $z_p < z_d$, with $z_d = 2$ being the dynamical exponent associated to NCOP coarsening. However, we found more useful to introduce a characteristic length $\ell_p(t)$ of the form

$$\ell_p(t) = \ell_d(t) t^{1/\zeta} \, , \tag{1.50}$$

with an exponent ζ to be determined. This length describes the transient between the initial state and the critical percolation scaling regime, in the same way as $\ell_d(t)$ represents the

typical radius up to which one can observe equilibrium properties at the target temperature, at time t. Then t_p is the time at which critical percolation properties extends to the whole system, that is to say,

$$\ell_p(t_p(L)) \sim L \quad . \tag{1.51}$$

By measuring various observables through numerical simulations and by studying their finite-size scaling behavior, we were able to estimate the exponent ζ. For the zero-temperature Glauber dynamics on the square lattice we found $\zeta \simeq 0.5$. From the knowledge of the exponent ζ it is then possible to extract the L-dependence of t_p. If one assumes that $\ell_d(t)$ has the expected power law behaviour $\ell_d(t) \sim t^{1/z_d}$ in the transient between the initial state and the onset of the critical-percolation-like scaling regime, then one can relate the exponent z_d, ζ and z_p through

$$\frac{1}{z_p} = \frac{1}{z_d} + \frac{1}{\zeta} \quad . \tag{1.52}$$

However, we found that the growth law $\ell_d(t) \sim t^{1/z_d}$ is always established a long time after the system has already reached the critical percolation scaling regime. Moreover, we expect the exponent ζ to depend on the particular lattice geometry. In App. A.2 we briefly present an analysis of the percolation phenomena appearing in the Ising model evolving with zero-temperature Glauber dynamics on a finite honeycomb lattice and we show that, in this case, $\ell_p(t)$ does not have the simple functional form expressed by Eq. (1.50).

In the analysis we mainly treated the zero-temperature Glauber dynamics, but we expect to find similar results in the early stages of the coarsening process in the case of finite temperature quenches, as long as the target temperature is not too close to the critical one. See for example the data shown in App. A.1.

Globally, we showed that after a subcritical quench the spin system evolves in three regimes that are well separated and can be identified numerically. These are the following.

- A transient between the initial fully disordered state and the critical-percolation-like dynamical scaling regime ($0 < t < t_p$), controlled by the growing length $\ell_p(t) \sim \ell_d(t) t^{1/\zeta}$.
- The critical-percolation-like scaling regime ($t_p < t < t_{\rm eq} \sim L^{z_d}$), in which $2d$ critical percolation features are observed on length scales longer than $\ell_d(t)$. In this regime the system is still very far away from the thermal equilibrium at the target temperature of the quench.
- The final relaxation regime, starting approximately at the time $t_{\rm eq} \sim L^{z_d}$, in which the system evolves towards the final state being either the fully magnetised state or one of the so-called "stripe" states, that is to say, states with flat domain walls.

Some issues regarding the metastability of the states characterised by "topologically" stable percolating domain walls, and their possible evolution into equilibrium states, in the case of the Glauber dynamics at temperature $T < T_c$, are briefly addressed in App. A.1.

Chapter 2

Coarsening and percolation in the $2d$ KIM evolving with COP dynamics.

2.1 Introduction

In this Chapter we analyse the main features of the coarsening process occurring in the Kinetic Ising Model evolving with stochastic spin update rules that preserve the value of the total magnetisation of the system, or, in short, conserved order parameter (COP) dynamics. We also refer to this type of dynamics as a spin-exchange dynamics, since the allowed transitions are only those ones between two spin configurations in which the value of the spins at two given lattice sites is exchanged, in contrast with the single spin-flip dynamics that was studied in the previous Chapter. We are going to consider two different versions of the spin-exchange dynamics. The first one is determined by the so-called Kawasaki spin update rule, which essentially consists in allowing the exchange of the spin only for a pair of nearest neighbour lattice sites, and thus it is an example of locally conserved order parameter (LCOP) domain growth. The second version is just the more general definition of the spin-exchange dynamics, that is to say, it allows the exchange of the spins between any two sites of the lattice. If one adopts this spin update rule, the dynamics preserves the magnetisation only globally, then we refer to the corresponding coarsening process as globally conserved order parameter (GCOP) coarsening.

As in the case of the KIM evolving with Glauber dynamics, we want the stochastic process that is ensued by the transition rates between different spin configurations to simulate the domain growth that the system, initially prepared at equilibrium at infinite temperature, is subjected to when the temperature is quenched below T_c. In particular, we want the stochastic dynamics to make the system relax asymptotically in time to a stationary state characterised by the Gibbs-Boltzmann statistics at the target temperature $T < T_c$. Then, naturally, the spin-exchange rates need to satisfy the detailed balance condition expressed by Eq. (2.2). However, the constraint imposed by the conservation of the total magnetisation (and by the conservation of the local magnetisation in the case of the Kawasaki update rule) limits drastically the ensemble of spin configurations that can be explored by the dynamics in the equilibrium regime, in comparison to what happens for the single spin-flip dynamics. In particular, since the dynamics starts with an equal concentration of the two spin alignments, at late times there are almost always long domain walls that percolate across the lattice.

An approach to a critical-percolation-like scaling regime, before the system reaches the ultimate stationary regime, was already observed and partially studied for the Kawasaki dynamics [3, 40] on $2d$ lattices. In this dissertation we expand the analysis of this intermediate regime and we try to determine the time-dependence of the associated characteristic length ℓ_p, as done for the KIM evolving with Glauber dynamics in Chap. 1. The analysis of the various observable measured through the numerical simulations confirm the existence of this characteristic length scale, in addition to the usual dynamical length ℓ_d characterising the growth of domains with equilibrium properties, which has the following form

$$\ell_p(t) \sim \ell_d(t)\, t^{1/\zeta} \ , \tag{2.1}$$

where the exponent ζ depends on the particular lattice geometry. We find that the value of the exponent ζ is different from that obtained in the case of the Glauber dynamics (given the same lattice).

The analysis developed below further suggests that percolation plays an important role in the early stages of the coarsening process in a KIM relaxing to the ordered phase, independently of the particular spin update rule.

2.2 Definition of the model

We consider again a Kinetic Ising Model (KIM) on a $2d$ lattice of finite size. The Hamiltonian of the system is that of an Ising model with homogeneous and isotropic nearest-neighbour ferromagnetic interactions, as given by Eq. (1.4).

In order to mimic an instantaneous quench in the temperature and the following relaxation towards an equilibrium state, we adopt the usual Monte Carlo method, with transition rates $W(s, s')$ satisfying the well-known detailed balance condition,

$$W(s, s')\, P_{\rm eq}(s) \ = \ W(s', s)\, P_{\rm eq}(s') \tag{2.2}$$

where $P_{\rm eq}(s) = \exp\left[-H_J\left(\{s_i\}\right)/(k_B T)\right]/Z(T)$ is the canonical equilibrium probability density for a given spin configuration $s = \{s_i\}$, with T being the target temperature, k_B the Boltzmann constant and $Z(T)$ the canonical partition function at the temperature T. We then focus on a spin update rule that conserves the total magnetization of the system. The allowed transitions consist simply in letting the starting spin configuration s pass to a new one s' that differs from it only by having two lattice sites exchange their spins. Given the two lattice sites i and j, an example is the transition $s \to s^{(i,j)}$, with the "arrival" spin configuration denoted by $s^{(i,j)}$, satisfying $s_k^{(i,j)} = s_k$ if $k \neq i, j$, while $s_i^{(i,j)} = s_j$ and $s_j^{(i,j)} = s_i$, for any lattice site k. The transition rates $W(s \to s^{(i,j)})$ and $W(s^{(i,j)} \to s)$ for the dynamics relaxing to equilibrium at the inverse temperature β need then to satisfy

$$\frac{W(s \to s^{(i,j)})}{W(s^{(i,j)} \to s)} = \frac{P_{\rm eq}(s^{(i,j)}; \beta)}{P_{\rm eq}(s; \beta)} = \exp\left\{-\beta \Delta E_{i,j}(s)\right\} \quad , \tag{2.3}$$

with

$$\Delta E_{i,j}(s) = J\left(s_i - s_j\right) \left(\sum_{k \in \mathcal{N}(i) \setminus \{j\}} s_k - \sum_{h \in \mathcal{N}(j) \setminus \{i\}} s_h \right) \tag{2.4}$$

where again, for a given lattice site k, $\mathcal{N}(k)$ is the set of its nearest-neihgbour sites. In our numerical simulations we used the Metropolis rule, that is to say, the spin-exchange rate

$w_{i,j}(s) = W(s \to s^{(i,j)})$ has the following form

$$w_{i,j}(s) = \min\{\ 1,\ \exp\left[-\beta \Delta E_{i,j}(s)\right]\} \quad . \tag{2.5}$$

If the two sites i and j whose spins one wants to exchange are chosen anywhere in the lattice, then the resulting stochastic dynamics preserves only the total magnetisation, $M = \sum_k s_k$. However, usually kinetic Ising models evolving with COP dynamics are used to simulate the process of phase separation in binary alloys [41, 42] (that is, a mixture of two different chemical compounds that is initially prepared in a homogeneous state), so that a rule that limits the distance at which the two lattice sites i and j can be picked gives rise to a coarsening dynamics that resembles more closely such physical systems. In particular, the most natural choice is to impose that i and j have to be nearest-neighbour lattice sites. In this case the spin-exchange rates given in Eq. (2.5) define the so-called Kawasaki dynamics [43, 44]. The more general case is also called nonlocal Kawasaki dynamics.

As in the case of the KIM evolving with Glauber dynamics (see Sec. 1.2), we adopt a continous-time Monte Carlo method. A numerical simulation of the stochastic dynamics practically works as follows: given that the system is in the spin configuration s at time t, we choose at random (with probability proportional to the corresponding spin-exchange rate) two lattice sites i and j that have spin of opposite alignment (and, in the case of the local Kawasaki dynamics, sites i and j are required to be nearest neighbours); we then always exchange the spin at the two sites (the method is rejection-free) and increase the time t by δt with δt drawn from an exponential distribution with mean

$$\mathbb{E}(\delta t) = \left(\sum_{\{k,l:\ s_k = -s_l\}} w_{k,l}(s) \right)^{-1} \tag{2.6}$$

where the summation runs over all the pairs k, l of distinct lattice sites such that $s_k = -s_l$ (and eventually with the restriction that k and l have to be nearest neighbours in the case of the local version of the dynamics). Note that the quantity $\sum_{\{k,l:\ s_k = -s_l\}} w_{k,l}(s)$ represents the probability per unit time that a transition that exchanges two antiparallel spins may occur, given that the system is in the configuration s.

The initial condition is always taken to be a random spin configuration with a fixed concentration p of one of the two spin alignments. In most cases, the results that we are going to show are relative to $p = 0.5$. The reason behind this choice is that even a small imbalance in the concentration of the two species of spin can affect greatly the possibility for the system to reach a critical-percolation-like state, as it will be explained in Sec. 2.4.2. Notice, however, that this way of choosing the initial spin configuration does not coincide exactly with drawing it from the equilibrium distribution of the IM at infinite temperature, even if such distribution is sharply peaked at the concentration $p = 0.5$ (and the peak becomes sharper as the size of the system increases).

In the rest of this Chapter we are going to analyse the coarsening process, and related percolation phenomena, characterising a KIM evolving with nearest-neighbour spin-exchange stochastic dynamics, *i.e.*, Kawasaki dynamics. We also performed a similar analysis for the nonlocal version of the spin-exchange dynamics. The results for this case are shown in App. B.1.

2.3 Kawasaki dynamics

Local spin-exchange dynamics, or Kawasaki dynamics, is a type of stochastic spin dynamics [43, 44] often used to mimic phase separation in systems in which hydrodynamic effects can be neglected [45]. In short, it describes the process whereby a binary mixture of components A and B, initially in a homogeneous phase, demix leading to the coexistence of two phases: one rich in A and the other in B. The system, initially in an unstable spatially uniform state, performs a coarsening process to approach its thermodynamically stable phase-separated state.

The behaviour of such physical systems at *late* times is well understood. In the long time limit they approach a dynamic scaling regime described by an extension of the Lifshitz-Slyozov-Wagner (LSW) theory [46, 47], in which the typical domain radius grows as [48]

$$\ell_d(t) \simeq t^{1/z_d} \qquad \text{with} \qquad z_d = 3 \quad . \tag{2.7}$$

Numerical results in favour of this law were published in [48, 49, 50, 51, 52] for the Kinetic Ising Model evolving with spin-exchange stochastic dynamics, although the time-dependence of the growth-law can be more complex in particle or polymer phase separating systems, see *e.g.* [42] and references therein.

It was noticed in [13] that the low-temperature evolution of a 50:50 mixture after a quench from infinite temperature shares many points in common with the one of NCOP dynamics. On the one hand, an initial approach to critical percolation was noticed, although the time-scale needed to reach this state was not studied in detail. On the other hand, the number density of domains was studied numerically and it was found to satisfy dynamic scaling with respect to the dynamic growing length $\ell_d(t) \simeq t^{1/z_d}$ with $z_d = 3$, the one that characterises the scaling properties of the space-time correlation functions.

We are interested in studying the early stages of the dynamical process (in contrast to the asymptotic LSW regime) and, in particular, the way in which the system approaches a state with a stable pattern of percolating domains. We confirm that this occurs for balanced mixtures whereas different behaviour is found for asymmetric ones [53].

Before delving into the analysis of the observables measured through the numerical simulations, let us describe in more detail the main aspects of the microscopic dynamics. One can reconsider the KIM evolving with nearest-neighbour spin-exchange transitions as a system of interacting particles occupying the sites of a lattice and jumping from site to site according to certain rules. Each site can be occupied by at most one particle and particles can not be created nor destroyed (thus their number is fixed). The configuration of the system can be then described by the occupation numbers $\{n_i\}$, with $n_i \in \{0, 1\}$ for each lattice site i. The correspondence between spins and particles is as follows: if a site i has spin $s_i = +1$, then it is occupied by a particle, otherwise it is empty. In terms of occupation numbers, $n_i = 2s_i - 1$. The dynamics consists in particles performing random jumps to empty nearest-neighbour sites. More precisely, the allowed transitions are of the form $n \to n^{(i,j)}$, with $n_i = 1$, $n_j = 0$, $n_i^{(i,j)} = 0$ and $n_j^{(i,j)} = 1$, consisting in a particle hopping from site i to an empty nearest-neighbour site j, with rate $W_{\text{hop}}(i \to j) = \min\{\ 1,\ \exp\left[-\beta \Delta E_{i,j}\right]\}$, where

$$\Delta E_{i,j} = 4J \left[\sum_{k \in \mathcal{N}(i) \setminus \{j\}} n_k \ - \sum_{h \in \mathcal{N}(j) \setminus \{i\}} n_h \right] . \tag{2.8}$$

In Fig. 2.1 we show graphically some of the possible situations that can happen for a particle "hopping", together with the corresponding transition rates, in the case of the

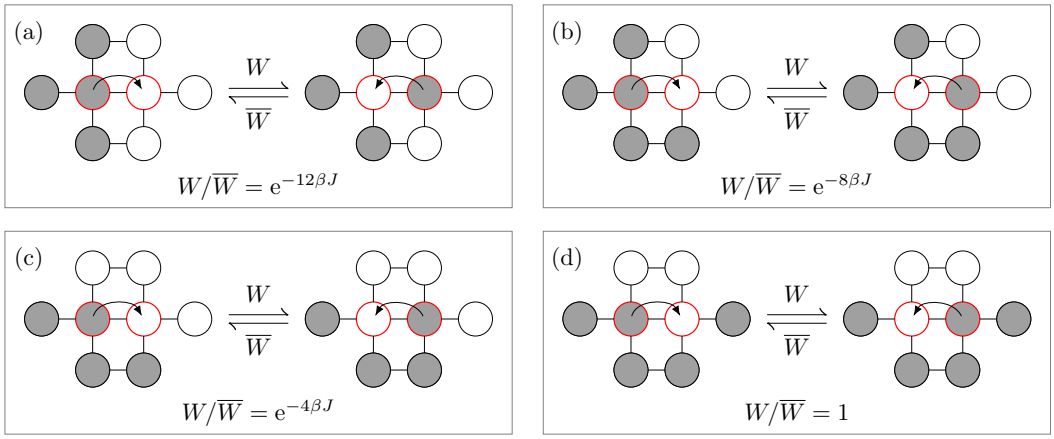

Figure 2.1: Some examples of (nearest-neighbour) spin-exchange transitions on a square lattice. Gray circles indicate sites with spin $+1$ (or occupied by a particle), while white circles indicate sites with spin -1 (or a vacancy). The two sites at the center are those involved in the exchange (or particle hopping), which is represented by an arrow. W is the transition rate from the configuration on the left to that on the right, while $\overline{W}$ is the rate associated with the inverse transition. They satisfy the detailed balance condition with respect to the canonical equilibrium distribution, $W/\overline{W} = \exp(-\beta\Delta E)$ with ΔE the change in energy due to the transition, and β the inverse temperature. Note that the "neighbourhood" that determines the transition rates consists of six lattice sites.

Kawasaki dynamics on a square lattice. Note that, since the transition rates depend on the spin configuration $\{s_i\}$ (or $\{n_i\}$) only through the energy change ΔE caused by the spin-exchange, and since this one has the form given by Eq. (2.8), there are only seven different types of transition, corresponding to the different values that ΔE can take.

One can notice some special cases. First, particles that are attached to large clusters by only one bond (see Fig. 2.2-(a)) can freely (without energy cost) "slide" across a flat domain wall, that is to say, they can perform a random walk by just moving in the direction parallel to the wall (always maintaining a single link to the cluster itself) until they get trapped by a "corner", as shown in Fig. 2.2-(b). Once a particle gets trapped in this situation, one needs to wait a typical time of order $t_{\text{detach}} \sim \mathrm{e}^{4\beta J}$ to observe the particle detach and start wandering again freely along the domain wall. On the other hand, hoppings in the direction perpendicular to the cluster wall are, on average, much less likely to occur. For example, the formation of a "dent" in a flat domain wall (see the case indicated by Fig. 2.2-(c)) happens with a probability per unit time $W = \mathrm{e}^{-12\beta J}$. In the limit $T \to 0$ this process becomes impossible.

An other interesting case is that of isolated particles, see Fig. 2.2-(d). Particles in this situation can also hop freely into any of the nearest-neighbour empty sites. They can perform a $2d$ random walk in the bulk of large empty regions of the lattice, until they get captured by nearby particle clusters.

These observations give an useful insight into the mechanism through which the microscopic dynamics generate the domain growth. In the early stages of the process, most of the transitions consist in the formation of small aggregates by means of energy-lowering hoppings and the reshaping of such aggregates by the energy-free motion of particles along their walls.

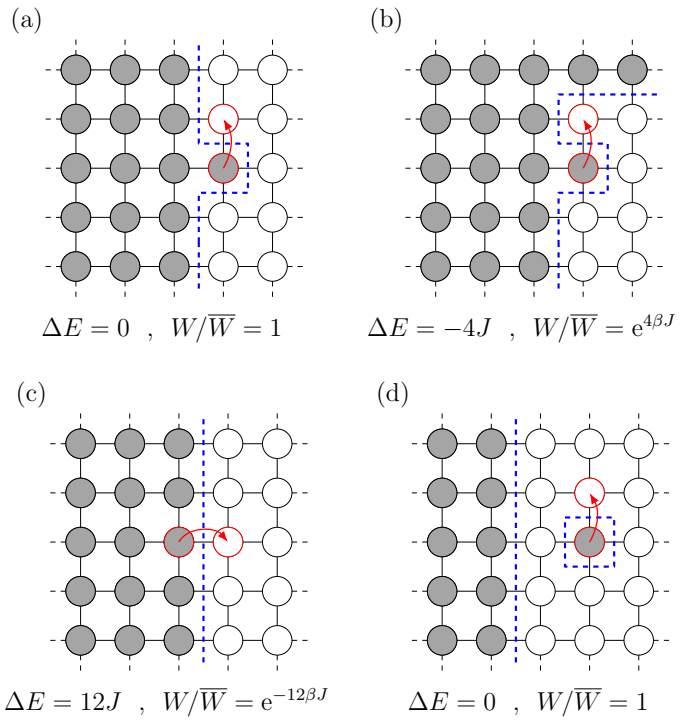

Figure 2.2: Some particular examples of transitions for the Kawasaki dynamics, seen in the "particle-vacancy" picture. Gray circles indicate sites with spin $+1$ (or occupied by a particle), while white circles indicate sites with spin -1 (or a vacancy). The arrows indicate the sites that are involved in the particle hopping. The blue dashed line represents the interface separating $+1$ spin regions from -1 spin regions. For each case, we indicate the change in energy ΔE that would be caused by the transition and the ratio $W/\overline{W}$ between the rates of the direct and inverse transitions.

Eventually, some of these aggregates that are very close to each other can fuse together to form large clusters. Some of these large clusters can even percolate across the lattice. At sufficiently late times, most of the cluster have smooth walls and the main mechanism accounting for the growth of the clusters is the recombination of "lone" particles that are diffusing in the empty regions. Small clusters that are not percolating slowly evaporate because of particles that detach from their external wall (with a positive cost in energy). These particles then diffuse freely in the empty regions, and are later likely to be captured by the large percolating clusters.

This difference in the main growth mechanism between short and long times causes a difference in the behaviour of the dynamical length $\ell_d(t)$. In fact, at short times, it was observed [54, 55, 56] that $\ell_d(t) \sim t^{1/4}$. This behaviour is attributed to the fact that, at early times, the diffusion of particles along cluster walls plays the dominant role. Only after the system has reached a situation in which ordered domains have smooth walls and are well separated between each other, the usual growth law $\ell_d(t) \sim t^{1/3}$, that characterises the LCOP coarsening, is recovered.

An analysis of the characteristic length $\ell_G(t)$, obtained as the inverse of the excess-energy will be presented in Sec. 2.4.1. This length is expected to be proportional to $\ell_d(t)$ (for not

too long times) and thus it has essentially the same dependence on time. As the reader will see, the expected law $\ell_G(t) \sim t^{1/z_d}$ with $z_d = 3$ is not at all observed in the time window that our simulations are able to explore.

2.3.1 Snapshots

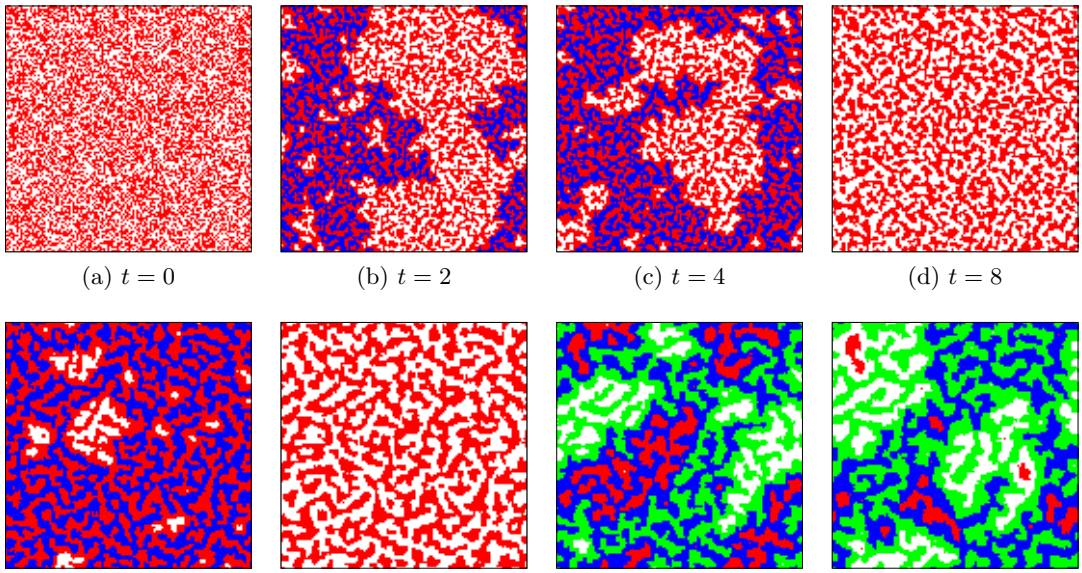

(a) $t = 0$ (b) $t = 2$ (c) $t = 4$ (d) $t = 8$

(e) $t = 128$ (f) $t = 256$ (g) $t = 512$ (h) $t = 1024$

Figure 2.3: Some snapshots of a KIM evolving under local Kawasaki dynamics, at target temperature $T = T_c/2$, on a square lattice with PBC and linear size $L = 128$. The initial state is a fully random spin configuration with equal concentration of the two species. Red sites and white sites represent $+1$ and -1 spins, respectively. Clusters that wrap around the system are highlighted in different colours, green for spin $+1$ wrapping clusters, blue for -1 wrapping clusters. The times selected are, from left to right, $t = 0$, 2, 4, 8 in the upper row, and $t = 128$, 256, 512, 1024 in the lower row.

In Fig. 2.3 we show some snapshots of the spin configuration evolving under the local Kawasaki update rule, at the target temperature $T = T_c/2$, for a fully disordered initial state with concentration $p = 0.5$ of either species of spin. The spin system is placed on a square lattice with PBC and linear size $L = 128$. Lattice sites with spin $+1$ and -1 are represented by red and white dots, respectively. In addition, clusters of $+1$ (-1) spins that are percolating in at least one direction are highlighted in green (blue).

Interestingly enough, already at $t = 2$, a spin cluster wrapping in the vertical direction appears. However, one must not confuse this time with the characteristic time t_p at which the system has reached the so-called critical-percolation-like scaling regime, as we defined it in Sec. 1.4. In fact, even if percolating spin clusters can emerge very early in the dynamics, they often do not survive for very long time or they can change their topology, as it can be observed, for example, in Fig. 2.3-(c) where the spin cluster that was previously wrapping only in the vertical direction is now wrapping in both directions of the lattice, and then in Fig. 2.3-(d) where it has broken. Only at a time $t \simeq 512$ we observe the formation of two large percolating clusters of opposite spin alignment that have become topologically stable,

in the sense that they survive with the same topology (in this case wrapping only across the vertical direction) for the rest of the dynamics. We expect these two large spin clusters to further grow by absorbing "particles" diffusing in the bulk of clusters of the opposite phase and to smoothen their walls by motion of spins in the direction parallel to the walls themselves, as explained in the previous Section. Eventually, at very long times, the spin configuration would consist of just two large spin clusters of opposite phase. Note that thermal fluctuations can still allow isolated spins or very small spin clusters to diffuse in the bulk of a large cluster of the opposite phase. However, for the range of temperatures that we have explored, $T < T_c/2$, these effects are negligible, and the typical features of the domain growth (in particular the geometrical and statistical properties of domains) are almost the same as in the zero-temperature dynamics, at least for not too long times.

The $T = 0$ Kawasaki dynamics has the same peculiarity of the $T = 0$ Glauber dynamics, that is to say, it gets trapped in the so-called frozen states and thus a (single) realization of the process is not ergodic. The situation, however, is more complex than what we have in the case of NCOP dynamics because of the constraint imposed by the conservation of the number of spins of either species and the limitation on nearest-neighbour exchanges. Spin configurations with flat interfaces are not the only ones to get blocked. Many more *blocked* spin configurations exist, with a richer structure. Since the zero-temperature LCOP domain growth is greatly affected by the presence of these blocked spin configurations, we preferred to simulate the Kawasaki dynamics at a small but positive temperature.

In particular, most of the results that we are going to show in the next Sections are relative to the Kawasaki dynamics at $T = T_c/2$. This value of the temperature is low enough to observe the same type of behaviour as that of the $T = 0$ dynamics in the early stages of the growth process (in particular, we observe the same behaviour in the time evolution of the characteristic length $\ell_d(t)$), but does not suffer significantly from the slowing down of the relaxation dynamics for $T \to 0$ when the system gets very close to one of the blocked configurations. This allows us to observe the type of phenomenology associated to critical percolation in the typical time window which is accessible by the numerical simulations.

2.4 Numerical analysis

In the following, we present the numerical results for the Ising model evolving under (local) Kawasaki dynamics at subcritical target temperature, on various $2d$ lattices, obtained through simulations using the continous-time Monte Carlo method. We follow the same lines of analysis as those in Chap. 1.

By measuring observables related to the geometry and statistics of the spin clusters (*e.g.* the winding angle for domain walls, the size of the largest cluster, the wrapping probabilities, etc.) we are able to show that a finite system attains the so-called critical-percolation-like dynamical scaling regime in which all properties of the domain pattern, after having rescaled all lengths by $\ell_d(t)$ (the usual coarsening length), are those of $2d$ critical percolation. The transient between the initial state and this regime is described in terms of the new growing length $\ell_p(t)$, so that critical percolation properties can be observed over distances r such that $\ell_d(t) \ll r \leq \ell_p(t)$. As done in the case of the single spin-flip dynamics in Chap. 1, we suppose $\ell_p(t) \sim \ell_d(t) t^{\zeta}$ and use finite-size scaling analysis to determine the exponent ζ.

2.4.1 The excess-energy growing length

We present here the measurements of the growing length $\ell_G(t)$ defined as the inverse of the the excess-energy, Eq. (1.16). As mentioned previously, we take this quantity as an estimate of the characteristic length $\ell_d(t)$ that, in the usual context of coarsening systems, represents the typical domain radius or typical distance between domain walls (or a length proportional to them). In Fig. 2.4 we show $\ell_G(t)$ for the local Kawasaki dynamics on square, honeycomb and triangular lattices, at temperatures $T_c/2$ and $T_c/4$ for the square lattice and $T_c/2$ in the other two cases.

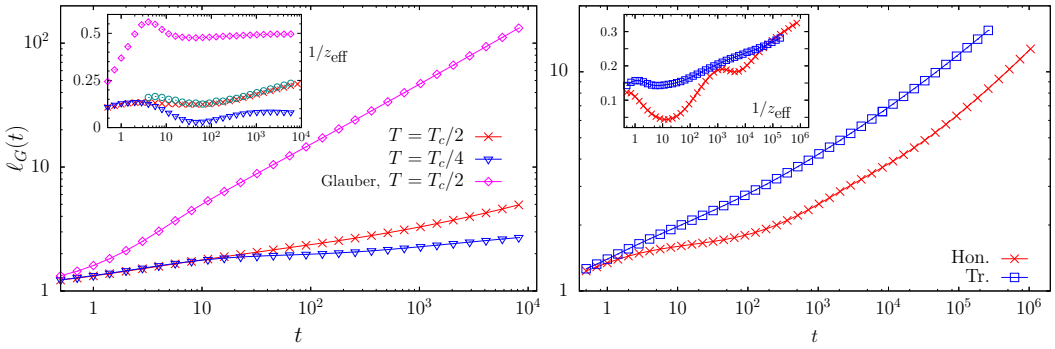

Figure 2.4: $2d$ Ising model evolving under local Kawasaki dynamics, with balanced densities of the two species, at a subcritical temperature. We show the excess-energy growing length $\ell_G(t) = 1/\epsilon(t)$ against time t. Left panel: model defined on a square lattice with PBC and with linear size $L = 640$, quenched to $T = T_c/2$ (red curve) and $T = T_c/4$ (blue curve) and, for comparison, data for the Glauber dynamics at $T_c/2$ (purple curve) on the same lattice. Right panel: growing length for Kawasaki dynamics on honeycomb and triangular lattices, in both cases with PBC, linear size $L = 320$ and target temperature $T_c/2$. In the insets, we show the effective growth exponent, $1/z_{\rm eff}(t)$, computed as the logarithmic derivative of the function $\ell_G(t)$, with the same colour code. In the inset of the left panel, we also include the effective growth exponent estimated from the scaling of $\langle \theta^2 \rangle$ (circles), see Sec. 2.4.3.

First, we note that the values reached by ℓ_G are notably smaller than the ones obtained with NCOP dynamics also shown in the left panel (labeled Glauber). Second, the data are temperature independent before $t \simeq 10$. At around this time, the data at $T_c/4$ slow down and deviate from the ones at higher temperature. Nowhere in the time span shown in the figure a stable algebraic increase of ℓ_G establishes. The evolution of the effective exponent $1/z_{\rm eff}(t)$, computed as the logarithmic derivative of $\ell_G(t)$, is followed in the inset. In the time-window used, at $T_c/2$, $1/z_{\rm eff}(t)$ varies between 0.1 and 0.25, approximately, implying that $z_{\rm eff}(t)$ goes from 10 to 4. Therefore, the measurement slowly approaches the expected value for the dynamic exponent $z_d = 3$ [48] but it is still far from it. The deviation is even worse at $T_c/4$ and the time-dependence of the effective exponent $z_{\rm eff}$ is non-monotonic. We stress here that the relatively short times at which we measured $\ell_G(t)$ are going to be the relevant ones for the study of the approach to the critical-percolation-like state. Contrary to what happens in the case of the IM evolving under Glauber dynamics, an asymptotic growth law $\ell_d(t) \sim t^{1/z_d}$ is not clearly observed and time scales of at least two orders of magnitude longer are needed to see $z_{\rm eff}$ converge to the expected $z_d = 3$ [49, 50]. Another interesting issue is that the local Kawasaki dynamics on the honeycomb lattice does not block as do the NCOP rules (see App. A.2), and the values of $z_{\rm eff}$ are similar to those for the square lattice.

The fact that the effective exponent varies so much in time and depends on temperature suggests to use the characteristic growing length $\ell_G(t)$ itself as a representative of $\ell_d(t)$ in all scaling relations, to analyse the pre-asymptotic regime with the eventual approach to critical percolation. The difficulties involved in using the exponent z_d and its effective evaluation are confirmed by the analysis of other observables.

2.4.2 Wrapping probabilities

The wrapping probabilities $\pi_{\rm h}$, $\pi_{\rm v}$, $\pi_{\rm hv}$, $\pi_{\rm diag}$ defined in Sec. 1.3 can be useful to determine the typical time required for the onset of the critical-percolation-like regime. In the left panel of Fig. 2.5, we show the wrapping probabilities for the Kawasaki dynamics on a square lattice, for different values of the lattice linear size L. The exact values of these probabilities for critical percolation on a torus with unit aspect ratio [24] are shown with dotted horizontal lines. As done in Sec. 1.5.2, the presence of the pre-percolation regime is exhibited by scaling time t as $t/\left(L/\ell_d(t)\right)^\zeta$, with the value of the exponent ζ chosen to make the datasets corresponding to different L collapse on a master curve. The value that gives the best collapse is, in this case, $\zeta \simeq 2.00$. Again, for $t/\left(L/\ell_d(t)\right)^\zeta \geq 1$ (or equivalently, for $t \geq t_p$ with t_p such that $\ell_p(t_p) = \ell_d(t_p)\ t_p^{1/\zeta} \sim L$) we should observe the time-dependent πs approach the constant values corresponding to $2d$ critical percolation wrapping probabilities.

In our case, we could not perform simulations long enough to observe a clear convergence, even though the data shown suggest that, for sufficiently large system sizes, the critical percolation wrapping probabilities should be the asymptotic values. Nevertheless, the scaling is very good for $t/\left(L/\ell_d(t)\right)^\zeta$ up to 10^{-1}, while, for larger values of the rescaled time, finite size effects are pronounced. These results can be compared to those for NCOP dynamics, shown in Sec. 1.5.2. The time t_p needed to approach the critical percolation wrapping probability values (and thus the time of the onset of the critical-percolation-like regime) can be computed approximately from these data. Concretely, from Fig. 2.5 we can use $t_p/\left(L/\ell_d(t_p)\right)^\zeta = 1$ as a criterium to measure t_p. In this way we find $t_p \simeq 233,\ 684,\ 1924,\ 5212,\ 13763$ for $L = 40,\ 80,\ 160,\ 320,\ 640$, respectively.

In Fig. 2.6 we show the same type of scaling on the honeycomb lattice. In this case, the value of ζ that gives the best collapse is $\zeta \simeq 1.15$. Notice also that we plotted the probabilities $\pi_{\rm h}$ and $\pi_{\rm v}$ separately, since the lattice that we implement in our numerical simulations has aspect ratio different from unity, see App. A.2 for more details on this issue. More precisely, the lattice mesh used in the simulations has aspect ratio $\sqrt{3}$, and we took the vertical side longer than the horizontal one, hence why $\pi_{\rm h} > \pi_{\rm v}$. Then, our measurements must be compared to the wrapping probabilities for $2d$ critical percolation on a lattice of aspect ratio $\sqrt{3}$. In general, one can compute the wrapping probabilities π for $2d$ critical percolation for any aspect ratio r [8, 57, 58]. For an aspect ratio $r = \sqrt{3}$ their values are given by $\pi_{\rm hv}^{(p)} \simeq 0.5120$, $\pi_{\rm h}^{(p)} \simeq 0.4221$, $\pi_{\rm v}^{(p)} \simeq 0.0408$ and $\pi_{\rm diag}^{(p)} \simeq 0.0250$.

It is also interesting to check the influence of an unbalance between the densities of the two species and, in particular, to investigate whether clusters retain the critical percolation properties during a certain time regime when the initial concentration of one of the two species is close to the percolation threshold, p_c.

In the right panel of Fig. 2.5 we display the time evolution of the various cluster wrapping probabilities for different concentrations of up spins, $p = 0.4,\ 0.42,\ 0.45,\ 0.47,\ 0.5$, in the case of the Kawasaki dynamics on a square lattice. We remind here that the site percolation threshold for the square lattice is $p_c \simeq 0.5927$. As one can see, when the concentration of one of the two species is larger than p_c (for the minority phase, this corresponds to the

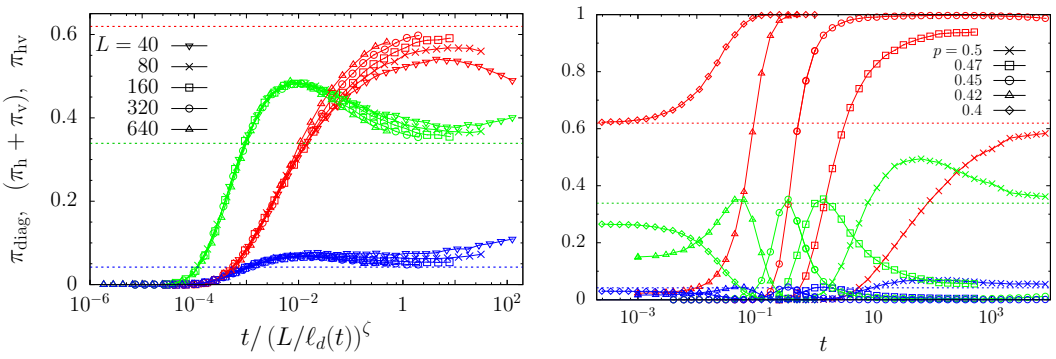

Figure 2.5: Probability that a spin cluster wraps in a certain direction, for the Ising model on a finite square lattice with PBC evolving under local Kawasaki dynamics at target temperature $T_c/2$. Red curves: clusters wrapping in both principal directions of the lattice in the so-called "cross" topology ($\pi_{\rm hv}$). Green curves: clusters wrapping in only one principal direction, either horizontally or vertically ($\pi_{\rm h}+\pi_{\rm v}$). Blue curves: clusters wrapping in a diagonal direction ($\pi_{\rm diag}$). The horizontal dotted lines are the exact values of the wrapping probabilities for critical percolation in $2d$. In the left panel, data for equal concentration of up and down spins, and different values of L, are plotted against the scaling variable $t/\left(L/\ell_d(t)\right)^{\zeta}$, with $\ell_d(t) = \ell_G(t)$ the characteristic length obtained from the inverse of the excess-energy. The value of the exponent $\zeta \simeq 2.00$ is chosen to make the datasets corresponding to different L collapse on the same master curve. In the right panel, a system with linear size $L = 160$ is prepared initially at $t = 0$ with a fixed concentration p of $+1$ spin, for $p = 0.5$, 0.47, 0.45, 0.42 and 0.4, and it is then let evolve. We show the same quantities as in the left panel with the same colour code.

condition $p < 1 - p_c$), the system has a cluster of the majority phase that percolates in both Cartesian directions already in the initial configuration, see the data for $p = 0.4$. Instead, for $1 - p_c < p < 1/2$, the curve $\pi_{\rm hv}(t)$ starts off from zero and slowly increases in a monotonic way, approaching 1 asymptotically.

For $p = 0.4 < 1 - p_c$, the probability of having a cluster wrapping along only one principal direction of the lattice, $\pi_{\rm h} + \pi_{\rm v}$ (green curves), starts off close to the corresponding critical percolation value and then decreases rapidly to zero. A similar behaviour is observed for $\pi_{\rm diag}$. In the cases in which $1 - p_c < p < 1/2$, the curves $\pi_{\rm h} + \pi_{\rm v}$ and $\pi_{\rm diag}$, start from values below the corresponding critical percolation probabilities, increase and approach them at a certain instant $t^\star$ that depends on p, but then rapidly detach from it and decrease to zero.

The curves for $p = 1/2$ (crosses) are the only ones that approach the non-trivial asymptotes shown with horizontal dotted lines in the late time regime. This result is consistent with the observation made in [53], where the segregating dynamics of a mixture of Bose-Einstein condensates was studied.

2.4.3 Average squared winding angle

In Sec. 1.5.3 we showed that the average squared winding angle, $\langle\theta^2\rangle$, for the hulls of spin clusters produced by NCOP dynamics, approaches the form given by Eq. (1.27) at around time t_p, and the time-dependence scales with the dynamic growing length $\ell_d(t)$. We can therefore use this observable to evaluate the approach to critical percolation and the effective dynamic exponent of phase separation, $z_{\rm eff}$.

In Fig. 2.7 we show the average squared winding angle for the hulls that form the interface

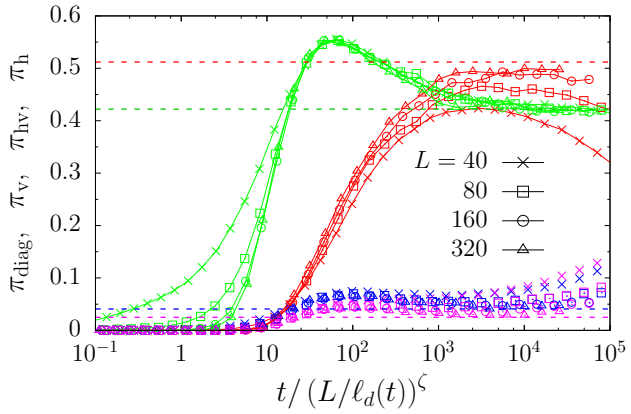

Figure 2.6: Ising model on a finite honeycomb lattice with PBC, evolving with local Kawasaki dynamics at target temperature $T_c/2$, for different values of L given in the key. The concentration of the two species is always $p = 1/2$. We show the probability that a cluster wraps in a certain direction at time t, against the rescaled time $t/\left(L/\ell_d(t)\right)^{\zeta}$, where $\ell_d(t) = \ell_G(t)$ is the characteristic length obtained from the inverse excess-energy and the value of the exponent ζ is chosen to make the data for different L collapse one onto the other. Red data points correspond to $\pi_{\rm hv}$, green ones to $\pi_{\rm h}$, blue ones to $\pi_{\rm v}$ and purple ones to $\pi_{\rm diag}$. The value $\zeta \simeq 1.15$ yields approximately the best collapse. The horizontal dashed lines correspond to the expected values at critical percolation for a rectangular sheet of aspect ratio $\sqrt{3}$.

of the largest spin cluster against the logarithm of the curvilinear coordinate x (left panel) in the case of the Kawasaki dynamics on a square lattice with linear size $L = 640$, at target temperature $T_c/2$. The interface of a cluster can be made of many components, as explained in Sec. 1.3, each one being a closed path on the dual lattice constructed by joining sites (of the dual lattice) with bonds that intersect "broken" bonds between nearest-neighbour antiparallel spins on the original lattice. To compute the quantity $\langle\theta^2\rangle$ shown in Fig. 2.7 we considered only the hulls of the largest cluster that are wrapping across the system, or said in another way, only those hulls that have zero total winding angle. Of course, these hulls exist only if the largest cluster is wrapping and they come always in pairs.

We observe that the curves shown in the left panel of Fig. 2.7 are very similar to the ones for NCOP dynamics (see Fig. A.7). The dotted straight line is a fit to the logarithmic dependence of the data at $t = 8192$ and yields an estimate of the SLE parameter $\kappa \simeq 6.8310$, relatively close to the one of critical percolation, $\kappa = 6$.

In the right panel we show the same data plotted against $\ln[x/\ell_d(t)]$. As already explained in Sec. 1.5.3, the idea behind this scaling is that there is a separation of length scales characterised by different fractal properties of the cluster hulls, with a crossover occurring at $\ell_d(t)$. If we measure the properties of the hulls over a curvilinear distance x smaller than $\ell_d(t)$ we are going to obtain the properties of the equilibrium at the target temperature of the relaxation dynamics, that is to say, domains with smooth walls. Indeed, for $x/\ell_d(t) \ll 1$ we observe that $\langle\theta^2\rangle$ converges to a plateau. Instead, for $x > \ell_d(t)$ the geometrical properties of the spin clusters should be those of critical percolation with $\langle\theta^2\rangle$ given by Eq. (1.27). This argument implies that, by rescaling the curvilinear distance x by $\ell_d(t)$, data for different t should collapse on the same master curve.

It was not possible to collapse the data over the whole range of times available from the

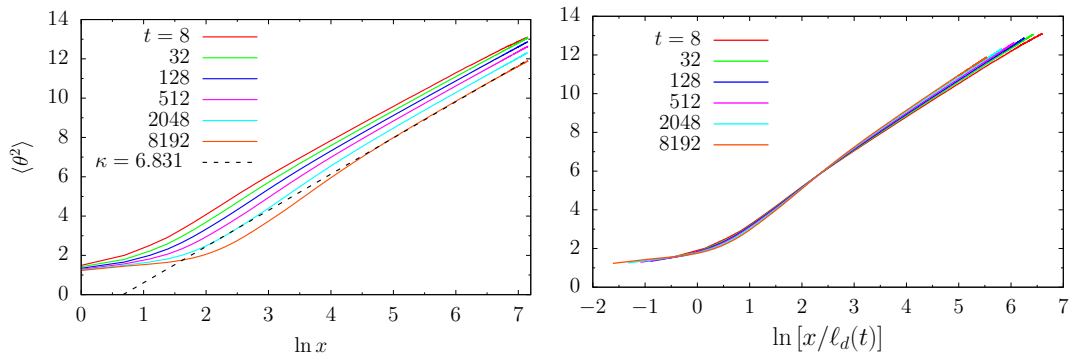

Figure 2.7: Ising model on a square lattice with PBC and $L = 640$, evolving under local Kawasaki dynamics at temperature $T_c/2$. Equal concentration of up and down spins. Left panel: the average squared winding angle $\langle\theta^2(x,t)\rangle$ for the wrapping hulls that form the largest cluster interface against the logarithm of the curvilinear coordinate x, at different times given in the key. A linear fit to the data obtained for the latest time simulated ($t = 8192$) is also shown in the left panel, yielding an SLE parameter $\kappa \simeq 6.8310$. Right panel: $\langle\theta^2(x,t)\rangle$ against the logarithm of $x/\ell_d(t)$ with $\ell_d(t) = \ell_G(t)$ the growing length measured from the inverse of the excess energy.

simulations by using the theoretical asymptotic power law behaviour of $\ell_d(t)$, $\ell_d(t) \propto t^{1/z_d}$, with a unique choice of the dynamical exponent $z_d = 3$. As already explained, in the range of times when the critical-percolation-like state is observed, the characteristic length scale $\ell_d(t)$ has not yet acquired the asymptotic behaviour of the LSW theory for LCOP dynamics. Thus, as done previously, $\ell_d(t)$ is taken to be the full time-dependent growing length obtained as the inverse of the excess-energy, $\ell_G(t) = \epsilon(t)^{-1}$. As one can see from the right panel in Fig. 2.7 the scaling thus achieved is very good.

On the other hand, we could estimate an effective growth exponent, or more precisely its inverse $z_{\rm eff}^{-1}(t)$, by attempting pairwise collapse of curves $\{\langle\theta^2(x,t_i)\rangle\}_i$ corresponding to consecutive measuring times t_i and t_{i+1}. We rescaled the distance x by the factor $(t_{i+1}/t_i)^\alpha$ and we looked for the value of the exponent α that made the curve $\langle\theta^2(x,t_{i+1})\rangle$ collapse onto the curve $\langle\theta^2(x,t_i)\rangle$, when the former is plotted against the rescaled distance. By performing this procedure for all i, we obtained an estimate α_i of the effective growth exponent for each time interval $[t_i, t_{i+1}]$. This estimate of $z_{\rm eff}^{-1}(t)$ is included in the inset to Fig. 2.4 (as green circles) and it is very close to the value of $z_{\rm eff}^{-1}(t)$ extracted from $\ell_G(t)$.

2.4.4 Largest cluster scaling

In this Section we report some results on the scaling properties of the largest cluster in the early time regime. The data shown correspond to local Kawasaki dynamics at temperature $T_c/2$ on the square lattice (Fig. 2.8) and on the honeycomb lattice (Fig. 2.9). We recall that the quantity A_c is the (average) size of the largest cluster, while l_c is the (average) length of the external hull of the largest cluster.

As already explained in Sec. 1.5.4, we need to distinguish two types of hulls. The "external" interface of a cluster that is wrapping across the system along only one direction (horizontal, vertical or in a diagonal direction) is always made of two wrapping hulls, while a cluster that is not wrapping or that wraps simultaneously in both principal directions of

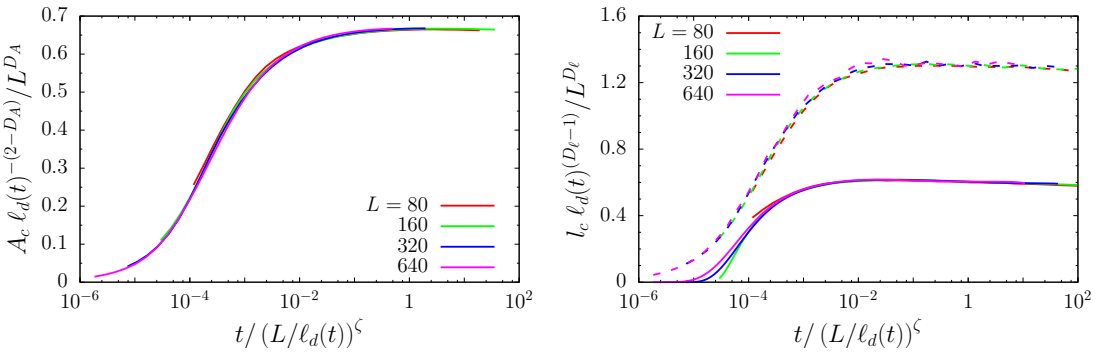

Figure 2.8: Ising model on a square lattice with PBC, evolving under local Kawasaki dynamics at target temperature $T_c/2$, with balanced concentration of the two species of spin. In the left panel we show $\left(A_c/L^{D_A}\right)\ \ell_d(t)^{-(2-D_A)}$, with A_c the largest cluster size, while in the right panel $\left(l_c/L^{D_\ell}\right)\ \ell_d(t)^{-(1-D_\ell)}$, with l_c the length of the largest cluster interface, for various values of L. The interface length l_c is computed separately for the non-wrapping hulls (indicated by dashed lines) and the wrapping hulls (indicated by continuous lines), if they exist. $\ell_d(t) = \ell_G(t)$ is the growing length extracted from the inverse of the excess-energy. All quantities are plotted against the rescaled time $t/\,(L/\ell_d(t))^{\zeta}$, where the exponent $\zeta \simeq 2.00$ was chosen to make the datasets corresponding to different L collapse onto each other.

the lattice does not possess any of these. On the other hand, the external interface of spin clusters that are not percolating is composed of just one (non-wrapping) hull. For all the cases that we show in this Section, we present the two contributions to the total length of the largest cluster interface, l_c, the one coming from wrapping hulls and the one coming from non-wrapping hulls, as two separate quantities. In general, they may have different scaling properties.

Following the same scaling arguments used in Chap. 1 for the ferromagnetic $2d$IM evolving under single spin-flip dynamics, the correct way of scaling the size of the largest cluster, $A_c(t, L)$, in order to take into account the effects of coarsening and percolation, is

$$\frac{A_c(t,L)}{L^{D_A}} \sim \ell_d(t)^{2-D_A}\, x_A\left(\frac{\ell_p(t)}{L}\right)\ , \tag{2.9}$$

with $D_A = 91/48$ the fractal dimension of the largest cluster in $2d$ critical percolation, $\ell_d(t)$ the characteristic length scale associated to the growth of domains, $\ell_p(t)$ the one associated to the approach to the critical percolation state and x_A an unknown scaling function. Analogously, the scaling for the largest cluster hulls is given by

$$\frac{l_c(t,L)}{L^{D_\ell}} \sim \ell_d(t)^{1-D_\ell}\, x_\ell\left(\frac{\ell_p(t)}{L}\right) \tag{2.10}$$

with $D_\ell = 7/4$ the fractal dimension of percolating domain hulls in $2d$ critical percolation and x_ℓ an unknown scaling function. As stated in Sec. 1.4.2 we suppose that $\ell_p(t)$ is given by $\ell_p(t) \simeq \ell_d(t)\, t^{1/\zeta}$, with ζ an exponent to be determined.

The above relations are supposed to hold for sufficiently large system size (ideally in the limit $L \gg r_0$), for $t \gg t_0$, with t_0 a microscopic time scale, and $t \ll t_{\rm eq}$, with $t_{\rm eq}$ the time needed by the system to reach the equilibrium state imposed by the bath temperature. Moreover, we expect that as $\ell_p(t) \to L$ the system reaches a critical-percolation-like

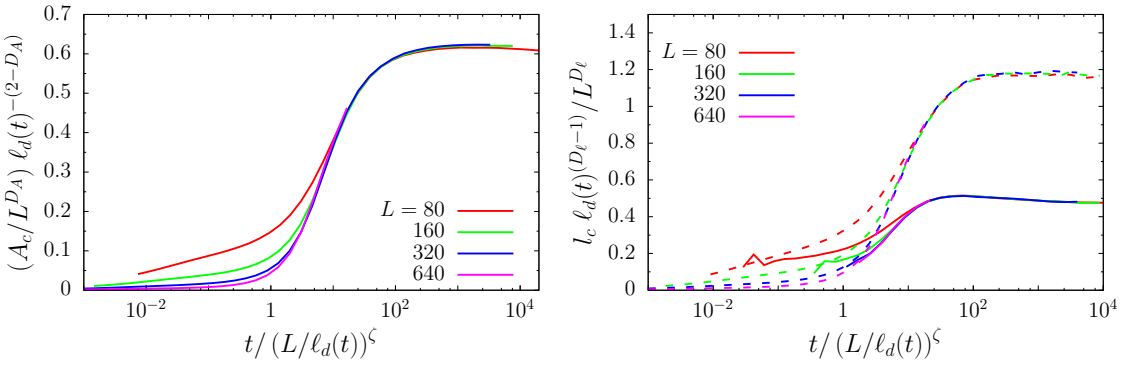

Figure 2.9: Ising model on a honeycomb lattice with PBC, evolving under local Kawasaki dynamics at target temperature $T_c/2$, with balanced concentration of the two species of spin. In the left panel we show $\left(A_c/L^{D_A}\right)\ \ell_d(t)^{-(2-D_A)}$, while in the right panel $\left(l_c/L^{D_\ell}\right)\ \ell_d(t)^{-(1-D_\ell)}$, for various values of L. As in Fig. 2.8, the interface length l_c is separated into two parts, one being the contribution coming from non-wrapping hulls (indicated by dashed lines), while the other one being the contribution due to wrapping hulls (indicated by continous lines), if they exist. Here $\ell_d(t) = \ell_G(t)$ is the characteristic length obtained by the inverse of the excess-energy. All the quantities are plotted against the rescaled time $t/\,(L/\ell_d(t))^{\zeta}$, where the exponent ζ was chosen to make the datasets corresponding to different L collapse one onto the other. The best collapse is obtained with $\zeta \simeq 1.15$, shown in the plots.

state on the scale of L, and for larger times both x_A and x_ℓ converge to constants so that $A_c(t,L)/L^{D_A} \simeq C_A\,\ell_d(t)^{2-D_A}$ and $l_c(t,L)/L^{D_\ell} \simeq C_\ell\,\ell_d(t)^{1-D_\ell}$, with C_A and C_ℓ some constants, as seen for the scaling behaviour of the largest cluster in the case of the Ising model evolving under zero-temperature Glauber dynamics.

We find acceptable scaling of the quantities $(A_c(t,L)/L^{D_A})\,\ell_d(t)^{-(2-D_A)}$ and $(l_c(t,L)/L^{D_\ell})\,\ell_d(t)^{-(1-D_\ell)}$ as functions of the rescaled time $t/\,(L/\ell_d(t))^{\zeta}$ (equivalently, as functions of $\ell_p(t)/L$) where the value of the exponent ζ is again determined by looking for the best data collapse. For the Kawasaki dynamics on the square lattice, at temperature $T_c/2$, the best collapse is found by taking $\zeta \simeq 2.00$ for both A_c and l_c, see Fig. 2.8, the same value obtained for the scaling of the wrapping probabilities, see Sec. 2.4.2.

In Fig. 2.9 we show the same type of scaling plots for the dynamics on the honeycomb lattice and again, consistently with the scaling of the wrapping probabilities, we find $\zeta \simeq 1.15$. Notice, however, that the quality of the collapse is not as good as for the case relative to the square lattice. More precisely, finite size effects are more pronounced.

2.4.5 Pair connectedness function

We show here some results regarding the time evolution of the pair connectedness function for the Kawasaki dynamics following a quench to $T_c/2$. The definition of the time-dependent pair connectedness $g(r,t)$ for a kinetic spin system is given in Sec. 1.3.

As in the case of the Glauber dynamics, we expect that the time-dependent pair connectedness $g(r,t)$ takes the same form as in $2d$ critical percolation (on the same lattice and with same boundary conditions) for times $t \geq t_p$ upon rescaling distances as $r \to r/\ell_d(t)$, that is

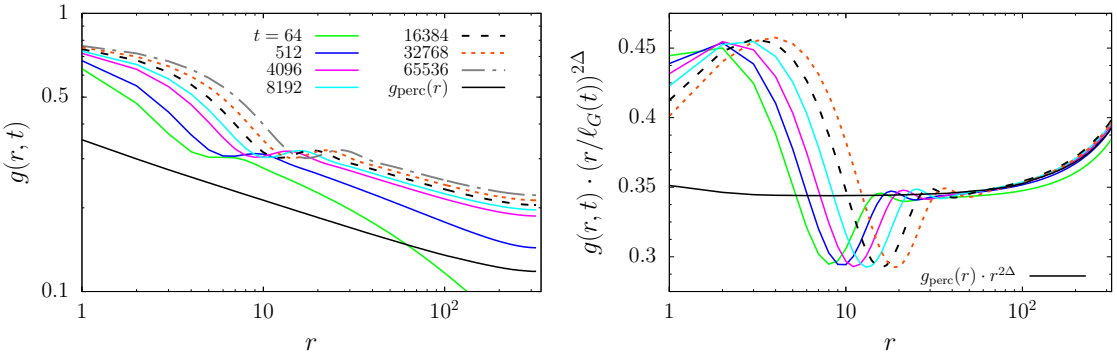

Figure 2.10: The pair connectedness function $g(r,t)$ for an Ising model evolving under Kawasaki dynamics at temperature $T_c/2$, on a square lattice with linear size $L = 640$ and PBC, for equal concentration of the two spin species. In the left panel, we show the comparison between the time evolving $g(r,t)$ and the pair connectedness for critical percolation, $g_{\rm perc}$, on the same lattice (same size L and same boundary conditions). In the right panel, we display the quantity $g(r,t)\cdot(r/\ell_G(t))^{2\Delta}$, where $\ell_G(t)$ is the characteristic length obtained as the inverse of the excess-energy and $\Delta = 2 - D_A$, with $D_A = 91/48$. The data for the dynamical problem has also been multiplied by a constant factor $\alpha \simeq 0.68$ in order to make it collapse onto that of critical percolation, for long distances. The color code for the different times is the same in both panels.

to say,

$$g(r,t) \sim g_{\rm perc}\left(\frac{r}{\ell_d(t)}\right) \ , \tag{2.11}$$

for $t \geq t_p$ and $r \gg \ell_d(t)$. Moreover, in the limit $L \to +\infty$, $g_{\rm perc}(r) \sim r^{-2\Delta}$, with $\Delta = 2 - D_A$ and $D_A = 91/48$ the fractal dimension of the incipient percolating cluster in $2d$ percolation.

This is shown in Fig. 2.10. In the left panel, we plot $g(r,t)$ against the distance r at different times t, for the dynamics on a square lattice with $L = 640$ and PBC. We compare it to that of random site percolation, $g_{\rm perc}(r)$, on a square lattice with the same linear size and boundary conditions, at the site occupation probability $p = 0.5927$ that is approximately the threshold value p_c (red dashed curve). Notice that, because of the PBC, the maximum allowed value of r is $L/2$. In the right panel, we show $g(r,t)\cdot(r/\ell_G(t))^{2\Delta}$ against r, where $\ell_G(t)$ is the characteristic length obtained as the inverse of the excess-energy, taken as a measure of the usual coarsening length $\ell_d(t)$. The collapse is good for large values of r, specifically for $r \gtrsim 40$. Moreover, over the large-distance tail the rescaled data for the dynamical problem match almost perfectly the data corresponding to $2d$ critical percolation, for times $t > 64$.

We reckon that both $g_{\rm perc}(r)\ r^{2\Delta}$ and the dynamical counterpart do not approach a constant for large values of the distance r, as one would expect, because of the periodic boundary conditions. On the other hand, the behaviour of $g(r,t)$ for small values of r is a characteristic of the coarsening process induced by the microscopic dynamics (in this case, the Kawasaki spin-exchange dynamics) and signals the fact that at small length scales the structure of clusters is very different from that of critical percolation. The same separation of length scales that was observed for the scaling behaviour of the average squared winding angle, $\langle\theta^2\rangle$, is also playing a role in the case of the pair connectedness. To make it more evident, in Fig. 2.11 we plot the rescaled pair connectedness, $g(r,t)\cdot(r/\ell_G(t))^{2\Delta}$, against the rescaled distance $r/\ell_G(t)$. As one can see, the data is correctly rescaled in the short-distance region

$(r/\ell_G(t) \lesssim 1)$ by using this scaling.

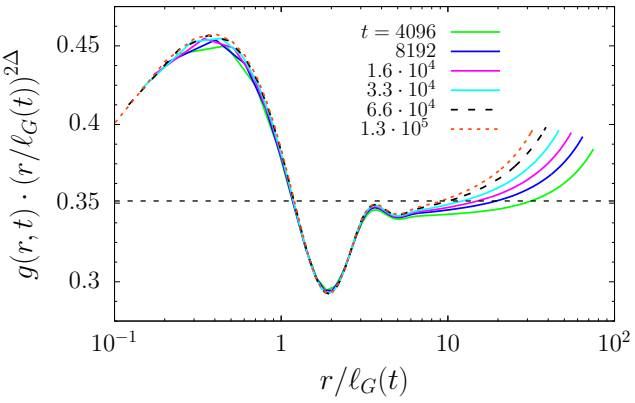

Figure 2.11: The pair connectedness function $g(r,t)$ for an Ising model evolving under Kawasaki dynamics at temperature $T_c/2$, on a square lattice with linear size $L = 640$ and PBC, for equal concentration of the two spin species. We plot the rescaled pair connectedness $g(r,t) \cdot (r/\ell_G(t))^{2\Delta}$ against the rescaled distance $r/\ell_G(t)$, where $\ell_G(t)$ is the characteristic length derived from the inverse of the excess-energy and $\Delta = 2 - D_A$ with $D_A = 91/48$. The horizontal dashed line is at p_c^2, with $p_c \simeq 0.5927$ the critical occupation probability for percolation on a square lattice.

2.4.6 Number density of domain areas

Following the same arguments exposed in the previous Chapter for the NCOP dynamics, we assume that the number density N of non-percolating spin clusters depends on the area A and time t as

$$N(A,t) \simeq 2c_d^{\text{eff}}(t) \, \frac{A^{1/2}}{\left[A^{3/2} + \ell_d^3(t)\right]^{\frac{(2\tau_A+1)}{3}}} \, \Phi\left(\frac{A/\ell_d^{2-D_A}(t)}{\ell_p^{D_A}(t)}\right) \tag{2.12}$$

where we defined an effective normalisation constant

$$c_d^{\text{eff}}(t) \equiv 2c_d \, [\, \ell_d(t) \,]^{2(\tau_A - 2)} \, . \tag{2.13}$$

This is the same form given by Eq. (1.24) with the addition of a pre-percolation scaling factor Φ that depends on A and t through

$$\frac{A/\ell_d^2(t)}{(\ell_p(t)/\ell_d(t))^{D_A}} \tag{2.14}$$

with $\ell_p(t)$ the characteristic length which governs the regime of approach to the critical-percolation-like state.

As explained in Sec. 1.5.5.2, the idea behind this scaling is that, at time t, on linear scales larger than $\ell_p(t)$, the system has not fully reached the critical percolation state yet, that is, domains with size A much larger than $\ell_p^{D_A}(t)$ have still some features of the initial fully disordered state. In this sense, $\ell_p(t)$ serves as a crossover scale between the percolation criticality and the high temperature disorder. Note that, in terms of areas, the corresponding

crossover scale is $\ell_p^{D_A}(t)$. Moreover, both A and $\ell_p(t)$ must be rescaled by $\ell_d(t)$ with the corresponding scaling dimensions to take into account the effects of usual coarsening.

Finally, we expect the pre-percolation scaling function Φ to satisfy $\Phi(x) \to 1$ for $x \ll 1$ so that we recover the expression given by Eq. (1.24) when $A/\ell_d^2(t) \ll (\ell_p(t)/\ell_d(t))^{D_A}$, *i.e.* for scales A such that the criticality of percolation has already established at time t.

2.4.6.1 *Domain area distribution for Kawasaki dynamics on a triangular lattice.*

On the triangular lattice the pre-percolating regime is absent since the initial spin configuration is already a realisation of critical percolation, hence Eq. (2.12) should hold without the pre-percolation factor Φ. To check the scaling with $\ell_d(t)$, in Fig. 2.12 we plotted the rescaled cluster size distribution $\mathcal{N}(A,t)\,\ell_d^4(t)$ against the rescaled area $A/\ell_d^2(t)$ for a system of linear size $L = 640$ evolving at $T = T_c/2$. We take $\ell_d(t)$ to be proportional to the inverse of the excess-energy, $\ell_d(t) = \alpha \ell_G(t)$, with the proportionality constant $\alpha = 2.78$. This value is approximately the one that gives us the best data collapse.

The master curve $f(x) = 2\,c_d\,x^{1/2}\left(1+x^{3/2}\right)^{-(2\,\tau_A+1)/3}$, the scaling function for the LCOP domain growth (see Eq. (1.26)), is shown with blue discontinuous line. Deviations from the master curve are expected at very large values of the scaling variable $A/\ell_d^2(t)$, that is to say, for domains with linear size comparable to L. Deviations are also expected at small values of $A/\ell_d^2(t)$ because of the discreteness of the lattice. The master curve from the data collapse slightly differs from the analytic form around the "shoulder", the point at which there is the crossover between the $\sqrt{A}$ behaviour for small domains and the power law decay $A^{-(2\,\tau_A+1)/3}$ for large domains.

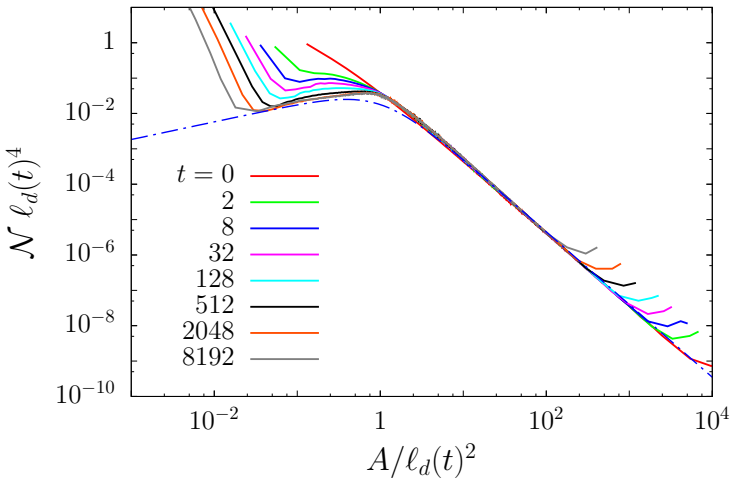

Figure 2.12: Ising model on a triangular lattice with PBC and $L = 640$, with balanced concentration of up and down spins, evolving under local Kawasaki dynamics at target temperature $T_c/2$. We show $\mathcal{N}(A,t)\,\ell_d^4(t)$ against the rescaled area $A/\ell_d^2(t)$, with $\ell_d(t) = \alpha\ell_G(t)$ the characteristic length associated to the coarsening process, and $\alpha = 2.78$. The value of α was chosen so that the datasets collapse onto the master curve $f(x) = 2\,c_d\,x^{1/2}\left(1+x^{3/2}\right)^{-(2\,\tau_A+1)/3}$, represented by the blue dashed line.

2.4.6.2 *Pre-percolation scaling.*

As we did for the scaling of the largest cluster size and interface length and for the wrapping probabilities, we assume that in the regime of approach to critical percolation the relevant length scale is $\ell_p(t) = \ell_d(t)\, t^{1/\zeta}$.

Neglecting for the moment the contribution of the large percolating clusters, the number density of domain areas has the following scaling behaviour,

$$\frac{A^{\tau_A}\,\mathcal{N}(A,t,L)}{2c_d^{\text{eff}}(t)} \simeq \begin{cases} \left(\dfrac{A}{\ell_d^2(t)}\right)^{\frac{2\tau_A+1}{2}} & A \ll \ell_d^2(t) \\ 1 & \ell_d^2(t) \ll A \ll \ell_p^{D_A}(t) \\ \Phi\left(\dfrac{A/\ell_d^{2-D_A}(t)}{\ell_p^{D_A}(t)}\right) & A \gtrsim \ell_p^{D_A}(t) \end{cases} \tag{2.15}$$

The data for the (local) Kawasaki dynamics at temperature $T_c/2$, on a square lattice with linear size $L = 640$, are presented in Fig. 2.13, where $A^{\tau_A}\,\ell_d(t)^{2(2-\tau_A)}\,\mathcal{N}(A,t,L)$ is plotted against A in the left panel and against the rescaled area $(A/\ell_d^{2-D_A}(t))/\ell_p^{D_A}(t)$ in the right panel. In both panels the critical percolation Fisher exponent, $\tau_A = 187/91$, and the fractal dimension of the percolating clusters at critical percolation, $D_A = 91/48$, were used.

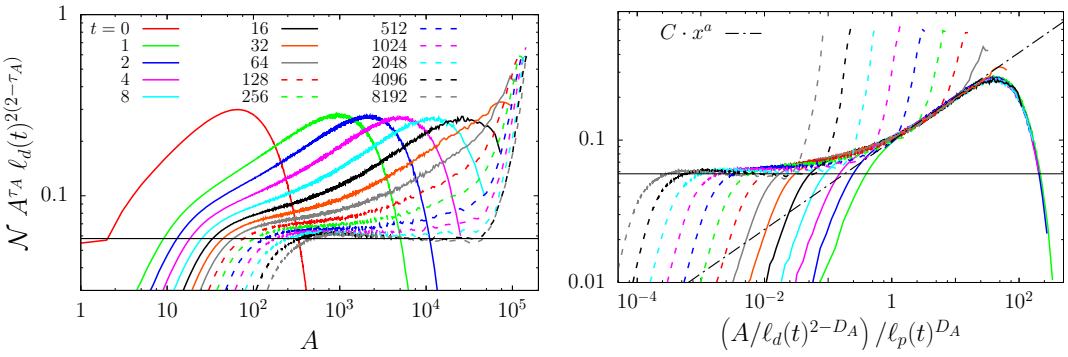

Figure 2.13: Ising model on a square lattice with PBC and $L = 640$, with balanced concentration of up and down spins, evolving under local Kawasaki dynamics at target temperature $T_c/2$. We show the data relative to the number density of domain areas, $\mathcal{N}(A,t,L)$, at different times given in the key. In the left panel we show the quantity $A^{\tau_A}\,\ell_d(t)^{2(2-\tau_A)}\,\mathcal{N}(A,t,L)$, with $\tau_A = 187/91$ the Fisher exponent for critical percolation and $\ell_d(t) = \alpha\ell_G(t)$, plotted against the area A. The proportionality constant α was tuned so that the plateau appearing in the data for the last time matched approximately the constant $2c_d \approx 0.0580$, indicated by the black horizontal line. In the right panel, the same quantity is plotted against the rescaled area $\left(A/\ell_d(t)^{2-D_A}\right)/\ell_p(t)^{D_A}$, with $\ell_p(t) = \ell_d(t)\, t^{1/\zeta}$, where the exponent ζ was chosen to make the datasets corresponding to different times collapse in the scaling region represented by the "shoulder". The best result is achieved by using $\zeta \simeq 2.00$. The function $\Phi(x) = C\,x^a$ has been fitted to the data at $t = 1$ in the interval $[1, 50]$ yielding $a \simeq 0.310$.

The coarsening characteristic length $\ell_d(t)$ has been taken to be proportional to $\ell_G(t)$, namely $\ell_d(t) = \alpha\ell_G(t)$. The value of the constant α was adjusted so that the plateau appearing in the data corresponding to the last time shown ($t = 8192$) matched approximately the constant $2c_d$; we found $\alpha \simeq 3.64$. The value of the exponent ζ was chosen to make

the datasets corresponding to different times collapse in the scaling region represented by the "shoulder". Consistently, the best result is achieved by using $\zeta \simeq 2.00$, the same value obtained from the finite-size scaling of the largest cluster size and the wrapping probabilities.

The pre-percolation regime scaling function Φ takes approximately the form $\Phi(x) = C\,x^a$, with $a > 0$. By fitting this function to the data at $t = 1$, in the region $[1, 50]$ of the scaling variable $\left(A/\ell_d(t)^{2-D_A}\right)/\ell_p(t)^{D_A}$, we found a value of a compatible with the one obtained for the NCOP dynamics, namely $a \simeq 0.310$ (the fit is indicated by a black dashed line in the left panel of Fig. 2.13).

An analogous scaling for the dynamics on the honeycomb lattice is presented in Fig. 2.14. In the left panel, at large values of t, the plateau corresponds to a range of areas obeying the critical percolation statistics. In the right panel, $A^{\tau_A}\ [\ell_d(t)]^{2(2-\tau_A)}\,\mathcal{N}(A,t,L)$ against the rescaled area $(A/\ell_d^{2-D_A}(t))/\ell_p^{D_A}(t)$ highlights the pre-percolating regime. Here again we set $\ell_p(t) = \ell_G(t)\,t^{1/\zeta}$, with the exponent ζ taking the same value as the one used for the finite-size scaling of the wrapping probabilities, namely $\zeta \simeq 1.15$. As one can see, the collapse is not as good as in the case of the Kawasaki dynamics on the square lattice, but the qualitative behaviour of the rescaled distribution is the same. Moreover, a fit of the function $\Phi(x) = C\,x^a$ to the data relative to $t = 1024$, in the interval $[5 \times 10^{-5}, 10^{-4}]$ of the scaling variable $x = (A/\ell_d(t)^{2-D_A})/\ell_p(t)^{D_A}$, yields $a \simeq 0.290$.

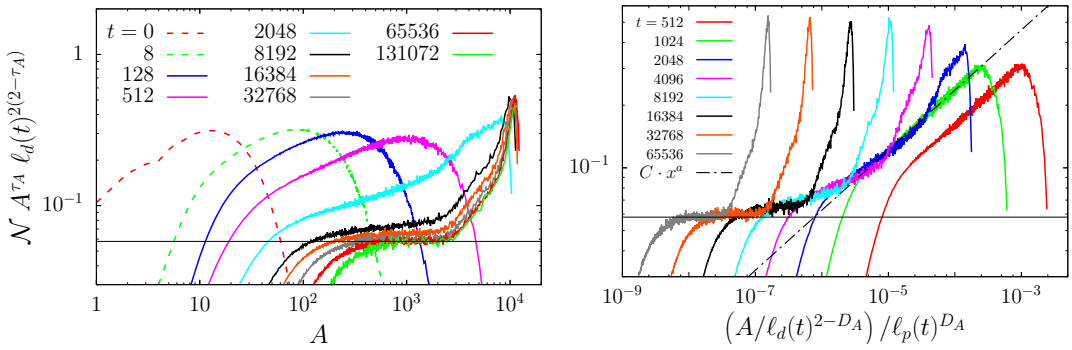

Figure 2.14: Ising model on a honeycomb lattice with PBC and $L = 160$, with balanced concentration of up and down spins, evolving under local Kawasaki dynamics at target temperature $T_c/2$. Same scaling plots as in Fig. 2.13. Here again $\ell_d(t) = \alpha\ell_G(t)$, with the value of α tuned so that the plateau appearing in the data for the latest time shown, $t \simeq 1.31 \cdot 10^5$, matched approximately the constant $2c_d \approx 0.0580$, indicated by the black horizontal line. The characteristic length $\ell_p(t)$ is given by $\ell_p(t) = \ell_d(t)\,t^{1/\zeta}$, where the value of the exponent ζ was chosen to be the same as that used for the scaling of the wrapping probabilities, that is $\zeta = 1.15$. In the right panel, the black dashed line represents a fit of the function $f(x) = C\,x^a$ to the data realtive to $t = 1024$ in the interval $[5 \times 10^{-5}, 10^{-4}]$ of the scaling variable, yielding $a \simeq 0.290$.

2.4.6.3 *Size distribution of percolating clusters.*

We present here an analysis of the size distribution of the spin clusters that are percolating (wrapping spin clusters, in the case of a finite lattice with PBC), the quantity N_p introduced in Sec. 1.3. Looking at this observable can be very useful, since the very few large clusters that survive the coarsening process in the late stages of the dynamics and that contribute to

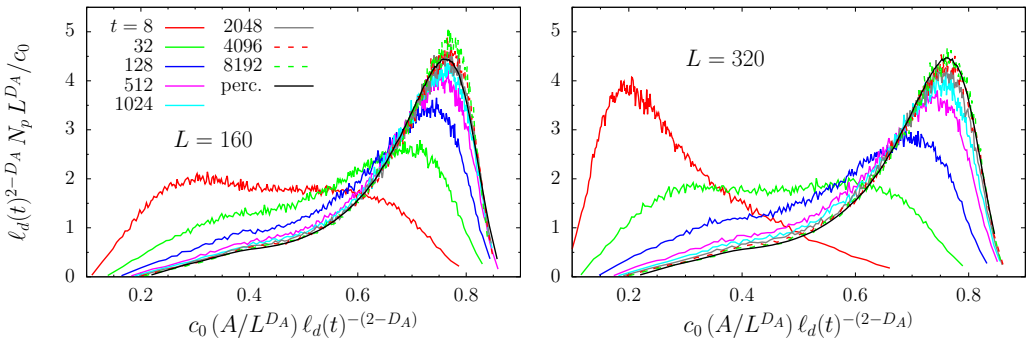

Figure 2.15: The size distribution of the two largest spin clusters, $N_p(A, t, L)$, for an Ising model on a square lattice with PBC, with balanced concentration of the two species, evolving under Kawasaki dynamics at temperature $T_c/2$. On the left the data for $L = 160$, while on the right that for $L = 320$. The color code for the measuring times (see the key in the left panel) is the same in the two plots. The distribution is multiplied by $L^{D_A}\,\ell_d(t)^{2-D_A}/c_0$ and plotted against the rescaled area $c_0\,(A/L^{D_A})\,\ell_d(t)^{-(2-D_A)}$, where D_A is the fractal dimension of the percolating cluster in $2d$ critical percolation, $\ell_d(t) = \ell_G(t)$ is the characteristic length obtained as the inverse of the excess energy, and $c_0 = 1.18$. The size distribution of the largest cluster for random site percolation, at the threshold occupation probability on a square lattice of corresponding size, is also shown with a black solid line, multiplied by L^{D_A} and plotted against A/L^{D_A}. The value of the constant c_0 was chosen so that the rescaled distributions for the dynamical problem collapsed onto the static one of critical percolation.

N_p, are those that signal the onset of the critical-percolation-like scaling regime. Around the time t_p, these clusters span most of the lattice and their geometrical and statistical properties coincide with those of the incipient percolating cluster occurring at critical site percolation (on the same lattice). Usually, at this time, only two large clusters, with opposite spin orientation, are percolating and become "stable" with respect to the microscopic dynamics. This is the reason why N_p can be effectively considered, for all practical purposes, as the size distribution of the two largest spin clusters in the system.

As already explained in Sec. 1.5.5.3 for the case of the Glauber dynamics, one has to take into account the effects of coarsening, and thus the size A needs to be rescaled by the factor $\ell_d(t)^{2-D_A}$. Given these considerations and the fact that N_p is a probability density, N_p should have the following finite-size scaling behaviour

$$N_p(A, t, L) \sim L^{-D_A} \ell_d(t)^{-(2-D_A)}\, n_p\left(A/L^{D_A}\,\ell_d(t)^{-(2-D_A)}\right) \tag{2.16}$$

in the limit $L \to \infty$ and for t approaching the characteristic time t_p. This scaling behaviour was already confirmed by numerical results in the case of the single spin-flip dynamics. It implies that if one plots the quantity $L^{D_A}\,\ell_d(t)^{2-D_A} N_p(A, t, L)$ (for the dynamical problem) against the rescaled size $(A/L^{D_A})\,\ell_d(t)^{-(2-D_A)}$, curves corresponding to different times t and lattice linear size L should approach the same master curve as $t \to t_p(L)$. Furthemore, this master curve should coincide with the scaling function n_p of critical percolation on the same lattice.

In Fig. 2.15 we show this scaling behaviour for the Kawasaki dynamics on a square lattice at target temperature $T_c/2$. Together with these data we also show the size distribution of the largest cluster, multiplied by L^{D_A}, for random site percolation on a square lattice of the

same size, at the threshold occupation probability ($p_c \simeq 0.5927$), against A/L^{D_A}. As one can see, for $L = 160$ (left panel), the data relative to times $t = 2048$ and $t = 4096$ collapse approximately on the master curve represented by the critical percolation size distribution (indicated by a black solid line). We then can say that the critical-percolation-like domain structure is attained at time $t_p \in [2048, 4096]$. Similarly for $L = 320$ (right panel) we obtain that the data for $t = 8192$ is the closest to match the critical percolation distribution. However, in order to get the collapse of the data relative to the quench dynamics onto the critical percolation ones we needed to include an additional scaling factor $c_0 \simeq 1.18$, which seems to be independent of L.

2.5 Conclusions

Let us summarise the main aspects studied in this Chapter.

We studied the early stages of the coarsening process emerging in the $2d$ KIM evolving with spin-exchange dynamics at a finite subcritical temperature and with equal concentration of the two species of spin. We considered the case of spin configuration transitions limited to nearest-neighbour spin-exchange (or Kawasaki dynamics), which in the long time limit can be described by the locally conserved order parameter (LCOP) coarsening theory.

First of all, we proved that extremely long time scales are needed to reach the algebraic growth law $\ell_d(t) \sim t^{1/3}$ for the typical domain radius predicted by LSW theory. Accordingly, we argued that in the scaling analysis the excess-energy growing length $\ell_G(t)$ should be used as a representation of $\ell_d(t)$.

By studying the dynamical scaling behaviour of several observables related to the geometrical properties of the spin clusters, in the case of the dynamics at a subcritical finite temperature and on different lattices, we observe that the domain growth process approaches a critical-percolation-like scaling regime at a time much smaller than the typical time scale $t_{\rm eq}$ associated with complete thermalization. In this dynamical regime, the domain pattern geometrical and statistical properties are the same as in critical percolation after having rescaled all the lengths by $\ell_d(t)$. In particular, the size of the largest spin cluster and the length of the percolating domain walls scale with the effective dynamical system size $L/\ell_d(t)$ with the fractal dimensions of $2d$ critical percolation. The approach to this critical percolation scaling regime is described by a characteristic length $\ell_p(t)$ that behaves as

$$\ell_p(t) \simeq \ell_G(t)\, t^{1/\zeta}$$

with $\ell_G(t)$ the growing length extracted from the excess-energy, and the exponent ζ which depends on the particular lattice geometry. In particular, we find $\zeta \simeq 2.00$ for the dynamics on the square lattice, while $\zeta \simeq 1.15$ for the dynamics on the honeycomb lattice. Essentially, the percolation critical features can be observed at time t on length scales R such that $\ell_d(t) < R < \ell_p(t)$, and the entire system enters in the critical percolation scaling regime at the time t_p such that $\ell_p(t_p) = L$. The model on the triangular lattice behaves differently since it is at the critical percolation point already at $t = 0$ and no additional length scale other than ℓ_d is needed.

In regards to the statistical distribution of the domain area, we found a number of common features with the results of NCOP coarsening. For example, the so-called pre-percolation scaling function Φ, describing the crossover between the algebraic tail in the number density of non-percolating spin clusters and the contribution to $\mathcal{N}$ that comes instead from percolating

ones, is within numerical accuracy of the same form, namely $\Phi(x) \propto x^a$ with $a \simeq 0.3$ in both NCOP and LCOP coarsening dynamics.

After the time t_p such that $\ell_p(t_p) = L$, the percolating cluster(s) become fatter and fatter and a second ordering regime characterised by the expected growing length $\ell_d(t) \simeq t^{1/z_d}$ with $z_d = 3$ should eventually establish. However, very long times are needed to reach this algebraic behaviour and these go beyond the accessible simulation time-window.

Chapter 3

Coarsening in the $2d$ Voter Model: hints of a new criticality.

3.1 Introduction

The voter model (VM) [59, 60, 61] is a purely dynamical stochastic system, used to describe the kinetics of catalytic reactions [62, 63, 64] and as a prototype model of opinion and population dynamics [65, 66, 67]. In its simplest realisation, a bi-valued opinion variable, $s_i = \pm 1$, is assigned to each site i of a given lattice or graph, with a probability $1/2$ of being $+1$ or -1, independently of all other sites. At each subsequent microscopic time step, a site is chosen at random and adopts the "opinion" of a randomly chosen nearest-neighbour. Therefore, the probability for the chosen site to change its opinion (or in the language of the kinetic Ising model, to flip) in a unit time step is simply given by the fraction of neighbours with opposite opinion. These moves mimic, in a very simple fashion, the influence of the neighbourhood on the individual opinion.

The model is parameter free and invariant under global inversion of the spin. Since a site surrounded by others sharing the same opinion can not change its own opinion, there is no bulk noise and the dynamics is uniquely driven by interfacial fluctuations. If the opinion values, $+1$ and -1, are seen as the two state of a spin variable, then the stochastic process can be legitimately thought as a particular version of kinetic Ising model, but evolving with a stochastic spin update rule that does not satisfy a detailed balance condition based on some canonical equilibrium distribution, $P_{\rm eq}(s)$. Instead, the dynamics is completely irreversible since it drives the system towards one of the two *absorbing* states, that is to say, the spin configurations in which all the sites have same opinion/spin. Nevertheless, the time evolution of the system is characterised by a coarsening process that is similar to the one appearing in the conventional KIM evolving at a target temperature $T < T_c$. In this sense, the VM dynamics can be classified in the nonconserved order parameter (NCOP) coarsening family.

Actually, it is possible to show that the voter model and the ferromagnetic KIM evolving with Glauber dynamics are two particular instances of a family of stochastic kinetic Ising models with up-down symmetry and equipped with isotropic and short-ranged single spin-flip transition rates, see App. C.1. This class of models is defined by a two-parameter dependent spin-flip transition rate, the two parameters basically controlling bulk and interfacial noise.

A thorough numerical investigation [1] of numerous macroscopic observables (interface density, space-time correlation, persistence, *etc.*) of VM on the square lattice corroborated the analytic predictions of the papers cited in the first paragraph. In [1] some features of

critical percolation were also observed in the late stages of the coarsening dynamics, even though it was not clear wether a truly long-lasting dynamical scaling regime in which the domain pattern have the scaling properties of critical percolation could exist. In that paper we claimed that the appearance of critical percolation properties in the VM dynamics on a finite square lattice with PBC occurs at a typical time $t_p \simeq L^{z_p}$, where L is the system linear size, with $z_p \simeq 1.67$. We must admit, however, that this result was suggested by an approximate analysis.

In this Chapter, we reformulate our statements on the approach to critical percolation making them much more detailed and precise. This is achieved by following the same methods used in the case of the Glauber dynamics (Chap. 1) and Kawasaki spin-exchange dynamics (Chap. 2). In particular, the measurement of the average squared winding angle for domain walls, $\langle \theta^2 \rangle$, will show that two type of criticalities occur during the evolution of the system: a first one, that corresponds to percolation, appears after a very short time span, and a second one, with different scaling properties, that establishes later. Furthermore, the finite-size scaling of various observables and the analysis of the domain area distribution will prove that there is no long-lasting lapse over which critical percolation is established, contrary to what happens for the $2d$IM evolving with NCOP and COP dynamics. Instead, at sufficiently long times the geometrical and statistical properties of the domain pattern grown by the VM stochastic dynamics are those of the second criticality.

Hence, we need to reformulate slightly the problem studied in Chap. 1 and Chap. 2. We introduce a typical time scale

$$t_c \sim L^z \ , \tag{3.1}$$

with $z \simeq 1.67$, to which one can associate a length scale

$$\ell_{\rm V}(t) \sim t^{1/z} \ , \tag{3.2}$$

that has the same meaning of the length $\ell_p(t)$ seen in the previous Chapters: the critical behaviour (in terms of the geometry and statistics of domains) can be observed over distances r such that $\ell_d(t) \ll r < \ell_{\rm V}(t)$, while for larger distances the system still looks like in the initial state.

3.2 Definition of the Model

We consider the simplest version of the voter model, which is sometimes called the symmetric voter model. Given a finite graph (or lattice) $\Lambda = (V, E)$, with set of vertices (sites) $V = \{v_1, v_2 \ldots, v_N\}$ and edges (bonds) $E = \{e_1, e_2 \ldots, e_M\}$, we assign to each vertex $i \in V$ a bi-valued opinion variable $s_i \in \{-1, 1\}$. We will always use the language of spin models and thus, for us, the specification of the values of the opinion/spin at each vertex of the graph (or lattice site), that is $s = \{s_i\}_{i \in V}$, is considered as the spin configuration of the system. A realisation of the VM stochastic process in the space of spin configurations is then determined by single spin flip transitions, that is to say, transitions of the type $s \to s^{(i)}$ for a given $i \in V$, with the "arrival" spin configuration $s^{(i)}$ obtained from the "starting" one s by flipping the spin at vertex i, and with transition rate given by

$$W(s \to s^{(i)}) = \frac{C}{2} \left(1 - \frac{1}{n_c(i)} \, s_i \sum_{j \in \mathcal{N}(i)} s_j \right) = C \, \frac{n_a(i|s)}{n_c(i)} \ , \tag{3.3}$$

where $\mathcal{N}(i)$ is the set of vertices connected to vertex i (set of nearest-neighbour lattice sites), $n_c(i) = |\mathcal{N}(i)|$ is the number of vertices connected to vertex i (coordination number of the

lattice) and $n_a(i|s) = (n_c(i) - s_i \sum_{j\in\mathcal{N}(i)} s_j))/2$ is the number of vertices amongst $\mathcal{N}(i)$ that have spin antiparallel to that of vertex i, given the configuration s. The constant C is arbitrary and just sets the order of magnitude of the typical time step in which, on average, one spin flip occurs (we will set it to 1).

Notice that $W(s \to s^{(i)})$ depends on the spin configuration $s = \{s_k\}_{k\in V}$ only through the quantity $h_i = s_i \sum_{j\in\mathcal{N}(i)} s_j$ (the "local field" acting on site i), as in the case of the Glauber update rule, see Sec. 1.2, Eq. 1.8. But, in the case of the VM, the dependence is linear in h_i, thus sometimes the VM is called linear Glauber model in the literature [68]. However, it is possible to define other voter-like models in which the spin-flip rate is not simply a linear function of the local field, but still satisfy the Z_2 symmetry and have similar properties [69, 70], see App. C.1. It is important to notice also that, since the spin-flip rate is linear in the local field h_i, the model can be solved exactly, in arbitray dimension [68, 71] (that is to say, the equations describing the time evolution of correlation functions of any order can be solved exactly). In App. C.2 we sketch the analytic calculations that allow us to obtain the average site magnetisation and the two-point correlation function.

Looking at the spin-flip rate given by Eq. (3.3), we see that if a lattice site is surrounded by neighbours that have the same opinion/spin, then its spin can not flip, meaning that those sites that are inside the bulk of spin clusters are inert. The growth of domains is driven purely by the fluctuations occuring at their interfaces. Moreover, the fully magnetized states, that is to say, the (two) spin configurations where all vertices have the same value of the spin, are *absorbing* states for the VM dynamics. Once the stochastic process falls in one of these states it can not escape from it. For this reason, the time-dependent probability distribution $P(s,t)$ for the spin configuration s converges towards a trivial 2-mass distribution, $P_\infty(s) = p_+ \ \delta_{s,\mathbf{1}} + (1-p_+) \ \delta_{s,-\mathbf{1}}$, where we denote by $\mathbf{1}$ the spin configuration in which all vertices have spin $+1$, and by $-\mathbf{1}$ the one in which all vertices have spin -1, and p_+ is the probability for the system to be trapped in the state $\mathbf{1}$. This implies also that the spin-flip transition rates $W(s \to s^{(i)})$ do not satisfy a detailed balance condition with some Boltzmann-like equilibrium distribution density $P_{\rm eq}(s) \sim \exp\{-U(s)\}$, for some energy function $U(s)$.

In the rest of this Chapter, we are going to consider the VM on a $2d$ lattice with finite linear size L and periodic boundary conditions (PBC). The spin-flip rate for site i reduces to

$$w_i(s) = \frac{1}{2}\left(1 - \frac{1}{n_c}\, s_i \sum_{j\in\mathcal{N}(i)} s_j\right) , \tag{3.4}$$

with n_c the coordination number of the lattice (by setting also $C = 1$), so that $w_i(s) = n_a(i|s)/n_c$ with $n_a(i|s) \in \{0, 1, \ldots, n_c\}$. The possible spin-flip transitions for the voter model on a square lattice are depicted schematically in Fig. 3.4. The initial spin configuration is always taken to be one with equal concentration of the two "opinions", randomly distributed over the lattice. In fact, the probability p_+ (p_-) for the system to end up in a configuration in which all sites have spin $+1$ (-1) is equal to the initial concentration of $+1$ (-1) spins (see App. C.2). An equal concentration of the two species at $t = 0$ makes sure that stochastic dynamics leads the system to the configuration $\mathbf{1}$ half of the times, and the other half to $-\mathbf{1}$.

To set the stage, in Fig. 3.2 we show some snapshots of the evolution of a spin configuration under VM dynamics on a triangular lattice with linear size $L = 128$ and PBC. The absence of bulk noise and the roughness of the interfaces are clear in all images. They look very different from those that we exhibited for the Ising model evolving with zero-temperature Glauber dynamics. The initial state has a wrapping (blue, -1) cluster which is later broken, see the snapshot at $t = 64$. In the last image at $t = 1024$ two spanning clusters having

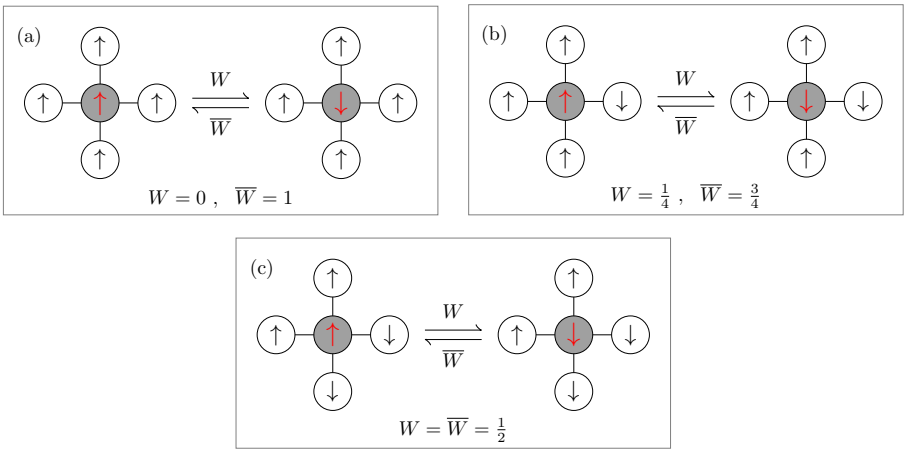

Figure 3.1: The possible spin-flip transitions for the voter model on a square lattice. In each case, the central site (gray circle) represents the lattice site whose spin is chosen to be flipped. The spins on the four nearest-neighbours are shown as well. W is the transition rate from the configuration on the left to that on the right, while $\overline{W}$ is the rate associated with the inverse transition. If q is the number of nearest-neighbours with antiparallel spin, then the spin-flip rate is given by $W = q/4$.

opposite phases are present. It is clear from the figures that a coarsening process takes place although there is no energy function to minimise in this model. At much later times one of the two phases will predominate and "conquer" the sample.

3.3 Numerical analysis

3.3.1 Average squared winding angle

As seen in Secs. 1.5.3 and 2.4.3, the measurements of the average squared winding angle, $\langle\theta^2\rangle$, can be used to determine the type of criticality that the system is approaching during its evolution.

Fig. 3.3 presents the data relative to $\langle\theta^2\rangle$ for the hulls of the largest cluster, in the case of the VM dynamics on a square lattice with $L = 640$, plotted against the logarithm of the curvilinear distance x. The data shown refer to just the wrapping hulls. A spanning cluster appears at a very early time, $t \simeq 5$ for $L = 640$. The "critical" function $c + 4\kappa/(8+\kappa)\ \ln x$ is fitted to the data corresponding to $t = 5.5$, yielding $\kappa \simeq 5.96$, a value which is very close to the $\kappa = 6$ of critical percolation. At later times, the long distance behaviour remains the same: the slope of the curves is approximately the same as that at $t = 5.5$ for distances $x > x_c(t)$, with x_c a crossover of the curvilinear distance. Meanwhile, for $x < x_c(t)$, the slope has changed but the behaviour is still critical in the sense that $\langle\theta^2(x)\rangle \simeq \text{const.} + C\ \ln x$. After a sufficiently late time, $\langle\theta^2\rangle$ acquires this second criticality over the whole range of x. By fitting the function $c + 4\kappa/(8+\kappa)\ \ln x$ to the data corresponding to the latest time we obtain $\kappa \simeq 3.82$. This result, associated to the interfaces, is very different from the one found for the $2d$IM with NCOP and COP dynamics, cases in which the interfaces at equilibrium are smooth and $\kappa = 0$ at short length scales. It is thus evident that there exists a transition between critical percolation at large distances and a new type of criticality (associated with

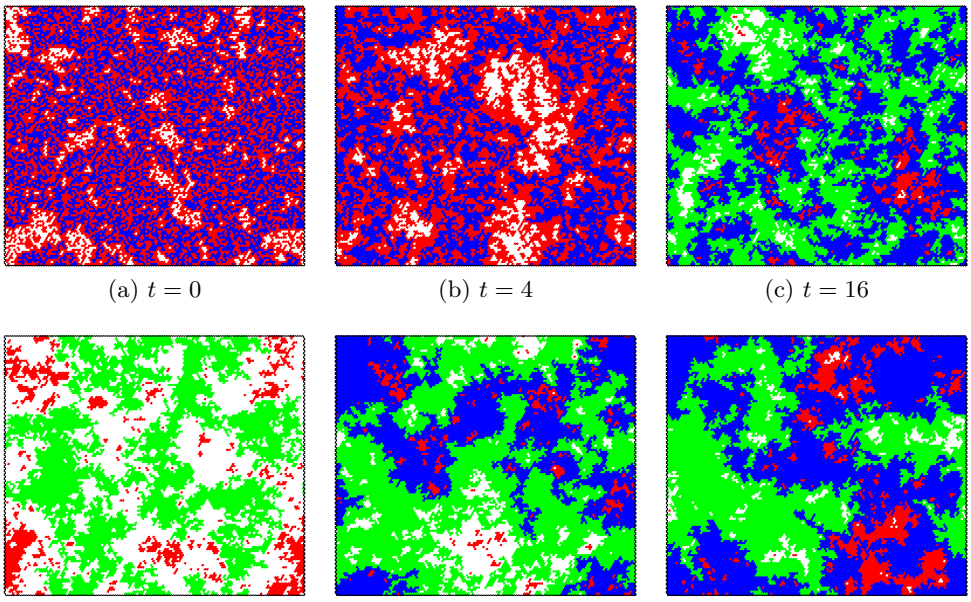

(a) $t = 0$ (b) $t = 4$ (c) $t = 16$

(d) $t = 64$ (e) $t = 256$ (f) $t = 1024$

Figure 3.2: Some snapshots of the evolution of a spin configuration under voter model dynamics on a triangular lattice with linear size $L = 128$ and PBC. Red cells and white cells represent $+1$ and -1 spins, respectively. Sites belonging to a cluster that wrap around the system are highlighted in green for a $+1$ wrapping cluster and in blue for a -1 wrapping cluster.

a SLE parameter $\kappa \simeq 3.82$) at small ones.

In order to highlight the crossover between these two regimes, in the inset of Fig. 3.3 we show the quantity $\langle\theta^2\rangle - b \ln t$ against the logarithm of the rescaled curvilinear distance x/t^α with $\alpha = 0.74$ and $b = 0.97$. The justification for this scaling is the following. The unscaled data show a crossover from the early critical percolation behaviour to a new kind of criticality at a time-dependent curvilinear distance $x_c(t) \propto t^\alpha$. Visually, $x_c(t)$ corresponds to the point where $\langle\theta^2\rangle$ (when plotted against $\ln x$) changes from one slope to another. This length scale is related to $\ell_d(t)$ by $x_c(t) \sim \ell_d^{D_\ell}(t) \propto t^{D_\ell/z_d}$ with D_ℓ the fractal dimension of the cluster hulls and z_d the dynamical exponent. Thus, α should be related to κ and z_d by $\alpha = D_\ell(\kappa)/z_d = (1 + \kappa/8)/z_d$. In the case indicated in Fig. 3.3, as t increases, $\langle\theta^2\rangle$ approaches a functional form with $\kappa = 3.82$ (see the fitting function). Using now $z_d = 2$ we deduce $D_\ell \simeq 1.48$ and $\alpha \simeq 1.48/2 = 0.74$, which is the value used to scale x in the inset. The coefficient b can be related to κ and z_d too. In fact, in order to obtain data collapse for different times we also need to subtract from $\langle\theta^2\rangle$ the winding angle variance corresponding to a length $x_c(t) \propto t^\alpha$, that is a quantity $4\kappa/(8 + \kappa) \ln t^\alpha$. Then we have $b = 4\,\alpha\,\kappa/(8 + \kappa) = \kappa/(2\,z_d) \simeq 0.97$.

For the other geometries, triangular and honeycomb lattices, similar fits yield $3 \leq \kappa \leq 4$ at short length scales, see the caption of Fig. 3.4 for the precise values found in each case. On the triangular lattice, as expected, critical percolation properties are already present at the moment of the quench, $t = 0$. The insets in Fig. 3.4 display the time scaling and confirm the arguments exposed in the previous paragraph.

The same scaling method was adopted by Blanchard *et al.* in [72] in the study of quenches *between critical points*; more precisely, in the analysis of the $2d$IM on the triangular lattice

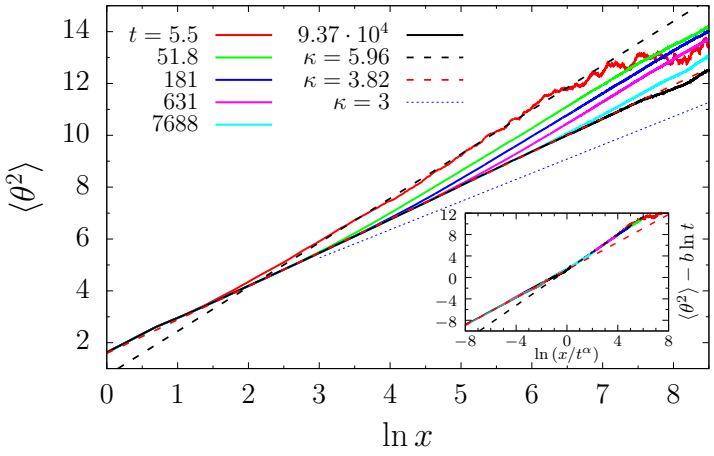

Figure 3.3: Voter dynamics on the square lattice. Average squared winding angle $\langle \theta^2(x,t) \rangle$ for the wrapping hulls that form the largest cluster interface, against the logarithm of the curvilinear coordinate x, at different times given in the key. The lattice has linear size $L = 640$. A fit of $c + 4\kappa/(8+\kappa)\ \ln x$ to the data at $t = 5.5$ yields $\kappa \simeq 5.96$ (black dashed line), while a fit to the data at late times, $t = 9.37 \cdot 10^4$, gives $\kappa = 3.82$ (red dashed line). We also show, for comparison, the slope associated to $\kappa = 3$ with dashed-dotted blue line. In the inset, we collapse the dynamic data by plotting $\langle \theta^2 \rangle - b \ln t$ against the rescaled curvilinear distance x/t^α, with $\alpha = 0.74$ and $b = 0.97$. See the text for an explanation of these parameters.

evolving with NCOP dynamics at $T = T_c$ after a sudden quench from $T \to \infty$. These dynamics show a crossover from the initial critical percolation point to the Ising critical point controlled by the growing length $\ell_c(t) \simeq t^{1/z_c}$ with z_c the critical dynamic exponent at T_c. In this case, the cluster hulls have the equilibrium geometrical features of the critical Ising point for $x < x_c(t)$, while they obey the properties of critical percolation for $x > x_c(t)$. This double criticality is similar to what we observe for the interfaces of the VM on the triangular lattice.

On the square lattice, the behaviour is also close to that found in the NCOP relaxation dynamics to the critical Ising point [73]. In this case, a short time is needed to see the wrapping hulls with $\kappa \simeq 6$, since the system is not already in a critical percolation state at $t = 0$ (in fact, it is always initiated in a completely random configuration, with equal probability of having either spin $+1$ or -1, at each site). But after this transient, it does not remain in a critical-percolation-like regime as it happens for the $2d$IM evolving with Glauber or Kawasaki dynamics at a subcritical temperature. Instead, it approaches a new type of criticality (in terms of the geometry of the domains).

Obtaining a result that is similar to that of a critical quench of the Ising model should not come as a surprise. Indeed, the VM and IM belong to the same class of $2d$ stochastic spin systems. In particular, if the model is defined on a square lattice, the spin-flip transition rate for VM (Eq. (3.4)) and that for IM (Eq. (1.8)) can be shown to be special cases of a general two-parameter spin-flip rate function, with the two parameters essentially being a "bulk" noise and an "interfacial" noise. VM is specifically obtained when only interfacial noise is switched-on. Moreover, the VM as well as the *critical* Ising model lie on a line of critical points separating a paramagnetic phase from a ferromagnetic phase, in the space spanned by these two noise parameters [69, 74]. While it is believed that the low temperature phase has

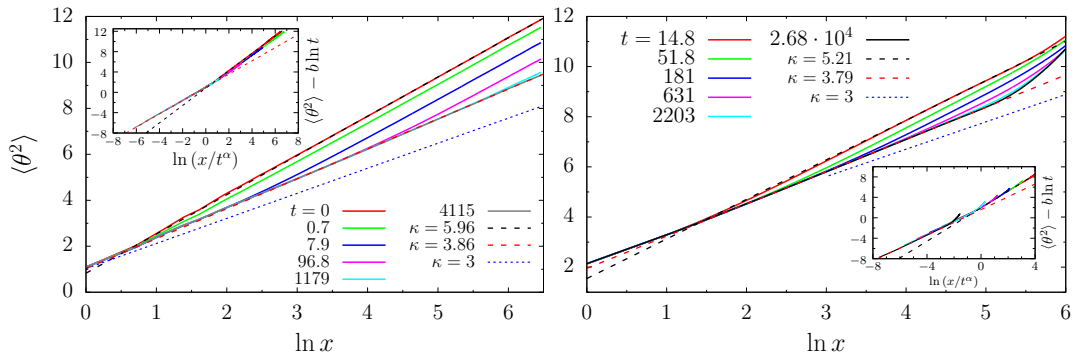

Figure 3.4: Voter dynamics on the triangular (left) and honeycomb (right) lattice with $L = 320$ and $L = 160$, respectively. Average squared winding angle $\langle\theta^2(x,t)\rangle$ for the wrapping hulls of the largest clusters against the logarithm of the curvilinear coordinate x, at different times given in the keys. We show fits of the function $c + 4\kappa/(8+\kappa)\ \ln x$ with dashed lines. In the left panel, a fit to the data at $t = 0$ yields $\kappa \simeq 5.96$ (black dashed line), while at $t = 4115$, the estimated value is $\kappa = 3.86$ (red dashed line). In the right panel, $\kappa \simeq 5.21$ at $t = 14.8$ and $\kappa = 3.79$ at $t = 2.68 \cdot 10^4$. In the insets $\langle\theta^2\rangle - b\ln t$ against x/t^α, with $\alpha = 0.74$ and $b = 0.97$ on the triangular lattice, and $\alpha = 0.74$ and $b = 0.95$ on the honeycomb lattice, yielding the best data collapse. See the text for an explanation of the meaning of the fitting parameters.

a universal behaviour (the one of the Ising model at zero temperature), the situation is less clear on this critical line. Our present results seem to indicate that a *new universality class*, at least for the behaviour of the domain walls, would exist for the VM.

Summarising, with the analysis of the winding angle we have shown the following.

- On the triangular lattice, the VM evolves in time leaving the initial random percolation criticality. The domain walls approach another kind of criticality, close to that of the equilibrium critical $2d$IM, namely $\kappa \simeq 3.86$, while $\kappa_{\text{IM}} = 3$.

- On the other lattices, the domain walls approach a critical percolation state in a relatively short span compared to the time required to reach the absorbing state. But then they soon depart from this kind of geometry to enter a different type of criticality in the late stages of the coarsening process, with an associated SLE parameter $\kappa \simeq 3.80$.

In both cases, the fractal dimension of the short length scales is approximately $D_\ell(\kappa = 3.8) = 1.48$ and the temporal scaling is controlled by the usual coarsening length $\ell_d(t) \simeq t^{1/z_d}$ with $z_d = 2$.

3.3.1.1 *Initial configuration with a flat interface*

The results shown up to now were obtained using a paramagnetic initial state in equilibrium at infinite temperature. We are now going to consider a "slab" initial state, which consists in a spin configuration where half of the sites take spin $+1$ and the other half take spin -1, and they are arranged into two "stripes". For example, a spin configuration where all sites with x-coordinate in $[1, L/2]$ have spin $+1$, while those with $x \in [L/2+1, L]$ have spin -1 (for L even). Due to PBC, the $+1$ domain and the -1 domain are separated by two straight (and wrapping) domain walls. Note that this is a *frozen* state for the zero-

temperature Glauber dynamics but it is not for the voter model spin update rule. Under the voter model dynamics, a flat interface can fluctuate.

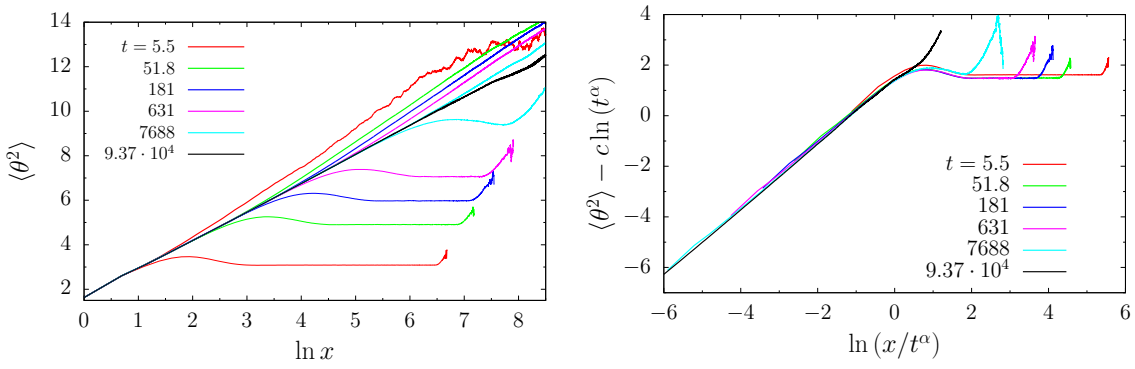

Figure 3.5: Voter model dynamics on a square lattice with $L = 640$ and PBC. We show the average squared winding angle $\langle\theta^2(x,t)\rangle$ measured for the wrapping hulls that form the largest cluster interface, against the logarithm of the curvilinear coordinate x, at different times given in the key. Left: Raw data. The data above the black line were produced in the case of a completely random and homogeneous initial condition (same data as in Fig. 3.3). The black line and the curves below are instead relative to the measurements obtained in the case of slab initial state. The color code is the same for the two sets of data. Right: scaling of the data for the slab initial condition. We plot the quantity $\langle\theta^2\rangle - c\ln(t^\alpha)$ against $\ln(x/t^\alpha)$, where $c = 4\kappa/(8+\kappa)$ with κ fixed to 3.85 , and the exponent $\alpha = 0.67$ chosen to yield the best data collapse.

In Fig. 3.5, left panel, we show the average squared winding angle, $\langle\theta^2\rangle$, measured along the walls of the largest spin cluster for the VM dynamics on a square lattice with $L = 640$, starting from the slab configuration defined above. $\langle\theta^2\rangle$ is shown as function of the logarithm of the curvilinear distance x along the domain wall. The figure also displays the data from Fig. 3.3, that is, the case corresponding to completely random and homogeneous initial condition. The times at which the data are collected are the same in the two cases. Concerning the latter set of data, at early times, $t = 5.5$, the domain walls separating the two large spin clusters in which the system is divided are fluctuating only up to some short distance, while over longer distances, they remain flat as in the initial state ($\kappa = 0$). As we let time pass, the distance up to which the domain wall "roughness" (and thus fractality) can be observed increases, and moreover the value of the SLE parameter κ associated with the slope of curve $\langle\theta^2(x)\rangle$ (considered as function of $\ln x$) tends to the same one that establishes at long times in the case of homogeneous initial condition. For the latest time shown, $t = 9.37 \cdot 10^4$, the data for the two kinds of initial conditions coincide, within numerical accuracy. This shows that the "second criticality" is not related to critical percolation, nor to the particular initial configuration of the system, but it is inherent to the long term behaviour of the domain walls under the voter model dynamics.

We identify a time-dependent crossover length, that we denote by $x_c(t)$. At curvilinear length scales larger than $x_c(t)$ the domain walls still retain the properties of the initial condition, that is, they are flat on average, while for smaller length scales the domain walls have fractal properties associated to $\kappa \simeq 3.85$. As done in the previous cases, we suppose that $x_c(t) \sim t^\alpha$ with an exponent α to be determined from the scaling. We show this scaling in the right panel of Fig. 3.5, where $\langle\theta^2\rangle - c\ln(t^\alpha)$ is plotted against $\ln(x/t^\alpha)$, with $c = 4\kappa/(8+\kappa)$ and κ fixed to 3.85. The best collapse is achieved with $\alpha \simeq 0.67$. Notice that this value

is close to the one obtained for the scaling of $\langle\theta^2\rangle$ in the case of infinite temperature initial condition.

3.3.2 Wrapping probabilities

We can now ask what are the implications that this new type of criticality, that emerges from the analysis of $\langle\theta^2\rangle$ in the late stages of the dynamics, has on the so-called wrapping probabilities, *i.e.* the probability that a spin cluster wraps around the system along a certain direction, at a given time. In the case of the $2d$IM evolving with either Glauber or Kawasaki spin update rules at zero or very low temperature, we have seen that, at a certain point of the coarsening process, wrapping domain walls become topologically stable against the microscopic stochastic dynamics: they can still fluctuate, but their number and the direction along which they percolate remain fixed, at least until the very late equilibration regime takes over (for $T > 0$). Moreover, they approach the values of $2d$ critical percolation. In the case of the voter model dynamics, we do not find the same behaviour, as it is shown in Figs. 3.6 and 3.7

Nevertheless, we are interested in the finite-size scaling of the πs. In the late stages of coarsening, we should expect

$$\pi_\alpha(t, L) \sim \tilde{\pi}_\alpha\left(\frac{t}{L^2}\right) \tag{3.5}$$

with $\tilde{\pi}_\alpha$ a scaling function, where the subscript α stands for the specific direction of the wrapping (only horizontally, only vertically, diagonally, etc.). The scaling of time t as t/L^2 is justified by the fact that, at very long time, the domain growth is described by the usual characteristic length $\ell_d(t) \sim t^{1/2}$ associated to NCOP dynamics, which also coincides with the dynamical scaling law found by studying the two-point correlation function (see App. C.2). However, we are interested in the possibility of the existence of a short-time regime in which finite-size scaling is realised with a dynamic exponent z different from $z_d = 2$ associated to NCOP coarsening.

In other words, we would like to determine if there exist a time scale $t_c \sim L^z$, with $z < 2$, corresponding to the typical time required by the system to grow domain walls with the fractal behaviour evidenced by $\langle\theta^2\rangle$, spanning the whole system. For $t \lesssim t_c \sim L^z$, the wrapping probabilities π_α should satisfy the scaling relation $\pi_\alpha(t, L) \simeq \tilde{\pi}_\alpha^{(c)}\,(t/L^z)$, with a scaling function $\pi_\alpha^{(c)}(x)$ different from $\pi_\alpha(x)$, the one associated with the late coarsening regime leading to the absorbing state. This is the same argument used for the other types of dynamics, where we showed that indeed there exists an early-time regime in which the coarsening process build critical percolation structures up to a distance $\ell_p(t)$, growing much faster than $\ell_d(t) \sim t^{1/z_d}$, so that a dynamical scaling regime, with critical percolation properties extending over the entire system, is attained at time t_p such that $\ell_p(t) \sim L$. In the case of the VM, we are not sure that the percolation criticality is what the system is approaching, and if it can last for very long period of time before the system enters in the final regime that leads to the absorbing state.

By looking at the finite-size scaling of the data we find that a good scaling at short times is achieved by using $z \simeq 1.67$. For large times instead, we recover the usual t/L^2 scaling, as expected. This is shown in Fig. 3.6 for the wrapping probabilities in the case of VM dynamics on a square lattice, and in Fig. 3.7 for the VM dynamics on a honeycomb lattice. Notice that, for the honeycomb lattice case, we need to show π_h and π_v (the probability for a spin cluster to wrap only horizontally and only vertically, respectively) separately, since the aspect ratio of the lattice implemented in the simulations is not 1, as explained in more detail

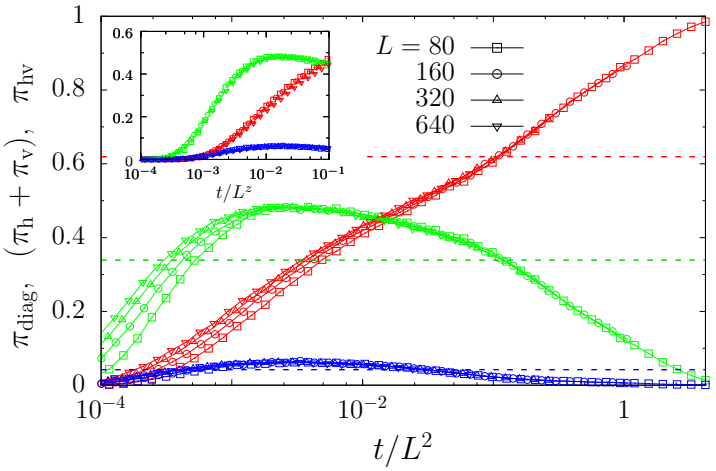

Figure 3.6: The wrapping probabilities for the VM dynamics on a finite square lattice for different values of L, indicated in the keys. We show $\pi_{\rm hv}$ (red points), $\pi_{\rm h}+\pi_{\rm v}$ (green points), and $\pi_{\rm diag}$ (blue points). The horizontal dashed lines correspond to the exact values of $2d$ critical percolation wrapping probabilities $\pi^{(p)}_{\rm hv}$, $\pi^{(p)}_{\rm h}+\pi^{(p)}_{\rm v}$ and $\pi^{(p)}_{\rm diag}$, for a lattice with unit aspect ratio, see Sec. 1.3. In the main plots, the wrapping probabilities are plotted against t/L^2. In the inset, the same data are plotted against the rescaled time t/L^z, with $z \simeq 1.67$.

in App. A.2. The curves do not show a long-lasting metastable state with the properties of critical percolation, contrary to what happens for the Ising model evolving under Glauber dynamics or Kawasaki dynamics. The πs approach the critical percolation values ($\pi_{\rm hv}$ from below, while $\pi_{\rm h}$, $\pi_{\rm v}$ and $\pi_{\rm diag}$ from above after a short transient in which they reach their maximum value) around a time $t^\star \simeq 0.1\, L^{z_d}$ (on the square lattice) and $t^\star \simeq 0.5\, L^{z_d}$ (on the honeycomb lattice), but later they continue to evolve towards the asymptotic values dictated by the absorbing states ($\pi_{\rm hv} = 1$ and $\pi_{\rm h} = \pi_{\rm v} = \pi_{\rm diag} = 0$). This is very different from what is shown, *e.g.*, in Fig. 1.11 for Glauber dynamics.

These measurements suggest that, in the cases in which the process does not start from a critical percolation state (as it happens instead for the model on a triangular lattice), there is a crossover between two different scaling regimes. In the first one, the relevant length scale is given by

$$\ell_{\rm V}(t) \sim t^{1/z}\,, \tag{3.6}$$

with $z \simeq 1.67$, which describes the approach to the new criticality. We use the subscript "V" to explicitly mean that this criticality is observed so far only for the voter model and to distinguish it from the characteristic length scale $\ell_p(t)$ controlling the pre-percolation regime for the other types of stochastic spin dynamics studied before. The second and usual NCOP coarsening regime, in which one observes the characteristic length scale $\ell_d(t) \sim t^{1/2}$, sets in roughly after $\pi_{\rm h}$ and $\pi_{\rm v}$ have reached their maximum value. At that point, in most realisations of the VM dynamics, one of the spin clusters that are wrapping only in one direction of the lattice (in a so called "stripe" configuration or "diagonal" one, see Fig. 1.2) starts percolating in both directions (*i.e.* with the so-called "cross" topology) at the expense of all the others.

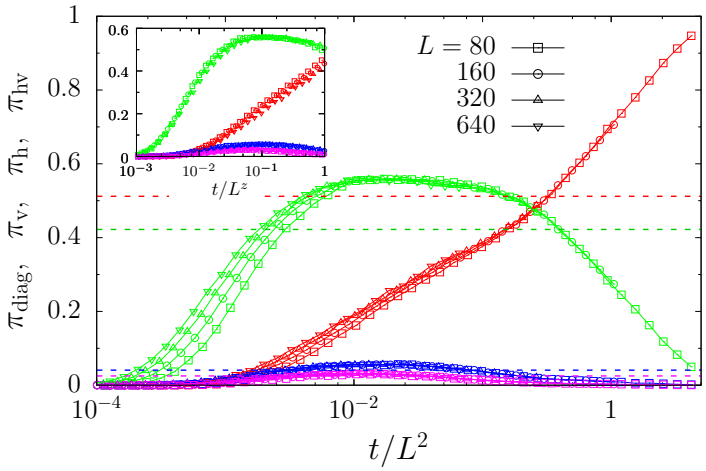

Figure 3.7: The wrapping probabilities for the VM dynamics on a finite honeycomb lattice, for different values of L. We show $\pi_{\rm hv}$ (red points), $\pi_{\rm h}$ (green points), $\pi_{\rm v}$ (blue points), and $\pi_{\rm diag}$ (purple points). The two probabilities $\pi_{\rm h}$ and $\pi_{\rm v}$ are shown separately, since the simulations are done on a lattice with aspect ratio $\sqrt{3}$. The horizontal dashed lines correspond to the exact values of $2d$ critical percolation wrapping probabilities for a lattice with aspect ratio $\sqrt{3}$, see Sec. 1.3. In the main plots, the data are plotted against t/L^2. In the inset, instead, they are plotted against the rescaled time t/L^z, with $z \simeq 1.67$.

3.3.3 Largest cluster scaling

In this Section we analyse the scaling properties of the size of the largest cluster, A_c, and the length of the hulls forming its interface, l_c, by using the same finite-size scaling argument adopted for the wrapping probabilities. We assume that A_c and l_c have the scaling behaviour

$$A_c(t,L) \sim L^{D_A^\star}\, \tilde{A}_c\left(\frac{t}{L^z}\right), \qquad l_c(t,L) \sim L^{D_\ell^\star}\, \tilde{l}_c\left(\frac{t}{L^z}\right), \tag{3.7}$$

with $\tilde{A}_c$ and $\tilde{l}_c$ some scaling functions, $D_A^\star$ and $D_\ell^\star$ the fractal dimensions of the largest cluster size and hull length, respectively. We use $D_A^\star$, $D_\ell^\star$ and z as free parameters to be adjusted together by looking at the best collapse of the datasets corresponding to different values of L. The aim is to prove that a finite-size scaling is achieved with $z \simeq 1.67$, as obtained from the analysis of the wrapping probabilities, and with $D_A^\star$, $D_\ell^\star$ taking values that are compatible with the SLE parameter κ estimated from the measurements of $\langle\theta^2\rangle$.

In Fig. 3.8 we display the scaling for the VM dynamics on a square lattice. The best collapse is achieved by using $D_A^\star \simeq 1.93$ and $D_\ell^\star \simeq 1.53$ for the largest cluster size and the length of its hull, respectively, and $z \simeq 1.67$. We confirm what is found for the scaling of the wrapping probabilities, that is to say, the existence of a time scale $t_c(L) \sim L^z$ that marks the end of a first scaling regime and the entrance into the last coarsening one. We find similar results for the dynamics on a honeycomb lattice, see Fig. 3.9, with $D_A^\star \simeq 1.90$, $D_\ell^\star \simeq 1.52$ and $z \simeq 1.67$. We note that the fractal dimension of the largest cluster hull, $D_\ell^\star$, estimated through this finite-size scaling method, is compatible, within numerical accuracy, with the value of κ obtained from the analysis of $\langle\theta^2\rangle$. For example, in the case of the data relative to the dynamics on the square lattice, $D_\ell^\star = 1.53$ would correspond to $\kappa = 4.24$. However, this is not the case for $D_A^\star$, since $D_A^\star \simeq 1.93$ would imply $\kappa \simeq 3.15$, a value which is much farther.

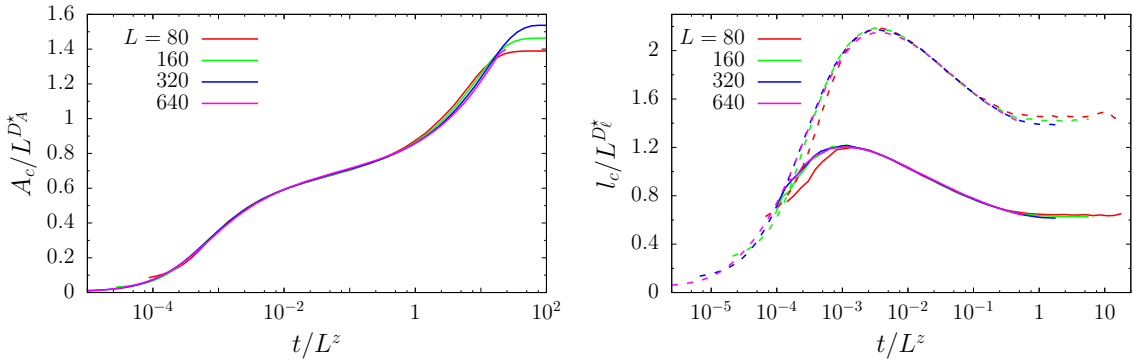

Figure 3.8: The scaling of the geometric properties of the largest cluster for the VM dynamics on a square lattice. The size of the largest cluster A_c divided by $L^{D_A^\star}$, with $D_A^\star = 1.93$ (left), and the length of its external hull l_c divided by $L^{D_\ell^\star}$, with $D_\ell^\star = 1.53$ (right), for various L. Regarding l_c, the contribution due to wrapping hulls is shown with continuous lines while the one due to non-wrapping hulls is shown with dashed lines. All the quantities are plotted against the rescaled time t/L^z, with $z = 1.67$. The values of $D_A^\star$, $D_\ell^\star$ and z were found by looking for the best collapse of the data corresponding to different L.

In Fig. 3.10 we display the same kind of scaling for the voter model dynamics on a triangular lattice. Again we find that the scaling relations in Eq. (3.7) are satisfied if we plot both $A_c/L^{D_A^\star}$ and $l_c/L^{D_\ell^\star}$ against t/L^z with $z \simeq 1.67$, and we use the fractal dimensions $D_A^\star \simeq 1.96$ and $D_\ell^\star \simeq 1.49$. Concerning the fractal dimensions, $D_A^\star$ is quite far from the one that would correspond to criticality at $\kappa = 3.85$, the value obtained from the analysis of $\langle\theta^2\rangle$ (for the VM dynamics on the triangular lattice) while $D_\ell^\star$ is very close. In the insets of Fig. 3.10 we present the same data but without rescaling time and using the fractal dimensions of critical percolation, $D_A = 91/48$ and $D_\ell = 7/4$. As one can see, the data collapse is perfect at very short times, since the system is initially in a critical percolation state (for the triangular lattice) which survives for a while over long distances after the beginning of the stochastic dynamics. Indeed, we recall that we are dealing here with the largest cluster, which is supposed to percolate already at $t = 0$ in the case of the VM dynamics on the triangular lattice. At longer times, the scaling breaks down, as expected, since the system evolves towards the second criticality.

To conclude, we found that the largest cluster size A_c and the length of its walls, l_c, satisfy finite-size scaling with respect to a typical time scale $t_c \sim L^z$ with $z \simeq 1.67$ at relatively short times, before entering the long-term coarsening process. During the transient regime the dynamics seem to approach a state with fractal scaling properties, different from those of critical percolation, but not associated to any well-known criticality. The SLE parameter κ estimated from the hull fractal dimension, $D_\ell^\star$, seems to be compatible with the one obtained from $\langle\theta^2\rangle$, even though we observe some variation due to the particular lattice geometry. On the other hand, the value of $D_A^\star$ is quite different. We suspect that this apparent disagreement is due to the fact that the only mechanism which is responsible for domain growth in the voter model dynamics is the interfacial noise. Thus, we expect that the fractal properties measured for the domain walls and those measured for the bulk are associated with two different types of critical behaviour.

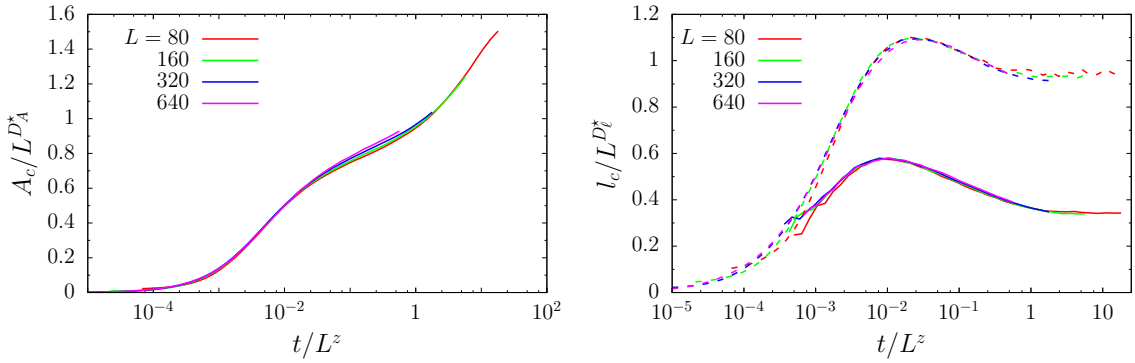

Figure 3.9: The scaling of the geometric properties of the largest cluster for the VM on a honeycomb lattice. The size of the largest cluster A_c divided by $L^{D_A^\star}$, with $D_A^\star = 1.90$ (left), and the length of its external hull l_c divided by $L^{D_\ell^\star}$, with $D_\ell^\star = 1.52$ (right), for various L. As in Fig. 3.8, the contribution to l_c due to wrapping hulls is shown with continuous lines while that from non-wrapping hulls is shown with dashed lines. All the quantities are plotted against the rescaled time t/L^z, with $z = 1.67$. The values of $D_A^\star$, $D_\ell^\star$ and z were found by looking for the best collapse of the data corresponding to different L.

3.3.4 Number density of domain areas

Let us now consider the full size distribution of the spin clusters that are grown by the VM dynamics, which is probed by the so-called number density of domain areas, $\mathcal{N}(A, t, L)$, defined in Sec. 1.3. We repeat the same type of analysis performed for the other types of stochastic spin dynamics seen in Chaps. 1 and 2.

First, we checked that $\mathcal{N}$ satisfies the dynamical scaling relation given by Eq. (1.25). This is shown in Fig. 3.11, where we display the data for the VM dynamics on a triangular lattice. The rescaled data seem to collapse on the master curve $f(x) = 2\,c_d\,(1+x)^{-\tau_A}$, with $\tau_A = 187/91 \approx 2.0550$ the $2d$ critical percolation Fisher exponent and $2\,c_d \simeq 0.0580$, that is, the scaling function for NCOP coarsening (see Eq. (1.26)). This form of the scaling function is valid only under the hypothesis that the system is able to reach a critical percolation state very soon in the course of the dynamics and that the spin clusters retain this criticality at any time t, over distances $r > \ell_d(t)$, if one rescale all lengths by $\ell_d(t)$ [10, 11]. For the VM dynamics, we have seen that the domain pattern is characterised, at sufficiently long times, by a different type of criticality. Indeed, if we fit the function $f(A) = C\ A^{-\tau}$ to the data collected at the latest time available, $t = 7688$, for areas A in the interval $[10^2, 10^4]$, we find $C \simeq 0.024$ and $\tau \simeq 2.016$. However, it is very difficult to distinguish this numerical estimate from the critical percolation value $\tau_A \simeq 2.0550$, because of the numerical error involved, therefore the scaling presented in Fig. 3.11 may be misleading.

As a side note, the "bump" that appears at the tail of the size distribution is due to boundary effects, *i.e.* the contribution coming from spin clusters whose radii are comparable with the linear size of the system, L, or even percolating spin clusters.

A better way to visualize the number density $\mathcal{N}$ is given in Fig. 3.12 (left panel), where we plot the quantity $A^\tau\,\mathcal{N}$ against A, with $\tau = 2.016$, the value obtained by the fit. The data at $t = 0$ complies with the critical percolation scenario, with an algebraic decay, $\mathcal{N}(A, t = 0) \simeq 2\,c_d\,A^{-\tau_A}$, with $\tau_A = 187/91$ (see the inset), since the initial spin configuration is always right at the critical percolation point in the case in which the model is defined on a triangular

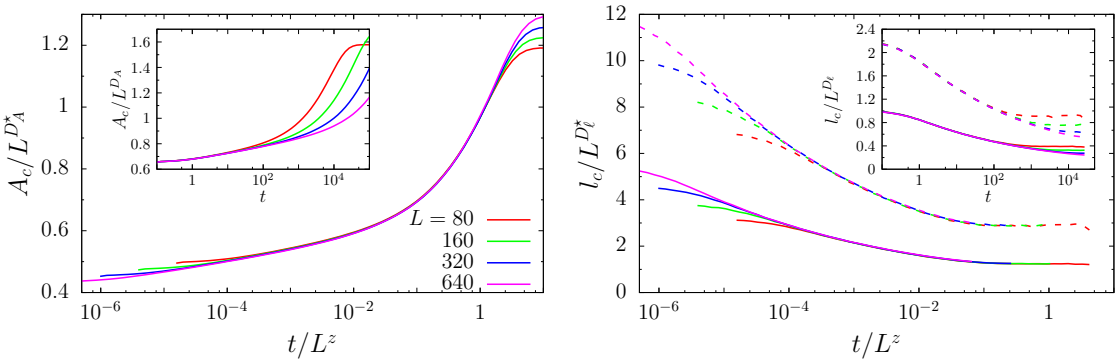

Figure 3.10: The scaling of the geometric properties of the largest cluster for the VM dynamics on a triangular lattice. In the left panel, the size of the largest cluster A_c divided by $L^{D_A^\star}$, with $D_A^\star = 1.96$, while in the right panel, the length of its external hull l_c divided by $L^{D_\ell^\star}$, with $D_\ell^\star = 1.49$, for various L. Regarding l_c, we have separated the contribution coming from wrapping hulls (continuous lines) from that coming from non-wrapping ones (dashed lines). All the quantities are plotted against the rescaled time t/L^z, with $z = 1.67$. The values of $D_A^\star$, $D_\ell^\star$ and z were found by looking for the best collapse of the data corresponding to different L. In the insets we scale the data using the fractal dimensions of $2d$ critical percolation, $D_A = 91/48$ and $D_\ell = 7/4$, and plot them against time t.

lattice. As the system evolves, $\mathcal{N}$ approaches the new criticality corresponding to an exponent slightly different from that of critical percolation, which corresponds to the lower plateau in the plot shown in Fig. 3.12 - left panel. The transition between the two regimes is very clear.

Indeed, at any intermediate time, there is a "smooth" crossover between the behaviour of the initial cluster size distribution, satisfying the statistics of critical percolation, and the "final" distribution that conforms to the new type of criticality. The point of crossover, at a given time t, can be collapsed by properly rescaling the area A by $t^{D/z}$, with $z \simeq 1.67$ and $D = 2/(\tau - 1) \simeq 1.97$, the domain fractal dimension associated with a Fisher exponent $\tau \simeq 2.016$, see Sec. 1.3 and Eq. (1.21). This scaling is shown in the right panel of Fig. 3.12. Moreover, we fitted the function $c\,x^a$ to $A^\tau\,\mathcal{N}(A)$, taken as function of the rescaled domain area $A/t^{D/z}$, obtaining $a \simeq 0.228$. We recall that a similar behaviour is found for the size distribution of the domains in the so-called pre-percolation regime in the case of a KIM evolving under Glauber dynamics (see Fig. 1.19) and Kawasaki dynamics (see Fig. 2.13).

A similar analysis is performed for the VM dynamics on the square and honeycomb lattices, see Fig. 3.13. The situation is a bit different from that observed in the case of the triangular lattice, since the initial state is not critical in terms of percolation. Moreover, we observe strong finite-size effects on the value of the exponent τ dictating the algebraic decay of $\mathcal{N}(A, t, L)$ at late times. In fact, for the VM on the square lattice, a fit of the data for $L = 640$ at $t = 16384$ to the function $C\,A^{-\tau}$, taking $A \in [10^2, 10^4]$, yields $\tau \simeq 1.983$ and $C \simeq 0.022$. In the case of VM dynamics on a honeycomb lattice with $L = 640$, a similar fit of the data at $t = 72942$ taking $A \in [10^2, 2 \times 10^3]$ yields $\tau \simeq 1.984$ and $C \simeq 0.024$. However, in the limit $L \to +\infty$ we should recover $\tau > 2$ in order to have a correct normalisation of $\mathcal{N}$.

The scaling behaviour of $\mathcal{N}$ is similar to what is observed in the case of the NCOP dynamics in Chap. 1. In fact, as one can see from Fig. 3.13, there is a clear crossover between the behaviour for large domains, that still satisfy the statistics of the initial state, and that

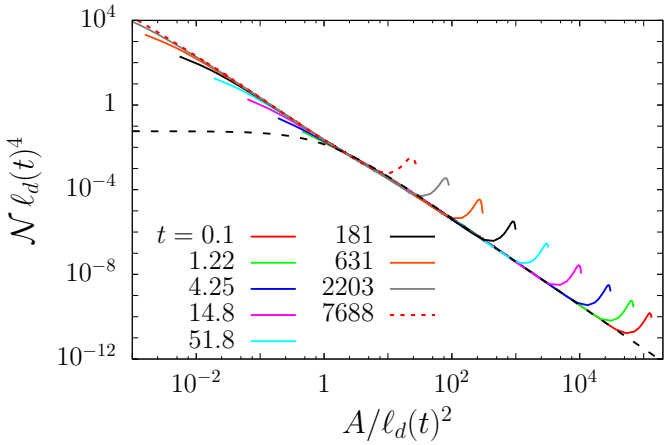

Figure 3.11: The cluster size number density, $\mathcal{N}(A, t, L)$, for the VM on a triangular lattice with linear size $L = 640$, at different times indicated in the key. The number density $\mathcal{N}$ is multiplied by $\ell_d^4(t)$ and plotted against the rescaled size $A/\ell_d^2(t)$, where we took $\ell_d(t)$ of the form $\ell_d(t) = (1+t)^{1/2}$. The black dashed curve is the function $f(x) = 2\,c_d\,(1+x)^{-\tau_A}$, with $\tau_A = 187/91$ the Fisher exponent for $2d$ critical percolation and $2\,c_d \simeq 0.058$.

for small ones that have already the statistics associated with the criticality that the system is approaching in the long-time regime, which corresponds to the plateau in the rescaled distribution $A^\tau \mathcal{N}(A)$ shown in the plot. The large-domain region is the equivalent of the pre-percolation regime observed for the other types of dynamics. The difference in this case is that the criticality that the system is reaching at long times (in terms of the geometry and statistics of spin clusters) is not that of percolation.

The point of crossover, at a given time t, occurs approximately at a characteristic domain size $\mathcal{A}(t) \sim t^\xi$. The exponent ξ is determined by looking at that value that produces the best collapse of the data. We found $\xi \simeq 1.18$ for the VM dynamics on the square lattice, and $\xi \simeq 1.17$ for that on the honeycomb lattice. The scaling is very good, apart from the deviations caused by finite-size effects that are occuring at very small A (due to the discreteness of the lattice) and in correspondence of very large domain areas, with the so-called "bump". If we assume that the characteristic size $\mathcal{A}(t) \sim t^\xi$ is given by $\mathcal{A}(t) = \ell_{\rm V}(t)^D \sim t^{D/z}$, with $\ell_{\rm V}(t)$ the length introduced in Sec. 3.3.2, and assume $z = 1.67$, the dynamical exponent obtained from analysing the scaling of the other observables, we can get an estimate of the fractal dimension D. For the VM dynamics on the square lattice we get $D \simeq 1.97$, while for the VM dynamics on the honeycomb lattice, $D \simeq 1.96$. These estimates are compatible, within numerical accuracy, with the values of $D_A^\star$ found by scaling the largest cluster size in Sec. 3.3.3. These results again imply that, at a given time t, the new criticality observed from the fractal properties of the domain walls extends up to a distance $\ell_{\rm V}(t) \sim t^{1/z}$.

We also fitted the power law $\Phi(x) = c\,x^a$ to the rescaled distribution, $\mathcal{N}(A,t)\,A^\tau$, in the ramp-like region as shown in Fig. 3.13. We obtain $a \simeq 0.260$ for the VM dynamics on the square lattice, while $a \simeq 0.366$ for the honeycomb lattice case. Note that the exponent a estimated in this way is in the same range of values observed for the other types of stochastic spin dynamics, see Sec. 1.5.5.2 and Sec. 2.4.6.2.

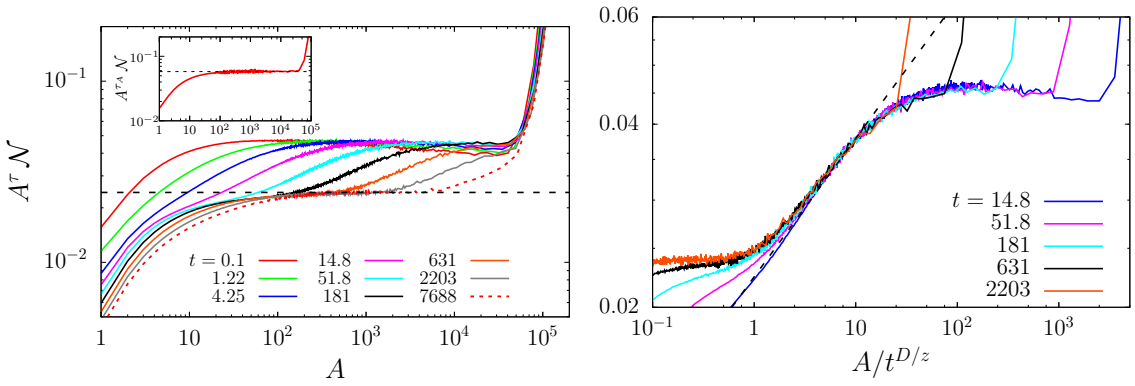

Figure 3.12: VM dynamics on a triangular lattice with linear size $L = 640$. In the left panel we show $A^\tau \mathcal{N}(A,t)$ against A, with $\tau \simeq 2.016$, at different times indicated in the key. The value of τ was found by fitting the function $C\,A^{-\tau}$ to the data relative to $t = 7688$, in the interval $[10^2, 10^4]$. The constant $C \simeq 0.024$ is shown with a black dashed line. In the inset, $A^{\tau_A}\mathcal{N}(A, t = 0)$, with $\tau_A = 187/91$ the Fisher exponent for $2d$ critical percolation, plotted against A. In the right panel, $A^\tau \mathcal{N}(A,t)$ is plotted against the rescaled size $A/t^{D/z}$, using the same value of τ as in the left panel, $z = 1.67$ and $D = 2/(\tau - 1) \simeq 1.97$. The function $c\,x^a$, fitted at $t = 14.8$ and in the interval $[2.5, 10]$ of the rescaled area $x = A/t^{D/z}$, yields $a \simeq 0.228$ and is shown by an inclined dashed line.

3.4 Conclusions

Let us summarise the main results shown in this Chapter.

We studied the early stages of the coarsening process occurring in a $2d$ kinetic Ising model evolving with voter model (VM) dynamics. We found a transient between the initial disordered state and a state in which spin clusters display long-distance fractal properties as the ones at critical percolation. This critical-percolation-like state, however, is not as stable and long-lived as the one observed for the other microscopic dynamics, the Glauber dynamics and the spin-exchange dynamics, which satisfy a detailed balance condition with respect to the Gibbs-Boltzmann probability distribution.

More precisely, the VM either starts from critical percolation (on the triangular lattice) or gets very close to such criticality in a very short time span (for the other lattices). However, differently to what happens with the other types of stochastic spin dynamics, the percolation state is not stable over a long period of time. The further evolution from the percolating state takes the system to a regime in which domain walls are still critical, but with fractal properties that are closer to those of the critical Ising point, though still different from them. We see from our simulations, for example, that the SLE κ parameter that we extract from the analysis of the winding angle measured on domain walls, moves from a value that is very close to 6, corresponding to critical percolation, to a value $\kappa \in [3.8, 4.2]$, approximately, at long times. Unfortunately, we were not able to associate this type of critical behaviour to any known model.

Having said this, from the finite-size scaling of the wrapping probabilities and other observables, a time scale $t_c \simeq L^z$ with $z = 1.67$ can be extracted, corresponding to the typical time needed to reach a state in which the "new" criticality extends over the entire system, in analogy with the time t_p required to reach the critical-percolation-like dynamical

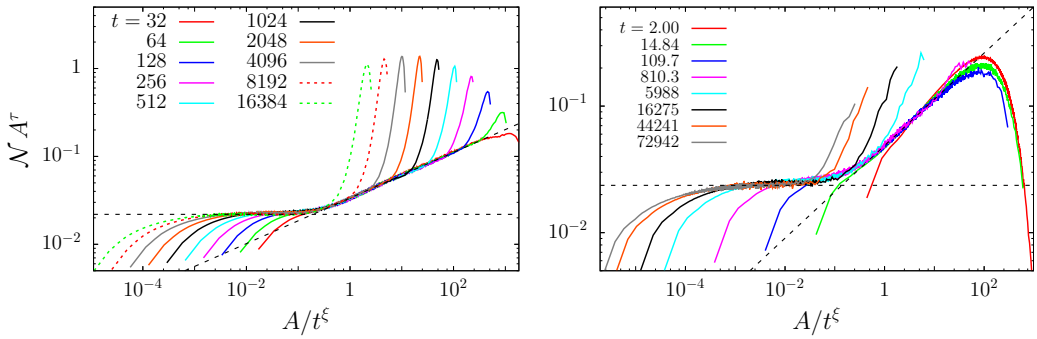

Figure 3.13: Scaling of the domain area number density, $\mathcal{N}(A,t)$, for the VM on a square lattice (left) and on a honeycomb lattice (right), both with $L = 640$. The quantity $A^{\tau}\,\mathcal{N}(A,t)$ is plotted against the rescaled size A/t^{ξ}, at different times indicated in the keys. As explained in the main text, the value of the exponent τ is not the one of critical percolation, but it has been estimated numerically by fitting the function $C\,A^{-\tau}$ to the unscaled distribution $\mathcal{N}(A,t,L)$ at the latest time t reached by our simulations. For the case of the dynamics on the square lattice, we found $\tau \simeq 1.983$, while for the honeycomb lattice case, $\tau \simeq 1.984$. The horizontal dashed lines correspond to $C \simeq 0.022$ in the left panel, and $C \simeq 0.024$ in the right panel. In both cases, the value of the exponent ξ was chosen to obtain collapse in the "ramp" region, finding $\xi \simeq 1.18$ for the square lattice and $\xi \simeq 1.17$ for the honeycomb one. The function $\Phi(x) = c\,x^{a}$ has been fitted to the rescaled distribution at $t = 64$ and in the interval $[1, 10^2]$ of the rescaled area $x = A/t^{\xi}$ in the square lattice case, while it has been fitted to the rescaled distribution at $t = 109.7$ and in the interval $[1, 10]$ of the rescaled area in the honeycomb lattice case, yielding $a \simeq 0.260$ and $a \simeq 0.366$, respectively. The fitting curve is shown by an inclined dashed line.

scaling regime in the other types of stochastic dynamics. This is also confirmed by the analysis of the size distribution of the spin clusters, from which we obtained the evidence for the existence of a new characteristic length

$$\ell_{\mathrm{V}}(t) \sim t^{1/z}\,, \tag{3.8}$$

which controls the crossover between the initial state and the critical behaviour at long times. Essentially, the critical properties associated with a SLE parameter $\kappa \in [3.8, 4.2]$ can be observed over distances r such that $\ell_d(t) \ll r < \ell_{\mathrm{V}}(t)$, while for larger distances the system still looks like in the initial state. In other words, $\ell_{\mathrm{V}}(t)$ is the analogous of the length $\ell_p(t)$ describing the pre-percolation regime in the Ising model evolving with either Glauber dynamics or spin-exchange dynamics, at subcritical temperatures.

The separation between the critical state reached at $t_c \simeq L^z$ and the late-time coarsening regime that brings the system to one of the absorbing state is not sharp. Indeed, the latter occurs in a typical time scale $t_{\mathrm{abs}} \sim L^2$, while we find $z \simeq 1.67$. This makes the distinction between the processes linked to the first and second regime difficult to disentangle.

Part II

Quench dynamics of the isolated $p = 2$ spherical spin glass model

Chapter 4

Quench dynamics of the isolated $p = 2$ spherical spin glass model.

4.1 Introduction

In recent years, the dynamics of isolated many-body quantum systems, and especially the search for a statistical description of their asymptotic evolution [75], have received great attention. One of the main motivations to study these issues from a theoretical point of view is the practical realisation of quenches of isolated ultra-cold atoms that are confined in optical lattices [76]. In this context, it is the possibility of tuning the strength of the effective interaction between the atoms, or even modify the dimensionality of the lattice, while keeping the system isolated, that allowed physicists to study experimentally the dynamics of quantum quenches. Another reason for the interest in these issues, is the recently proposed mechanism of many-body localisation that is used to describe the metal-insulator transition in materials with quenched disorder [77].

A quantum quench consists in the process where a system, which is initially prepared in the ground state of a certain Hamiltonian H_0 (or, more generally, a mixed state of H_0) is let evolve unitarily with a different Hamiltonian H, usually obtained from H_0 by just changing one of its parameters (for example, the strength of the coupling between the degrees of freedom). One can think of realising a similar procedure also for a classical system. In the classical setting, a quench would consist in preparing a system in an equilibrium state in the canonical Gibbs-Boltzmann ensemble with respect to a given Hamiltonian H_0, and then let it evolve under Hamiltonian dynamics (*i.e.* removing the contact with the thermal bath) with respect to a new Hamiltonian H, with the same form, but with different parameters. This problem has not received as much attention as the quantum version, although we will show that it raises very similar questions. Usually, one is interested in determining whether the system is able to provide a bath for itself, allowing it to reach asymptotically a new equilibrium state *à la* Gibbs-Boltzmann, thanks to the interactions between the many degrees of freedom.

It is known that two classes of systems fail to reach an equilibrium state of Gibbs-Boltzmann kind in the late stages of the dynamics after a quench. These are the *integrable systems*, that is, systems with a macroscopic number of conserved quasi-local quantities [78], and *many-body localized quantum systems*, whose trajectories remain confined in localised states that are close to their initial conditions because of the presence of "frozen" randomness. Indeed, some of the ultra-cold atoms instances realised in the laboratory are low-dimensional and considered to be integrable. This implies that they are not able to act as a bath on

themselves, even though they clearly reach a stationary regime asymptotically in time. A natural question is then how to characterise this stationary regime. A possibility is represented by the Generalised Gibbs Ensemble (GGE) [79, 80], an extension of the canonical Gibbs-Boltzmann ensemble that aims to include the effect of all relevant conserved charges (see, for example, the review articles [75, 81, 82]).

Similar equilibration problems can arise in classical isolated systems. A first study of the dynamics of isolated interacting (classical) disordered models appeared in [83]. More precisely, the model considered was the p-spin interaction spherical spin glass model (or in short, p-spin spherical model), which represents a paradigm in the mean-field description of glassy physics. It is a solvable model (in the thermodynamic limit) whose relaxation dynamics, for $p \geq 3$, successfully reproduces some properties of fragile glasses. The literature on the static, metastable and stochastic dynamics of the p-spin spherical model is vast. Numerous aspects of their behaviour are very well characterised, even analytically (see Refs. [84, 85, 86]). The corresponding Hamiltonian dynamics, following a quench in the strength of the disorder, is realised by adding a kinetic term to the standard p-spin spherical model potential energy. The resulting model is thus equivalent to the motion of a particle on an $(N-1)$-sphere under the effect of a complex quenched random potential [87, 88, 89]. For the case $p \geq 3$, it was found that, for all quenches starting from an equilibrium paramagnetic state, the system reaches an asymptotic stationary regime in which either FDT with a single temperature is satisfied, or an *ageing* behaviour arises, characterised by a two-step non-equilibrium relaxation. In a certain sense, the dynamics of the isolated system resembles the purely dissipative relaxation dynamics of the same model in contact with a heat bath.

In the present Dissertation, we study the post-quench Hamiltonian dynamics of the $p = 2$ case, in a similar fashion to what was done in Ref. [83] in the case $p = 3$. This model, both in its classical and quantum formulations, has a connection with coarsening phenomena, made *via* its relation to the $O(N)$-$\lambda\phi^4$ model, in the infinite N limit. Furthermore, the model has recently appeared in a semiclassical study of the Sachdev-Ye-Kitaev model [90]. The interest towards the Hamiltonian dynamics of the $p = 2$ model was sparked by its resemblence to the Neumann integrable system of classical mechanics [91], the constrained motion of a classical particle on S_{N-1} under a harmonic potential, for a special choice of the spring constants. The only difference is that in the $p = 2$ model one imposes the spherical constraint on average while in Neumann's model one does strictly, on each trajectory. This difference, however, should not be important in the $N \to \infty$ limit. We will exploit results found in literature, notably the exact expressions of the $N - 1$ conserved charges in involution [92, 93, 94].

The quench protocol amounts to a uniform change of the (random) interaction matrix, that is to say, $J^0_{ij} \mapsto J_{ij} = (J/J_0)J^0_{ij}$, and the initial conditions are sampled from canonical equilibrium at a given temperature, choosing in this way initial configurations typical of a paramagnetic state at high temperature, or a condensed, ferromagnetic-like, state at low temperature. The dynamics was studied both in $N \to \infty$ limit, through the Schwinger-Dyson equations describing the time-evolution of the two-time autocorrelation and linear response functions, and in the case of N finite, with N the number of spin degrees of freedom, by directly integrating their equations of motion. Most of the results that we are going to show have been obtained by integrating numerically these equations.

The change in the potential energy landscape induces finite injection or extraction of energy density in the sample, thus one would expect that, for sufficient energy injection a system initially prepared in an equilibrium condensed state can reach a paramagnetic state in the post-quench dynamics, while for sufficient energy extraction a system initially prepared in an equilibrium paramagnetic state can be brought to a condensed state. A naive asymptotic

analysis of the Schwinger-Dyson equations for the two-time correlation and linear response functions also suggests that a stationary state in which FDT is satisfied can be reached, with a "final" temperature T_f tha can be computed. However, the scenario that we discover by studying the numerical solutions is not so simple. Depending on the asymptotic behaviour of the two-time autocorrelation function and static susceptibility, in the limit $N \to \infty$, we can identify three different phases in the space of the parameters that control the quench dynamics. In particular, for a condensed initial state, we observe that, for certain choices of the quench parameters, the system remains confined in a condensed state (close to the original one) in the post-quench dynamics, while, for other choices, it aquires a paramagnetic behaviour. However, in none of these dynamical phases a Gibbs-Boltzmann equilibrium measure is reached, contrary to what happens in the strongly interacting $p = 3$ case. This is due to the fact that, asymptotically in time, the system reduces effectively to a collection of decoupled harmonic oscillators. The role played by the $N - 1$ Neumann integrals of motion on the lack of equilibration of the system will be then discussed.

4.2 Background

This Section presents the definition of the spherical spin glass model with 2-spin interactions, and a summary of the main analytical results that are available for the equilibrium behaviour and the relaxation dynamics.

4.2.1 Definition of the model

The spherical spin glass model with 2-spin interactions was first introduced and studied by Kosterlitz, Thouless and Jones [95] as one of the simplest possible magnetic models with quenched random interactions.

The model consists of N degrees of freedom, denoted by $s_1, s_2, \ldots, s_N$, that interact amongst themselves through 2-body interactions. The potential energy of the system is given by

$$H_{\text{pot}}(\{s_i\}, \{J_{ij}\}) = -\frac{1}{2} \sum_{i \neq j}^{N} J_{ij} s_i s_j \ . \tag{4.1}$$

where the couplings J_{ij} are independent identically distributed random variables drawn from a Gaussian distribution with average and variance

$$\mu_J = [J_{ij}] = 0 \ , \qquad \sigma_J^2 = [J_{ij}^2] = \frac{J^2}{N} \ , \tag{4.2}$$

respectively, with the brackets $[\ \cdot\ ]$ denoting the expectation with respect to the probability distribution of the J_{ij}. The couplings are symmetric under the exchange of indices, $J_{ij} = J_{ji}$, and we set $J_{ii} = 0$ for any i. The parameter J characterises the width of the Gaussian distribution. Notice that $\sigma_J^2 \propto N^{-1}$ in order to have H_{pot} of order N.

In the standard spin-glass setting the variables $\{s_i\}$ are Ising spins, that is to say, $s_i \in \{-1, 1\}$ for any i, and the model given by the Hamiltonian in Eq. (4.1) is known as the Sherrington-Kirkpatrick (SK) spin-glass model [96]. We will, instead, consider the spherical limit (or soft-spin version), which consists in taking the s_i as real variables, $s_i \in \mathbb{R}$ for $i = 1, \ldots, N$, subject to the constraint

$$\sum_{i=1}^{N} s_i^2 = N \quad . \tag{4.3}$$

Such spherical constraint is imposed by adding a term of the following form

$$H_{\text{constr}}(\{s_i\}, z) = \frac{z}{2} \left(\sum_{i=1}^{N} s_i^2 - N \right) \tag{4.4}$$

to the Hamiltonian, with z a Lagrange multiplier.

This quadratic model is a particular case of the family of p-spin interaction spin glass models, defined by the Hamiltonian

$$H_{\text{pot}}(\{s_i\}, \{J_{ij}\}) = - \sum_{i_1 < i_2 < \ldots < i_p}^{N} J_{i_1 \ldots i_p} s_{i_1} \ldots s_{i_p} \ . \tag{4.5}$$

where p is an integer ($p \geq 2$), and $J_{i_1 \ldots i_p}$ are i.i.d. random variables with mean $[J_{i_1 \ldots i_p}] = 0$ and variance $[J^2_{i_1 \ldots i_p}] = \frac{J^2 p!}{2N^{p-1}}$. As observed in Ref. [97], from an equilibrium point of view, the $p = 2$ model belongs to a different *universality class* from the one corresponding to the models with $p \geq 3$. For example, its free-energy landscape and relaxation dynamics are much simpler. It is, indeed, a model that, in the limit of large N, resembles strongly the $O(N)$ model for ferromagnetism. More generally, the form given by Eq. (4.5) is one instance of a generic random potential $V(\{s_i\})$ with zero mean and correlations given by [87, 88, 89]

$$[V(\{s_i\}) V(\{s'_i\})] = -N \mathcal{V} \left(\frac{|\boldsymbol{s} - \boldsymbol{s}'|^2}{N} \right) \quad , \tag{4.6}$$

with $\mathcal{V}(x) = -\frac{1}{2} \left(1 - \frac{x}{2}\right)^p$ in the case of the p-spin spherical model.

The model thus defined does not have an intrinsic dynamics. Usually, in the context of statistical physics applications, one is interested in the time evolution of the system when it is coupled to a thermal bath at a given temperature, which can be described either by a Monte Carlo Markov chain, whose transition rates satisfy detailed balance condition with respect to the canonical equilibrium distribution, or by the Langevin equations [98]

$$\frac{\mathrm{d}s_i(t)}{\mathrm{d}t} = -\frac{\partial}{\partial s_i} H_{\text{pot}}(\{s_k\}) - z(t) s_i(t) + 2T \xi_i(t) \tag{4.7}$$

where the Lagrange multiplier z needs to be time-dependent to enforce the spherical constraint in the course of time, ξ_i with $i = 1, \ldots, N$ are istances of Gaussian white noise with zero mean and correlations $\langle \xi_i(t) \xi_j(t') \rangle = \delta_{ij} \ \delta(t - t')$, and T is the temperature of the bath. However, in this Dissertation, we are going to study the evolution of the system under *Hamiltonian dynamics*. To do so, we introduce a kinetic energy

$$H_{\text{kin}}(\{\dot{s}_i\}) = \frac{m}{2} \sum_{i=1}^{N} (\dot{s}_i)^2 \ , \tag{4.8}$$

where $\dot{s}_i = \frac{\mathrm{d}s_i}{\mathrm{d}t}$ and $m > 0$ is a parameter of the model, the "mass" of a particle who is forced to move on the $(N-1)$-sphere with radius $\sqrt{N}$, and whose coordinates in $\mathbb{R}^N$ are given by $\boldsymbol{s} = (s_1, \ldots, s_N)$. The total energy of the *Hamiltonian spherical 2-spin model* is then given by

$$H = H_{\text{kin}} + H_{\text{pot}} + H_{\text{constr}} \quad , \tag{4.9}$$

and the equations of motions by

$$m \ddot{s}_i(t) = -\frac{\partial}{\partial s_i} H(\{s_k\}) = \sum_{j(\neq i)} J_{ij} s_j(t) - z(t) s_i(t) \ , \tag{4.10}$$

for $i = 1, \ldots, N$. The choice of the initial condition $\{s_i(0), \dot{s}_i(0)\}$ is very important in this setting. Essentially, what we are going to do is to draw the initial configuration of the system randomly from the canonical equilibrium ensemble at a given temperature T and with respect to a given potential energy $H_{\text{pot}}(\{s_k\}, \{J_{ij}^{(0)}\})$, and then evolve this initial configuration with the Hamiltonian dynamics described above (thus decoupling the system from the bath), but with a new potential $H_{\text{pot}}(\{s_k\}, \{J_{ij}\})$. More details on this procedure will be given in a following Section.

4.2.2 The potential energy landscape

The simplicity of the 2-spin spherical spin model comes from the fact that the potential energy is quadratic in the degrees of freedom and the interaction matrix $\{J_{ij}\}$ is real symmetric. Let us denote by $\mathbf{J}$ the $N \times N$ real symmetric matrix whose (i, j)-element is J_{ij}. As already stated, the elements of this matrix are i.i.d. random variables with Gaussian distribution, thus the matrix belongs to the so called Gaussian Orthogonal Ensemble (GOE), of which many properties are known in the thermodynamic limit [99, 100, 101]. In particular, we are interested in the distribution of the eigenvalues of $\mathbf{J}$,

$$\rho_N(\lambda) = \frac{1}{N} \left\langle \sum_{\mu=1}^{N} \delta(\lambda - \lambda_\mu) \right\rangle_{\{J_{ij}\}} \tag{4.11}$$

where $\{\lambda_\mu\}_{\mu=1,\ldots,N}$ denote the eigenvalues of $\mathbf{J}$. In the limit $N \to +\infty$, it is known [99] that the eigenvalues of a random symmetric matrix are distributed according to the so-called Wigner semi-circle law,

$$\lim_{N \to +\infty} \rho_N(\lambda) = \rho_{\text{GOE}}(\lambda) = \frac{1}{\pi J} \sqrt{1 - \left(\frac{\lambda}{2J}\right)^2} \; \Theta(2J - |\lambda|) \quad , \tag{4.12}$$

assuming $\langle J_{ij} \rangle = 0$ and $\langle J_{ij}^2 \rangle = J^2/N$, and $\Theta(x)$ being the Heaviside step function. The largest possible eigenvalue is $\lambda_{\max} = 2J$.

Let us label the eigenvalues of $\mathbf{J}$ in such a way that they are ordered: $\lambda_1 \leq \lambda_2 \leq \cdots \leq \lambda_N$. We denote their associated eigenvectors by $\boldsymbol{v}_\mu$ with $\mu = 1, \ldots, N$ and we take them to be orthonormal, $\boldsymbol{v}_\mu^2 = 1$. We now consider the energy landscape given by

$$H_{\mathbf{J}}(\{s_i\}, z) = H_{\text{pot}}(\{s_i\}, \{J_{ij}\}) + H_{\text{constr}}(\{s_i\}, z) \tag{4.13}$$

with z taken as a degree of freedom itself. The stationary points $(\boldsymbol{s}^*, z^*)$ of the potential energy hyper-surface satisfy the equations

$$\left.\frac{\partial H_{\mathbf{J}}}{\partial \boldsymbol{s}}\right|_{\boldsymbol{s}^*, z^*} = (z^* \mathbb{1} - \mathbf{J}) \; \boldsymbol{s}^* = 0 \quad , \quad \sum_{i=1}^{N} (s_i^*)^2 = N \; .$$

Now, supposing the eigenvalues $\{\lambda_\mu\}$ are all distinct, there are $2N$ stationary points given by $z_\mu^* = \lambda_\mu$ and $\boldsymbol{s}_{\mu,\pm}^* = \pm\sqrt{N}\boldsymbol{v}_\mu$, for $\mu = 1, \ldots, N$. The points $\boldsymbol{s}_{\mu,\pm}^*$ on the $(N-1)$-sphere of radius $\sqrt{N}$ simply lie in the direction corresponding to the eigenvector $\boldsymbol{v}_\mu$ of the interaction matrix $\mathbf{J}$. All of these stationary points are associated to metastable states for the system at zero temperature, apart from two of them that are marginally stable ground states. To

see this we need to compute the Hessian of the potential energy surface on each stationary point. The Hessian at the stationary points $(\boldsymbol{s}^*_{\mu,\pm}, z^*_\mu)$ is given by

$$\mathcal{H}^{(\mu)}_{ij} = \left.\frac{\partial H_{\mathbf{J}}}{\partial s_i \partial s_j}\right|_{\boldsymbol{s}^*_{\mu,\pm}, z^*_\mu} = -J_{ij} + z^*_\mu \delta_{ij} = -J_{ij} + \lambda_\mu \delta_{ij} \tag{4.14}$$

which can be easily diagonalised to get eigenvalues $h^{(\mu)}_\nu = \lambda_\mu - \lambda_\nu$. Thus, on the stationary points $(\boldsymbol{s}^*_{\mu,\pm}, z^*_\mu)$, the Hessian has one vanishing eigenvalue (for $\nu = \mu$), $\mu - 1$ positive eigenvalues (for $\nu < \mu$), and $N - \mu$ negative eigenvalues (for $\nu > \mu$). This implies that each saddle point labeled by μ is characterised by one marginally stable direction, $\mu - 1$ stable directions and $N - \mu$ unstable directions. The number of stable directions plus the marginally stable one is given by the index μ labelling the eigenvalue associated to the stationary state. In conclusion, the energy landscape has two maxima, corresponding to $\boldsymbol{s}^* = \pm\sqrt{N}\boldsymbol{v}_1$ and $z^* = \lambda_1$, that are associated to the smallest eigenvalue $\lambda_{\min} = \lambda_1$ of the interaction matrix $\mathbf{J}$, $2N - 4$ saddle points and two (marginally stable) minima, corresponding to $\boldsymbol{s}^* = \pm\sqrt{N}\boldsymbol{v}_N$ and $z^* = \lambda_N$, that are associated to the largest eigenvalue $\lambda_{\max} = \lambda_N$.

At each stationary point $(\boldsymbol{s}^*, z^*)$, the energy of the system (at zero temperature) is given by

$$E^*_\mu \equiv H_{\mathbf{J}}\left(\boldsymbol{s}^* = \pm\sqrt{N}\boldsymbol{v}_\mu \, , z^* = \lambda_\mu\right) = -\frac{1}{2}\lambda_\mu N \, . \tag{4.15}$$

In the thermodynamic limit, the eigenvalues λ_μ of the (random) interaction matrix $\mathbf{J}$ are well-separated between each other (because of an effective level "repulsion" characterising the eigenvalue distribution of Gaussian matrix ensembles), so that the energy levels E^*_μ corresponding to the stationary points of the energy landscape are also well-separated.

The analysis of large dimensional random potential energy landscapes [102, 103, 100, 104] is a research topic in itself with implications in condensed matter physics, notably in glass theory [105, 106], but also claimed to play a role in string theory [107, 108], evolution [109] or other fields. The $p = 2$ spherical model provides a particularly simple case in which the potential energy landscape can be completely elucidated.

4.2.3 The equilibrium behaviour

It is known [84, 110] that the general p-spin interaction spherical spin glass model is characterised by an equilibrium phase transition between a high-temperature paramagnetic phase and a low-temperature spin glass phase. In the following, we outline the main steps of the standard calculations used to derive the equilibrium behaviour in the case $p = 2$.

Traditionally, the derivation of the disorder averaged free-energy density, in the case of general p, is done by using the famous replica method [110, 111] (with a replica symmetry breaking *Ansatz* required to find the stable solutions in the low-temperature phase). In the following, instead, we recall a simpler method [95] which is based on the fact that the special case $p = 2$ is (almost) a quadratic model and also exploits the fact that the probability distribution of the eigenvalues of the interaction matrix is known, in the thermodynamic limit.

The partition function reads

$$Z_{\mathbf{J}}(\beta) = \prod_{k=1}^{N} \int_{-\infty}^{\infty} ds_k \; e^{\frac{\beta}{2}\sum_{j\neq l} J_{jl} s_j s_l} \; \frac{1}{2\pi i} \int_{c-i\infty}^{c+i\infty} dz \; e^{-\frac{\beta z}{2}\left(\sum_{j=1}^{N} s_j^2 - N\right)} \tag{4.16}$$

where β is the inverse temperature and c is a real constant to be fixed below. Since $\mathbf{J}$ is a real symmetric matrix, as usual, it is convenient to perform the change of variables that diagonalises the matrix itself, namely, $\boldsymbol{s} \mapsto \boldsymbol{x}$ with new coordinates $x_\mu = \boldsymbol{s} \cdot \boldsymbol{v}_\mu$ being the projections of $\boldsymbol{s}$ on the direction of the eigenvectors $\boldsymbol{v}_\mu$. In this way the partition function can be recast in the following form

$$Z_{\mathbf{J}}(\beta) = \frac{1}{2\pi i} \int_{c-i\infty}^{c+i\infty} dz \left(\prod_{\mu=1}^{N} \int_{-\infty}^{\infty} dx_\mu \;\; e^{N\left[\frac{\beta z}{2} + \frac{\beta}{2N} \sum_{\nu=1}^{N} (\lambda_\nu - z) x_\nu^2\right]} \right) \quad , \tag{4.17}$$

where we have interchanged the order of integration over the variables x_μ and z, and we choose the constant c in a way such that the integral over the variable z is done on a contour located on the right of the largest eigenvalue of the interaction matrix. The only problem which could arise from this last procedure comes from the fact that the eigenvalue spectrum of $\mathbf{J}$ is bounded only in the limit $N \to +\infty$. However, for sufficiently large N, the probability for $\mathbf{J}$ to have an eigenvalue larger than $2J$ (the maximum in the thermodynamic limit) is so small that the error made by choosing incorrectly the contour of the integral over z is negligible. Thus, assuming $z > \max(\{\lambda_\mu\})$ and carrying out the integration over the x_μ, one obtains

$$Z_{\mathbf{J}}(\beta) = \frac{\pi^{N/2}}{2\pi i} \int_{c-i\infty}^{c+i\infty} dz \; e^{-N f(z,\beta,\{\lambda_\mu\})} \; , \tag{4.18}$$

where $f(z,\beta,\{\lambda_\mu\}) = -\frac{\beta}{2} z + \frac{1}{2N} \sum_{\mu=1}^{N} \ln\left[\frac{\beta}{2}(z-\lambda_\mu)\right]$. The saddle-point equation for the Lagrange multiplier z is then given by

$$\frac{1}{N\beta} \sum_{\mu=1}^{N} \frac{1}{(z_{\rm sp} - \lambda_\mu)} \;\; = \;\; 1 \quad . \tag{4.19}$$

In the thermodynamic limit, we can replace the sum $\frac{1}{N}\sum_{\mu=1}^{N} g(\lambda_\mu)$, for any given function $g(\lambda)$, with the integral $\int d\lambda \; \rho(\lambda) g(\lambda)$, where ρ is the density of the distribution of eigenvalues given in Eq. (4.12). This means that Eq. (4.19), in the limit $N \to +\infty$, becomes the following

$$\frac{1}{\pi J} \int_{-2J}^{2J} d\lambda \sqrt{1 - \left(\frac{\lambda}{2J}\right)^2} (z_{\rm sp} - \lambda)^{-1} = T^{-1} \quad . \tag{4.20}$$

For $T \geq J$, this equation has solution $z_{\rm sp} = T + \frac{J^2}{T}$, while for $T < J$ it has no solution and the saddle-point value of z sticks at $2J$, the largest possible eigenvalue. Then we can identify $T_c = J$ as the critical temperature. Hence, the equilibrium value of the Lagrange multiplier is given by

$$z_{\rm eq}(T) = \begin{cases} T + \frac{J^2}{T} & \text{for } T > T_c \\ 2J & \text{for } T < T_c \end{cases} \quad . \tag{4.21}$$

The free-energy per spin, averaged over the distribution of the eigenvalues of the interaction matrix, has then the following form

$$\begin{aligned} [f(\beta)]_{\mathbf{J}} \;\; &\equiv \;\; \lim_{N\to+\infty} \left[-\frac{1}{N} \ln Z_{\mathbf{J}}(\beta) \right]_{\mathbf{J}} \simeq -\frac{\beta z_{\rm eq}}{2} + \frac{1}{2} \int d\lambda \; \rho(\lambda) \ln\left[\beta(z_{\rm eq} - \lambda)/2\right] \\ &= \;\; \begin{cases} -\frac{\beta z_{\rm eq}}{2} + \frac{1}{2}\ln(\beta J) + \frac{1}{2}\left(\frac{z_{\rm eq}}{2J}\right)^2 - \ln\left[\frac{z_{\rm eq}}{2J} + \sqrt{\left(\frac{z_{\rm eq}}{2J}\right)^2 - 1}\right] , & \beta < \beta_c \, , \\ -\beta J + \frac{1}{2}\ln(\beta J) \; , & \beta > \beta_c \end{cases} \end{aligned} \tag{4.22}$$

with $\beta_c = 1/T_c = 1/J$ (and $z_{\rm eq} = \beta^{-1} + \beta J$ for the paramagnetic case).

If one now checks whether the spherical constraint is satisfied by using the saddle-point approximation for the Lagrange multiplier, one verifies that it is in the high temperature phase, but it is not in the low temperature phase, where

$$\sum_{i=1}^{N} \langle s_i^2 \rangle = \sum_{\mu=1}^{N} \langle x_\mu^2 \rangle = \frac{T}{T_c} N \ , \tag{4.23}$$

(with $\langle \cdot \rangle$ denoting the thermal average). The way to solve this problem is to give a macroscopic "weight" to the projection of the spin in the direction of the eigenvector that corresponds to the largest eigenvalue of the interaction matrix:

$$\boldsymbol{s} \cdot \boldsymbol{v}_N = x_N \ \sim \ \pm \sqrt{\left(1 - \frac{T}{T_c}\right) N} + \delta x_N \tag{4.24}$$

with $\langle \delta x_N \rangle \to 0$ and $\langle \delta x_N^2 \rangle \to 0$ as $N \to +\infty$, so that

$$\sum_{\mu=1}^{N} \langle x_\mu^2 \rangle = \langle x_N^2 \rangle + \sum_{\nu=1}^{N-1} \langle x_\nu^2 \rangle \sim \left(1 - \frac{T}{T_c}\right) N + \frac{T}{T_c} N = N \ . \tag{4.25}$$

The thermal average of the projection of the spin on any direction corresponding to one of the eigenvectors vanishes for $T > T_c$, while for $T < T_c$ one has

$$|\langle x_\mu \rangle| \ = \ \begin{cases} [N(1 - T/T_c)]^{\frac{1}{2}} & \text{if } \lambda_\mu = \lambda_{\max} \ , \\ 0 & \text{if } \lambda_\mu < \lambda_{\max} \ , \end{cases} \tag{4.26}$$

(the sign of $\langle x_N \rangle$, the projection along the direction of the largest eigenvalue, is picked once one breaks the symmetry $\boldsymbol{s} \to -\boldsymbol{s}$). The quantity $\langle x_\mu \rangle^2$ can be thought as the order parameter. Essentially, for $T < T_c$, the configuration of the system (represented by the vector $\boldsymbol{s}$) *condenses* onto the direction of the eigenvector associated to the largest eigenvalue, with the projection carrying a weight proportional to $\sqrt{N}$. Going back to the original spin basis, $(s_1, \ldots, s_N)$, the average magnetisation per degree of freedom vanishes at all temperatures, but the average of the square of the local magnetisation, that defines the Edwards-Anderson parameter, is not when $T < T_c$:

$$q_{\rm EA} \equiv \left[\langle s_i^2 \rangle \right]_{\mathbf{J}} \ = \ \begin{cases} 0 & \text{if } T > T_c \ , \\ 1 - \frac{T}{T_c} & \text{if } T < T_c \ , \end{cases} \tag{4.27}$$

for all $i = 1, \ldots, N$, with $T_c = J$. The order parameter $q_{\rm EA}$ vanishes at T_c and the static transition is of second order.

The disorder averaged free-energy density can also be computed using the replica trick [112] and a replica symmetric *Ansatz*. This *Ansatz* corresponds to an overlap matrix between replicas $Q_{ab} = \delta_{ab} + q_{\rm EA} \epsilon_{ab}$, with $\epsilon_{ab} = 1$ for $a \neq b$ and $\epsilon_{ab} = 0$ for $a = b$. When $N \to \infty$ the saddle point equations fixing the parameter $q_{\rm EA}$ yield 0 above T_c and a marginally stable solution with $q_{\rm EA} = 1 - T/T_c$ for $T < T_c$, with the same physical properties as those discussed above. The equilibrium energy is given by

$$e_{\rm eq}^{\rm pot} \ = \ \begin{cases} -\frac{J^2}{2T} \left[1 - \left(1 - \frac{T}{J} \right)^2 \right] = \frac{1}{2}(T - \lambda_{\max}) & T < T_c \ , \\ -\frac{J^2}{2T} & T > T_c \ . \end{cases} \tag{4.28}$$

We added here a superscript "pot" since, in the modified model that we will study in this paper, the total energy will also have a kinetic energy contribution.

4.2.4 Relaxation dynamics

So far we have considered just the static properties of the $p = 2$ spherical model. Since we are going to present a study of the Hamiltonian dynamics of the model following a quench in the interaction matrix, it is useful to first recall the main aspects of the relaxation dynamics.

By relaxation dynamics we refer to the following setting: the system is prepared in an equilibrium state at a certain temperature T_0 and then is let evolve through a stochastic dynamics which mimics the coupling to a Markovian bath at a given temperature $T < +\infty$, different from T_0. Essentially, this procedure corresponds to an instantaneous quench in the temperature of the bath, and its aim is to relax the system to an equilibrium state at the "target" temperature T [113, 114, 115, 116, 117]. In terms of the degrees of freedom of the system, the relaxation dynamics is described by the set of Langevin equations

$$\dot{s}_i(t) = -z(t)s_i(t) - \frac{\partial H_{\rm pot}(\{s_k\})}{\partial s_i} + 2T\xi_i(t) + h_i(t) \tag{4.29}$$

for $i = 1, \ldots, N$, with $\xi_i(t)$ a Gaussian white noise with zero mean, *i.e.* $\langle \xi_i(t) \rangle = 0$ and $\langle \xi_i(t)\xi_j(t') \rangle = \delta_{ij}\delta(t - t')$. Notice that we have also added an external field h_i, which is coupled linearly to s_i in the potential energy associated with the Langevin equation, and is used to compute the linear response function through

$$R(t_1, t_2) \equiv \frac{1}{N} \sum_{i=1}^{N} \left[\frac{\delta \langle s_i(t_1) \rangle_h}{\delta h_i(t_2)} \bigg|_{h \to 0} \right]_{\mathbf{J}} \quad , \tag{4.30}$$

where the brackets $\langle \cdot \rangle_h$ denotes the thermal average in the presence of a nonzero external field, while $[\cdot]_{\mathbf{J}}$ again indicates the average over the (quenched) random couplings $\{J_{ij}\}$. Let us also introduce the two-time autocorrelation function, which is given by the following

$$C(t_1, t_2) \equiv \frac{1}{N} \left[\sum_{i=1}^{N} \langle s_i(t_1) s_i(t_2) \rangle_h \bigg|_{h \to 0} \right]_{\mathbf{J}} \quad . \tag{4.31}$$

It is convenient to diagonalise the (random) interaction matrix $\{J_{ij}\}$ in order to work with the projections of the spin variable onto the direction of the eigenvectors $\{\boldsymbol{v}_\mu\}$. In terms of the projections, $x_\mu = \boldsymbol{s} \cdot \boldsymbol{v}_\mu$, the Langevin equations become

$$\dot{x}_\mu(t) = (\lambda_\mu - z(t))x_\mu(t) + 2T\tilde{\xi}_\mu(t) + \tilde{h}_\mu(t) \quad , \tag{4.32}$$

for $\mu = 1, \ldots, N$, with $\lambda_1 < \lambda_2 < \ldots < \lambda_N$ the eigenvalues of the interaction matrix, and $\tilde{h}_\mu$ and $\tilde{\xi}_\mu$ the projection of the external field $\boldsymbol{h} = (h_1, \ldots, h_N)$ and that of the thermal noise $\boldsymbol{\xi} = (\xi_1, \ldots, \xi_N)$ onto the eigenvector $\boldsymbol{v}_\mu$, respectively. The general solution to this equation, for a given realisation of the quenched disorder J_{ij} and of the the noise $\xi_i(t)$, is given by

$$x_\mu(t) = x_\mu(0) \mathrm{e}^{\lambda_\mu t - \int_0^t d\tau\, z(\tau)} + \int_0^t dt'\, \mathrm{e}^{\lambda_\mu (t-t') - \int_{t'}^t d\tau\, z(\tau)} \left[\tilde{\xi}_\mu(t') + \tilde{h}_\mu(t') \right] \, , \tag{4.33}$$

and the Lagrange multiplier $z(t)$ can be fixed by imposing the spherical constraint $\sum_\mu x_\mu^2(t) = N$, for any t. This yields a self-consistent equation for $z(t)$. However, it is easier to work directly with the two-time autocorrelation function. In absence of an external field, and in the thermodynamic limit, using Eq. (4.33) one obtains [115, 116]

$$C(t, t') = \frac{1}{\sqrt{\Gamma(t)\Gamma(t')}} \left[\Gamma\left(\frac{t + t'}{2} \right) - 2 \int_{t'}^{(t+t')/2} d\tau\; T\; \Gamma(\tau) \langle\langle\, \mathrm{e}^{\lambda(t+t'-2\tau)}\, \rangle\rangle_\lambda \right] \, , \tag{4.34}$$

for $t \geq t'$, where $\langle\langle\ g(\lambda)\ \rangle\rangle_\lambda$ stands for $\int_{-\infty}^{+\infty} d\lambda\ \rho(\lambda) g(\lambda)$, with $\rho(\lambda)$ the density of the distribution of the eigenvalues of the interaction matrix in the thermodynamic limit (given by Eq. (4.12)), and

$$\Gamma(t) \equiv \exp\left(2\int_0^t d\tau\ z(\tau)\right) \quad . \tag{4.35}$$

By imposing the constraint $C(t,t) = 1$, for any t, one can compute self-consistently the function $\Gamma(t)$ as the solution of the following Volterra equation of the second type:

$$\Gamma(t) = \langle\langle\ [x_\lambda(0)]^2 \mathrm{e}^{2\lambda t}\ \rangle\rangle_\lambda + 2\int_0^t d\tau\ T\ \Gamma(\tau) \langle\langle\ \mathrm{e}^{2\lambda(t-\tau)}\ \rangle\rangle_\lambda\ , \tag{4.36}$$

with $x_\lambda(0)$ being the projection of the spin vector onto the eigenvector associated with the eigenvalue λ (in the limit $N \to +\infty$) at $t = 0$. Analogously, by using Eq. (4.33), one can derive [115] the following expression for the linear response function,

$$R(t,t') = \sqrt{\frac{\Gamma(t')}{\Gamma(t)}}\ \langle\langle\ \mathrm{e}^{\lambda(t-t')}\ \rangle\rangle_\lambda \quad . \tag{4.37}$$

Notice that, so far, the results that have been presented correspond to a given choice of the initial configuration $\{s_i(0)\}$ (or equivalently, $\{x_\mu(0)\}$). Moreover, in the $N \to +\infty$ limit, the initial condition needs to be translated in a prescription for the function $\eta(\lambda) = x_\lambda(0)$. The asymptotic behaviour of the system depends on this particular initial condition, as shown in Ref. [115]. Let us limit ourselves to the case of an initial condition drawn randomly from equilibrium at $T_0 \to +\infty$.

In the case of quenches from $T_0 \to +\infty$ to $T > T_c = J$ (with J^2 the variance of the couplings J_{ij}), the system reaches very quickly an equilibrium state at the target temperature T. The Lagrange multiplier rapidly converges to $z_{\mathrm{eq}} = T + J^2/T$, that is to say, the value given by the saddle-point approximation for $T > T_c$. After a short transient, the two-time autocorrelation and the linear response function become invariant under time translation and related by the fluctuation dissipation theorem (FDT),

$$\begin{cases} \lim_{t' \gg 1} C(t,t') = C_{\mathrm{st}}(t-t') \\ \lim_{t' \gg 1} R(t,t') = R_{\mathrm{st}}(t-t') \end{cases} \quad , \quad R_{\mathrm{st}}(\tau) = -\frac{1}{T}\frac{d}{d\tau} C_{\mathrm{st}}(\tau) \quad . \tag{4.38}$$

Instead, in the case in which an initial configuration taken from equilibrium at $T_0 \to +\infty$ is let evolve in contact with a bath at a temperature $T < T_c$, the autocorrelation and response function display a behaviour that is similar to that observed in coarsening systems [23, 118, 119, 120]. Precisely, a two-stage relaxation consisting of a short time-delay regime, $(t-t')/t' \ll 1$, in which they show a stationary behaviour, and a long time-delay regime, $(t-t')/t' \gg 1$, in which they are characterised by strong non-stationary behaviour. In particular, the scaling of the correlation in the non-stationary regime presents similarities with the *ageing* phenomenon that is observed in structural spin glasses [106, 121]. Approximately, $C(t,t')$ and $R(t,t')$ are given by the sum of two contributions, representing these two regimes,

$$C(t,t') \simeq C_{\mathrm{st}}(t-t') + C_{\mathrm{ag}}(t,t')\ , \tag{4.39a}$$

$$R(t,t') \simeq R_{\mathrm{st}}(t-t') + R_{\mathrm{ag}}(t,t')\ , \tag{4.39b}$$

where $C_{\mathrm{st}}(\tau)$ and $R_{\mathrm{st}}(\tau)$ satisfy the FDT relation expressed in Eq. (4.38), while the ageing terms, C_{ag} and R_{ag}, satisfy a similar relation, but with a time-dependent (non-equilibrium)

effective temperature [122, 123],

$$R_{\rm ag}(t,t') \;=\; \frac{1}{T_{\rm eff}(t,t')}\frac{\partial}{\partial t'}C_{\rm ag}(t,t')\;, \tag{4.40}$$

for $t > t'$. In the asymptotic limit, the two terms evolve in different regimes in the sense that when one changes the other one is constant and vice versa. The limiting values of the two contributions to the correlation function are

$$C_{\rm st}(0) = 1-q\;, \qquad \lim_{t-t'\to\infty} C_{\rm st}(t-t') = 0\;, \tag{4.41a}$$

$$\lim_{t'\to t^-} C_{\rm ag}(t,t') = q\;, \qquad \lim_{t\gg t'} C_{\rm ag}(t,t') = 0\;, \tag{4.41b}$$

with the parameter q given by

$$q = 1-\frac{T}{J}\;, \tag{4.42}$$

for $T < T_c = J$. This expression coincides with the Edwards-Anderson parameter for the equilibrium low-temperature phase, see Eq. (4.27).

The complete solution of the Langevin equations allows one to deduce the exact scaling forms of the stationary and ageing contributions to the correlation and linear response. In particular, the latter are given by [115]

$$C_{\rm ag}(t,t') \sim f_C\left(\frac{t'}{t}\right) \quad , \qquad R_{\rm ag}(t,t') \sim t^{-3/2}\, f_R\left(\frac{t'}{t}\right) \quad , \tag{4.43}$$

for $t \gg t'$, with $f_C(x) = x^{3/4}$ and $f_R(x) = \frac{x^{-3/4}}{(1-x)^{3/2}}$. This implies that $T_{\rm eff}(t,t') \sim t^{1/2} f_T(t'/t)$, with $f_T(x) = x(1-x)^{3/2}$, for $t \gg t'$. The behaviour of the effective temperature is special in the $p = 2$ spherical model since, contrary to what happens in the $p \geq 3$ cases [98], it is not constant but grows with time. This implies, that the ageing regime does not contribute to the asymptotic potential energy. In fact, the average potential energy (per degree of freedom), that can be shown to be given by

$$e^{\rm pot}(t) \equiv \lim_{N\to+\infty}\frac{1}{N}[\langle H_{\rm pot}(t)\rangle]_{\mathbf{J}} = \lim_{N\to+\infty}\frac{1}{N}\left[\sum_{\mu=1}^{N}\lambda_\mu\langle x_\mu^2(t)\rangle\right]_{\mathbf{J}} = \frac{1}{2}\left(T - z(t)\right)\;, \tag{4.44}$$

has the following behaviour for large times,

$$e^{\rm pot}(t) \sim \frac{T}{2} - J\left(1+\frac{3}{8t}\right)\;, \tag{4.45}$$

and thus it converges to the value

$$e^{\rm pot}_{\rm asympt} = \frac{T}{2} - J = -\frac{J^2}{2T}(1-q^2)\;, \tag{4.46}$$

which is identical to the equilibrium one, see Eq. (4.28), once $q = q_{\rm EA} = 1 - T/J$ is used. This means that, for $T < T_c$, the Lagrange multiplier approaches the value $z_{\rm asympt} = 2J$, corresponding to the largest possible eigenvalue of the interaction matrix (in the limit $N \to +\infty$), with the power law $z(t) - z_{\rm asympt} \sim t^{-1}$. The slow approach to the asymptotic value is determinant to allow for the non-stationary slow relaxation.

In terms of the projections of the spin onto the directions corresponding to the eigenvectors of the interaction matrix, one can show that, in the large t limit,

$$m_\mu(t) \equiv [\langle x_\mu(t)\rangle]_{\mathbf{J}} \sim (4\pi)^{1/4}\ q^{3/4}\ \mathrm{e}^{(\lambda_\mu - 2J)t} \tag{4.47}$$

for $\lambda_\mu < 2J$, where again $q = 1 - \frac{T}{J}$. Thus, for all μ that do not correspond to the largest eigenvalue of the interaction matrix (in the thermodynamic limit), $\lambda_{\max} = 2J$, m_μ decays to zero exponentially, with a decay rate that increases with the distance of the associated eigenvalue λ_μ from $\lambda_{\max}$. Instead, for the projection onto the eigenvector associated with the largest eigenvalue, one can show that the magnetisation grows with time as a power law: $m_{\max}(t) \equiv [\langle x_{\max}(t)\rangle]_{\mathbf{J}} \sim t^{3/4}$. The behaviour is similar to that observed in the $O(N)$ model of ferromagnetism studied in the large N limit [124]. The progressive *condensation* of the spin "vector" on the direction of the eigenvector corresponding to the largest eigenvalue of the interaction matrix is the equivalent of the ordering process in the $O(N)$ model, that is to say, the condensation on the zero wave-vector mode.

In conclusion, in the case of quenches from $T_0 \to +\infty$ to $T < T_c$, the system does not reach an equilibrium state, in the sense that time translation invariance (TTI) and the fluctuation dissipation theorem (FDT) are violated, even though the asymptotic value of the energy coincides with the equilibrium value at the target temperature.

The same technique, based on the projection of the spin vector on the eigenvectors of J_{ij}, can also be implemented in the case in which there is inertia and the differential equation has a second order time derivative. The dynamics is recast into that of a collection of harmonic oscillators coupled by a self-consistent time-dependent Lagrange multiplier. We will use this formulation in Sec. 4.4.

4.3 Dynamics of the isolated system after a quench of the disorder strength

In this Section we formulate the problem under study: the Hamiltonian dynamics of the isolated 2-spin spherical spin glass model, subject to an instantaneous quench of the "strength" of the (quenched) disorder. We start by giving a brief description of the main steps that allow us to obtain the mean-field equations that couple the correlation function and the linear response function, and completely characterise the evolution of the model in the $N \to \infty$ limit. The equations ruling their evolution are easily derived using the Martin-Siggia-Rose (MSR) functional formalism [98, 111, 125].

The generic set of equations of motion that describe the time evolution of the degrees of freedom of the system, the spin variables $\{s_i\}$, coupled to a bath at a temperature T, is given by

$$m\ddot{s}_i + \gamma\dot{s}_i(t) + z(t)s_i(t) = \sum_{j\neq i} J_{ij}s_j(t) + \xi_i(t)\ , \tag{4.48}$$

where the random forces ξ_i have a Gaussian distribution with zero mean and correlations given by $\langle \xi_i(t)\xi_j(t')\rangle = 2\gamma T\delta_{ij}\delta(t-t')$. In the following, the brackets $\langle\ \cdot\ \rangle$ will be indicating the average over the thermal noise $\{\xi_i(t)\}$, unless otherwise specified. For the moment we will keep the friction term $\gamma\dot{s}_i(t)$ and the thermal noise $\xi_i(t)$ (that is to say, the terms that are used to model the coupling to the bath) in these equations of motion for completeness and to make contact with the stochastic setting that is usually used in the study of this model. The Hamiltonian dynamics, or said in other words, the dynamics of the isolated system, is obtained by setting $\gamma = 0$.

In order to fully formulate the problem, one has to specify the initial conditions $\{s_i(0)\}$ and $\{\dot{s}_i(0)\}$ for the Eqs. (4.48). In our case, we want to study the time evolution of the system when it is initially prepared in an equilibrium state at a given temperature $T' = 1/\beta'$. Thus, the initial conditions must be distributed according to the Gibbs-Boltzmann measure,

$$P_0(\{s_i(0),\ \dot{s}_i(0)\}) = Z(\beta')^{-1}\ \exp\left[-\beta' H_0\left(\{s_i(0),\ \dot{s}_i(0)\}\right)\right] , \tag{4.49}$$

where we denote by $H_0\left(\{s_i(0),\ \dot{s}_i(0)\}\right)$ the pre-quench Hamiltonian of the system, namely

$$H_0\left(\{s_i,\ \dot{s}_i\}\right) = \frac{m}{2}\sum_{i=1}^{N}\ \dot{s}_i^2\ - \sum_{i<j} J_{ij}^0\ s_i s_j\ , \tag{4.50}$$

with J_{ij}^0 the pre-quench random couplings. The J_{ij}^0 are i.i.d. Gaussian random variables with mean $[J_{ij}^0] = 0$ and variance $[(J_{ij}^0)^2] = J_0^2/N$. For $t > 0$, the system evolves with the equations of motion given above where

$$J_{ij} = \frac{J}{J_0} J_{ij}^0 \tag{4.51}$$

with $J, J_0 > 0$. Hence, the post-quench couplings are also independent Gaussian random variables with zero mean and variance J^2/N, and the eigenvalues of the post-quench interaction matrix $\{J_{ij}\}$ are simply given by the pre-quench values rescaled by a factor J/J_0, $\lambda_\mu = \frac{J}{J_0}\lambda_\mu^0$. Notice that the kinetic term is left unchanged, but one can easily adapt the following derivation in the case in which also the mass parameter m is quenched.

The dynamical equations for the correlation function and linear response function, for purely dissipative dynamics, in the case of a completely random initial state ($T_0 \to +\infty$), are well-known and can be found in Refs. [126, 98, 127, 111]. The method has been modified to take into account the effect of equilibrium initial conditions at $T < \infty$ in [125] and it was applied to the relaxation dynamics of the p-spin model in [128, 129]. It can be adapted to the Hamiltonian dynamics of the isolated model with just minor modifications. In the following, we present the outcome without giving many details on the derivation. In order to facilitate the comparison with the expressions that are obtained for the purely dissipative case, we keep the coupling to the heat bath. Later on, we will focus on the isolated case.

The Martin-Siggia-Rose (MSR) generating functional for our problem is given by

$$\mathcal{Z}\left[\{s_i(t), \dot{s}_i(t), \hat{s}_i(t)\}, \{J_{ij}\}\right] = \int \mathrm{D}s(t)\ \mathrm{D}\hat{s}(t)\ \mathrm{e}^{S[\{s_i(t),\dot{s}_i(t),\hat{s}_i(t)\},\{J_{ij}\}]} \tag{4.52}$$

with the action S given by

$$S = \sum_{i=1}^{N}\int_0^{+\infty} \mathrm{d}t\ \hat{s}_i(t)\left(\gamma\ T\hat{s}_i(t) + \gamma\dot{s}_i(t) + m\ddot{s}_i(t) + \frac{\partial H_{\mathrm{pot}}}{\partial s_i} + z(t)s_i(t)\right)\ , \tag{4.53}$$

where $H_{\mathrm{pot}}(\{s_i\}) = -\sum_{i<j} J_{ij}s_i s_j$ is the post-quench potential energy.

While dealing with the generating functional $\mathcal{Z}$, we also need to take into account the average over the quenched disorder represented by the random couplings J_{ij}. In order to do so, one can use the famous replica trick, as explained in [125]. This means that the spin variables evaluated at the initial time have to be replicated, that is to say, we need to introduce the set of replicas $\{s_i^a(0)\}$ with $a = 1, \ldots, n$, in order to perform the average over the J_{ij}. The subsequent evolution of each of these replicas has to be followed in time, and it turns

out that the replica structure of the initial condition is conserved. The *replicated* dynamical action that also includes the contribution from the distribution of the initial conditions reads

$$\begin{aligned}\mathcal{S}^{(n)} &= \sum_{a=1}^{n}\left\{\sum_{i=1}^{N}\int_0^{+\infty}\mathrm{d}t\ \hat{s}_i^a(t)\left(\gamma\ T\hat{s}_i^a(t)+\gamma\dot{s}_i^a(t)+m\ddot{s}_i^a(t)+\frac{\partial H_{\rm pot}}{\partial s_i^a}+z(t)s_i^a(t)\right)+\right.\\ &\left.-\frac{1}{T'}H_0\left(\{s_i^a(0),\dot{s}_i^a(0)\}\right)\right\}\ .\end{aligned} \tag{4.54}$$

Let us now carry out the average of the quantity $\mathrm{e}^{\mathcal{S}^{(n)}}$ over the distribution of the quenched disorder. Notice that, in the action defined above, only two terms depend on the random couplings J_{ij}, or equivalently, on the couplings $J_{ij}^{(0)}$ (since J_{ij} and $J_{ij}^{(0)}$ are not independent, but just proportional). These are the term corresponding to the forces $-\frac{\partial H_{\rm pot}}{\partial s_i^a}\left(\{s_i^a(t)\}\right)$, and the term corresponding to the initial contribution $H_0\left(\{s_i^a(0),\dot{s}_i^a(0)\}\right)$. In theory, $z(t)$ should depend on the particular realisation of the random couplings J_{ij} through the spherical constraint. However, for the moment, we assume that $z(t)$ does not depend on the J_{ij} (in a certain sense, we will impose the spherical constraint only after having performed the average over the J_{ij}, and after taking the limit $N\to+\infty$).

We collect the disorder-dependent terms in the "disordered" part of the action,

$$\mathcal{S}_{\rm dis}^{(n)}=-\sum_{i<j}J_{ij}\left[\beta'\frac{J_0}{J}\sum_{a=1}^{n}s_i^a(0)s_j^a(0)+\sum_{a=1}^{n}\int_0^{+\infty}\mathrm{d}t\ \left(\hat{s}_i^a(t)s_j^a(t)+s_i^a(t)\hat{s}_j^a(t)\right)\right]\ . \tag{4.55}$$

Notice that we have symmetrized the term originating from $\hat{s}_i^a(t)\frac{\partial H_{\rm pot}}{\partial s_i^a}$. The average of the exponential of this quantity over the disorder is then given by

$$\begin{aligned}\left[\mathrm{e}^{\mathcal{S}_{\rm dis}^{(n)}}\right]_{J_{ij}}\propto\prod_{i<j}\int\mathrm{d}J_{ij}\exp\left[-\frac{N}{2J^2}J_{ij}^2-J_{ij}\sum_{a=1}^{n}\left(\beta'\frac{J_0}{J}s_i^a(0)s_j^a(0)\right.\right.\\ \left.\left.+\int_0^{+\infty}\mathrm{d}t\ \left(\hat{s}_i^a(t)s_j^a(t)+s_i^a(t)\hat{s}_j^a(t)\right)\right)\right]\ ,\end{aligned} \tag{4.56}$$

where we have chosen to integrate over the post-quench couplings J_{ij}. By performing the Gaussian integrations we obtain

$$\begin{aligned}&\left[\mathrm{e}^{\mathcal{S}_{\rm dis}^{(n)}}\right]_{J_{ij}}\propto\prod_{a,b}\exp\left\{\frac{J^2}{2N}\left[\left(\frac{\beta'J_0}{J}\right)^2\frac{1}{2}\left[\boldsymbol{s}^a(0)\cdot\boldsymbol{s}^b(0)\right]^2\right.\right.\\ &+2\ \frac{\beta'J_0}{J}\int_0^{+\infty}\mathrm{d}t\ \left(\boldsymbol{s}^a(0)\cdot\hat{\boldsymbol{s}}^b(t)\right)\left(\boldsymbol{s}^a(0)\cdot\boldsymbol{s}^b(t)\right)\\ &\left.\left.+\int_0^{+\infty}\mathrm{d}t\int_0^{+\infty}\mathrm{d}t'\left(\left(\hat{\boldsymbol{s}}^a(t)\cdot\hat{\boldsymbol{s}}^b(t')\right)\left(\boldsymbol{s}^a(t)\cdot\boldsymbol{s}^b(t')\right)+\left(\boldsymbol{s}^a(t)\cdot\hat{\boldsymbol{s}}^b(t')\right)\left(\hat{\boldsymbol{s}^a}(t)\cdot\boldsymbol{s}^b(t')\right)\right)\right]\right\},\end{aligned} \tag{4.57}$$

where we used the following notation

$$\boldsymbol{s}^a(t)\cdot\boldsymbol{s}^b(t')=\sum_{i=1}^{N}s_i^a(t)s_i^b(t') \tag{4.58}$$

and equivalent ones for all other products between replicas appearing in the exponential, $\hat{\boldsymbol{s}}^a(t)\cdot\boldsymbol{s}^b(t')$, $\hat{\boldsymbol{s}}^a(t)\cdot\hat{\boldsymbol{s}}^b(t')$, etc. Let us now decouple the four-spin coupling terms by using the

so-called *dynamical overlap* functions,

$$\begin{aligned}\left[\mathrm{e}^{\mathcal{S}_{\mathrm{dis}}^{(n)}}\right]_{J_{ij}} \propto & \int \prod_{a,b}\left(\mathrm{D}Q_1^{ab}\ \mathrm{D}Q_2^{ab}\ \cdots \mathrm{D}Q_6^{ab}\right)\times \\ & \delta\left(NQ_1^{ab}(t,t')-\hat{s}^a(t)\cdot\hat{s}^b(t')\right)\ \delta\left(NQ_2^{ab}(t,t')-s^a(t)\cdot s^b(t')\right)\ \times \\ & \delta\left(NQ_3^{ab}(t,t')-\hat{s}^a(t)\cdot s^b(t')\right)\ \delta\left(NQ_4^{ab}(t,t')-s^a(t)\cdot\hat{s}^b(t')\right)\times \\ & \delta\left(NQ_5^{ab}(t)-\hat{s}^a(t)\cdot s^b(0)\right)\ \delta\left(NQ_6^{ab}(t)-s^a(t)\cdot s^b(0)\right)\times \\ & \delta\left(NQ_7^{ab}-s^a(0)\cdot s^b(0)\right)\ \exp\left(\mathcal{S}_{\mathrm{dis}}\left[\left\{Q_k^{ab}\right\}\right]\right), \end{aligned} \tag{4.59}$$

where

$$\begin{aligned}\mathcal{S}_{\mathrm{dis}}\left[\left\{Q_k^{ab}\right\}\right] = & \frac{NJ^2}{2}\sum_{a,b}\left[\frac{1}{2}\alpha^2\left[Q_7^{ab}\right]^2+2\alpha\int \mathrm{d}t\ Q_5^{ab}(t)\ Q_6^{ab}(t)+\right. \\ & \left.+\int \mathrm{d}t\ \mathrm{d}t'\ \left(Q_1^{ab}(t,t')\ Q_2^{ab}(t,t')+Q_3^{ab}(t,t')\ Q_4^{ab}(t,t')\right)\right], \end{aligned} \tag{4.60}$$

where we use the notation $\alpha = \beta' J/J_0$. Notice that the matrix Q_7^{ab} coincides with the static overlap matrix $Q_{ab} = \frac{1}{N}\sum_k s_k^a s_k^b$, while the function $Q_2^{ab}(t,t') = \frac{1}{N}\sum_k s_k^a(t)s_k^b(t')$ is the dynamical equivalent. Moreover, $Q_3^{ab}(t,t')$ and $Q_4^{ab}(t,t')$ are both response functions, *i.e.* functions of the form $\langle s(t)\cdot\hat{s}(t')\rangle$, but with their time arguments exchanged.

In order to rewrite the integral in Eq. (4.59) in a more convenient way, we give the exponential representation of the δ-functions. For example,

$$\delta\left(NQ_1^{ab}(t,t')-\hat{s}^a(t)\cdot\hat{s}^b(t')\right)=\int \mathrm{D}l_1^{ab}\exp\left[iN\int \mathrm{d}t\ \mathrm{d}t'\ l_1^{ab}\left(Q_1^{ab}(t,t')-N^{-1}\hat{s}^a(t)\cdot\hat{s}^b(t')\right)\right] \tag{4.61}$$

and analogous expressions for the δ-functions involving the other Q's, with the introduction of the variables l_k^{ab}. The new action in terms of the variables Q_k^{ab} and l_k^{ab} then takes the following form,

$$\begin{aligned}\tilde{\mathcal{S}}_{\mathrm{dis}}\left[\left\{Q_k^{ab},l_k^{ab}\right\}\right] = & \mathcal{S}_{\mathrm{dis}}\left[\left\{Q_k^{ab}\right\}\right]+iN\sum_{a,b}\int \mathrm{d}t\ \mathrm{d}t'\left[+l_1^{ab}\ \left(Q_1^{ab}(t,t')-N^{-1}\hat{s}^a(t)\cdot\hat{s}^b(t')\right)\right. \\ & +l_2^{ab}\ \left(Q_2^{ab}(t,t')-N^{-1}s^a(t)\cdot s^b(t')\right)+l_3^{ab}\ \left(Q_3^{ab}(t,t')-N^{-1}\hat{s}^a(t)\cdot s^b(t')\right) \\ & \left.+l_4^{ab}\ \left(Q_4^{ab}(t,t')-N^{-1}s^a(t)\cdot\hat{s}^b(t')\right)\right] \\ & +iN\sum_{a,b}\int \mathrm{d}t\ \left[+l_5^{ab}\ \left(Q_5^{ab}(t)-N^{-1}\hat{s}^a(t)\cdot s^b(0)\right)\right. \\ & \left.+l_6^{ab}\ \left(Q_6^{ab}(t)-N^{-1}s^a(t)\cdot s^b(0)\right)\right] \\ & +iN\sum_{a,b}\ l_7^{ab}\ \left(Q_7^{ab}-N^{-1}s^a(0)\cdot s^b(0)\right). \end{aligned} \tag{4.62}$$

Since we are considering the limit $N\to+\infty$ of the dynamical equations, we can use a saddle-point approximation to compute the integral. By setting to zero the derivatives with respect

to all the Q's, we get a set of equations for the stationary points

$$\begin{aligned} i\ l_1^{ab} &= -\tfrac{J^2}{2} Q_2^{ab}\,, \qquad i\ l_2^{ab} = -\tfrac{J^2}{2} Q_1^{ab}\,, \\ i\ l_3^{ab} &= -\tfrac{J^2}{2} Q_4^{ab}\,, \qquad i\ l_4^{ab} = -\tfrac{J^2}{2} Q_3^{ab}\,, \\ i\ l_5^{ab} &= -\alpha J^2 Q_6^{ab}\,, \qquad i\ l_6^{ab} = -\alpha J^2 Q_5^{ab}\,, \\ i\ l_5^{ab} &= -\tfrac{\alpha^2 J^2}{2} Q_7^{ab}\,. \end{aligned} \tag{4.63}$$

By substituting these stationary points in the action $\tilde{\mathcal{S}}_{\rm dis}\left[\left\{Q_k^{ab}, l_k^{ab}\right\}\right]$ and computing the averages of the form $\langle s^a(t)\cdot\hat{s}^b(t')\rangle$ with respect to the generating functional evaluated at the saddle, one finds the following self-consistent equations for the dynamical overlap functions,

$$Q_1^{ab}(t,t') = \frac{1}{N}\sum_k \langle \hat{s}_k^a(t)\hat{s}_k^b(t')\rangle\,, \tag{4.64a}$$

$$Q_2^{ab}(t,t') = \frac{1}{N}\sum_k \langle s_k^a(t)s_k^b(t')\rangle\,, \tag{4.64b}$$

$$Q_3^{ab}(t,t') = \frac{1}{N}\sum_k \langle \hat{s}_k^a(t)s_k^b(t')\rangle = Q_4^{ba}(t',t)\,, \tag{4.64c}$$

$$Q_5^{ab}(t) = \frac{1}{N}\sum_k \langle \hat{s}_k^a(t)s_k^b(0)\rangle\,, \tag{4.64d}$$

$$Q_6^{ab}(t) = \frac{1}{N}\sum_k \langle s_k^a(t)s_k^b(0)\rangle = Q_2^{ab}(t,0)\,, \tag{4.64e}$$

$$Q_7^{ab} = \frac{1}{N}\sum_k \langle s_k^a(0)s_k^b(0)\rangle\,, \tag{4.64f}$$

where the average $\langle\,\cdot\,\rangle$ is taken both over the thermal noise and over the initial conditions, after having averaged the disordered part of the dynamical generating function. At first glance it may appear very difficult to self-consistently solve the system for these seven functions which depend on both time and replicas. However, one can make many simplifications thanks to physical arguments, in particular, causality. In fact, it turns out that [125, 130] $Q_1^{ab}(t,t')$ and $Q_5^{ab}(t)$ are identically zero for all a, b, and

$$Q_3^{ab}(t,t') = Q_4^{ab}(t,t') = Q_6^{ab}(t) = 0\,, \tag{4.65}$$

for all $a \neq b$. Moreover, $Q_2^{ab}(t,t')$ is simply the correlation between the state of the replica a at time t and the state of the replica b at time t', while $Q_3^{aa}(t,t') = Q_4^{aa}(t',t)$ represents the response of the system at time t' due to a small field applied at time t (for the replica a). Hence, we use the following notation

$$C_{ab}(t,t') \equiv Q_2^{ab}(t,t')\,, \quad R(t,t') \equiv Q_3^{aa}(t,t') = Q_4^{aa}(t',t)\,. \tag{4.66}$$

As already stated above, Q_7^{ab} coincides with the static overlap matrix Q_{ab} in the equilibrium initial condition. If one takes into account these simplifications, the part of the action that depends on the disorder reduces to

$$\begin{aligned} \mathcal{S}_{\rm dis} = \sum_a \int_{-\infty}^{+\infty} \mathrm{d}t\ \hat{s}^a(t)\cdot\Bigg[\frac{J^2}{2}\int_{-\infty}^{+\infty}\mathrm{d}t' \sum_b\ C_{ab}(t,t')\ \hat{s}^b(t') \\ + J^2\int_{-\infty}^{+\infty}\mathrm{d}t' R_{aa}(t,t')s^a(t') + \alpha J^2 \sum_b\ C_{ab}(t,0)s^b(0)\Bigg] \\ + \frac{\alpha^2 J^2}{2}\ \sum_{ab} Q_{ab}\ s^a(0)\cdot s^b(0)\,, \end{aligned} \tag{4.67}$$

(note that the variables s are meant to be vectors $(s_1, \ldots, s_N)$). Then we can combine this back together with the rest of the original replicated action $\mathcal{S}^{(n)}$, to obtain

$$\begin{aligned}\mathcal{S}^{(n)} &= \sum_a \int_{-\infty}^{+\infty} \mathrm{d}t\ \hat{s}^a(t) \cdot \Bigg[\mathcal{D}_t s^a(t) + \gamma T \hat{s}^a(t) + \frac{J^2}{2} \int_{-\infty}^{+\infty} \mathrm{d}t' \sum_b\ C_{ab}(t,t') \hat{s}^b(t') \\ &\quad + J^2 \int_{-\infty}^{+\infty} \mathrm{d}t' R_{aa}(t,t') s^a(t') + \alpha J^2 \sum_b\ C_{ab}(t,0) s^b(0) \Bigg] \\ &\quad + \frac{\alpha^2 J^2}{2}\ \sum_{ab} Q_{ab}\ s^a(0) \cdot s^b(0) + \text{const.}\ , \end{aligned} \tag{4.68}$$

where we denoted by $\mathcal{D}_t$ the differential operator $m\partial_t^2 + \gamma \partial_t + z(t)$, and we neglected terms that do not depend on the spin variables. Notice that, at this point, the spin variables s_k are all decoupled in the action of the generating functional. Therefore we can write an effective Langevin equation for a (replicated) scalar degree of freedom $s^a(t)$ based on $\mathcal{S}^{(n)}$,

$$\mathcal{D}_t s^a(t) = J^2 \int_{-\infty}^{+\infty} \mathrm{d}t' R_{aa}(t,t') s^a(t') + \alpha J^2 \sum_b\ C_{ab}(t,0) s^b(0) + \eta^a(t)\ , \tag{4.69}$$

where the effective noise η^a is not δ-correlated anymore, but instead satisfies

$$\langle \eta^a(t) \eta^b(t') \rangle = 2\gamma T\ \delta_{ab}\ \delta(t-t')\ + J^2 C_{ab}(t,t')\ . \tag{4.70}$$

By averaging over the disorder we have thus introduced an explicit memory term in the effective Langevin equation, that is to say, a non-local kernel which couples the time t with all times $t' < t$ (whereas the original Langevin equation was describing a Markovian stochastic process).

We can now write the self-consistent equations for the two-time correlations and the response functions by using the effective Langevin equation given above. In the case of the response function, by using the relation $R(t_1,t_2) = \left\langle \frac{\delta s(t_1)}{\delta \eta(t_2)} \right\rangle$ we get

$$\begin{aligned}\mathcal{D}_{t_1} R_{aa}(t_1,t_2) &= \mathcal{D}_{t_1} \left\langle \frac{\delta s^a(t_1)}{\delta \eta^a(t_2)} \right\rangle = \left\langle \frac{\delta}{\delta \eta^a(t_2)} \mathcal{D}_{t_1} s^a(t_1) \right\rangle = \\ &= J^2 \int_{-\infty}^{+\infty} \mathrm{d}t' R_{aa}(t_1,t') R_{aa}(t',t_2) + \delta(t_1 - t_2)\ . \end{aligned} \tag{4.71}$$

The equation for the correlation function $C_{aa}(t_1,t_2)$ is obtained by multiplying the effective Langevin equation by $s(t_2)$ and then averaging over the thermal noise,

$$\begin{aligned}\mathcal{D}_{t_1} C_{aa}(t_1,t_2) &= \mathcal{D}_{t_1} \langle s^a(t_1) s^a(t_2) \rangle = \langle \mathcal{D}_{t_1} s^a(t_1) s^a(t_2) \rangle = \\ &= J^2 \int_{-\infty}^{+\infty} \mathrm{d}t' R_{aa}(t_1,t') C_{aa}(t',t_2) \\ &\quad + \alpha J^2 \sum_b C_{ab}(t_1,0) C_{ab}(t_2,0) + \langle \eta^a(t_1) s^a(t_2) \rangle\ , \end{aligned} \tag{4.72}$$

where

$$\begin{aligned}\langle \eta^a(t_1) s^a(t_2) \rangle &= \int_{-\infty}^{+\infty} \mathrm{d}t' R_{aa}(t_2,t') \langle \eta^a(t_1) \eta^a(t') \rangle \\ &= 2\gamma T R_{aa}(t_1,t_2) + J^2 \int_{-\infty}^{+\infty} \mathrm{d}t' R_{aa}(t_2,t') C_{aa}(t_1,t')\ . \end{aligned} \tag{4.73}$$

Analogously, for the "off-diagonal" correlations C_{ab} one has

$$\mathcal{D}_{t_1} C_{ab}(t_1,t_2) = \left\langle \mathcal{D}_{t_1} s^a(t_1) s^b(t_2) \right\rangle = J^2 \int_{-\infty}^{+\infty} \mathrm{d}t' R_{aa}(t_1,t') C_{ab}(t',t_2) + \alpha J^2 \sum_c C_{ac}(t_1,0) C_{bc}(t_2,0) \; . \tag{4.74}$$

Finally, by using the relation $\partial_{t_1} \langle s(t_1) s(t_2) \rangle \big|_{t_2 \to t_1^-} = 0$, which comes from the fact that the velocity vector $(\dot{s}_1(t), \ldots, \dot{s}_N(t))$ is perpendicular to the spin vector $(s_1(t), \ldots, s_N(t))$ (due to the spherical constraint), one can obtain an equation for the Lagrange multiplier $z(t)$,

$$\begin{aligned} z(t_1) &= \left[\mathcal{D}_{t_1} C_{aa}(t_1,t_2) - m \partial_{t_1}^2 C_{aa}(t_1,t_2) \right] \Big|_{t_2 \to t_1^-} = \\ &= 2J^2 \int_{-\infty}^{+\infty} \mathrm{d}t' R_{aa}(t_1,t') C_{aa}(t_1,t') + \alpha J^2 \sum_b C_{ab}(t_1,0)^2 \\ &\quad - m \, \partial_{t_1}^2 C_{aa}(t_1,t_2) \Big|_{t_2 \to t_1^-} \; . \end{aligned} \tag{4.75}$$

Since the initial conditions are taken from equilibrium, the replica structure at $t = 0$ is symmetric (see Ref. [95]), thus we have

$$C_{aa}(0,0) = 1 \quad \forall a \qquad \text{and} \qquad C_{ab}(0,0) = q_{\text{in}} \quad \forall b \neq a \tag{4.76}$$

with q_{in} the Edwards-Anderson parameter in the initial equilibrium state, that is $q_{\text{in}} = 0$ for $T' > T_{0,c}$, while $q_{\text{in}} = 1 - \frac{T'}{J_0}$ for $T' < T_{0,c}$, where $T_{0,c} = J_0$ is the critical temperature for the pre-quench Hamiltonian. This initial replica structure has an effect on the equation for the time-dependent correlation functions. Indeed, because of the symmetry between replicas, there are just two kinds of independent correlations

$$C(t_1,t_2) \equiv C_{aa}(t_1,t_2) \quad \text{for any } a \; , \tag{4.77a}$$

$$Q(t_1,t_2) \equiv C_{ab}(t_1,t_2) \quad \text{for any } a,b \text{ distinct.} \tag{4.77b}$$

The first one is the correlation between the configuration of one replica of the system at time t_1 and the configuration of the same replica at time t_2. The second one, instead, is the correlation between the configuration of one replica of the system at time t_1 and the configuration of a different replica at time t_2. Notice that C is symmetric in its arguments, $C(t_1,t_2) = C(t_2,t_1)$. Concerning the linear response function, we have already argued that $R_{ab}(t,t') \equiv 0$ for all a,b distinct, while $R_{aa}(t,t')$ is the same for all replicas a, thus we denote it by $R(t,t')$ in the following.

Although we could write the evolution equation for the two-time correlation between different replicas, $Q(t_1,t_2)$, for all $t_1, t_2 \geq 0$, actually we do not need it for $t_2 > 0$ since we are interested only in the self-correlation $C(t_1,t_2)$, the response $R(t_1,t_2)$ and the Lagrange multiplier $z(t)$, and only $Q(t_1,0)$ intervenes in the integro-differential equations for these functions. This is the only correlation between different replicas that will appear in the calculations.

In absence of dissipation, that is, in the limit $\gamma \to 0$, Eqs. (4.71), (4.72), (4.74) and (4.75)

reduce to

$$\left(m\partial_{t_1}^2 + z(t_1)\right) R(t_1,t_2) = J^2 \int_{t_2}^{t_1} dt' R(t_1,t') R(t',t_2) + \delta(t_1 - t_2) \,, \tag{4.78a}$$

$$\left(m\partial_{t_1}^2 + z(t_1)\right) C(t_1,t_2) = J^2 \int_0^{t_1} dt' R(t_1,t') C(t',t_2) + J^2 \int_0^{t_2} dt' R(t_2,t') C(t_1,t') + \frac{JJ_0}{T'} \left[C(t_1,0)C(t_2,0) + (n-1)Q(t_1,0)Q(t_2,0)\right] \,, \tag{4.78b}$$

$$\left(m\partial_{t_1}^2 + z(t_1)\right) Q(t_1,0) = J^2 \int_0^{t_1} dt' \; R(t_1,t') Q(t',0) + \frac{JJ_0}{T'} \left[C(t_1,0)q_{\rm in} + Q(t_1,0) + (n-2)Q(t_1,0)q_{\rm in}\right] \,, \tag{4.78c}$$

$$z(t_1) = -m\partial_{t_1}^2 C(t_1,t_2)|_{t_2 \to t_1^-} + 2J^2 \int_0^{t_1} dt' R(t_1,t') C(t_1,t') + \frac{JJ_0}{T'} \left[C(t_1,0)^2 + (n-1)Q(t_1,0)^2\right] \,. \tag{4.78d}$$

(where we have used causality of $R(t,t')$ to restrict the limits of the integrals). One can check that these equations coincide with the ones in [128, 129] when inertia is neglected, $p = 2$ and $J = J_0$, and a coupling to a bath is introduced. With respect to the equations studied in [83], they correspond to $p = 2$ and they have the extra ingredient of the influence of equilibrium initial conditions with a non-trivial replica structure, allowing for condensed initial states in proper thermal equilibrium. Eqs. (4.78a)-(4.78d) must also be complemented with the following equal-time conditions

$$C(t_1,t_1) = 1 \,, \tag{4.79a}$$

$$R(t_1,t_1) = 0 \,, \tag{4.79b}$$

$$\partial_{t_1} C(t_1,t_2)|_{t_2 \to t_1^-} = \partial_{t_1} C(t_1,t_2)|_{t_2 \to t_1^+} = 0 \,, \tag{4.79c}$$

$$\partial_{t_1} Q(t_1,t_2)|_{t_2 \to t_1^-} = \partial_{t_1} Q(t_1,t_2)|_{t_2 \to t_1^+} = 0 \,, \tag{4.79d}$$

$$\partial_{t_1} R(t_1,t_2)|_{t_2 \to t_1^-} = \frac{1}{m} \,, \tag{4.79e}$$

for all $t_1, t_2 \geq 0^+$. In the limit $n \to 0$, Eqs. (4.78a)-(4.78d) finally become

$$\left(m\partial_{t_1}^2 + z(t_1)\right) R(t_1,t_2) = J^2 \int_{t_2}^{t_1} dt' R(t_1,t') R(t',t_2) + \delta(t_1 - t_2) \,, \tag{4.80a}$$

$$\left(m\partial_{t_1}^2 + z(t_1)\right) C(t_1,t_2) = J^2 \int_0^{t_1} dt' R(t_1,t') C(t',t_2) + J^2 \int_0^{t_2} dt' R(t_2,t') C(t_1,t') + \frac{JJ_0}{T'} \left[C(t_1,0)C(t_2,0) - Q(t_1,0)Q(t_2,0)\right] \,, \tag{4.80b}$$

$$\left(m\partial_{t_1}^2 + z(t_1)\right) Q(t_1,0) = J^2 \int_0^{t_1} dt' \; R(t_1,t') Q(t',0) + \frac{JJ_0}{T'} \left[q_{\rm in} C(t_1,0) + (1 - 2q_{\rm in})Q(t_1,0)\right] \,, \tag{4.80c}$$

$$z(t_1) = -m\partial_{t_1}^2 C(t_1,t_2)|_{t_2 \to t_1^-} + 2J^2 \int_0^{t_1} dt' R(t_1,t') C(t_1,t') + \frac{JJ_0}{T'} \left[C(t_1,0)^2 - Q(t_1,0)^2\right] \,. \tag{4.80d}$$

Eqs. (4.80a)-(4.80d) represent the (classical) Schwinger-Dyson equations [131] associated with the Langevin process described by Eq. (4.48) (in the limit $\gamma \to 0$).

We found convenient to numerically integrate these integro-differential equations using an expression of the Lagrange multiplier that trades the second-time derivative of the correlation function into the total conserved energy after the quench. More precisely, we proceed as explained below.

Let us first introduce the kinetic energy density and the potential energy density,

$$e_{\rm kin}(t) \equiv \left\langle \frac{1}{N}\sum_{i=1}^{N} (\dot{s}_i(t))^2 \right\rangle , \tag{4.81a}$$

$$e_{\rm pot}(t) \equiv -\left\langle \frac{1}{N}\sum_{i<j} J_{ij} s_i(t) s_j(t) \right\rangle , \tag{4.81b}$$

with $\langle \cdot \rangle$ the average over the initial conditions (eventually one can consider also an average over the disorder on top) By using the spherical constraint

$$\sum_{i=1}^{N} \langle s_i(t)^2 \rangle = N , \tag{4.82}$$

one can easily derive the following expression for $\partial_{t_1}^2 C(t_1,t_2)|_{t_2\to t_1^-}$,

$$\begin{aligned} \lim_{t_2\to t_1^-} \partial_{t_1}^2 C(t_1,t_2) &= \lim_{t_2\to t_1^-} \frac{1}{N}\sum_{i}^{N} \partial_{t_1}^2 \langle s_i(t_1) s_i(t_2)\rangle = \frac{1}{N}\sum_{i}^{N} \langle \ddot{s}_i(t_1) s_i(t_1)\rangle = \\ &= -\frac{1}{N}\sum_{i}^{N} \langle \dot{s}_i(t_1)^2\rangle = -\frac{2}{m} e_{\rm kin}(t_1) \quad , \end{aligned} \tag{4.83}$$

where we used the relation $\langle \sum_i s_i(t)\dot{s}_i\rangle = 0$ coming from the spherical constraint. On the other hand, if we take the equation of motion for s_i (Eqs. (4.10)) evaluated at time t_1, multiply it by $s_i(t_2)$ and take the average over the initial conditions, we obtain

$$m\langle \ddot{s}_i(t_1) s_i(t_2)\rangle = -\sum_{i\neq j} J_{ij}\langle s_j(t_1) s_i(t_2)\rangle - z(t_1)\langle s_i(t_1) s_i(t_2)\rangle , \tag{4.84}$$

where we have considered $z(t)$ as independent from the initial conditions. If we now sum over the index i, normalising by N, and take the limit $t_2 \to t_1^-$, we get the following

$$\begin{aligned} \frac{m}{N}\lim_{t_2\to t_1^-}\sum_{i=1}^{N}\langle \ddot{s}_i(t_1) s_i(t_2)\rangle &= m\lim_{t_2\to t_1^-}\partial_{t_1}^2 C(t_1,t_2) = -\frac{2}{N}\sum_{i<j} J_{ij}\langle s_i(t_1) s_j(t_2)\rangle - z(t_1) = \\ &= -2e_{\rm pot}(t_1) - z(t_1) . \end{aligned} \tag{4.85}$$

Thus

$$e_{\rm pot}(t) = -\frac{1}{2}\left(m \lim_{t'\to t^-} \partial_t^2 C(t,t') + z(t)\right) \tag{4.86}$$

and combining this expression with Eq. (4.83) we find a relation between $e_{\rm pot}(t)$, $e_{\rm kin}(t)$ and $z(t)$

$$e_{\rm kin}(t) - e_{\rm pot}(t) = \frac{1}{2} z(t) . \tag{4.87}$$

This relation corresponds to the imposition of the spherical constraint on average over the initial conditions. The problem described by the dynamical equations given in (4.80a)-(4.80d), together with this relation (or, equivalently, the constraint given by Eq. (4.82)) is slightly different from the one that one would obtain by using the equation of motions in (4.10) and imposing the spherical constraint for each trajectory, that is to say, $\sum_i s_i(t)^2 = N$ for all t. However, in the limit $N \to \infty$, we expect the difference to be negligible.

The sum of $e_{\rm kin}(t)$ and $e_{\rm pot}(t)$ is equal to the total energy of the system (per degree of freedom). Since for $t > 0$ the system evolves under Hamiltonian dynamics, its total energy is conserved post-quench, and then we can write

$$e_{\rm kin}(t) = \frac{e_f}{2} + \frac{1}{4} z(t) \,, \tag{4.88a}$$

$$e_{\rm pot}(t) = \frac{e_f}{2} - \frac{1}{4} z(t) \,, \tag{4.88b}$$

for $t > 0$, with e_f the post-quench total energy per degree of freedom. By using these relations we can rewrite Eq. (4.80d) in the following form

$$z(t) = 2e_f + 4J^2 \int_0^t dt' R(t,t') C(t,t') + 2\frac{JJ_0}{T'} \left[C(t,0)^2 - Q(t,0)^2 \right] \,. \tag{4.89}$$

4.3.1 Energy change

We now determine the change in the total energy that is induced at $t = 0$ by the istantaneous quench of the strength of the disorder. As already mentioned above, the quench protocol consists in a uniform rescaling of the interaction matrix $\{J_{ij}\}$, namely

$$J^0_{ij} \mapsto J_{ij} = \frac{J}{J_0} J^0_{ij} \,, \quad \text{for all } i,j \,. \tag{4.90}$$

The post-quench interaction matrix is just proportional to the pre-quench one, hence the eigenvalues $\lambda^0_1, \ldots, \lambda^0_N$ of the pre-quench interaction matrix are transformed in $\lambda_1, \ldots, \lambda_N$, with $\lambda_\mu = \frac{J}{J_0} \lambda^0_\mu$.

The kinetic energy density before the quench is given by

$$e_{\rm kin}(0^-) = \frac{m}{2} \frac{1}{N} \sum_{i=1}^N \langle (\dot{s}_i(0^-))^2 \rangle = \frac{T'}{2} \,, \tag{4.91}$$

the last equality being due to the fact that we consider equilibrium initial conditions at temperature T'. The pre-quench potential energy density is given (in the thermodynamic limit) by

$$e_{\rm kin}(0^-) = -\frac{1}{N} \sum_{i<j} J_{ij} \langle s_i(0^-) s_j(0^-) \rangle \underset{N\to\infty}{=} e^{\rm pot}_{\rm eq}(T') = -\frac{J_0^2}{2T} \left(1 - q^2_{\rm in} \right) \,, \tag{4.92}$$

with $e^{\rm pot}_{\rm eq}$ the expression given in Eq. (4.28), and $q_{\rm in} = 0$ in the paramagnetic phase ($T' \geq T_{0,c} = J_0$) while $q_{\rm in} = 1 - \frac{T'}{J_0}$ in the condensed phase ($T' < T_{0,c} = J_0$). The kinetic energy is left unchanged by the quench, since we are assuming that the mass m does not change and the velocities $\dot{s}_i$ do not change in the infinitesimal interval taking from 0^- to 0^+, hence

$$e_{\rm kin}(0^+) = \frac{m}{2} \frac{1}{N} \sum_{i=1}^N \langle (\dot{s}_i(0^+))^2 \rangle = \frac{T'}{2} \,. \tag{4.93}$$

The post-quench potential energy density can be estimated from the relation between the Lagrange multiplier and the energy densities given by Eqs. (4.87),

$$e_{\rm pot}(0^+) = e_{\rm kin}(0^+) - \frac{1}{2}\, z(0^+) \tag{4.94}$$

and the dynamical equation for $z(t)$ (Eq. (4.89)) evaluated at $t = 0^+$,

$$\begin{aligned} z(0^+) &= 2e_{\rm pot}(0^+) + 2e_{\rm kin}(0^+) + \frac{2JJ_0}{T'}\left[C(0,0)^2 - Q(0,0)^2\right] = \\ &= 2e_{\rm pot}(0^+) + 2e_{\rm kin}(0^+) + \frac{2JJ_0}{T'}(1 - q_{\rm in}^2)\ . \end{aligned} \tag{4.95}$$

Thus

$$e_{\rm pot}(0^+) = -\frac{JJ_0}{2T'}(1 - q_{\rm in}^2)\ . \tag{4.96}$$

As one would have expected, the potential energy is just rescaled by a factor J/J_0 after the quench. The change in energy caused by the quench is then given by

$$\Delta e_{\rm tot} = e_{\rm tot}(0^+) - e_{\rm tot}(0^-) = \left(1 - \frac{J}{J_0}\right)\frac{J_0^2}{2T'}\left(1 - q_{\rm in}^2\right)\ . \tag{4.97}$$

One can clearly see that the energy variation is controlled by the parameter $x = \frac{J}{J_0}$. Quenches with $x > 1$ correspond to extraction of energy from the system, while quenches with $x < 1$ correspond to injection of energy into the system. It is not difficult to imagine what happens in the case in which also the mass parameter m is quenched. For a simultaneous quench of the mass and disorder strength, the change in energy is given by

$$\Delta e_{\rm tot} = \left(\frac{m}{m_0} - 1\right)\frac{T'}{2} + \left(1 - \frac{J}{J_0}\right)\frac{J_0^2}{2T'}\left(1 - q_{\rm in}^2\right)\ , \tag{4.98}$$

where m_0 and m are the pre-quench value and the post-quench value of the mass, respectively. However, in this Dissertation, we will consider only quenches of the potential energy, and we will trace a dynamical phase diagram using the parameters

$$y = \frac{T'}{J_0} \qquad\qquad x = \frac{J}{J_0}\ . \tag{4.99}$$

We will show that the parameter space is split in at least three sectors displaying fundamentally different dynamical behaviours.

4.3.2 Asymptotic analysis

As already mentioned in the introduction of this Chapter, the goal of our study is to determine whether the system, initially prepared in an equilibrium state and evolving under Hamiltonian dynamics after a quench of the disorder strength, can reach a late-time stationary regime in which one can observe the typical properties of Gibbs-Boltzmann equilibrium, for certain choices of the quench parameters. This is possible by just looking at the behaviour of the two-time auto-correlation and linear response function, in the limit $N \to \infty$. However, a method to obtain a fully analytical solution for $C(t_1, t_2)$ and $R(t_1, t_2)$ from Eqs. (4.80a)-(4.80d), for every choice of the parameters $y = T'/J_0$ and $x = J/J_0$, is not known (at least to us). Thus, in order to grasp the main aspects of the dynamics in the long-time regime one

needs to make some hypotheses that simplify them. All the results that we obtain with this approximate analysis are going to be tested against the solutions that we gain by numerically integrating Eqs. (4.80a)-(4.80d) and that we are going to show in Sec. 4.5.

In this Section we are going to study the asymptotic behaviour of the system, in the limit $N \to \infty$, under the following assumptions

- for sufficiently large t_2, time-translational invariance (TTI) holds, that is to say,

$$\lim_{t_2 \gg 1} C(t_1, t_2) = C_{\mathrm{st}}(t_1 - t_2) \,, \tag{4.100a}$$

$$\lim_{t_2 \gg 1} R(t_1, t_2) = R_{\mathrm{st}}(t_1 - t_2) \,, \tag{4.100b}$$

  for $t_1 > t_2$, with C_{st} and R_{st} the "stationary" version of the two-time autocorrelation and linear response, respectively ;

- the Lagrange multiplier converges to a certain constant, $\lim_{t \to +\infty t} z(t) = z_f$;

- the fluctuation-dissipation theorem (FDT) holds for C_{st} and R_{st},

$$R_{\mathrm{st}}(\tau) = -\frac{1}{T_f} \frac{\partial C_{\mathrm{st}}(\tau)}{\partial \tau} \tag{4.101}$$

  for $\tau > 0$, with T_f the "final" temperature of the system ;

- the kinetic energy density approaches $\lim_{t \to +\infty} e_{\mathrm{kin}}(t) = T_f/2$, with T_f the same temperature appearing in the FDT relation.

These assumptions correspond to saying that the system is able to reach an equilibrium state at the temperature T_f in the long-time limit. We also define the following asymptotic values

$$q \equiv \lim_{t_2 \gg 1} \lim_{(t_1 - t_2) \to +\infty} C(t_1, t_2) = \lim_{\tau \to +\infty} C_{\mathrm{st}}(\tau) \,, \tag{4.102a}$$

$$q_0 \equiv \lim_{t \to +\infty} C(t, 0) \,, \tag{4.102b}$$

$$q_1 \equiv \lim_{t \to +\infty} Q(t, 0) \,. \tag{4.102c}$$

We expect q to be zero if the system reaches an equilibrium state in the paramagnetic phase, that is, if $T_f > T_c$, while $q = 1 - T_f/J$ if the system reaches equilibrium in the condensed phase, that is, if $T_f < T_c$, with $T_c = J$ the critical temperature associated with the post-quench potential energy. Moreover we should obtain

$$z_f = \begin{cases} T_f + \frac{J^2}{T_f} & \text{for } T_f \geq J \\ 2J & \text{for } T_f < J \end{cases} \,, \tag{4.103}$$

according to the equilibrium values of the Lagrange multiplier for the $p = 2$ spherical spin glass model, as seen in Sec. 4.2.3. The above assumptions are not obvious and, as we will show analytically in some cases and numerically in the next Section, they do not apply to all quenches. Still, we find useful to explore their consequences and derive from them a set of relations between the control parameters for which special behaviours arise.

Let us consider what we can obtain from Eqs. (4.80a)-(4.80d) when we make the simplifications implied above, without assuming anything on the constants T_f, z_f, q, q_0 and q_1.

We start by considering the dynamical equation for the response function. Notice that this equation does not contain an explicit dependence on $C(t_1, t_2)$ and the initial condition of the system (these dependences are, in fact, hidden in the Lagrange multiplier $z(t)$). If one assumes TTI, than Eq. (4.80a) reduces to

$$m\ \partial_\tau^2 R_{\rm st}(\tau) + z(t_2+\tau)\ R_{\rm st}(\tau) = J^2 \int_{t_2}^{t_2+\tau} {\rm d}t'\ R_{\rm st}(t_2+\tau-t') R_{\rm st}(t'-t_2) + \delta(\tau)\ . \quad (4.104)$$

By exploiting the causality of $R_{\rm st}$, *i.e.* $R_{\rm st}(\tau) = 0$ for $\tau < 0$, and then taking the limit $t_2 \to +\infty$, this equation becomes

$$m\ \partial_\tau^2 R_{\rm st}(\tau) + z_f\ R_{\rm st}(\tau) = J^2 \int_{-\infty}^{+\infty} {\rm d}s\ R_{\rm st}(\tau-s) R_{\rm st}(s) + \delta(\tau)\ , \quad (4.105)$$

where we have introduced the asymptotic value of the Lagrange multiplier. The Fourier transform of $R_{\rm st}$, which we denote by $\hat{R}_{\rm st}$, satisfies then the following equation,

$$J^2 \hat{R}_{\rm st}(\omega)^2 - (z_f - m\omega^2)\hat{R}_{\rm st}(\omega) + 1 = 0\ , \quad (4.106)$$

with general solution given by

$$\hat{R}_{\rm st}(\omega) = \frac{1}{J^2}\left[z_f - m\omega^2\ \pm m\sqrt{(\omega^2-\omega_+^2)(\omega^2-\omega_-^2)}\right] \quad (4.107)$$

where we define $\omega_\pm^2 = (z_f \pm 2J)/m$. Let us assume, for the moment, that these two quantities are non-negative (intuitively, z_f must be larger than or at most equal to the largest eigenvalue of the post-quench interaction matrix, if the system reaches equilibrium, thus $z_f \geq 2J$). By using the fact that $R_{\rm st}(\omega) \sim -(m\omega^2)^{-1}$ as $\omega \to +\infty$, one obtains

$$\mathrm{Im}\hat{R}_{\rm st}(\omega) = \frac{1}{2J^2}\begin{cases} \pm m\sqrt{(\omega^2-\omega_-^2)(\omega_+^2-\omega^2)} & \text{for} \quad \omega_- \leq \omega \leq \omega_+ \\ 0 & \text{otherwise} \end{cases} \quad (4.108a)$$

$$\mathrm{Re}\hat{R}_{\rm st}(\omega) = \frac{1}{2J^2}\begin{cases} z_f - m\omega^2 \pm m\sqrt{(\omega_-^2-\omega^2)(\omega_+^2-\omega^2)} & \text{for}\ \ \omega \leq \omega_- \\ z_f - m\omega^2 & \text{for}\ \ \omega_- \leq \omega \leq \omega_+ \\ z_f - m\omega^2 + m\sqrt{(\omega^2-\omega_-^2)(\omega^2-\omega_+^2)} & \text{for}\ \ \omega_+ \leq \omega \end{cases} \quad (4.108b)$$

The sign of the imaginary part of $\hat{R}_{\rm st}(\omega)$ in the interval $[\omega_-, \omega_+]$ and that appearing in the real part, $\mathrm{Re}\hat{R}_{\rm st}(\omega)$, for $\omega < \omega_-$, in front of the square root, are decided *a posteriori* by looking at the behaviour of the Fourier transform of the correlation, which should be related to $\hat{R}_{\rm st}$ through the FDT relation, as we will see below. Notice also that $|\hat{R}_{\rm st}(\omega)|^2 = 1/J^2$ in the interval $[\omega_-, \omega_+]$. The zero-frequency linear response, also called static susceptibility, is given by

$$\chi_{\rm st} \equiv \hat{R}_{\rm st}(0) = \int_0^{+\infty} {\rm d}\tau\ R_{\rm st}(\tau) = \frac{1}{2J^2}\left(z_f - \sqrt{z_f^2 - 4J^2}\right)\ . \quad (4.109)$$

Let us now turn to the dynamical equation for $C(t_1, t_2)$ and consider the long-time regime $t_2 \gg 1$, with the assumption that time-translational invariance (TTI) is satisfied. We also allow for the two-time correlation function not to decay to zero, but to a finite value q, and separate explicitly this contribution from the stationary term $C_{\rm st}$, *i.e.* $C(t_1, t_2) \sim q + C_{\rm st}(t_1 - t_2)$ in the limit $t_2 \to +\infty$ with $t_1 - t_2$ fixed, and we assume $\lim_{\tau\to\infty} C_{\rm st}(\tau) = 0$. We expect $q > 0$ if the system is able to reach asymptotically an equilibrium state in the condensed phase, otherwise $q = 0$.

With these assumptions and using the definitions of the asymptotic values of $C(t,0)$ and $Q(t,0)$ given in Eqs. (4.102), for $t_2 \gg 1$ and $\tau = t_1 - t_2$ fixed, Eq. (4.80b) reduces to

$$\begin{aligned}\left(m\partial_\tau^2 + z_f\right)(q + C_{\rm st}(\tau)) = \frac{JJ_0}{T'}(q_0^2 - q_1^2) + J^2 q \int_{-t_2}^{+\infty} {\rm d}s\ R_{\rm st}(\tau - s) + J^2 q \int_{-\infty}^{t_2} {\rm d}s\ R_{\rm st}(s) \\ + J^2 \int_{-t_2}^{+\infty} {\rm d}s\ R_{\rm st}(\tau - s) C_{\rm st}(s) \\ + J^2 \int_{-\infty}^{t_2} {\rm d}s\ R_{\rm st}(s) C_{\rm st}(\tau + s)\ . \end{aligned} \tag{4.110}$$

(where we also used the causal property of $R_{\rm st}$ to extend the limits of the integrals to $+\infty$ or $-\infty$). Taking now the limit $t_2 \to +\infty$ and computing the Fourier transform in the variable τ, one obtains

$$\begin{aligned}\left(-m\omega^2 + z_f - J^2 \hat{R}_{\rm st}(\omega)\right)\hat{C}_{\rm st}(\omega) &= \left(-z_f q + \frac{JJ_0}{T'}(q_0^2 - q_2^2) + 2J^2\, q\ \chi_{\rm st}\right)\delta(\omega) \\ &\quad + J^2\, \hat{C}_{\rm st}(\omega)\hat{R}^*_{\rm st}(\omega)\ , \end{aligned} \tag{4.111}$$

with $\hat{R}^*_{\rm st}(\omega)$ the complex conjugate of $\hat{R}_{\rm st}(\omega)$. In order to obtain a solution for $\hat{C}_{\rm st}$ that is continous at $\omega = 0$ we need to impose the following condition,

$$-z_f q + \frac{JJ_0}{T'}(q_0^2 - q_1^2) + 2J^2\, q\ \chi_{\rm st} = 0\ . \tag{4.112}$$

Eq. (4.111) is then recast as

$$\left(-m\omega^2 + z_f - J^2 \hat{R}_{\rm st}(\omega)\right)\hat{C}_{\rm st}(\omega) = J^2\, \hat{C}_{\rm st}(\omega) R^*_{\rm st}(\omega)\ , \tag{4.113}$$

and by using Eq. (4.106), we obtain

$$\hat{C}_{\rm st}(\omega) = J^2 \left|\hat{R}_{\rm st}(\omega)\right|^2\ \hat{C}_{\rm st}(\omega) \tag{4.114}$$

Unfortunately, this equation does not give much information about $\hat{C}_{\rm st}(\omega)$. From it we can only conclude that for ω such that $\hat{C}_{\rm st}(\omega) \neq 0$, $\hat{R}_{\rm st}$ has constant modulus, $|\hat{R}_{\rm st}(\omega)|^2 = 1/J^2$. If one supposes that the FDT relation between $C_{\rm st}$ and $R_{\rm st}$ holds true, that is to say, $\omega\, \hat{C}_{\rm st}(\omega) = -T_f\ {\rm Im}\hat{R}_{\rm st}(\omega)$ for some T_f, then one can also conclude that $\hat{C}_{\rm st}(\omega)$ is nonzero only in the interval $[\omega_-, \omega_+]$ (since ${\rm Im}\hat{R}_{\rm st}(\omega)$ is nonzero only in this interval, as seen above). Moreover, FDT also implies

$$\chi_{\rm st} = \int_0^{+\infty} {\rm d}t\ R_{\rm st}(t) = -\frac{1}{T_f}\left(1 - \lim_{t\to+\infty} C_{\rm st}(t)\right) = \frac{1-q}{T_f}\ . \tag{4.115}$$

Next we consider the asymptotic behaviour of $z(t)$, the Lagrange multiplier. Starting from Eq. (4.89) and considering the limit $t \to \infty$, we can write

$$z_f = 2e_f + 4J^2 \lim_{t\to+\infty} \int_0^t {\rm d}t'\ R(t,t')C(t,t') + \frac{2JJ_0}{T'}\left(q_0^2 - q_1^2\right)\ . \tag{4.116}$$

To proceed in the calculation we assume that we can substitute the integrand $R(t,t')C(t,t')$ with $R_{\rm st}(t-t')C_{\rm st}(t-t')$ and we use the FDT property $R_{\rm st}(\tau) = -\frac{1}{T_f}\partial_\tau C_{\rm st}(\tau)$, obtaining

$$z_f = 2e_f - \frac{4J^2}{T_f} \lim_{t\to+\infty} \int_0^t {\rm d}t'\ \ \partial_\tau \left[C_{\rm st}(\tau)^2\right]\Big|_{t-t'} + \frac{2JJ_0}{T'}\left(q_0^2 - q_1^2\right)\ . \tag{4.117}$$

By doing so we assume that the contribution to the integral of any possible transient between the time 0 and t occuring before TTI and FDT establish can be neglected. In other words, we assume that the time $t_{\rm tr}$, at which the transient ends and the true stationary regime begins, is very small compared to t (which is true in the limit $t \to +\infty$), and the contribution to the integral coming from the interval $[0, t_{\rm tr}]$ has a negligible effect. If one believes this approximation, Eq. (4.117) then reduces to

$$z_f = T_f + \frac{J^2}{T_f}(1-q^2) + \frac{JJ_0}{T'}\left(q_0^2 - q_1^2\right) \ . \tag{4.118}$$

where we have used the relation $e_f = e_{\rm kin}(t) + e_{\rm pot}(t) = 2e_{\rm kin}(t) - z(t)/2$ and assumed that $\lim_{t\to\infty} e_{\rm kin}(t) = T_f/2$, *i.e.* "equipartition" at the final temperature T_f, as mentioned above.

By performing a similar approximation for Eq. (4.80b) evaluated at $t_2 = 0$, we obtain the following relation

$$z_f q_0 = \frac{JJ_0}{T'}\left(q_0 - q_{\rm in} q_1\right) + J^2 q_0 \lim_{t\to+\infty} \int_0^t {\rm d}t' \ R_{\rm st}(t-t') \ . \tag{4.119}$$

Again we assume that the initial transient before the onset of the TTI regime is very short and that $C(t,0)$ converges very rapidly to the asymptotic value q_0. By using the FDT relation we then obtain

$$z_f q_0 = \frac{JJ_0}{T'}\left(q_0 - q_{\rm in} q_1\right) + \frac{J^2}{T_f} q_0 (1-q) \ . \tag{4.120}$$

Finally, let us consider the asymptotic behaviour of the dynamical equation for the correlation $Q(t,0)$ (Eq. (4.80c)). By repeating the same approximations as above one gets the following relation,

$$z_f q_1 = \frac{JJ_0}{T'}\left(q_{\rm in} q_0 - (1-2q_{\rm in}) q_1\right) + \frac{J^2}{T_f} q_1 (1-q) \ . \tag{4.121}$$

By using together Eqs. (4.112), (4.118), (4.120) and (4.121), (together with the FDT assumption $\chi_{\rm st} = (1-q)/T_f$) one can determine the values of the constants z_f, q, q_0 and q_1. If one assumes that $q = 0$, then one obtains

$$q_0 = q_1 = 0 \quad \text{and} \quad z_f = T + J^2/T_f \quad ,$$

that is to say, the "final" state is an equilibrium state in the paramagnetic phase. On the other hand, if $q > 0$ and under the assumption $q_0 = q_1 > 0$ one finds that

$$q = 1 - \frac{T_f}{J} \quad \text{and} \quad z_f = 2J \quad ,$$

as in an equilibrium condensed state at temperature T_f.

4.3.2.1 *Final temperature under the equilibrium assumption*

It is actually very easy to derive a relation between T_f and the parameters that control the quench dynamics, $x = J/J_0$ and $y = T'/J_0$, under the only assumption that the system is asymptotically approaching Gibbs-Boltzmann equilibrium. In fact, if one assumes that

$$e^f_{\rm pot} = \lim_{t\to+\infty} e_{\rm pot}(t) = e^{\rm pot}_{\rm eq}(T_f) = -\frac{J^2}{2T_f}(1-q^2) \ , \tag{4.122a}$$

$$e^f_{\rm kin} = \lim_{t\to+\infty} e_{\rm kin}(t) = e^{\rm kin}_{\rm eq}(T_f) = \frac{T_f}{2} \ , \tag{4.122b}$$

then, because of the conservation of energy in the post-quench dynamics, the following relation holds

$$\frac{T'}{2} - \frac{J_0 J}{2T'}\left(1 - q_{\rm in}^2\right) = \frac{T_f}{2} - \frac{J_0^2}{2T_f}\left(1 - q^2\right) \ . \tag{4.123}$$

If the *final* state is paramagnetic ($T_f/J \geq 1$), then we should impose $q = 0$ and from the above equation one obtains then

$$\frac{T_f}{J} = \frac{1}{2y}\left\{\frac{y^2}{x} - 1 + q_{\rm in}^2 + \sqrt{\left(\frac{y^2}{x} - 1 + q_{\rm in}^2\right)^2 + 4y^2}\right\} \ , \tag{4.124}$$

where $q_{\rm in}(y) = 0$ if $y \geq 1$, while $q_{\rm in}(y) = 1 - y$ if $y < 1$. Instead, if the system reaches an equilibrium state in the condensed phase ($T_f/J < 1$), we should have $q = 1 - T_f/J$ and thus

$$\frac{T_f}{J} = 1 + \frac{y}{2x} - \frac{1}{2y}\left(1 - q_{\rm in}^2\right) \ . \tag{4.125}$$

In particular, if the initial state is paramagnetic, that is to say, $q_{\rm in} = 0$, then we have

$$\frac{T_f}{J} = 1 + \frac{y}{2x} - \frac{1}{2y} \ , \tag{4.126}$$

while, if the initial state is in the condensed phase, which means $q_{\rm in} = 1 - y$, then we have

$$\frac{T_f}{J} = \frac{y}{2}\left(1 + \frac{1}{x}\right) \ . \tag{4.127}$$

In order for this derivation to be consistent, we need to complement Eq. (4.124) with the condition $T_f/J > 1$, and Eq. (4.125) with the condition $T_f/J < 1$. Moreover, we also need to require that $T_f/J > 0$ in both cases. By imposing all of these conditions we find a particular line in the x-y parameter space, given by the following two-piece function

$$g_{\rm c}(x) \quad = \quad \begin{cases} \sqrt{x} & \text{for} \quad x \geq 1 \ , \\ \dfrac{2x}{x+1} & \text{for} \quad x \leq 1 \ , \end{cases} \tag{4.128}$$

for $x > 0$. For quenches such that $y > g_{\rm c}(x)$, Eq. (4.124) is satisfied (and not Eq. (4.125)) and thus, assuming the system reaches asymptotically an equilibrium state, this state should be paramagnetic. On the contrary, for quenches such that $y < g_{\rm c}(x)$, Eq. (4.125) is satisfied (and not Eq. (4.124)) and thus the system should reach an equilibrium state in the condensed phase. In terms of the energy change induced by the quench, the interpretation of these bounds is the following. Consider, as an example, a case in which the system starts from an equilibrium state in the condensed phase, that is to say, $y = T'/J_0 < 1$. Quenches such that $1 > x > y/(2-y)$ inject an amount of energy into the system which is not sufficient to make it approach a paramagnetic state in the long-time post-quench regime, thus it remains confined in the condensed phase. On the other hand, in the case of a paramagnetic initial condition ($y > 1$), quenches such that $1 < x < y^2$ do not extract enough energy for the system to reach an equilibrium state in the condensed phase.

From this simple analysis, it seems that the x-y parameter space is divided in just two regions. However, we are going to show by using the results obtained by numerically integrating the Schwinger-Dyson equations for the correlation, response function and Lagrange multiplier, that, apart from some exceptional cases, the system never reaches a stationary state with the properties of Gibbs-Boltzmann equilibrium, as stated above.

4.4 Dynamics of the finite-size system

In this Section we describe how the dynamics of a finite-size system can be solved by using the basis in which the interaction matrix is diagonalised, so that the system becomes effectively a collection of harmonic oscillators coupled only through the Lagrange multiplier. We show that these oscillators decouple under the assumption $z(t) \to z_f$ allowing for a simple approximate solution of the problem that can, however, be relevant for $N \to \infty$ only (otherwise, for finite N, $z(t)$ does not reach a constant).

Given a particular realization of the interaction matrix $\{J_{ij}\}$, for finite N, let $\lambda_1, \ldots, \lambda_N$ be its eigenvalues, in increasing order, and $\boldsymbol{v}_1, \ldots, \boldsymbol{v}_N$ the corresponding eigenvectors. If we denote by $s_\mu(t) = \boldsymbol{s}(t) \cdot \boldsymbol{v}_\mu$ the projection of the spin vector in the direction of the μ-th eigenvector of the interaction matrix, the N "rotated" equations of motion read

$$m\ddot{s}_\mu(t) + (z(t) - \lambda_\mu)s_\mu(t) = 0 \; . \tag{4.129}$$

This set of equations has to be complemented with the initial conditions $s_\mu(0)$ and $\dot{s}_\mu(0)$. They are very similar to the equations for a parametric oscillator, the difference being that, in our case, the time-dependent frequency depends on the variables themselves *via* the Lagrange multiplier.

Once the equations of motion for the s_μ are solved, we can recover the trajectories for $\boldsymbol{s}$ using $\boldsymbol{s}(t) = \sum_\mu s_\mu(t)\boldsymbol{v}_\mu$. In particular, the two-time autocorrelation function is given by

$$C_J(t_1, t_2) = \frac{1}{N}\sum_\mu \langle s_\mu(t_1)s_\mu(t_2)\rangle \; , \tag{4.130}$$

where the subscript J means that the result depends, in principle, on the particular realisation of the random interaction matrix $\{J_{ij}\}$, and the angular brackets represent an average over initial conditions. One could then perform the disorder average or analyse the self-averageness properties of the correlation in different time regimes. The dependence on the J_{ij} should disappear in the $N \to \infty$ limit.

At variance with the $N \to \infty$ approach, the finite size study allows one to access the details of the dynamics of each mode. In the following, we define some mode-observables that will provide valuable information. Of particular interest are the mode energies, given by

$$\epsilon_\mu^{\rm kin}(t) = \frac{m}{2}\langle \dot{s}_\mu^2(t)\rangle \; , \tag{4.131a}$$

$$\epsilon_\mu^{\rm pot}(t) = \frac{1}{2}(z(t) - \lambda_\mu)\langle s_\mu^2(t)\rangle \; , \tag{4.131b}$$

$$\epsilon_\mu^{\rm tot}(t) = e_\mu^{\rm kin}(t) + e_\mu^{\rm pot}(t) \; . \tag{4.131c}$$

Notice that in the analysis of the $N \to \infty$ model, we defined a potential energy density as $e_{\rm pot} = -1/(2N)\sum_\mu \lambda_\mu \langle\, s_\mu^2 \,\rangle$ (see Eq. (4.81b)), without the term proportional to $z(t)$. The values of these energies at $t = 0^-$ are given by the fact that all modes are in equilibrium at the same temperature:

$$\epsilon_\mu^{\rm tot}(0^-) = 2\epsilon_\mu^{\rm kin}(0^-) = 2\epsilon_\mu^{\rm pot}(0^-) = T' \; . \tag{4.132}$$

Immediately after the quench, they are given by

$$\epsilon_\mu^{\rm kin}(0^+) = \frac{m}{2}\langle \dot{s}_\mu^2(0^+)\rangle = \frac{T'}{2} \; , \qquad \epsilon_\mu^{\rm pot}(0^+) = \frac{T'}{2}\frac{z(0^+) - \lambda_\mu}{z(0^-) - \lambda_\mu^0} \; . \tag{4.133}$$

where $\lambda_1^0, \ldots, \lambda_N^0$ are the eigenvalues of the pre-quench interaction matrix.

In order to study the eventual thermalisation of the system, we can define an effective time-dependent mode temperature through the total mode energy

$$T_\mu(t) \equiv \epsilon_\mu^{\rm tot}(t) \tag{4.134}$$

based on the fact that the modes are (quasi) decoupled. Whenever the system enters a stationary regime in which $z(t)$ is constant, see Sec. 4.4.3, the mode temperatures T_μ are independent of time, since the system behaves as a collection of non-coupled harmonic oscillators. We can also define mode temperatures by taking the time-average of the kinetic and potential mode energies over a certain interval,

$$\overline{T}_\mu^{\rm kin,pot} \equiv \frac{1}{2} \lim_{\tau \gg 1} \frac{1}{\tau} \int_{t_{\rm st}}^{t_{\rm st}+\tau} dt' \, e_\mu^{\rm kin,pot}(t') \; . \tag{4.135}$$

where $t_{\rm st}$ is the time required for the system to reach the stationary regime.

Other useful observables are the time-delayed mode correlation functions

$$C_\mu(t_1, t_2) = \langle s_\mu(t_1) s_\mu(t_2) \rangle \tag{4.136}$$

and the mode linear response functions

$$R_\mu(t_1, t_2) = \left. \frac{\delta \langle s_\mu(t_1) \rangle_h}{\delta h_\mu(t_2)} \right|_{h_\mu \to 0} \tag{4.137}$$

which are computed by adding an external field h_μ linearly coupled to the mode s_μ, for each μ (the brackets $\langle \cdot \rangle_h$ indicate the average over the initial conditions in presence of the external field).

4.4.1 Formal solution of the mode dynamics

One possible approach to solve the dynamics of each mode starting from canonical equilibrium initial conditions is to take a large ensemble of initial configurations drawn from the Gibbs-Boltzmann distribution, numerically integrate the Newton equations Eq. (4.129) for each initial condition, and then calculate the observables averaging over the trajectories corresponding to the different initial states. Such approach is feasible but computationally very demanding. In this Section we describe a more convenient method to solve the dynamics for each mode that heavily uses the tools developed to treat a paradigmatic problem in classical mechanics, the one of *parametric oscillators* [132, 133].

In order to solve Eq. (4.129) we propose an amplitude-phase *Ansatz* [132, 133, 134]

$$s_\mu(t) = \frac{A}{\sqrt{\Omega_\mu(t)}} \exp\left[-i \int_0^t dt' \, \Omega_\mu(t') \right] . \tag{4.138}$$

Inserting this *Ansatz* in the μth mode Newton equation, we obtain an equation for the mode and time dependent auxiliary function $\Omega_\mu(t)$,

$$\frac{1}{2} \frac{\ddot{\Omega}_\mu(t)}{\Omega_\mu(t)} - \frac{3}{4} \left(\frac{\dot{\Omega}_\mu(t)}{\Omega_\mu(t)} \right)^2 + \Omega_\mu^2(t) = \omega_\mu^2(t) \; , \tag{4.139}$$

where $\omega_\mu^2(t) \equiv (z(t) - \lambda_\mu)/m$. The last equation has to be complemented by the initial values $\Omega_\mu(0)$ and $\dot{\Omega}_\mu(0)$. If we choose

$$\dot{\Omega}_\mu(0) = 0 \,, \tag{4.140}$$

we find that the projection of the spin configuration is

$$s_\mu(t) = s_\mu(0)\sqrt{\frac{\Omega_\mu(0)}{\Omega_\mu(t)}}\,\cos\left(\int_0^t dt'\,\Omega_\mu(t')\right) + \frac{\dot{s}_\mu(0)}{\sqrt{\Omega_\mu(t)\Omega_\mu(0)}}\,\sin\left(\int_0^t dt'\,\Omega_\mu(t')\right), \tag{4.141}$$

which is reminiscent of the general solution of the harmonic oscillator problem, here with a time-dependent "frequency" $\Omega_\mu(t)$.

We still have to specify the initial condition for $\Omega_\mu(0)$. A possible choice is given by

$$m\;\Omega_\mu^2(0) = z(0) - \lambda_\mu \tag{4.142}$$

that enforces $\ddot{\Omega}_\mu(0) = 0$ [134]. However, this choice is consistent with real $\Omega_\mu(t)$ only if $z(0) - \lambda_\mu \geq 0$, which is verified uniquely for $J \leq J_0$, *i.e.* uniquely for energy injection. An initial condition ensuring real and positive $\Omega_\mu(t)$ for all μ for any quench is

$$\Omega_\mu^2(0) = \lambda_N - \lambda_\mu \,. \tag{4.143}$$

We choose this initial condition for the numerical calculations.

In order to solve for $\Omega_\mu(t)$ we consider the equal-times mode correlation function

$$\begin{aligned} C_\mu(t,t) \equiv \langle s_\mu^2(t)\rangle = \langle s_\mu^2(0)\rangle\,\frac{\Omega_\mu(0)}{\Omega_\mu(t)}\,\cos^2\left(\int_0^t dt'\,\Omega_\mu(t')\right) + \frac{\langle \dot{s}_\mu^2(0)\rangle}{\Omega_\mu(0)\Omega_\mu(t)}\,\sin^2\left(\int_0^t dt'\,\Omega_\mu(t')\right) \\ + \frac{\langle s_\mu(0)\dot{s}_\mu(0)\rangle}{\Omega_\mu(t)}\,\sin\left(\int_0^t dt'\,\Omega_\mu(t')\right)\cos\left(\int_0^t dt'\,\Omega_\mu(t')\right) \,, \end{aligned} \tag{4.144}$$

in terms of which we write the potential energy as

$$e_{\rm pot}(t) = -\frac{1}{2N}\sum_\mu \lambda_\mu C_\mu(t,t) \,. \tag{4.145}$$

Replacing this equation in $z(t) = 2e_f - 4e_{\rm pot}(t)$, we find an expression for the Lagrange multiplier as a function of the mode correlations at equal times

$$z(t) = 2e_f + \frac{2}{N}\sum_\mu \lambda_\mu C_\mu(t,t) \,. \tag{4.146}$$

Finally, we note that the system conformed by Eqs. (4.139), (4.144) and (4.146) is closed and allows one to find the time evolution of the Lagrange multiplier and the auxiliary functions $\Omega_\mu(t)$. This set of equations is amenable to numerical integration. Once we obtain $\Omega_\mu(t)$, the most interesting observables can be calculated using the general solution in the form given in Eq. (4.138). The advantage of this method is that we do not need to draw initial states $\{s_\mu(0), \dot{s}_\mu(0)\}$ but we only have to specify the initial averages $\langle s_\mu^2(0)\rangle$ and $\langle \dot{s}_\mu^2(0)\rangle$.

4.4.2 Initial conditions: equilibrium averages for finite N

In this Section we address the calculation of equilibrium averages at finite N in order to provide suitable initial conditions for the numerical integration of the mode dynamics explained in the previous Section.

If we were to naively integrate the mode equations, we would need to draw initial vectors, $\boldsymbol{s}(0) = (s_1(0), \ldots, s_N(0))$ and $\dot{\boldsymbol{s}}(0) = (\dot{s}_1(0), \ldots, \dot{s}_N(0))$, mimicking an initial thermal state at finite temperature, be it $T' > T_{0,c} = J_0$ or $T' < T_{0,c} = J_0$, for a given realisation of the $N \times N$ interaction matrix. Averages over these initial states of the interesting observables should then be computed. This method is computationally expensive as a large number of samples of the initial condition should be drawn to get smooth and reliable results. Instead, the numerical method that was explained in the previous Section is such that only the averages $\langle\, s_\mu^2(0)\,\rangle_{\rm eq}$ and $\langle\, \dot{s}_\mu^2(0)\,\rangle_{\rm eq}$ are needed as input for the initial conditions. We then focus on determining these averages in a finite size system in equilibrium.

The canonical equilibrium probability density of the configuration $\{p_\mu = m\dot{s}_\mu, s_\mu\}$ at temperature T', for a given realization of disorder, is

$$P_{\rm GB}(\{p_\mu, s_\mu\}) = \frac{1}{Z} \exp\left[-\frac{1}{T'} \sum_\mu \frac{p_\mu^2}{2m} - \frac{1}{T'} \sum_\mu (z_{\rm eq}^{(N)} - \lambda_\mu^0) s_\mu^2 \right], \tag{4.147}$$

with Z the partition function. The quadratic averages of the velocities are thus simply given by

$$\langle\, \dot{s}_\mu^2 \,\rangle_{\rm eq} = \frac{T'}{m} \qquad \forall \mu,\, N\,, \tag{4.148}$$

just as for the infinite N case, and the initial conditions will be $\langle\, \dot{s}_\mu^2(0^+)\,\rangle = \langle\, \dot{s}_\mu^2 \,\rangle_{\rm eq}$.

As long as the equilibrium value of the Lagrange multiplier be strictly larger than the largest eigenvalue, $z_{\rm eq}^{(N)} > \lambda_{\rm max}^0 = \lambda_N^0$, the weight of the coordinates s_μ are well-defined independent Gaussians. We will see that the self-consistent solution complies with this bound. Relying on the spherical constraint being imposed by the Lagrange multiplier, we obtain

$$\langle\, s_\mu^2 \,\rangle_{\rm eq} = \frac{T'}{z_{\rm eq}^{(N)} - \lambda_\mu^0} \qquad \forall \mu, N\,. \tag{4.149}$$

The difference between the two equilibrium phases will be codified in the value of $z_{\rm eq}^{(N)}$, which can be obtained as the solution of the spherical constraint equation

$$\sum_{\mu=1}^{N} \langle s_\mu^2 \rangle_{\rm eq} = \sum_{\mu=1}^{N} \frac{T'}{z_{\rm eq}^{(N)} - \lambda_\mu^0} = N\,. \tag{4.150}$$

We solved this equation numerically to determine $z_{\rm eq}^{(N)}$ and we found that the solution turns out to be always greater than $\lambda_{\rm max}^0$, for any value of the temperature and finite N, and for typical realisations of the interaction matrix. In Fig. 4.1-(a) we show $z_{\rm eq}^{(N)}$ as a function of temperature for three values of N, and a single realisation of the random interaction matrix in each case. At high temperatures all the curves collapse (on the scale of the figure) on the paramagnetic curve $z_{\rm eq} = T' + J_0^2/T'$, irrespective of the system size. At low temperatures (inset), $z_{\rm eq}^{(N)}$ is always larger than $\lambda_{\rm max}^0$ and, as expected, the difference between them decreases with the system size.

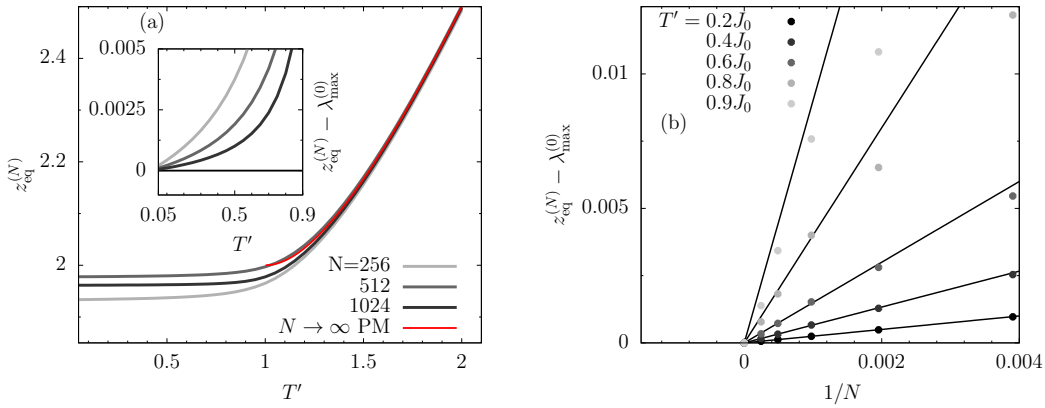

Figure 4.1: **Equilibrium properties of the finite-N system.** (a) Equilibrium Lagrange multiplier at finite N. We show the numerical solution to Eq. (4.150), as a function of the temperature T', using one particular realisation of the disorder, for different values of N. The non-monotonic N-dependence of the plateau is of the order of magnitude of the variation with N of the largest eigenvalue. Inset: difference between the Lagrange multiplier and the largest eigenvalue of the interaction matrix in the condensed region as a function of temperature. The trend is now monotonic in N. (b) System size scaling of the Lagrange multiplier in the condensed phase. We show the difference between the Lagrange multiplier, as obtained from the solution to Eq. (4.150), and the largest eigenvalue of the interaction matrix as a function of $1/N$ for different system sizes, using one particular realization of disorder for each size. The dashed lines are $T'/(Nq_{\rm in})$, with $q_{\rm in} = 1 - T'/J_0$ the value of the self-overlap in the $N \to \infty$ limit.

Once the finite size Lagrange multiplier is obtained, we replace it in Eq. (4.149) to obtain the initial conditions $\langle\, s_\mu^2(0^+)\,\rangle$ for the mode dynamics. To gain insight into the scaling of $z_{\rm eq}^{(N)}$ with the system size N, in Fig. 4.1-(b) we plot the difference between $z_{\rm eq}^{(N)}$ and $\lambda_{\rm max}^0$ for temperatures in the condensed phase as a function of $1/N$. The straight dashed lines have slope $T'/q_{\rm in}$, where $q_{\rm in} = 1 - T'/J_0$ is the $N \to \infty$ value of the self-overlap. For temperatures sufficiently below the transition, the finite-size data, obtained for one particular realisation of the random matrix J_{ij}, match pretty accurately the infinite-size results. For temperatures close to the transition, there appear deviations for the smallest system sizes (largest $1/N$). In conclusion, we find that for large system sizes or temperatures not too close to the transition, the solution to Eq. (4.150) behaves as

$$z_{\rm eq}^{(N)} \simeq \lambda_{\rm max}^0 + \frac{T'}{N q_{\rm in}} \quad , \qquad T' < J_0 \; . \tag{4.151}$$

Based on this, we define a finite size version of the equilibrium self-overlap

$$q_{\rm in}^{(N)} \equiv \frac{T'}{N(z_{\rm eq}^{(N)} - \lambda_N^0)} \; , \tag{4.152}$$

which is non-zero if the highest mode is macroscopically populated. In Fig. 4.2-(a) we show $q_{\rm in}^{(N)}$ as a function of temperature, for a single realisation of the interaction matrix. We can observe the convergence of the finite size results towards the $N \to \infty$ predictions as the system size is increased.

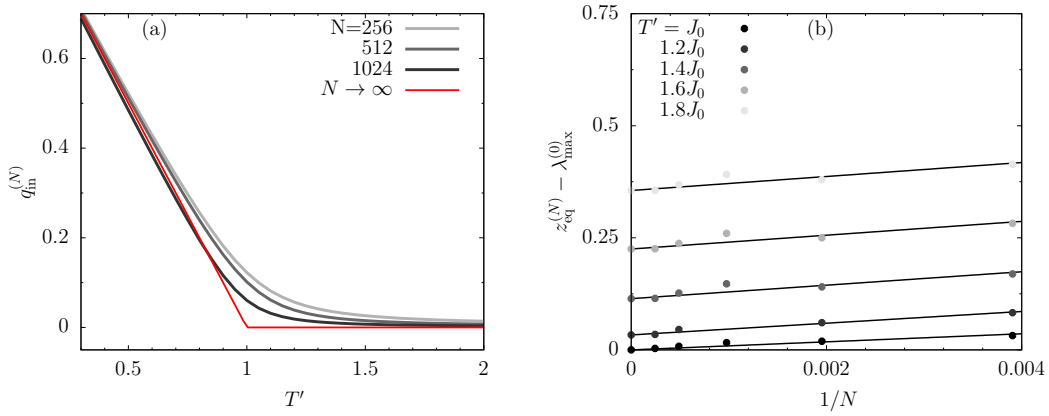

Figure 4.2: **Equilibrium properties of the finite-N system.** (a) Equilibrium $q_{\rm in}$ at finite N, as a function of the temperature T', using one particular realization of the disorder. Finite-N corrections are more significant near the transition ($T' = J_0 = 1$). (b) System size scaling of the Lagrange multiplier in the paramagnetic phase. Difference between the Lagrange multiplier, as obtained from the solution of Eq. (4.150), and the largest eigenvalue of the interaction matrix as a function of $1/N$ for different system sizes, using one particular realisation of disorder for each size. The non-vanishing value at $1/N \ll 1$ corresponds to $z_{\rm eq}^{(N\to\infty)} - 2J_0$.

We have also investigated the finite N corrections to $z_{\rm eq}^{(N)}$ in the paramagnetic phase, $T' > J_0$. We find that a linear scaling in $1/N$ also applies here, but the value of $z_{\rm eq}^{(N)} - \lambda_{\rm max}^0$ at $N \to \infty$ does not vanish and it is given instead by $T' + J_0^2/T' - 2J_0$, as expected. We find approximately,

$$z_{\rm eq}^{(N)} - \lambda_{\rm max}^0 \simeq z_{\rm eq}^{(N\to\infty)} - 2J_0 + \frac{c}{N} \quad , \tag{4.153}$$

with c some constant, see Fig. 4.2-(b).

Let us now compute the finite-N equilibrium values of the kinetic and potential energy densities before and after the quench, using the finite size averages for $\langle\, s_\mu^2 \,\rangle_{\rm eq}$ and $\langle\, \dot{s}_\mu^2 \,\rangle_{\rm eq}$ proposed above, and compare them with the equilibrium $N \to \infty$ results obtained in Sec. 4.3.1. The kinetic energy right before the quench is given by

$$e_{\rm kin}^{(N)}(0^-) = \frac{m}{2N} \sum_{\mu=1}^{N} \langle\, \dot{s}_\mu^2 \,\rangle_{\rm eq} = \frac{T'}{2} \quad , \tag{4.154}$$

which coincides with the infinite-N result. The pre-quench potential energy instead reads

$$e_{\rm pot}^{(N)}(0^-) = -\frac{1}{2N} \sum_{\mu=1}^{N} \lambda_\mu^0 \langle\, s_\mu^2 \,\rangle_{\rm eq} = -\frac{T'}{2N} \left(\sum_{\mu=1}^{N} \frac{\lambda_\mu^0 - z_{\rm eq}^{(N)}}{z_{\rm eq}^{(N)} - \lambda_\mu^0} + z_{\rm eq}^{(N)} \sum_{\mu=1}^{N} \frac{1}{z_{\rm eq}^{(N)} - \lambda_\mu^0} \right) = \frac{T'}{2} - \frac{z_{\rm eq}^{(N)}}{2} \tag{4.155}$$

where we used Eq. (4.150). In the equilibrium condensed phase we can rely on $z_{\rm eq}^{(N)} = \lambda_{\rm max}^0 + T'/(N q_{\rm in}^{(N)})$ to obtain

$$e_{\rm pot}^{(N)}(0^-) = -\frac{\lambda_{\rm max}^0}{2} + \frac{T'}{2} - \frac{T'}{2N q_{\rm in}^{(N)}} \, . \tag{4.156}$$

The $N \to \infty$ result is $e_{\rm pot}(0^-) = -J_0 + T'/2$, consistent with Eq. (4.156), since $\lim_{N\to\infty} \lambda^0_{\rm max} = 2J_0$. In the paramagnetic phase $q^{(N)}_{\rm in} \ll 1$ and the third term in Eq. (4.156) induces important corrections. In this case, using Eq. (4.153) we can write

$$e^{(N)}_{\rm pot}(0^-) \simeq -\frac{J_0^2}{2T'} - \left(\frac{\lambda^0_{\rm max}}{2} - J_0\right) - \frac{c}{2N} \tag{4.157}$$

and one readily recovers the $N \to \infty$ limit $e_{\rm pot}(0^-) = -J_0^2/(2T')$.

In order to compute the values of the kinetic and potential energy densities immediately after the quench, we just need to consider the transformation $\lambda^0_\mu \mapsto \lambda_\mu = (J/J_0)\lambda^0_\mu$ for all μ, since we are dealing with a uniform quench of the random couplings. The kinetic energy is not affected by the quench in the interaction and, just as in the $N \to \infty$ limit (see Sec. 4.3.1), we have that

$$e^{(N)}_{\rm kin}(0^+) = e^{(N)}_{\rm kin}(0^-) = \frac{T'}{2} \, . \tag{4.158}$$

For the potential energy it is enough to note that

$$e^{(N)}_{\rm pot}(0^+) = -\frac{1}{2N}\sum_{\mu=1}^{N} \lambda_\mu \langle\, s^2_\mu \,\rangle_{\rm eq} = -\frac{1}{2N}\frac{J}{J_0}\sum_{\mu=1}^{N} \lambda^0_\mu \langle\, s^2_\mu \,\rangle_{\rm eq} = \frac{J}{J_0} e^{(N)}_{\rm pot}(0^-) \, . \tag{4.159}$$

Using that $z^{(N)}(0^+) = 2(e^{(N)}_{\rm kin}(0^+) - e^{(N)}_{\rm pot}(0^+)) = T' - 2J/J_0\, e^{(N)}_{\rm pot}(0^-)$ it is now easy to find the initial value of the Lagrange multiplier. When the initial conditions are taken from the condensed phase, we can write

$$z^{(N)}(0^+) = \lambda_{\rm max} + T'\left(1 - \frac{J}{J_0}\right) + \frac{JT'}{NJ_0 q^{(N)}_{\rm in}} \, . \tag{4.160}$$

For initial states in the paramagnetic phase, instead we have

$$z^{(N)}(0^+) \simeq \frac{JJ_0}{T'} + T' + (\lambda_{\rm max} - 2J) + \frac{J}{J_0}\frac{c}{N} \, . \tag{4.161}$$

4.4.3 Behaviour under stationary conditions

Let us assume that the system reaches stationarity and that the Lagrange multiplier approaches a constant

$$\lim_{t\to\infty} z(t) = z_f \, . \tag{4.162}$$

Moreover, we suppose that most of the evolution of $z(t)$ occurs in a finite time $t_{\rm st}$, that is to say, we assume we can make the approaximation $z(t) \simeq z_f$ for $t > t_{\rm st}$. The equation of motion of each mode, for $t \gg t_{\rm st}$, then becomes

$$m\ddot{s}_\mu(t) + (z_f - \lambda_\mu)s_\mu(t) = 0 \tag{4.163}$$

and can be thought of as Newton's equation for the mode Hamiltonian

$$H_\mu = \frac{1}{2}m\dot{s}^2_\mu + \frac{1}{2}m\omega^2_\mu s^2_\mu \tag{4.164}$$

with $\omega_\mu^2 \equiv (z_f - \lambda_\mu)/m$, *i.e.* a simple harmonic oscillator. This equation has three types of solutions depending on the sign of ω_μ^2:

$$\omega_\mu^2 > 0\,, \qquad s_\mu(t) = s_\mu(t_{\rm st})\cos\left[\omega_\mu(t-t_{\rm st})\right] + \frac{\dot s_\mu(t_{\rm st})}{\omega\mu}\sin\left[\omega_\mu(t-t_{\rm st})\right]\ , \tag{4.165a}$$

$$\omega_\mu^2 = 0\,, \qquad s_\mu(t) = s_\mu(t_{\rm st}) + \dot s_\mu(t_{\rm st})(t-t_{\rm st})\ , \tag{4.165b}$$

$$\omega_\mu^2 < 0\,, \qquad s_\mu(t) = s_\mu(t_{\rm st})\cosh\left(|\omega_\mu|(t-t_{\rm st})\right) - \frac{\dot s_\mu(t_{\rm st})}{|\omega_\mu|}\sinh\left(|\omega_\mu|(t-t_{\rm st})\right)\ , \tag{4.165c}$$

that is to say, oscillatory solutions with constant amplitude in the first case, diffusive behaviour in the intermediate case, and exponentially diverging solutions in the last case. We insist upon the fact that the reference time is taken to be $t_{\rm st}$, the time needed to reach the stationary state.

If the Lagrange multiplier approaches, then, a value that is larger than λ_N, all modes oscillate indefinitely. In Gibbs-Boltzmann equilibrium in the PM phase, $z_{\rm eq} > \lambda_N$ and such a fully oscillating behaviour is expected. In equilibrium in the low-temperature (condensed) phase $z_{\rm eq} = \lambda_{\rm max} = \lambda_N$ for $N \to \infty$ and the $\mu = N$ mode should grow linearly in time while all other modes should oscillate with frequency $\omega_\mu = \sqrt{(z_f - \lambda_\mu)/m}$. The amplitude of each mode is determined by the initial conditions, that are actually matching conditions at time $t_{\rm st}$, the time at which stationarity is reached. For finite N, one finds a more complicated scenario. In fact, we recall that the spacing between the largest eigenvalue and the second largest one of a Gaussian symmetric matrix, $\lambda_N - \lambda_{N-1}$, scales as $N^{-2/3}$ [99]. This means that, under the assumption $z_f \to \lambda_N$, $z_f - \lambda_{N-1} \sim N^{-2/3}$ and one should expect the existence of *almost diffusive* modes close to the largest one, in the large N limit. However, the simulations at finite N show that for finite N, z_f is almost always greater than λ_N and thus all modes are oscillatory. Even for "condensed-type" dynamics, z_f is greater than λ_N, although very close to it.

As expected from Birkhoff's theorem [135], the long-time averages, say taken after $t_{\rm st}$, should be constant and one can expect them to be equal to half the total energy,

$$\overline{\epsilon_\mu^{\rm kin}} = \overline{\epsilon_\mu^{\rm pot}} = \frac{1}{2}\epsilon_\mu^{\rm tot} = \frac{1}{4}m\omega_\mu^2 s_\mu(t_{\rm st})^2 + \frac{1}{4}m[\dot s_\mu(t_{\rm st})]^2\ . \tag{4.166}$$

If one now associates a temperature to these values, arguing equipartition of quadratic degrees of freedom, one has $T_\mu = 2\overline{\epsilon_\mu^{\rm kin}} = 2\overline{\epsilon_\mu^{\rm pot}} = \epsilon_\mu^{\rm tot}$. Thus, the mode temperatures depend on the averages at the end of the transient, and on the mode frequencies given by $\omega_\mu^2 = (z_f - \lambda_\mu)/m$, which depend on the asymptotic limit of the Lagrange multiplier z_f and the eigenvalues λ_μ.

In the argument above we implicitly assumed that ω_μ^2 does not vanish. The case $\mu = N$ is tricky. If one naively sets ω_μ^2 to zero from the outset, then $2\epsilon_N^{\rm pot} = \omega_\mu^2\langle s_N^2\rangle$ apparently vanishes as $N \to +\infty$. The correct way of treating the largest mode is to remember that the projection on it condenses and that $\langle s_N^2\rangle$ is proportional to N. This will ensure that $\lim_{N\gg 1}\langle s_N^2\rangle \propto N$, in such a way that $\lim_{N\to\infty}\omega_\mu^2\langle s_N^2\rangle = 2\overline{\epsilon_\mu^{\rm kin}}$, similarly to what happens in equilibrium at a temperature T, where $\langle s_N^2\rangle = q_{\rm EA}N$ and the Lagrange multiplier is such that $(z_{\rm eq} - \lambda_N)q_{\rm EA}N = T$.

Let us now make a brutal approximation in which we assume that the asymptotic value z_f is reached instantaneously after the quench, that is $z(0^+) \simeq z_f$ (or in other words, $t_{\rm st} \simeq 0$), so that we can use

$$\langle \dot s_\mu^2(0^+)\rangle \approx\ \omega_\mu^2\langle s_\mu^2(0^+)\rangle \approx \frac{T'}{m} \tag{4.167}$$

instead of the unknown values at the end of the transient regime, $\langle \dot{s}_\mu^2(t_{\rm st})\rangle$ and $\omega_\mu^2\langle s_\mu^2(t_{\rm st})\rangle$. Under this assumption the "final" (*i.e.* post-quench) mode temperatures are given by

$$T_\mu^f \equiv 2\overline{e_\mu^{\rm pot}} = 2\overline{e_\mu^{\rm kin}} = \frac{T'}{2}\left(\frac{\omega_\mu^2}{\omega_{0\,\mu}^2}+1\right) = \frac{T'}{2}\left(\frac{z_f-\lambda_\mu}{z_{\rm eq}(T',J_0)-\lambda_\mu^0}+1\right) . \tag{4.168}$$

with $\overline{e_\mu^{\rm kin}}$ and $\overline{e_\mu^{\rm pot}}$ the time-averaged values of kinetic and potential mode energies, respectively, defined in Eq. (4.135). This relation can be easily obtained for a potential energy quench of the simple harmonic oscillator, see App. D.1 for details.

We would like to know which is the condition satisfied by z_f under this approximation. We note that the time-dependent spherical constraint imposes that

$$\sum_{\mu=1}^N \langle s_\mu^2(t)\rangle = N . \tag{4.169}$$

which implies that

$$\sum_{\mu=1}^N \overline{\langle s_\mu^2(t)\rangle} = N , \tag{4.170}$$

where $\overline{\langle s_\mu^2(t)\rangle}$ denotes the average over time of $\langle s_\mu^2(t)\rangle$ in the stationary regime ($t > t_{\rm st}$). Inserting the independent harmonic oscillator approximation in the above equation, we find an equation for z_f

$$\frac{T'}{2m}\sum_{\mu=1}^N (\omega_\mu)^{-2}\left[\left(\frac{\omega_\mu}{\omega_\mu^0}\right)^2+1\right] = \frac{T'}{2}\sum_{\mu=1}^N\left[\frac{1}{z_{\rm eq}(T',J_0)-\lambda_\mu^0}+\frac{1}{z_f-\lambda_\mu}\right] = N . \tag{4.171}$$

Since $z_{\rm eq}(T',J_0)$ satisfies the constraint

$$\sum_{\mu=1}^N \frac{T'}{z_{\rm eq}-\lambda_\mu^0} = N , \tag{4.172}$$

we find the following equation for z_f,

$$\sum_{\mu=1}^N \frac{T'}{z_f-\lambda_\mu} = N . \tag{4.173}$$

In other words, under this approximation, z_f is equal to the equilibrium Lagrange multiplier for a system in equilibrium at temperature T' with respect to a disorder strength J. In the $N\to\infty$ limit, we thus have $z_f = 2J$ if $T' < J$ and $z_f = T' + J^2/T'$ if $T' > J$.

We will put these predictions to the test in Sec. 4.5 using the numerical solution to the finite-N equations of motion for the spin degrees of freedom. We will find that, in various regions of the parameter space, this *a priori* brutal approximation is in strikingly good agreement with the numerical data.

4.5 Numerical results

This Section summarises what we found numerically by solving the $N\to\infty$ Schwinger-Dyson equations that couple the two-time autocorrelation and linear response function (Eqs. (4.80a)-(4.80d)), and the equation of motions for the mode projections s_μ, in the finite N case (Eqs. (4.139), (4.144) and (4.146) together).

The finite N results are consistent with the infinite N ones and help us understanding the mechanism whereby the dynamics takes place. We first present a description of the dynamical phase diagram and a summary of the behaviour of the various observables in each sector of this diagram. Later, we give further details on the dynamics at constant energy (no quench) and in each of the dynamical phases identified after a quench.

We will make a special effort to show, in each case considered, that an asymptotic state characterised by the single temperature T_f, obtained from the naive asymptotic analysis presented in Sec. 4.3.2, is almost never attained. The investigations that lead to this conclusion are very instructive not only because they prove the lack of Gibbs-Boltzmann equilibrium but also because they lead to the evaluation of the mode temperatures. We will see that a state with a single T_f characterising the fluctuation-dissipation relation is reached numerically in the following two cases only:

- the no quench-dynamics, *i.e.* $x = J/J_0 = 1$;
- quenches for which the special relation $y = \sqrt{x}$ holds, for $y = T'/J_0 > 1$.

In all other cases no equilibrium results *à la* Gibbs-Boltzmann are found for the global observables (correlation function, linear response function, kinetic and potential energies) but a different statistical description, of a generalised kind, should be adopted. We recall that in the case of the p-spin spherical model with $p \geq 3$ the behaviour is very different [83]. On the one hand, equilibrium towards a proper paramagnetic state, and within confining metastable states, were reached in two sectors of its dynamic phase diagram. On the other hand, an ageing asymptotic state in a tuned regime of parameters was also found. In the $p = 2$ model instead, we do not find any choice of parameters that yields an ageing asymptotic state.

In all the cases that we are going to show, we have set $J_0 = 1$ and $m = 1$, unless otherwise stated. The Schwinger-Dyson equations for the two-time correlations, linear response function and the Lagrange multiplier were integrated by using a Runge-Kutta method. A time step of order $\delta t \simeq 0.001$ was sufficient to assure numerical convergence of our results. In the integration of the finite N problem we used a similar method but found a weak dependence on δt. Nevertheless, a time step $\delta t = 0.001$ gave acceptable results.

4.5.1 The phase diagram

In the following we show the phase diagram determined by the value of the static susceptibility, $\chi_{\rm st}$, and by the value of the asymptotic value of the Lagrange multiplier, z_f, both obtained by solving numerically either the Schwinger-Dyson equations for the correlation and response functions (for the $N \to +\infty$ case) or the equations of motion for the spin variables in the finite N case. We determine their values through the variation of the parameter J/J_0, for fixed T'/J_0. In the phase diagram presented in Fig. 4.5 and the ensuing discussion we call $y = T'/J_0$ the vertical axis and $x = J/J_0$ the horizontal one. The former determines the initial state and the latter the kind of quench performed with injection of energy for $x < 1$, and extraction of energy for $x > 1$.

In Fig. 4.3 we show the value of the zero-frequency linear response, or static susceptibility, $\chi_{\rm st} = \lim_{t_2 \gg 1} \int_0^{+\infty} {\rm d}\tau R(t_2 + \tau, t_2)$, with $R(t_1, t_2)$ obtained from the numerical integration of the $N \to \infty$ Schwinger-Dyson equations. We plot T' $\chi_{\rm st}$ against J/T', and we observe

approximately the following behaviour,

$$T'\ \chi_{\rm st} \simeq \begin{cases} 1 & \text{for } \frac{T'}{J} \geq 1 \\ T'/J & \text{for } \frac{T'}{J} < 1 \end{cases} \ . \tag{4.174}$$

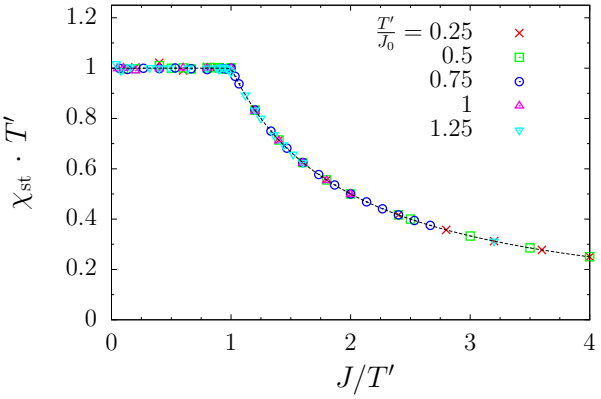

Figure 4.3: **The zero-frequency linear response**, $\chi_{\rm st} = \lim_{t_2 \gg 1} \int_0^{+\infty} {\rm d}\tau R(t_2+\tau, t_2)$ computed from $R(t_1, t_2)$ obtained by numerically integrating the Schwinger-Dyson dynamical equations, for several choices of initial conditions given in the key, with both $y < 1$ (condensed) and $y > 1$ (paramagnetic) cases, together with the curve given in Eq. (4.174), plotted with a dashed line.

The change in the behaviour of $\chi_{\rm st}$ at the point $J/T' = 1$ is accompanied by a change in the asymptotic value of z. This fact is shown in Fig. 4.4, where we present the data relative to z_f, estimated numerically both in the $N \to \infty$ case and the finite N case (panels (a) and (b), respectively), as a function of the quench parameter $x = J/J_0$. For $x < y$, the numerically estimated $z_f(x)$ in the case $N \to \infty$, for fixed y, were fitted with the polynomial $f(x) = a\,x^2 + b\,x + c$. We obtained very good results with $a \simeq 1/y$, $b \simeq 0$ and $c \simeq y$ (the precision of the fit is very high in terms of reduced χ^2). These results strongly suggest the following dependence of z_f on the parameters x and y,

$$z_f(x,y) \ = \ J_0 \begin{cases} \dfrac{x^2}{y} + y & \text{for } \ x \leq y \ , \\ 2\,x & \text{for } \ x \geq y \ . \end{cases} \tag{4.175}$$

The analysis of the finite N data was done along the same lines, see Fig. 4.4-(b), with the difference that the data for $x < y$ were fitted by $T' + \lambda_{\rm max}^2/(4T')$ and those for $x > y$ with $J\lambda_{\rm max}$, with $\lambda_{\rm max} = \lambda_N$ the largest eigenvalue of the post-quench interaction matrix, finding again very good agreement. (We found an appreciable deviation in the fit for $x > y$ had we used $2J$ instead of $J\lambda_{\rm max}$. Regarding the results for $x < y$ we could have used $T' + J^2/T'$ with a similar quality for the fit.)

It seems thus that there exists a "critical" line in the x-y parameter space, corresponding to the points $x = y$. This result somehow contradicts the asymptotic analysis performed in Sec. 4.3.2, where we found that a transition from a paramagnetic equilibrium final state to a condensed equilibrium final state occurs on the line

$$g_{\rm c}(x) \ = \ \begin{cases} \sqrt{x} & \text{for } \ x \geq 1 \ , \\ \dfrac{2x}{x+1} & \text{for } \ x \leq 1 \ . \end{cases} \tag{4.176}$$

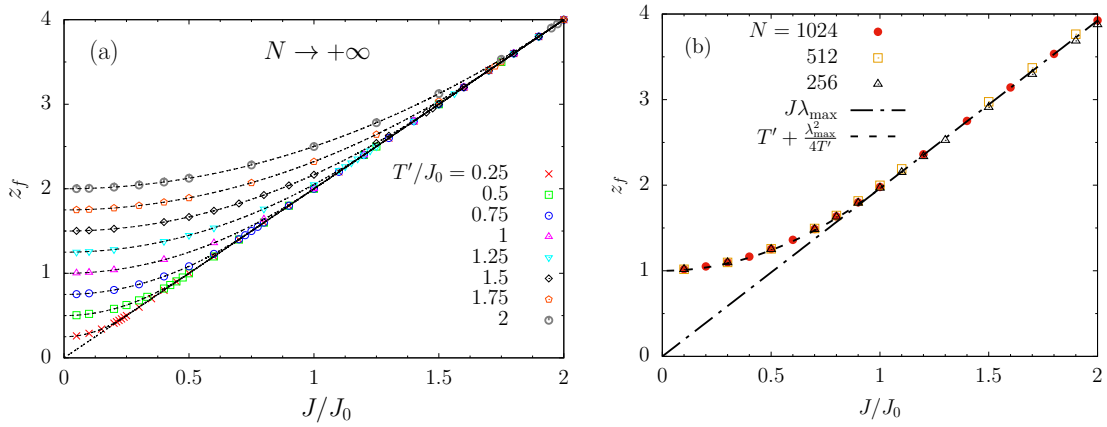

Figure 4.4: **Estimated asymptotic value of** $z(t)$ as function of J/J_0, for different values of T'/J_0, as indicated in the keys. (a) $N \to \infty$ results. The dashed curved lines are the functions $f(x,y) = y + x^2/y$ for $x < y$ where $x = J/J_0$ and $y = T'/J_0$. We also show the diagonal $2\,x$ to let the reader see the crossover between the two regimes. (b) Results for the quench dynamics at $T'/J_0 = 1$, for different finite size systems. The straight dashed line is $J\lambda_{\max}$, the other curve is $T' + \lambda_{\max}^2/(4T')$, the finite size version of the infinite N fits. We have taken the value of $\lambda_{\max}$ corresponding to the $N = 1024$ instance.

One could object that the above critical line was obtained under the assumption that the system is able to reach asymptotically an equilibrium state, while here we are just considering $\chi_{\rm st}$ and the asymptotic value of the Lagrange multiplier, z_f, without taking into account the eventual stationarity of the correlation and linear response functions. However, for quenches corresponding to $x < y$ (that is, $J < T'$) we can already see, just by looking at the values of $\chi_{\rm st}$ and z_f, that the equilibrium picture is not realised. Nevertheless, the numerical estimates of $\chi_{\rm st}$ and z_f are consistent with the relation given by Eq. (4.109), for every choice of the parameters x and y.

Concerning the long-time behaviour of $C(t_1, t_2)$, we observe the following trends:

- For $x < x_c(y) = y$, $C(t_1, t_2)$ tends to be stationary, though it does not fully reach this limit within the time scales explored by the numerics when y is too small. In most instances, $C(t_1, t_2)$ oscillates around 0, exceptions being the quenches corresponding to the choice of parameters $x = y$, or very close to this curve, in which cases zero is approached asymptotically from below. The time average of C computed on intervals far from the initial transitory regime vanishes in all cases suggesting an effective $q = 0$.

- For $x > x_c(y) = y$, $C(t_1, t_2)$ is rapidly stationary and one can clearly identify the asymptotic value $q = \lim\limits_{\substack{t_2 \gg 1 \\ t_1 - t_2 \gg 1}} C(t_1, t_2)$. For $y < 1$ one has $q > 0$, while for $y > 1$ $q = 0$.
  The asymptotic value $q_0 = \lim_{t_2 \gg t_0} C(t_1, 0)$ is different from q in the cases in which both are non-vanishing.

By using the above observations, we are able to construct an approximate dynamic phase diagram for the Hamiltonian dynamics of the $p = 2$ spherical spin glass model following a uniform quench of the interaction matrix. This is shown in Fig. 4.5. So far we have indentified three large regions corresponding to three different dynamical behaviour in the long-time limit, namely

- $x < x_c(y) = y$, where $\chi_{\rm st} = 1/T'$, $z_f = T' + J^2/T'$ and $q = 0$;

- $y > 1$ and $x > x_c(y) = y$, where $\chi_{\rm st} = 1/J$, $z_f = 2J$ and $q = 0$;
- $y < 1$ and $x > x_c(y) = y$, where $\chi_{\rm st} = 1/J$, $z_f = 2J$ and $q > 0$.

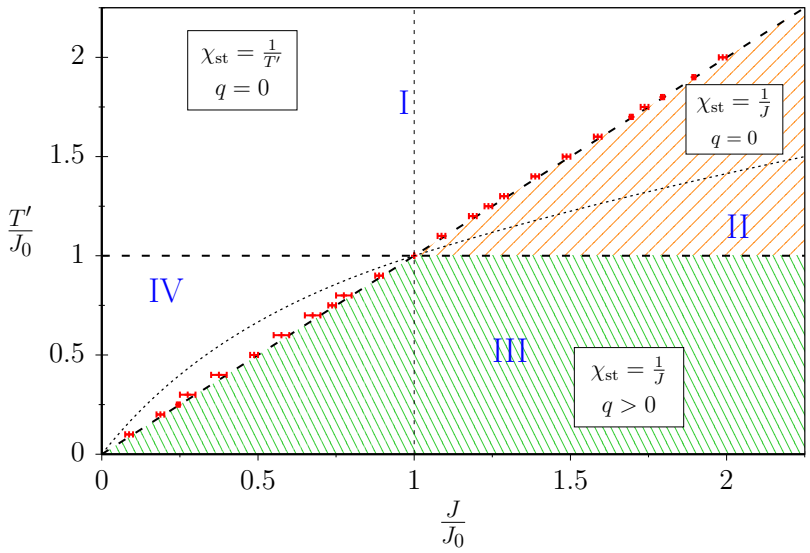

Figure 4.5: **The dynamic phase diagram.** The parameter $x = J/J_0$ controls the energy injection/extraction, with $x < 1$ corresponding to energy injection ($\Delta e > 0$), while $x > 1$ to energy extraction ($\Delta e < 0$). The parameter $y = T'/J_0$ represents the pre-quench equilibrium temperature. The dotted line corresponds to the function $g_c(x)$, with $g_c(x) = \sqrt{x}$ for $x > 1$ and $g_c(x) = 2x/(1+x)$ for $x \leq 1$, the "critical" line separating a phase with paramagnetic final state and one with condensed final state, under the Gibbs-Boltzmann equilibrium assumption, see Sec. 4.3.2. The red data points equipped with error bars indicate the numerical estimate of x_c, the value of x at which the transition in the behaviour of $\chi_{\rm st}$ (or z_f) actually occurs, for several values of $y = T'/J_0$. The Roman numerals indicate the four sectors in which we divide the paramater space: $y > 1$ and $y > x$ (Sector I), $x > y > 1$ (Sector II), $y < 1$ and $y < x$ (Sector III), $x < y < 1$ (Sector IV). The three regions that are characterised by different behaviour of z_f, $\chi_{\rm st}$ and the long-time limit of $C(t_1, t_2)$ are highlighted with different colors: white for Sectors I+IV, red for Sector II, green for Sector III.

In the following Sections we are going to treat in detail examples of quenches in each region of the phase diagram, confirming the preliminary analysis presented above. Based on the quench parameters $y = T'/J_0$ and $x = J/J_0$, we will consider separately quenches in the following four sectors,

- Sector I: $y > 1$ and $y > x$,
- Sector II: $y > 1$ and $y < x$,
- Sector III: $y < 1$ and $y < x$,
- Sector IV: $y < 1$ and $y > x$.

4.5.2 Constant energy dynamics

4.5.2.1 *No-quench dynamics in the paramagnetic phase*

Let us start with the analysis of the dynamics in the case in which there is no quench, *i.e.* $x = J/J_0 = 1$. Since the Hamiltonian of the system remains unchanged, going from the equilibrium state at $t = 0^-$ to the proper dynamics at $t > 0^+$, we should expect time translation invariance to hold for all $t \geq 0$. Moreover, given that the system is initially prepared in a Gibbs-Boltzmann equilibrium state at a temperature T', we expect that it remains in this state for $t \geq 0$, when it evolves isolated from the thermal bath, and thus we should recover the FDT relation between the two-time autocorrelation and the linear response function, at all times $t \geq 0$, with respect to the temperature T'.

We consider first the situation in which $y = T'/J_0 > 1$, that is to say, an initial state in the paramagnetic phase. In Fig. 4.6 we analyse the results of the numerical integration of the $N \to \infty$ Schwinger-Dyson equations for the particular case $T' = 1.25\ J_0$ (and $J = J_0$). The figure shows the time evolution of the two-time autocorrelation function (Fig. 4.6-(a)), the deviation of the Lagrange multiplier from its equilibrium value (Fig. 4.6-(b)), the fluctuation-dissipation parametric plot (Fig. 4.6-(c)), and the relation between $C(t_1, t_2)$ and $R(t_1, t_2)$ in the frequency domain (Fig. 4.6-(d) and Fig. 4.6-(e)).

As one can see from Fig. 4.6-(a), $C(t_1, t_2)$ depends on t_1 and t_2 only through the difference $t_1 - t_2$, meaning that time translation invariance is indeed satisfied. All the correlations relax to zero, as expected from a paramagnetic state, that is to say, $q = q_0 = 0$. The fluctuation-dissipation relation (FDR) is also satisfied with the temperature of the initial condition. This fact can be proven in general for Newtonian evolution of initial configurations drawn from Gibbs-Boltzmann equilibrium [136]. This is confirmed by the parametric plot in Fig. 4.6-(c). In this figure we display the integrated linear response, $\chi(t_1, t_2) = \int_{t_2}^{t_1} dt'\, R(t_1, t')$, also sometimes referred to as dynamical susceptibility, plotted against the two-time autocorrelation, $C(t_1, t_2)$, for two different waiting times t_2. Together we also show the expected behaviour of this parametric curve (parametric in t_1), that is to say, $\chi = (1 - C)/T'$. In fact, if the system were to reach a stationary state in which FDT is satisfied with respect to a certain temperature T, then we should observe $\chi(t_1, t_2) = (1 - C(t_1, t_2))/T$ for all times t_2 in the stationary regime. In the case of no-quench dynamics, we observe that this relation is satisfied at all times $t_2 \geq 0$.

The Lagrange multiplier remains constant throughout the evolution of the system and equal to the predicted value, $z_{\text{eq}} = T' + J_0^2/T'$, apart from small deviations due to the numerical errors introduced by the numerical integration scheme, see Fig. 4.6-(b). The plot showing $z(t)$ proves that the relative error in this quantity is at most of order 10^{-7}. All these results are compatible with Gibbs-Boltzmann equilibrium in the paramagnetic phase. We do not show the time evolution of the replica correlation with respect to the initial configuration, $Q(t, 0)$, since it is identically zero at all times. In fact, for a paramagnetic initial state, we have $Q(0, 0) = q_{\text{in}} = 0$, and it is easy to see from the Schwinger-Dyson equations (Eqs. (4.80a)-(4.80d)) that this initial condition for the function $Q(t, 0)$ implies the solution $Q(t, 0) = 0$ for all $t > 0$. In general, this is true for all quenches starting from a paramagnetic initial state, *i.e.* for $T'/J_0 > 1$.

In Fig. 4.6-(d) we show the Fourier transforms of the correlation and response functions, $\hat{C}(\omega, t_2)$ and $\hat{R}(\omega, t_2)$ respectively: the transform is performed on the variable $\tau = t_1 - t_2$

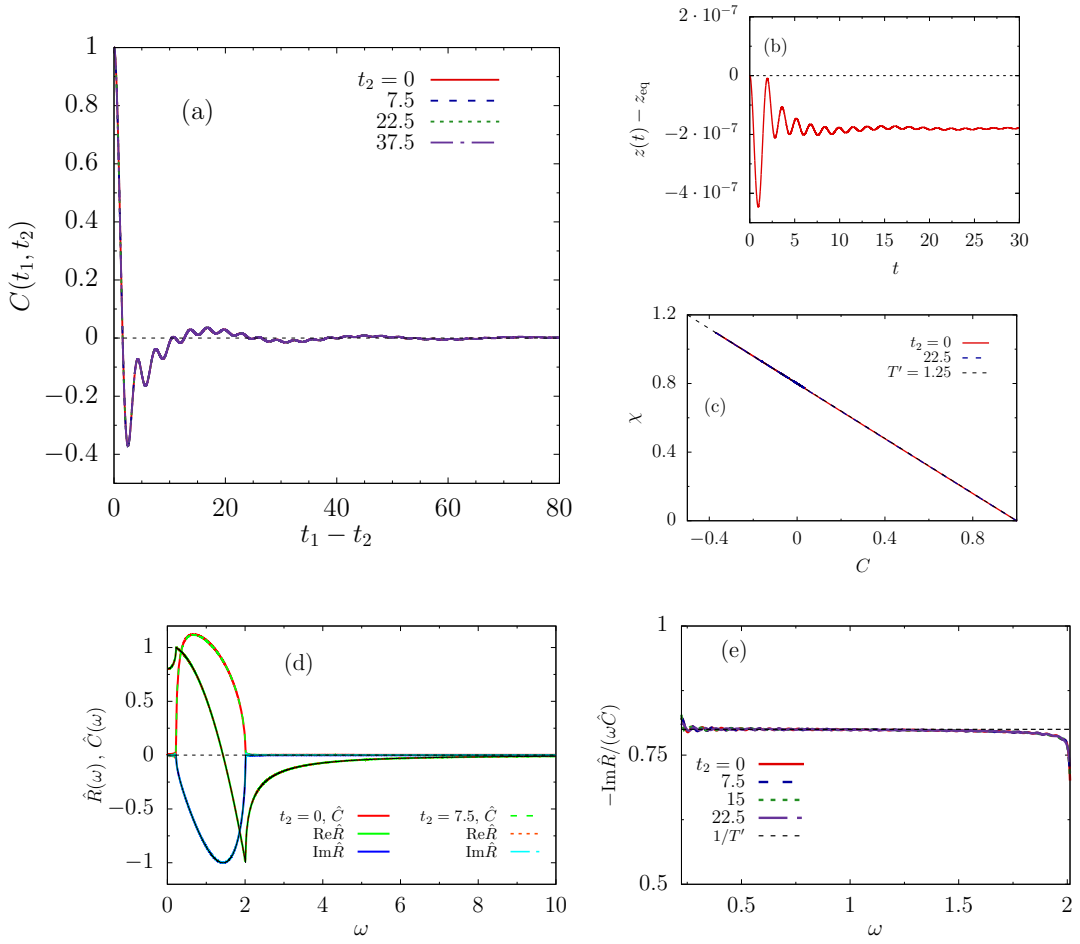

Figure 4.6: **Constant energy dynamics of the $N \to \infty$ system in the PM phase**. We show the no-quench dynamics ($J = J_0$) for the case $T'/J_0 = 1.25$, which represents a paramagnetic initial condition. (a) The two-time autocorrelation function, $C(t_1, t_2)$, plotted against $t_1 - t_2$ for various choices of the waiting time t_2, given in the key. (b) The difference between the numerical Lagrange multiplier, $z(t)$, and the expected value at equilibrium, $z_{\rm eq} = T' + J_0^2/T'$. (c) The parametric plot of the integrated linear response, $\chi(t_1, t_2)$, vs. the correlation $C(t_1, t_2)$, for fixed t_2, for two different values of t_2. The dashed line shows the expected behaviour from FDT, that is to say, $\chi = (1-C)/T'$. (d) Fourier transforms of the autocorrelation and the linear response, $\hat{C}(\omega, t_2)$ and $\hat{R}(\omega, t_2)$ respectively, for two values of t_2. The black solid lines represent the theoretical prediction for $\hat{R}(\omega)$ in the stationary regime, given by Eq. (4.108b). We chose to use a convention such that the imaginary part of $\hat{R}$ is negative. (g) The ratio $-{\rm Im}\hat{R}(\omega)/(\omega\hat{C}(\omega))$ in the interval $[\omega_-, \omega_+]$, together with $1/T'$ indicated by a dashed horizontal line.

with t_2 fixed. More precisely, they are defined as

$$\hat{C}(\omega, t_2) = \int_{-\infty}^{+\infty} {\rm d}\tau \; (C(t_2 + \tau, t_2) - q) \; {\rm e}^{-i\omega\tau} \; , \tag{4.177a}$$

$$\hat{R}(\omega, t_2) = \int_{-\infty}^{+\infty} {\rm d}\tau \; R(t_2 + \tau, t_2) \; {\rm e}^{-i\omega\tau} \; , \tag{4.177b}$$

where $q = \lim_{\tau \to +\infty} C(t_2 + \tau, t_2)$, and with the implicit assumptions that $C(t_2 + \tau, t_2) =$

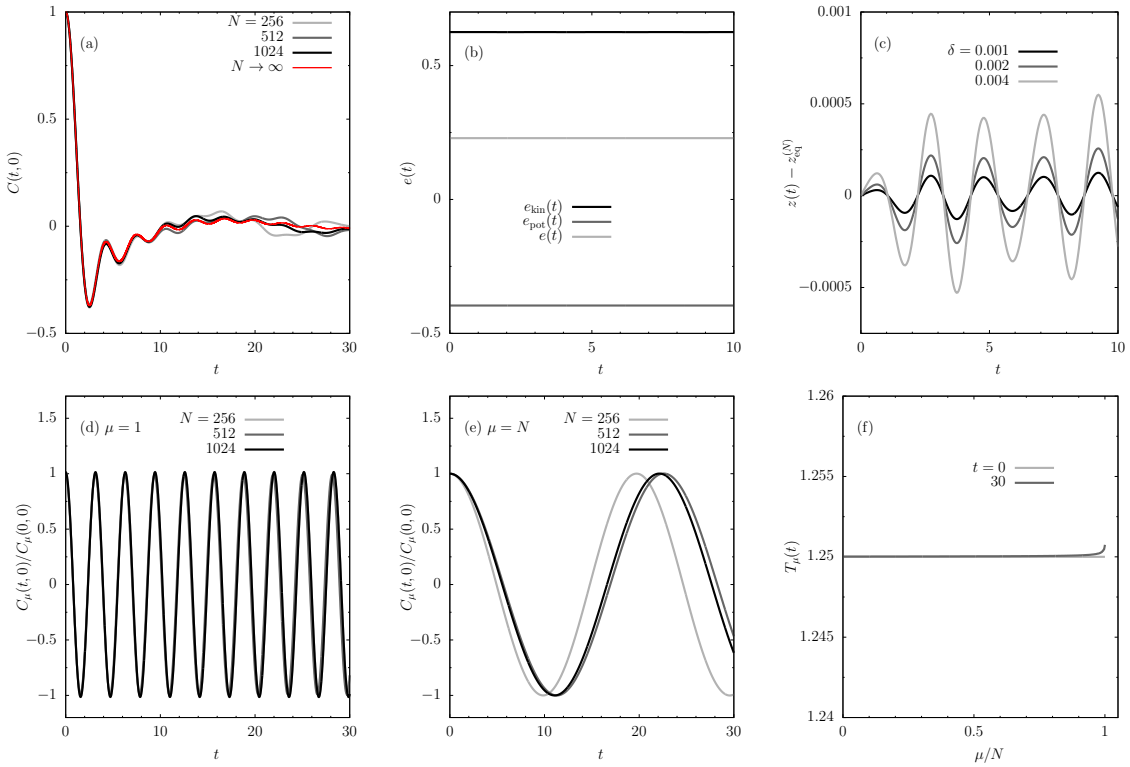

Figure 4.7: **Constant energy dynamics of a finite $N = 1024$ system in the PM phase.** The initial condition is paramagnetic, with $T'/J_0 = 1.25$. (a) The correlation function between a configuration at time t and the initial condition for different system sizes (grey curves) and the one for $N \to \infty$ (red curve). (b) The kinetic, potential and total energy densities as a function of time. (c) The difference between the time-dependent Lagrange multiplier $z(t)$ obtained from the numerics and the expected asymptotic equilibrium value $z_{\rm eq}^{(N)}$, for finite N, for different choices of the discretisation step δ. (d)-(e) Mode correlations for different system sizes, for $\mu = 1$ and $\mu = N$, respectively. (f) Mode temperatures at different times. In panels (a), (b), (d)-(f) we use $\delta = 0.001$.

$C(t_2 - \tau, t_2)$ (thus $\hat{C}(\omega, t_2)$ has only real part), and $R(t_2 + \tau, t_2) = 0$ for $\tau < 0$, for all t_2. Notice that, since we are computing the transforms from the solutions $C(t_1, t_2)$ and $R(t_1, t_2)$ given by numerically integrating Eqs. (4.80a)-(4.80d), we need to truncate the integral at the upper limit, and thus we introduce an error at small frequencies. Moreover, in some cases it is difficult to determine q with great precision. However, in most cases the maximum time difference $t_1 - t_2$, that we are able to explore through the numerical integration, is large enough for these two sources of error to be negligible.

In Fig. 4.6-(d), the black solid lines represent the theoretical prediction for the real and imaginary parts of the Fourier transform of the response function in the stationary regime, $\hat{R}_{\rm st}(\omega)$, given by Eq. (4.108b). As one can see the agreement with the numerical data is almost perfect. As expected, $\mathrm{Im}\hat{R}(\omega)$, the imaginary part of $\hat{R}(\omega)$, is non-vanishing only in the interval $[\omega_-, \omega_+]$ (with $\omega_\pm^2 = (z_{\rm eq} \pm 2J_0)/m$), and since $\mathrm{Im}\hat{R}(\omega)$ and $\hat{C}(\omega)$ must be proportional because of the FDT relation, $\hat{C}(\omega)$ must be non-vanishing only in this interval too. In Fig. 4.6-(e), the ratio $-\mathrm{Im}\hat{R}(\omega)/(\omega\hat{C}(\omega))$, together with the prediction $1/T'$ from FDT, is shown. The agreement with the prediction is very good over all the interval $[\omega_-, \omega_+]$,

for all times t_2 shown, apart from noticeable deviations near the edges of the frequency spectrum. This is due to the fact that, for frequencies close to ω_- or ω_+, the ratio approaches $0/0$ and the numerical error is amplified.

In Fig. 4.7 we show results obtained by solving the dynamics of each mode for a finite-N system with the method explained in Sec. 4.4.1. In Fig. 4.7-(a) we see that the correlation with the initial condition quickly relaxes to 0, as expected in the PM phase, with a weak N-dependence for long times. We only show the correlation with the initial configuration since we have checked that the time-delayed one is stationary. Also included in this panel is the same correlation function obtained from solving the Schwinger-Dyson equations (the same as in Fig. 4.6-(a)). We see perfect agreement with the finite N results at short times and small deviations at longer times. In Fig. 4.7-(b) we observe that the kinetic, potential and total energy densities are constant, as expected. The Lagrange multiplier is shown in panel (c) of the same figure, where we plot its deviation from $z_{\rm eq}^{(N)}$, calculated as the solution to Eq. (4.150), that in the $N \to \infty$ limit yields $z_{\rm eq}^{(N)} \to T' + J^2/T'$. The very weak (oscillatory) deviation from $z_{\rm eq}^{(N)}$ decreases with the size of the time-step used in the numerical integration.

In Fig. 4.7-(d) and (e) we show the single mode autocorrelation for modes $\mu = 1$ and $\mu = N$, respectively. Notice that finite-size effects are almost absent in the case $\mu = 1$, while they are particularly significant for $\mu = N$, the mode associated with the largest eigenvalue, in the range of sizes that have been used. In Fig. 4.7-(f) we display the mode temperatures $T_\mu(t)$ at the initial time and after a long time evolution. The mode temperatures coincide with the expected equilibrium value T', except for the largest modes, where there is a very small deviation. These variations represent small numerical errors due to the finite time-step discretisation used in the numerical integration scheme, and are hard to improve algorithmically. We have also checked (not shown) that the mode correlations $C_\mu(t_1, t_2)$ and the mode response function $R_\mu(t_1, t_2)$ satisfy the fluctuation-dissipation relation with a temperature given by T', for all μ.

4.5.2.2 *No-quench dynamics in the condensed phase*

We now turn to the constant energy dynamics for a system that is initially prepared in an equilibrium state in the condensed phase, *i.e.* $y = T'/J_0 < 1$. The behaviour that we observe is the same as shown above for the paramagnetic initial condition: stationarity is present at all times $t \geq 0$ and the FDT relation between the autocorrelation and the linear response function is satisfied with respect to the initial temperature T'. The only differences are given by the fact that the correlation does not vanish asymptotically, that is to say, $\lim_{\tau \to +\infty} C(t_2 + \tau, t_2) = q = 1 - T'/J_0 > 0$ for all $t_2 \geq 0$, and the Lagrange multiplier $z(t)$ converges to $z_{\rm eq} = 2J_0$, corresponding to the largest eigenvalue of the interaction matrix in the limit $N \to +\infty$, which implies that the zero-frequency mode has a non-vanishing amplitude (reflected in the fact that $\hat{C}(\omega) \neq 0$). This just means that the system remains confined in the initial condensed state, as expected.

This is shown in Fig. 4.8 with the solution obtained by integrating numerically the Schwinger-Dyson equations for the autocorrelation and linear response function, for the particular case $T' = 0.5\ J_0$ (and $J = J_0$). Stationarity is satisfied as well as the FDT in the time domain, with respect to the initial temperature T', see panels (a) and (c). As already stated, we observe that $C(t_2 + \tau, t_2)$ relaxes to the non-vanishing constant $q = q_{\rm in} = 1 - T'/J_0$ as $\tau \to +\infty$, for all $t_2 \geq 0$. As seen from Fig. 4.8-(b), the Lagrange multiplier $z(t)$ oscillates around the initial value $z(0) = z_{\rm eq} = 2J_0$, with the amplitude of these oscillations rapidly decaying in time. This behaviour is just an artefact of the error intrinsic in the numerical

integration and we checked that, as the time step of the integration decreases, the amplitude of this oscillations decreases. Contrary to what happens for a paramagnetic initial state, the correlation between the system at time t and a replica in the initial equilibrium state, *i.e.* the function $Q(t,0)$, is nonzero and we observe that it remains approximately constant in time, with the constant value being $q_{\rm in}$, as shown in the inset of Fig. 4.8-(a) (the small deviation, due to numerical error, decreases with the time step of the integration).

Stationarity and FDT are also confirmed by the Fourier transforms of $C(t_1,t_2)$ and $R(t_1,t_2)$ in the variable $\tau = t_1 - t_2$, with t_2 fixed, computed numerically from the solutions of the Schwinger-Dyson equations. These are shown in Fig. 4.8-(d), for two different values of t_2. The black solid lines represent the theoretical prediction for the real and imaginary parts of the Fourier transform of the response function in the stationary regime, $\hat{R}_{\rm st}(\omega)$, given by Eq. (4.108b). Notice that, since $z(t) = z_{\rm eq} = 2J_0$, $\omega_- = 0$ and thus $\hat{C}(\omega = 0, t_2)$ is non-vanishing, while $\chi_{\rm st} = \hat{R}(\omega = 0, t_2) = 1/J_0$, for all $t_2 \geq 0$ (we recall that we always set $J_0 = 1$). In panel (e) we display the ratio $-{\rm Im}\hat{R}(\omega)/(\omega\hat{C}(\omega))$ together with the prediction $1/T'$ from FDT indicated by a dashed horizontal line. We find very good agreement with the FDT prediction, *i.e.* $-{\rm Im}\hat{R}(\omega)/(\omega\hat{C}(\omega)) = 1/T'$, with the proviso that the behaviour close to edges of the interval $[0,\omega_+]$ is contaminated by the numerical error.

In Fig. 4.9 we show the finite-N mode dynamics for initial conditions in equilibrium at $T'/J_0 = 0.5$. From Fig. 4.9-(b) we notice that the total energy is conserved and that the kinetic and potential contributions are also constant, consistent with thermal equilibrium in the isolated system. In Fig. 4.9-(c) we show the Lagrange multiplier, which should be constant in the no-quench dynamics. However, in the numerical solution, the Lagrange multiplier exhibits oscillations around the initial value $z_{\rm eq}^{(N)}$ (obtained from Eq. (4.150)) whose amplitude decreases consistently with the integration step δ. The two-time (global) autocorrelation, $C(t_1,t_2) = \frac{1}{N}\sum_\mu \langle s_\mu(t_1)s_\mu(t_2)\rangle$, is stationary for all N used, so we only show the autocorrelation with $t_2 = 0$. As one can see from Fig. 4.9-(a), at variance with the paramagnetic case, the dynamics of the correlation function $C(t,0)$ has a strong dependence on the system size. After a fast decay from the initial value, the correlation shows a slow-decaying region around the value $q = q_{\rm in} = 1 - T'/J_0$ (the asymptotic value in the $N \to +\infty$ limit). After this region, $C(t,0)$ decays eventually to zero asymptotically. However, as N increases, we observe that this slow-decaying region becomes more and more close to a plateau at the constant $q = q_{\rm in}$. The source of this size dependence is the behaviour of the largest mode, the one which has a vanishing frequency in the thermodynamic limit. In Fig. 4.9-(f) we show the time dependence of the largest mode autocorrelation function $C_N(t,0)$ for different system sizes. A similar finite-size effect is seen in the dynamics of the next-to-largest mode in panel (e). Since the largest modes dominate the long-time dynamics, this effect causes the emergence of a plateau with increasing lifetime as N increases. For $N \to \infty$ the oscillation frequency of the N-th mode goes to zero, allowing for the presence of an infinite plateau. On the contrary, the modes lying far from the upper edge of the spectrum ($\lambda_\mu \ll \lambda_N = \lambda_{\rm max}$) have almost no N-dependence, as shown in panel (d) for the case $\mu = 1$. We do not show the mode temperatures obtained by time-averaging the mode kinetic (or potential) energies (see Eq. (4.135)), since the result is analogous to what is displayed in Fig. 4.7-(f). The T_μ are constant in time and equal for all modes μ, apart from deviations close to the edge $\mu = N$ due to numerical errors.

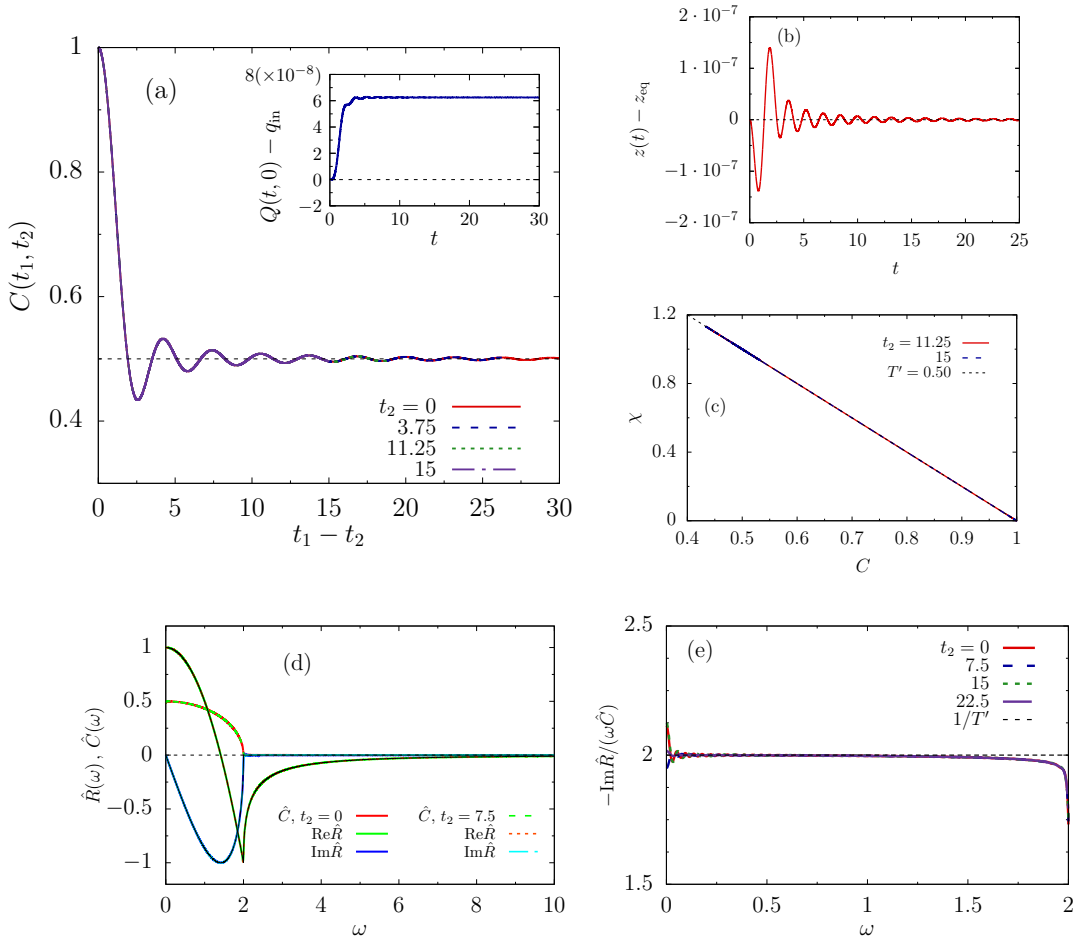

Figure 4.8: **Constant energy dynamics of the $N\to\infty$ system in the condensed phase.** We show the no-quench dynamics ($J=J_0$) for the case $T'/J_0=0.5$, which corresponds to an initial condition in the condensed phase. (a) The two-time autocorrelation function, $C(t_1,t_2)$, plotted against t_1-t_2 for various choices of the waiting time t_2, given in the key. (b) The difference between the numerical Lagrange multiplier, $z(t)$, and the expected value at equilibrium, $z_{\rm eq}=2J_0$. (c) The integrated linear response, $\chi(t_1,t_2)$, plotted against the correlation $C(t_1,t_2)$, for fixed t_2 and parametrized by t_1. The dashed line shows the expected behaviour from FDT, that is to say, $\chi=(1-C)/T'$. (d) The time-delayed Fourier transforms of the correlation and linear response functions, $\hat{C}(\omega,t_2)$ and $\hat{R}(\omega,t_2)$ respectively, for two different values of t_2 indicated in the key. The black solid lines represent the theoretical prediction for the real and imaginary parts of the Fourier transform of the response function in the stationary regime, $\hat{R}_{\rm st}(\omega)$, given by Eq. (4.108b). In panel (e), the ratio $-\mathrm{Im}\hat{R}(\omega)/(\omega\hat{C}(\omega))$ together with the prediction $1/T'$ from FDT plotted with a dashed horizontal line.

4.5.3 Quench dynamics

4.5.3.1 *Sector I: paramagnetic initial condition*

Let us now turn to the study of the quench dynamics. In this Subsection we give a brief summary of the main results obtained for the dynamics of a system prepared in equilibrium

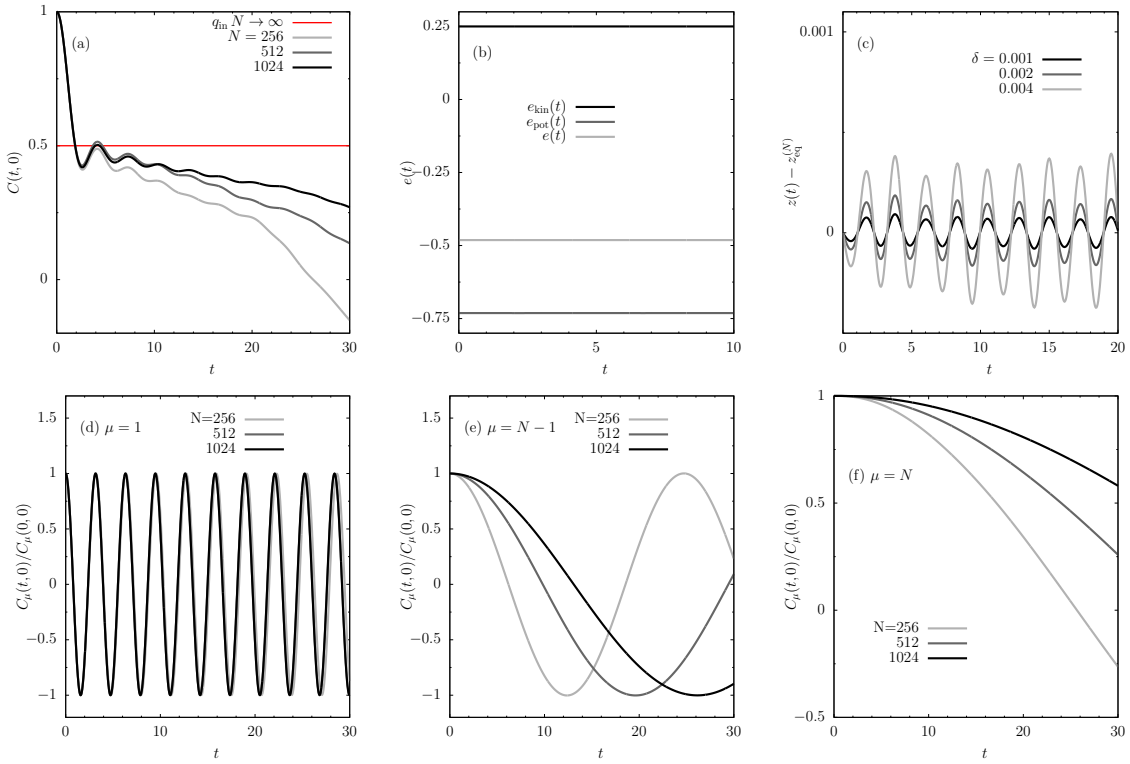

Figure 4.9: **Constant energy dynamics in the condensed phase.** Results from the integration of the Newton equations for the finite-N system, for initial condition $T'/J_0 = 0.5$ and a single disorder realisation. (a) Dynamics of the global correlation function with respect to the initial condition for different system sizes. (b) Time-evolution of the kinetic, potential and total energy densities. (c) Difference between the time-dependent Lagrange multiplier $z(t)$ obtained from the numerics and the expected asymptotic equilibrium value $z_{\rm eq}^{(N)}$, for finite N, for various choices of the time-step δ used in the integration scheme. (d)-(f) Mode correlation functions $C_\mu(t_1, t_2)$, normalised by their values at equal times, for $\mu = 1$, $N-1$, N and different system sizes indicated in the key. The mode correlations are stationary, so we only show results for $t_2 = 0$.

in the paramagnetic state, $y > 1$, and then quenched to a value of $x = J/J_0$ such that $y > x$. This choice of the parameters x and y corresponds to what we called Sector I in the phase diagram, in Fig. 4.5. Two cases need to be further distinguished within this Sector. For $x < 1$, energy is injected in the quench, while for $y > x > 1$, a small amount of energy is extracted from the system.

As already stated in Sec. 4.5.1, the common behaviour observed from the numerical solutions, for all quenches, is given by

$$\chi_{\rm st} \simeq \begin{cases} \frac{1}{T'} & \text{for} \quad y \geq x \\ \frac{1}{J} & \text{for} \quad y < x \end{cases} , \qquad z_f \simeq \begin{cases} T' + \frac{J^2}{T'} & \text{for} \quad y \geq x \\ 2J & \text{for} \quad y < x \end{cases} , \tag{4.178}$$

which is consistent with the relation $\chi_{\rm st} = \left(z_f - \sqrt{z_f^2 - 4J^2} \right) / (2J^2)$, see Eq. (4.109), obtained by only assuming that $R(t_1, t_2)$ satisfies stationarity and $z(t)$ converges to z_f. In Fig. 4.10, we show the numerical solutions from the Schwinger-Dyson equations, for the particular case

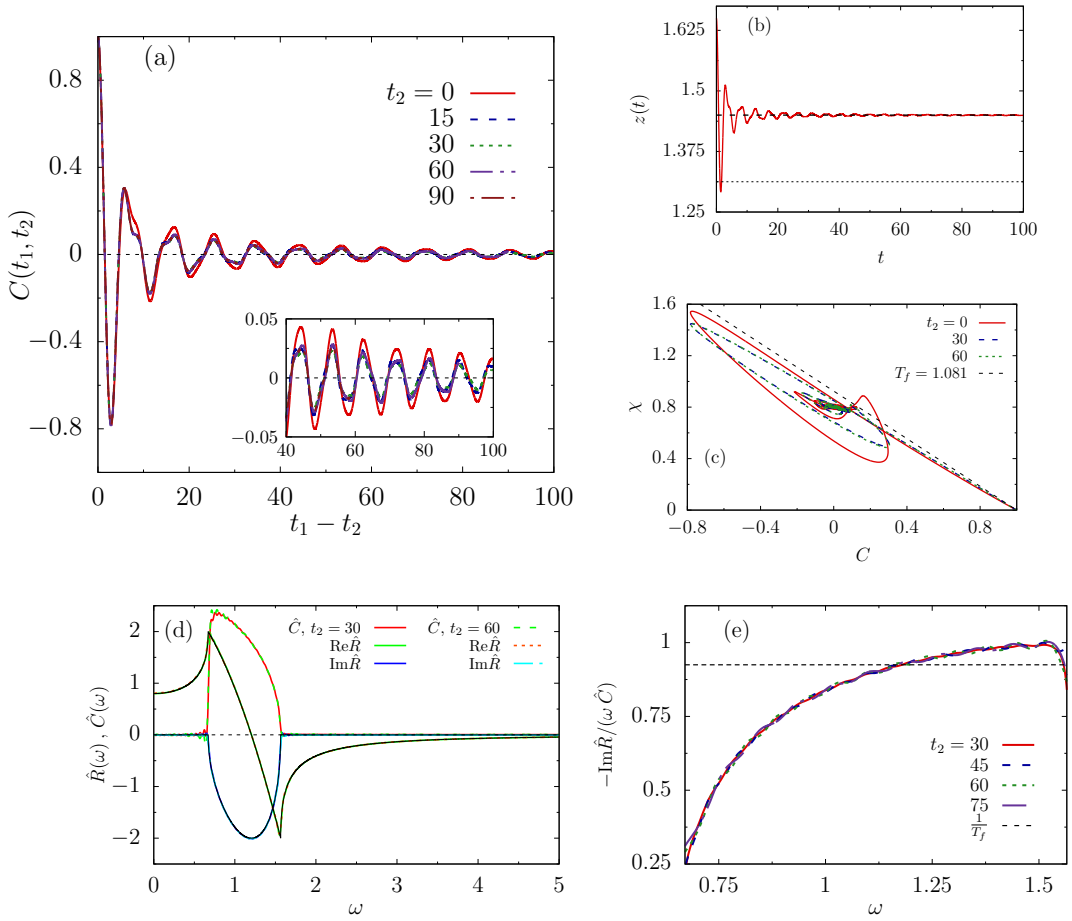

Figure 4.10: **Sector I. Energy injection on a paramagnetic initial state.** We show the solution obtained by integrating numerically the Schwinger-Dyson equations for the parameter choice $T' = 1.25\,J_0$, $J = 0.50\,J_0$. (a) The two-time autocorrelation function, $C(t_1, t_2)$, plotted as a function of $t_1 - t_2$. The horizontal dashed line is at $q = 0$. In the inset we show a "zoom" over the time interval $[40, 100]$. (b) Time evolution of the Lagrange multiplier, $z(t)$, along with the constant $T_f + J^2/T_f$, with T_f given by Eq. (4.124), and the "true" asymptotic value $z_f = T' + J^2/T'$ (above), both represented by dashed horizontal lines. (b) The parametric plot of the integrated linear response function, χ, against the correlation, C, for two waiting times t_2. The black dashed line shows the FDT relation with respect to temperature T_f, expected under the assumption of final Gibbs-Boltzmann equilibrium state. (d) The Fourier transforms of $C(t_2 + \tau, t_2)$ and $R(t_2 + \tau, t_2)$ with respect to the time delay τ, shown for different values of t_2. The black solid lines represent the real and imaginary parts of $\hat{R}_{\rm st}(\omega)$, given by Eq. (4.108b). In panel (f), the ratio $-\mathrm{Im}\hat{R}(\omega)/(\omega\hat{C}(\omega))$ together with $1/T_f$.

$y = T'/J_0 =$ and $x = J/J_0 = 0.5$, that complies with the behaviour described above. As one can see from panel (b), $z(t)$ goes from the initial value $z(0^+) = T' + JJ_0/T'$ (see Eq. (4.94)) to the constant $z_f \simeq T' + J^2/T'$, and it does not converges instead to $z_f = T_f + J^2/T_f$, the value which is expected by assuming Gibbs-Boltzmann equilibrium at the temperature T_f given by Eq. (4.124) (indicated by a dotted line in the plot). In parallel, the static susceptibility, $\chi_{\rm st} = \hat{R}(\omega = 0)$, consistently takes the value $\chi_{\rm st} = 1/T'$, as seen from Fig. 4.10-(d).

We see that $C(t_1, t_2)$ and $R(t_1, t_2)$ reach a stationary regime at a sufficiently large t_2, as shown in Fig. 4.10-(a) for $C(t_1, t_2)$. However, stationarity is not accompanied by a FDT relation between the two, as one can see from Fig. 4.10-(c), where we plot the dynamical susceptibility, $\chi(t_1, t_2) = \int_{t_2}^{t_1} \mathrm{d}t' R(t_1, t')$, against $C(t_1, t_2)$, for fixed t_2 and varying t_1. The parametric curve χ *vs.* C is very far from being the expected form $\chi = (1 - C)/T_f$. This is confirmed by the behaviour of the ratio $-\mathrm{Im}\hat{R}(\omega, t_2)/(\omega\hat{C}(\omega, t_2))$, as displayed in Fig. 4.10-(e). The effective frequency-dependent inverse temperature $\beta_{\mathrm{eff}}(\omega) = -\mathrm{Im}\hat{R}(\omega, t_2)/(\omega\hat{C}(\omega, t_2))$ has a non-trivial behaviour. Nevertheless, the numerically computed Fourier transform of the linear response function is consistent with the analytic prediction given by Eq. (4.108b). In particular, the imaginary part is non-vanishing only in the interval $[\omega_-, \omega_+]$ (save some small oscillations around zero outside this interval, due to numerical error), with $m\omega_\pm^2 = z_f \pm 2J$, when we take $z_f = T' + J^2/T'$. We also observe that $\hat{C}(\omega, t_2))$ vanishes outside this interval, a behaviour which is expected since, in the long-time limit, the system can be approximated by a collection of decoupled simple harmonic oscillators with frequency spectrum given by $m\omega_\lambda^2 = z_f - \lambda$, where λ is confined in the interval $[-2J, 2J]$ (being an eigenvalue of the interaction matrix in the $N \to +\infty$ limit), as discussed in Sec. 4.4.3.

In Fig. 4.11 we show the numerical solution for a finite-N system for the same choice of quench parameters and a particular realisation of the disorder. In the first four panels in Fig. 4.11 we display the time dependence of the mode kinetic and potential energies, $\epsilon_\mu^{\mathrm{kin}}(t)$ and $\epsilon_\mu^{\mathrm{pot}}(t)$, for some choices of μ. These functions oscillate in time in opposition of phase, with an amplitude that increases with μ, the eigenvalue index. If one assumes $z^{(N)}(t) \to z_f^{(N)} = \text{const.}$, then one can approximate the system by a collection of N independent simple harmonic oscillators, and consequently the mode total energies $\epsilon_\mu^{\mathrm{tot}}(t) = \epsilon_\mu^{\mathrm{kin}}(t) + \epsilon_\mu^{\mathrm{pot}}(t)$ also approach constant values, as observed in the plots. In fact, as shown in Fig. 4.11-(e), the Lagrange multiplier asymptotically approaches a value which is very close to the finite-N prediction $z_f^{(N)} = T' + \lambda_{\mathrm{max}}^2/(4T')$, according to the approximation given in Sec. 4.4.3 (with $\lambda_{\mathrm{max}} = \lambda_N$ the largest eigenvalue of the finite-N interaction matrix). We also observe that all modes are in equilibrium with themselves, in the sense that, for each $\mu = 1, \ldots, N$, the time-averaged potential, kinetic and total mode temperatures (defined in Eq. (4.135)) coincide, except for small deviations close to the largest modes (see Fig. 4.11-(f)). T_f, the temperature obtained assuming an equilibrium paramagnetic final state, see Eq. (4.124), is clearly different from the mode temperatures and is not obtained by averaging over the modes either, confirming that under these quenches the system does not thermalize asymptotically in time.

Finally, panel (g) displays the comparison between the mode inverse temperatures, T_μ^{-1} and the frequency-dependent effective inverse temperature $\beta_{\mathrm{eff}}(\omega)$ in the limit $N \to +\infty$ (the same shown in Fig. 4.10-(e)). The correspondence between the eigenvalue index μ and the frequency ω is given by $m\omega_\mu^2 = z_f^{(N)} - \lambda_\mu$. The agreement is very good over the whole spectrum, except for small deviations at the edges due to the numerical error. In the same plot we have also included the analytical prediction given by Eq. (4.168) (when taking $z_f = T' + J^2/T'$), that seems to capture the numerical behaviour rather accurately. We recall that it was derived assuming that the Lagrange multiplier takes its asymptotic value immediately after the quench, at time $t = 0^+$, and that the ensuing dynamics is the one of independent harmonic oscillators with mode-dependent frequencies.

In sector I of the x-y parameter space we can also have quenches with energy extraction, which are realised for $x = J/J_0 > 1$. We performed the same kind of analysis as in the case of energy injection for several choices of the quench parameters in this region, but we

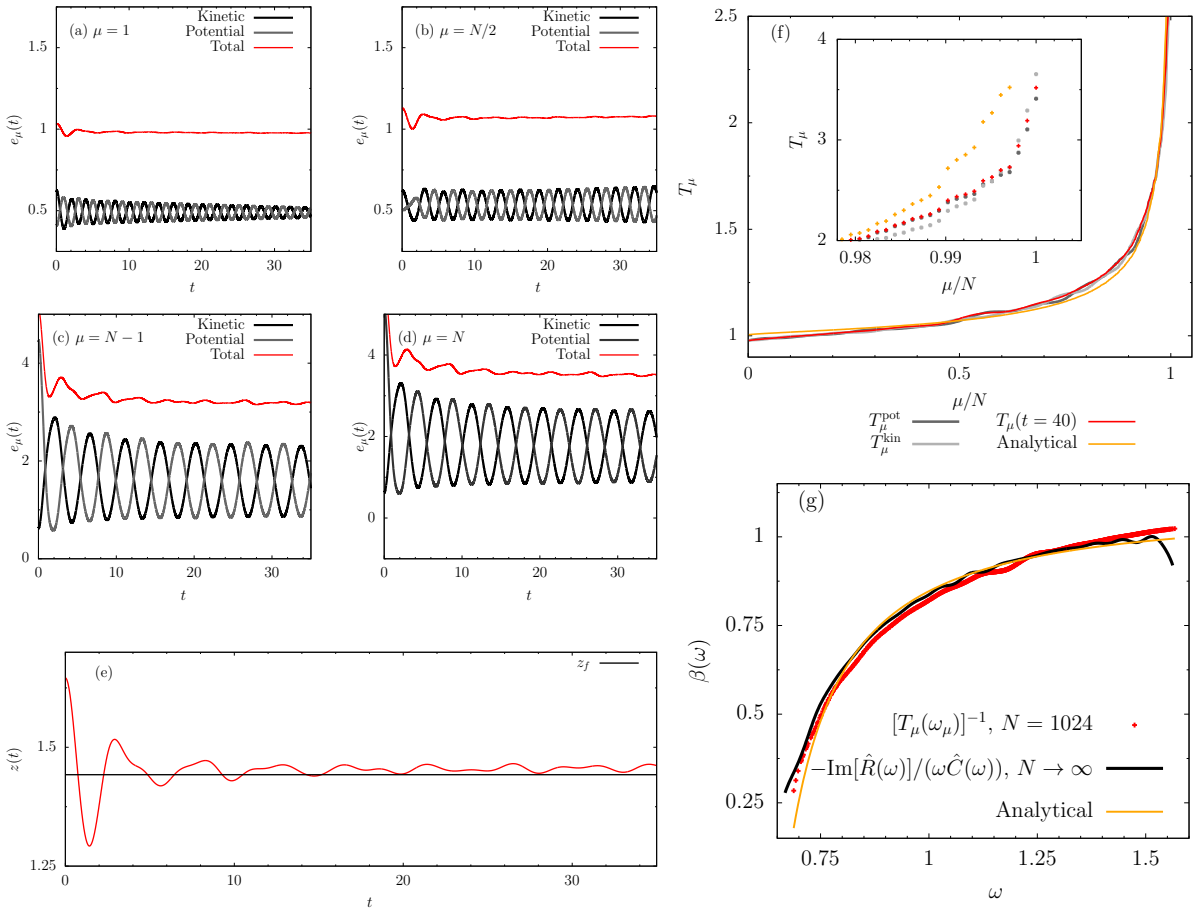

Figure 4.11: **Sector I. Energy injection on a paramagnetic initial state.** We show the analysis for the finite-N system in the case $T' = 1.25\,J_0$ and $J = 0.5\,J_0$. (a)-(d) The time-dependent energy densities of four selected modes. (e) The Lagrange multiplier compared to the analytic prediction $z_f = T' + \lambda_{\rm max}^2/(4T')$, from Sec. 4.4.3, indicated by the horizontal line. (f) Mode temperatures extracted from the use of equipartition, $T_\mu^{\rm kin,pot} = 2\bar{e}_\mu^{\rm kin,pot}$, with $\bar{e}_\mu^{\rm kin,pot}$ the time-averaged kinetic and potential mode energies. Inset: detail of the behaviour of the largest modes. (g) Comparison between the modes inverse temperatures and the inverse effective temperature given by the ratio $-{\rm Im}\hat{R}(\omega, t_2)/(\omega\hat{C}(\omega, t_2))$, with $\hat{R}(\omega, t_2)$ and $\hat{C}(\omega, t_2)$ the Fourier transforms of the linear response and autocorrelation, respectively, in the thermodynamic limit, for $t_2 \gg 1$. In (f) and (g) the yellow curves represent the analytical prediction for T_μ given by Eq. (4.168), when taking $z_f = T' + J^2/T'$.

choose to not show all the data since there are no fundamental variations. Having said so, the mode temperatures do present an interesting difference, that is shown in Fig. 4.12 for the particular case $T' = 1.2\,J_0$ and $J = 1.1\,J_0$. In this case, the (time-averaged) temperatures of the modes are approximately all the same for the low-lying modes, while a clear mode dependence appears close to the right edge of the spectrum, *i.e.* for modes corresponding to eigeinvalues λ_μ near the maximum value. However, the temperatures of the largest modes are lower than the temperatures of the lower modes (see also the inset of panel (a)), contrary to what happens for the energy-injection case (see Fig. 4.11-(f)). In Fig. 4.12-(b), we confront these mode inverse temperatures to those given by $\beta_{\rm eff}(\omega) = -{\rm Im}\hat{R}(\omega, t_2)/(\omega\hat{C}(\omega, t_2))$ for the

$N \to +\infty$ limit, and, once again, the agreement is very good. Moreover, the data are also in good agreement with the analytical prediction given by Eq. (4.168).

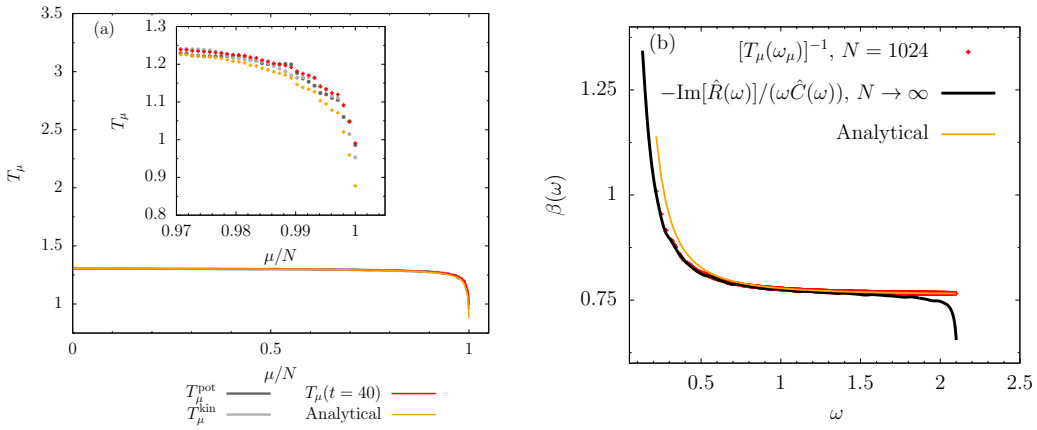

Figure 4.12: **Sector I. Energy extraction from a paramagnetic initial state.** The data shown is relative to the quench dynamics with extraction of energy for a system initially prepared in an equilibrium state in the paramagnetic phase. The particular case considered corresponds to the choice $y = T'/J_0 = 1.25$ and $J/J_0 = 1.1$, that satisfies the condition $y > x$. (a) Mode temperature profile (for finite N) obtained from time-averaging the kinetic and potential mode energies (at sufficiently long time after the initial transient). Inset: zoom over the behaviour of the largest modes. (b) Comparison of the inverse mode temperatures with the frequency-dependent effective inverse temperature $-{\rm Im}\hat{R}(\omega)/(\omega\hat{C}(\omega))$ for the $N \to +\infty$ limit. Also shown with a yellow solid line is the analytical prediction given by Eq. (4.168).

4.5.3.2 *Sector II: large energy extraction from a paramagnetic initial state*

For $y = T'/J_0$ and $x = J/J_0$ in Sector II of the phase diagram, that is, $1 < y < x$, the quench extracts an amount of energy from the system that is sufficient to make it aquire a condensed-like behaviour in terms of the Lagrange multiplier and linear response, specifically $z_f \to 2J$ and $\chi_{\rm st} = \hat{R}(\omega = 0) = 1/J$. In other words, the zero-frequency mode gets a non-vanishing amplitude and, within the independent harmonic oscillators approximation, it aquires a diffusive behaviour, as discussed in Sec. 4.4.3. Thus we should expect the system to condense around one of the minima of the potential energy. However, the behaviour of the autocorrelation is still paramagnetic-like. This is due to the fact that the system is prepared initially in a paramagnetic equilibrium state and, as a consequence, when it is quenched it can fall in one of the two "valleys" corresponding to the minima of the potential energy hypersurface with *a priori* equal probability. Averaging over all possible initial conditions results in the autocorrelation $C(t_1, t_2)$ vanishing as $t_1 - t_2 \to +\infty$.

We can distinguish two different regions in this Sector, separated by the curve $y = \sqrt{x}$. We recall that this curve, for $y = T'/J_0 > 1$, corresponds to the "limiting" curve separating paramagnetic-like behaviour from condensed-like one, under the assumption that the system reaches, in the long-time limit, an equilibrium state with Gibbs-Boltzmann measure, with respect to the post-quench Hamiltonian (see Sec. 4.3.2.1). In the following we give a brief

summary of the main properties observed in these different regions.

For $y > \sqrt{x}$ (and $y < x$), the two-time autocorrelation function becomes stationary after a very short transient, and, once it enters in the stationary regime, it rapidly approaches zero with progressively decaying oscillations. However, the linear response and the autocorrelation functions are not related by an FDT with a single temperature, and in this respect there are no important differences with respect to what we have just shown for energy extraction processes in Sector I. For this reason we choose not to show data relative to such quenches.

For $y < \sqrt{x}$ (and $y > 1$), we chose to show data for the case $T' = 1.25\, J_0$ and $J = 2\, J_0$. As one can see from Fig. 4.13-(a), the two-time autocorrelation $C(t_1, t_2)$, considered as a function of the time delay $t_1 - t_2$, shows a rapid decay towards a value close to 0.05, around which it oscillates once, and next decays towards zero with damped oscillations. In the initial fast transient, $C(t_1, t_2)$ and $R(t_1, t_2)$ actually satisfy the FDT relation with respect to the temperature T_f, obtained under the assumption of equilibrium *à la* Gibbs-Boltzmann, as shown by the parametric plot of the integrated linear response, χ, against C (panel (c)). FDT holds approximately until the point at which C reaches the first minimum, then the dependence between χ and C becomes non-trivial. In particular, χ oscillates around the static value $\chi_{\rm st} = 1/J$, but not in phase with the autocorrelation C. This behaviour is reminiscent of the *ageing* phenomenon observed for the Hamiltonian dynamics of the $p = 3$ spherical model, for equivalent quenches (see Ref. [83]), or in the case of the purely dissipative relaxation dynamics [115].

If an actual ageing behaviour were to manifest, we would observe a two-step relaxation in the evolution of $C(t_2 + \tau, t_2)$ in the time delay τ: a first stationary fast relaxation from $C = 1$ to a plateau at $C_{\rm ag} > 0$, with the "lifetime" of the plateau increasing with t_2; then a second, very slow, non-stationary relaxation from the plateau to zero. In terms of the relation between autocorrelation and linear response, we would observe that FDT is satisfied in the first stationary regime, $C > C_{\rm ag}$, while not in the subsequent relaxation, or at least, not with the same temperature. In particular, in the case of the Hamiltonian dynamics of the $p = 3$ spherical model, an ageing regime was found with a constant effective temperature [83], so that in the parametric plot χ *vs.* C one sees two distinct regions: for $C > C_{\rm ag}$, $\chi \sim (1-C)/T_{\rm eq}$ with $T_{\rm eq}$ the temperature obtained under the thermal equilibrium assumption, while for $C < C_{\rm ag}$, $\chi \sim (1 - C)/T_{\rm eff}$, with $T_{\rm eff}$ an effective non-equilibrium temperature. We do not find this behaviour in our case. However, the fact that χ seems to saturate when C falls under a certain threshold suggests that $T_{\rm eff} \to +\infty$, if a true ageing regime exists.

In Fig. 4.13-(d) and (e) we show the mode temperatures given by time-averaging the mode energies obtained from the numerical solution of the equation of motions for a finite-N system, under the same quench parameters. These finite-N results support the scenario that we pictured above. In fact, we can see that almost all the low-lying modes have the same temperature, which is approximately equal to T_f, the temperature predicted by assuming Gibbs-Boltzmann equilibrium for a system starting in a paramagnetic state and falling in a condensed state in the post-quench dynamics, see Eq. (4.126). This is consistent with the fact that the dynamics satisfies FDT for very short time delays, which are dominated by the highest frequencies or "fast modes", corresponding to the smallest eigenvalues (since $m\omega_\mu^2 = z_f - \lambda_\mu$). On the other hand, we observe significant deviations for the largest modes (or as $\omega \to 0$). These modes dominate the dynamics in the long-time limit and are responsible for the violation of the FDT. Nevertheless, the behaviour close to the upper edge of the eigenvalue spectrum seems to be captured pretty well by the analytical prediction for the T_μ^f given by Eq. (4.168), when one takes $z_f = 2J$.

Something very interesting happens in the case in which the quench parameters $x = J/J_0$

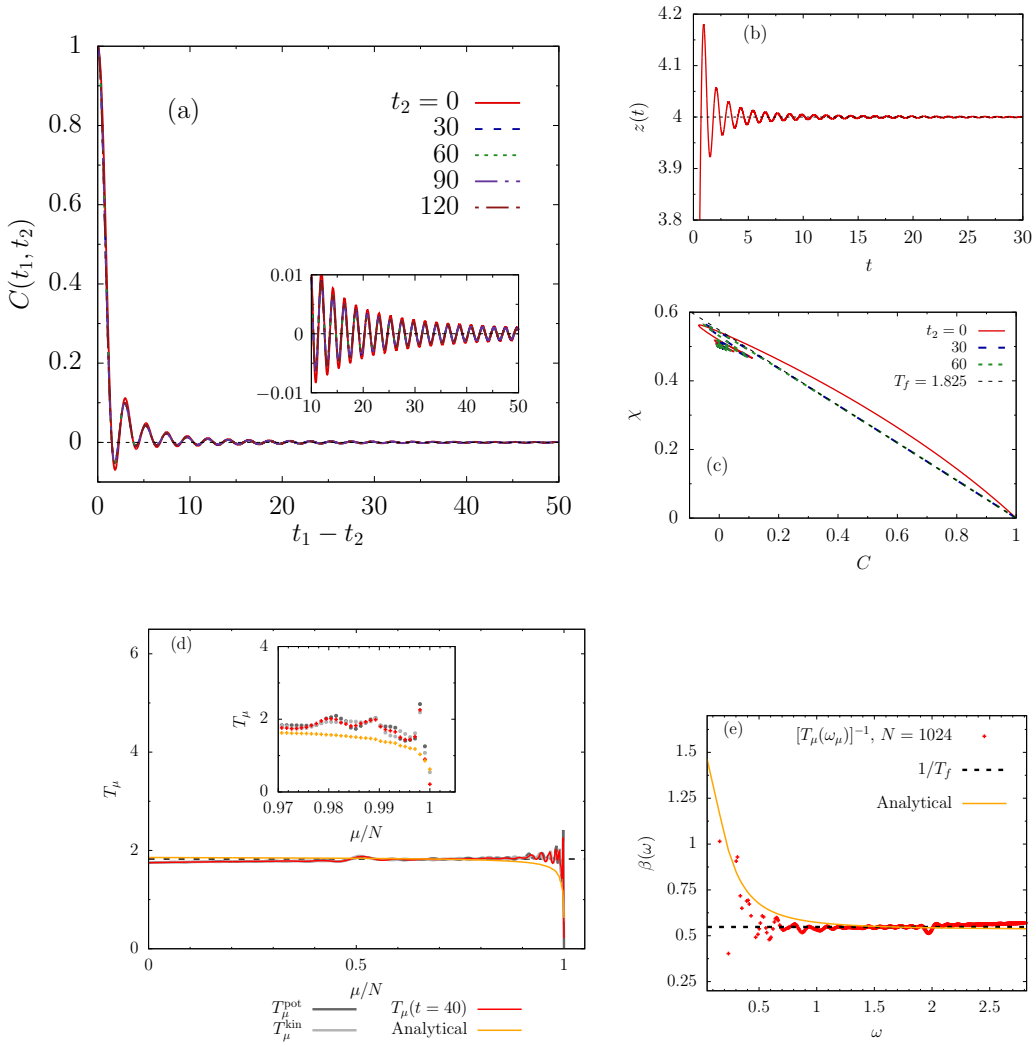

Figure 4.13: **Sector II. Energy extraction from a paramagnetic initial state.** We show data relative to the quench dynamics corresponding to parameters $T'/J_0 = 1.25$ and $J/J_0 = 2$. (a) The two-time autocorrelation function, $C(t_1, t_2)$ against the time delay $t_1 - t_2$, for various t_2. In the inset, a zoom over the time interval $[10, 50]$ is shown. (b) The time evolution of the Lagrange multiplier, $z(t)$. The horizontal dashed line corresponds to the asymptotic value $z_f = 2J$. (c) The parametric plot $\chi(t_2 + \tau, t_2)$ against $C(t_2 + \tau, t_2)$, for two different values of the waiting time t_2. The black dashed line is the result expected from FDT, with respect to the temperature T_f obtained from Eq. (4.126). (d) The mode temperatures obtained from the time-average of the mode kinetic (or potential) energies, for a finite-N system under the same quench conditions. Inset: Detail of the largest modes. (e) The inverse mode temperatures (red points), compared to the temperature T_f (dashed horizontal line) expected in case of equilibrium. In both panels (d) and (e), the yellow curve represents the outcome of the independent harmonic oscillator approximation given in Eq. (4.168), when one takes $z_f = 2J$.

and $y = T'/J_0$ lie on the curve $x = y^2$, for $y > 1$. Along this curve, we find that FDT with respect to the temperature $T_f = J$ is satisfied for sufficiently large waiting times t_2. This is

shown in Fig. 4.16 where the quantity $T_f\ \chi(t_2+\tau,t_2)$ is plotted against the autocorrelation $C(t_2+\tau,t_2)$, for fixed $t_2 \gg 1$ and varying τ, with $T_f = J$, for four different cases of quench along the curve $x = y^2$. Each case matches perfectly the FDT relation $\chi = (1-C)/T_f$. Thus, we can say that the line $x = y^2$ corresponds to quenches that bring the system to a final state in equilibrium at the critical (static) point, $T_f = T_c(J) = J$. Additional support on the fact that the dynamics after the quench occurs as in equilibrium at the critical point is given in panel (b) in the same figure, where we show that the two-time autocorrelation (obtained from the numerical solution of the Schwinger-Dyson equations) for a particular case of quench such that $J/J_0 = (T'/J_0)^2$ coincides with the one of "no-quench" dynamics for a system initially prepared at equilibrium with quenched disorder having strength J, at temperature $T' = J$ (thus at the critical point).

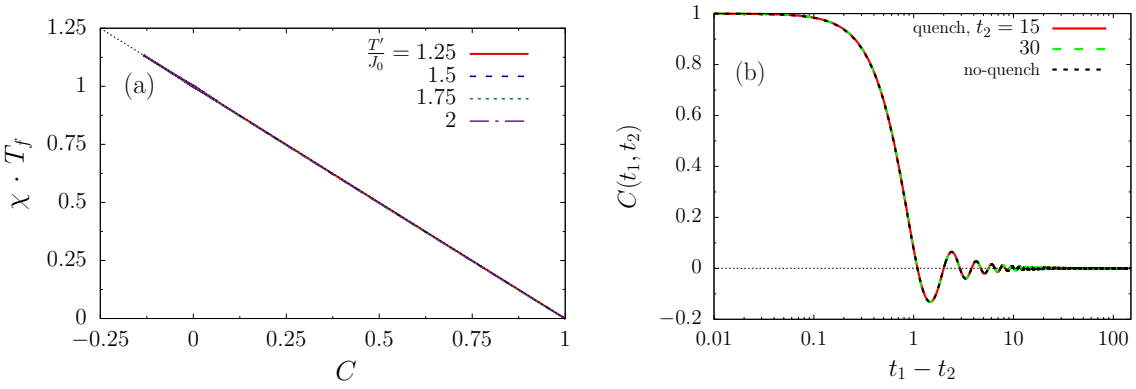

Figure 4.14: **Sector II. Energy extraction from a paramagnetic initial state**, for parameters $y = T'/J_0$ and $x = J/J_0$ lying on the special curve $y = \sqrt{x}$. (a) Check of FDT through the parametric plot $T_f \cdot \chi(t_2+\tau,t_2)$ *vs.* $C(t_2+\tau,t_2)$, where $T_f = J$, for four cases of quench on the curve $y = \sqrt{x}$, indicated by the key. For each case we choosed t_2 sufficiently long for $C(t_2+\tau,t_2)$ and $\chi(t_2+\tau,t_2)$ to be stationary. (b) Comparison between the time-delayed correlation in the post-quench dynamics for a quench with $T' = 1.75J_0$ and $J = 3.065J_0$, for two values of the waiting time t_2 (red and green lines), and the time-delayed correlation for the no-quench dynamics in the case of a system initially prepared in an equilibrium state with quenched disorder having strength $J = 3.065J_0$, at temperature $T' = J$ (black dashed line).

4.5.3.3 *Sector III: initial and final condensed states*

In the following we present some data relative to quenches in Sector III of the parameter space, that is to say, for $y = T'/J_0$ and $x = J/J_0$ such that $y < 1$ and $y < x$. The system is initially prepared in a condensed equilibrium state, thus the function $Q(t,0)$, the correlation between the system at time t (after the quench) and a replica at equilibrium at the initial temperature, can be non-zero and plays a role in the dynamical equations for the two-time autocorrelation, linear response and Lagrange multiplier. We recall that $Q(0,0) = q_{\rm in} = 1 - T'/J_0$, with $q_{\rm in}$ the Edwards-Anderson order parameter at equilibrium.

In general, what we observe from the solutions obtained by integrating numerically either the Schwinger-Dyson equations or the equations for a finite-N system is the following. After waiting a sufficiently long time, the system is able to reach a stationary state with the global

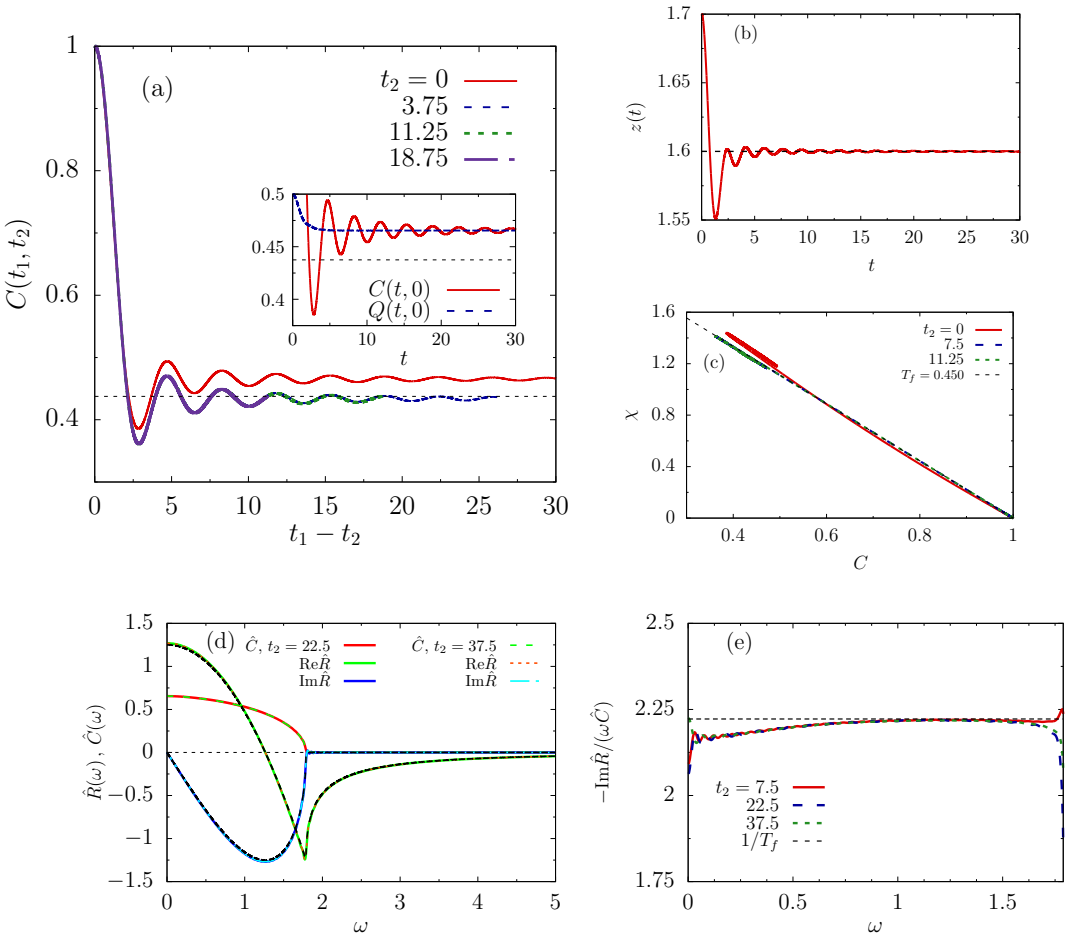

Figure 4.15: **Sector III. Energy injection, shallow quench from condensed to condensed.** The data shown is relative to a quench of the disorder strength corresponding to $J = 0.80\ J_0$, for a system initially prepared in a condensed state at temperature $T' = 0.5\ J_0$. The small energy injection is not sufficient to drive the system out of a condensed state. (a) The two-time autocorrelation, $C(t_1, t_2)$, plotted against the time-delay $t_1 - t_2$, for various t_2. The horizontal dashed line is at $q = 1 - T_f/J$, with T_f from Eq. (4.127). In the inset we show $C(t, 0)$ and $Q(t, 0)$, the latter being the correlation between the state of the system at time t and a replica at $t = 0$. (b) Time evolution of the Lagrange multiplier, $z(t)$, and the constant $z_f = 2J$ shown with a dashed line. (c) The integrated linear response, $\chi(t_1, t_2)$, against $C(t_1, t_2)$ for fixed t_2 and using $t_1 - t_2$ as a parameter. The black dashed line shows the FDT curve with respect to the temperature T_f. (d) The Fourier transforms of the (time-delayed) autocorrelation and linear response, $\hat{C}(\omega, t_2)$ and $\hat{R}(\omega, t_2)$, for two values of t_2. The black dashed lines represent the real and imaginary parts of $\hat{R}_{\mathrm{st}}(\omega)$ given by Eq. (4.108b). (e) The ratio $-\mathrm{Im}\hat{R}(\omega, t_2)/(\omega\hat{C}(\omega, t_2))$, for various t_2.

properties of a condensed state, that is to say, $q = \lim_{t_2 \gg 1} \lim_{\tau \to +\infty} C(t_2, t_2 + \tau) > 0$, $z(t) \to z_f = 2J$ and $\chi_{\mathrm{st}} = 1/J$. However, FDT is not satisfied with a single temperature T_f, the one obtained under the assumption of Gibbs-Boltzmann equilibrium (specifically Eq. (4.127)). This is clearly seen from the effective inverse temperature $\beta_{\mathrm{eff}}(\omega) = -\mathrm{Im}\hat{R}(\omega)/(\omega\hat{C}(\omega))$ and from the mode temperatures obtained by solving the finite-N system. Moreover, the asymp-

totic value of the time-delayed autocorrelation, q, does not coincide with the one expected from equilibrium in the post-quench dynamics, $q_{\rm eq} = 1 - T_f/J$.

In Fig. 4.15 we show the numerical solutions obtained from the Schwinger-Dyson equations for the particular case $T' = 0.5\ J_0$ and $J = 0.8\ J_0$, that corresponds to a quench that injects a *small* amount of energy into the system. Panel (a) proves that the two-time autocorrelation approaches a non-vanishing value asymptotically. The horizontal dashed line is at $q = 1 - T_f/J$, the theoretical value derived from the assumption of equilibration *à la* Gibbs-Boltzmann. We notice that, indeed, the asymptotic value of the autocorrelation is pretty close to it. Although, this is just a consequence of the fact that the particular case of quench we are considering is close to the no-quench line, $x = 1$. For *deep* quenches, $x \gg 1$ or $0 < x \ll 1$, we observe clearly a difference between the asymptotic value $q = \lim_{t_2 \gg 1} \lim_{\tau \to +\infty} C(t_2, t_2 + \tau)$ and the expected $q_{\rm eq} = 1 - T_f/J$, In the inset of Fig. 4.15-(a) we show the time evolution of $C(t, 0)$ and $Q(t, 0)$. $Q(t, 0)$ starts at the value $q_{\rm in}$ and decreases monotonically approaching very quickly a constant value. $C(t, 0)$ approaches the same constant, although it does it with superimposed oscillations. We observed a similar behaviour in all the cases of quench in Sector III of the parameter space (but also in Sector IV, as we will show later). This confirms our claim stated in Sec. 4.3.2 that

$$\lim_{t \to +\infty} C(t, 0) = q_0 = q_1 = \lim_{t \to +\infty} Q(t, 0)\ . \tag{4.179}$$

In Fig. 4.15-(c) we show the parametric plot of the dynamical susceptibility χ against the autocorrelation C. The data for long t_2 suggest that FDT has established at temperature T_f given by the equilibrium assumption (Eq. (4.127)). However, a better analysis is done by looking at the ratio $-{\rm Im}\hat{R}(\omega, t_2)/(\omega \hat{C}(\omega, t_2))$, with $\hat{R}(\omega, t_2)$ and $\hat{C}(\omega, t_2))$ the Fourier transform of the time-delayed linear response and autocorrelation functions, respectively, shown in Fig. 4.15-(e). Indeed, in this case, the parametric plot does not provide an accurate information since most part of the time evolution of C (and χ) consist in very small oscillations around zero, where usually effects of numerical errors are large. The behaviour of C and R in the frequency domain can help determine if truly FDT is satisfied. As one can see, the FDT relation with respect to the temperature T_f holds only for fast modes, while for $\omega \to 0$ deviations are significant and not due to numerical error (on the contrary the behaviour at $\omega \to \omega_+$ is due to numerical error because of a 0/0 division). This explains also why the the asymptotic value of the autocorrelation, q, is not given by the equilibrium expectation $q_{\rm eq} = 1 - T_f/J$. At long times, the modes with vanishing frequency are dominant and these are not equilibrated at the temperature T_f.

Fig. 4.16-(a) shows q against J/J_0 for three values of T'/J_0, together with the *naive* single temperature prediction $q = 1 - T_f/J$, with $2T_f = 2T_{\rm kin} = T'(1 + J/J_0)$ (see Eq. (4.127)). The agreement is good only close to $x = 1$, while deviations are noticeable close to the critical line $x_c(y) = y$ (separating Sector III from Sector IV), and for large energy extraction processes ($x \gg 1$). Note that the prediction of equilibration *à la* Gibbs-Boltzmann implies that $q > 0$ at $x_c(y)$, but this fact is not very clear from the data due to the limitations of the numerical integration. Also shown in this plot is $q_0 = \lim_{t \to +\infty} C(t, 0)$. We find that $q_0 > q$ for $x < 1$ (energy injection) and $q_0 < q$ for $x > 1$ (energy extraction).

The companion data for the finite-N system are shown in Fig. 4.17. First of all, panels (a)-(d) display the time dependence of the mode energies, for modes $\mu = 1,\ N/2,\ N-1$ and N, for a system with $N = 1024$ in the case of a quench with parameters $T'/J_0 = 0.5$ and $J/J_0 = 0.8$. While the modes $\mu = 1,\ N/2$ show the usual oscillatory behaviour of a harmonic oscillator, the largest modes $\mu = N - 1$ and $\mu = N$ are clearly out of equilibrium. The Lagrange multiplier

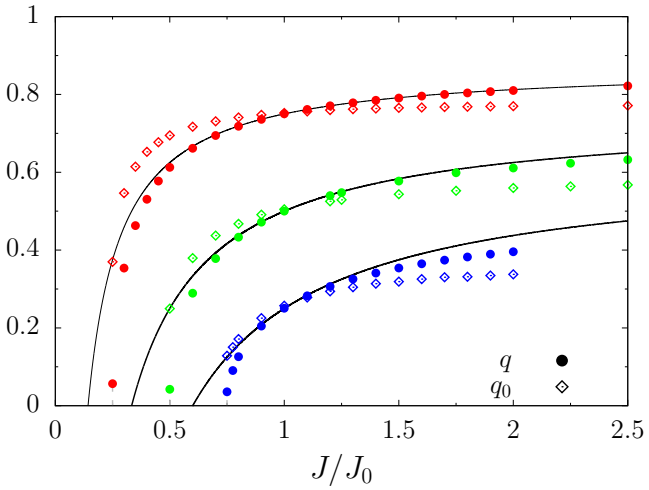

Figure 4.16: **Sector III, quenches from condensed to condensed.** The numerically estimated asymptotic value of the autocorrelation function, $q = \lim_{(t_1-t_2)\to+\infty, t_2\gg 1} C(t_1, t_2)$ (filled circles), and $q_0 = \lim_{t\to+\infty} C(t, 0)$ (diamonds), against J/J_0 for the three values of $T'/J_0 < 1$: $T'/J_0 = 0.25$ (red), 0.5 (green), 0.75 (blue), from top to bottom. The solid lines are the equilibrium predictions for q, $q = 1 - T_f/J$, with T_f given by Eq. (4.127).

converges very rapidly to the largest eigenvalue of the post-quench interaction matrix, $\lambda_{\max} = \lambda_N$, within numerical accuracy. The mode temperatures, obtained from either the mode kinetic energies or mode potential energies, are plotted in Fig. 4.17-(f), with a zoom over the largest modes in the inset. The profile is very close to an equilibrium one, *i.e.* T_μ independent of μ, apart from the large deviations at the edge $\mu/N \to 1$. Finally, panel (g) shows the comparison between the inverse mode temperatures, computed numerically for the finite N system, and the inverse temperature obtained from the assumption of independent harmonic oscillators (given by Eq. (4.168)), as functions of the mode frequency $\omega_\mu = \sqrt{(z_f - \lambda_\mu)/m}$. Notice that if ones uses $z_f = 2J$ (which is true in the limit $N \to +\infty$), T_μ^f in Eq. (4.168) becomes independent of μ (for quenches starting from a condensed equilibrium state). Higher modes (low frequency) have temperatures slightly above the predicted temperature while lower modes (high frequencies) have temperatures slightly below it. This fact is another warning concerning the claim of complete equilibration to a Gibbs-Boltzmann measure.

4.5.3.4 *Sector IV: large energy injection on a condensed state*

Finally, we consider what happens for quenches in Sector IV, that is to say, for $y = T'/J_0$ and $x = J/J_0$ such that $1 > y > x$. As already stated in Sec. 4.5.1, with the condition $y > x$ we observe that $q = \lim_{t_2\gg 1} \lim_{\tau\to+\infty} C(t_2 + \tau, t_2) = 0$, $z(t) \to T' + J^2/T'$ and $\chi_{\rm st} = 1/T'$, that correspond to a paramagnetic-like behaviour at temperature T'. FDT is not satisfied at all and, furthemore, the autocorrelation $C(t_2 + \tau, t_2)$ requires a very long time t_2 to reach a stationary regime.

In Fig. 4.18 we show the results obtained by integrating the Schwinger-Dyson equations in the particular case $T' = 0.5\ J_0$ and $J = 0.25\ J_0$. This quench injects a large amount of energy into the system which, according to the asymptotic analysis done in Sec. 4.3.2 under the assumption of post-quench Gibbs-Boltzmann equilibrium, should be sufficient to drive

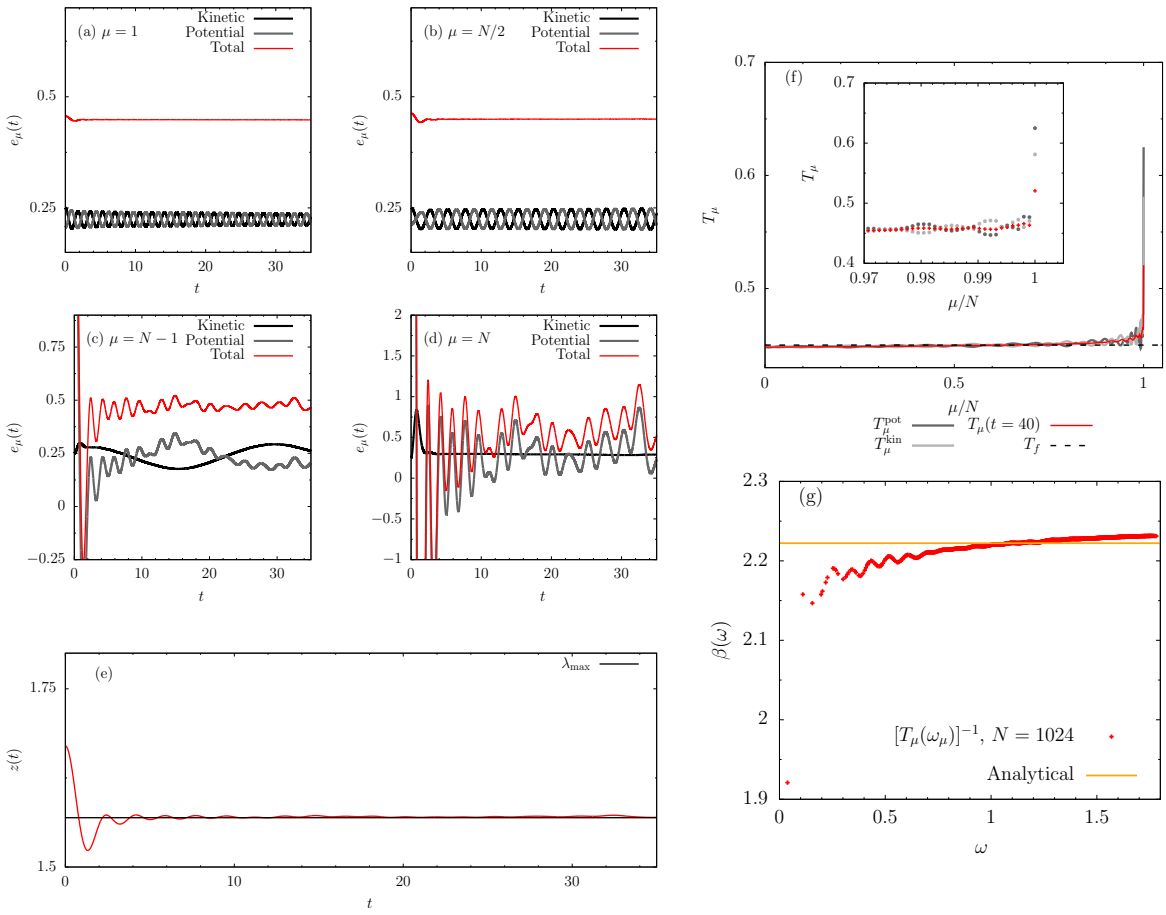

Figure 4.17: **Sector III, condensed initial conditions and small energy change.** The data shown has been obtained form the numerical solution of a finite system with $N = 1024$, for the quench corresponding to parameters $T'/J_0 = 0.5$ and $J/J_0 = 0.8$. (a)-(d) Time evolution of the mode energies for the modes $\mu = 1,\ N/2,\ N-1$ and N. (e) The Lagrange multiplier, $z(t)$. The horizontal solid line corresponds to the largest eigenvalue of the post-quench interaction matrix, $\lambda_{\max}$. (f) Mode temperatures, with a zoom over the largest modes in the inset. (g) The inverse mode temperatures together with the temperature predicted by independent harmonic oscillators approximation (horizontal line), see Eq. (4.168).

the system out of the initial condensed state and bring it to a paramagnetic equilibrium state. Had the system reached an equilibrium paramagnetic state asymptotically, its temperature would be given by Eq. (4.124). However, this is not the case. First, as one can see from Fig. 4.18-(a), the autocorrelation $C(t_1, t_2)$ has a very slow relaxation and a non-trivial t_2-dependence, that we did not observe in any of the other sectors of the parameter space. Up to the maximum time that our numerical solver was able to reach ($t_2 \sim 100$ and $t_1 - t_2 \sim 300$, in this particular case), we observe that the oscillations of C around zero remain quite large, with both their amplitude and frequency depending on t_2 in a non-monotonic way. Only after waiting a very long time t_2, we find that $C(t_2 + \tau, t_2)$ seems to aquire a stationary behaviour, $C(t_2 + \tau, t_2) \simeq C_{\rm st}(\tau)$, but even then we can not make a precise statement. This is reflected in the behaviour of the correlation function $Q(t, 0)$ (shown in Fig. 4.18-(b)). $Q(t, 0)$,

which represents the correlation between the state of the system at time t and a replica in the initial equilibrium state, has very wide oscillations whose amplitude decrease very slowly in time. On the contrary, in the case of a quench in Sector III, as we have seen in the previous Subsection, $Q(t,0)$ was relaxing monotonically and very quickly to its asymptotic value. Moreover, $C(t,0)$ and $Q(t,0)$ seem to approach asymptotically the same oscillating form. The different behaviour we observe in this case, compared to all other sectors of the phase diagram, suggests that the sytem retains memory of its initial condition for a very long period of time, possibly for the entire post-quench evolution.

The parametric plot of the dynamical susceptibility χ against the correlation C, as one can see from Fig. 4.18-(d), has a rather complex behaviour which is very far from the FDT prediction $\chi = (1-C)/T_f$, with T_f the putative target temperature given by Eq. (4.124). Panel (c) demonstrates that $z(t)$ is far from the value expected from the equilibrium assumption, $z_f = T_f + J^2/T_f$, for an equilibrium paramagnetic state, and relaxes instead to the value $T' + J^2/T'$, which is consistent with the approximation given in Sec. 4.4.3.

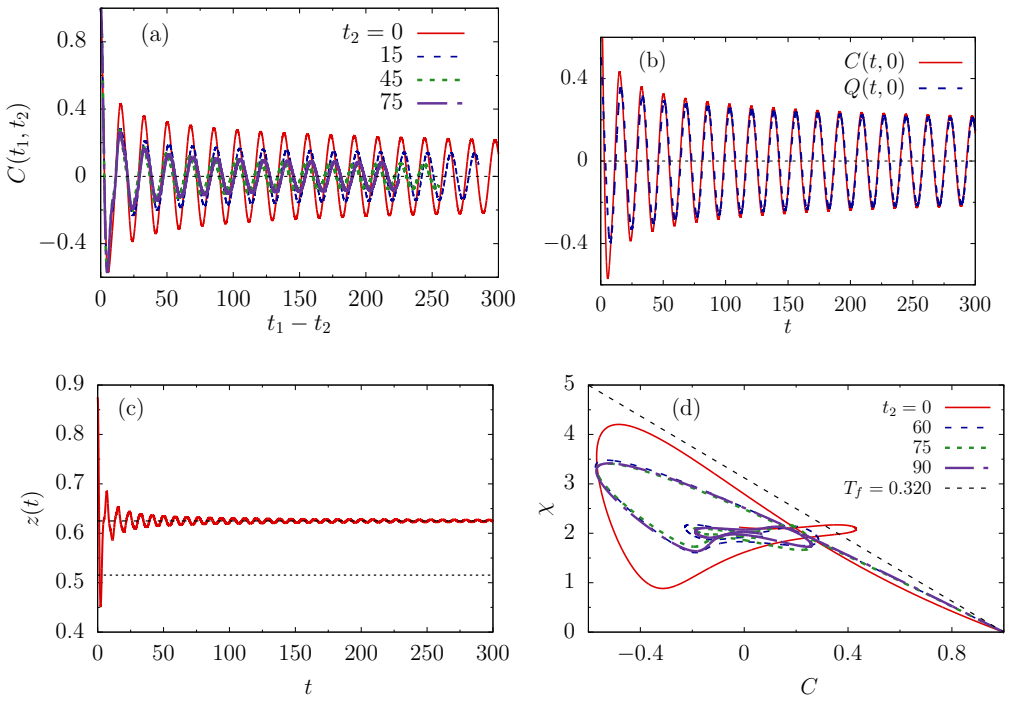

Figure 4.18: **Sector IV. Large energy injection on a condensed state.** The data shown is for the quench dynamics corresponding to the choice $T'/J_0 = 0.50$ and $J/J_0 = 0.25$. (a) The two-time autocorrelation $C(t_1,t_2)$ plotted against $t_1 - t_2$, for various t_2. (b) The correlation between the state at time t and the initial state, $C(t,0)$, and the correlation between the state at time t and a replica at $t = 0$, $Q(t,0)$. (c) The Lagrange multiplier $z(t)$, together with the expected asymptotic value from the equilibrium assumption, $z_f = T_f + J^2/T_f$ (dotted line, below), and the observed asymptotic value, $T' + J^2/T'$ (dashed line). (d) The dynamical susceptibility, $\chi(t_2+\tau,t_2)$, against $C(t_2+\tau,t_2)$, with τ taken as a parameter, for four values of t_2 specified in the key. The black dashed line is the FDT curve with respect to the temperature T_f given by Eq. (4.124).

The lack of FDT relation between the autocorrelation and the linear response is confirmed

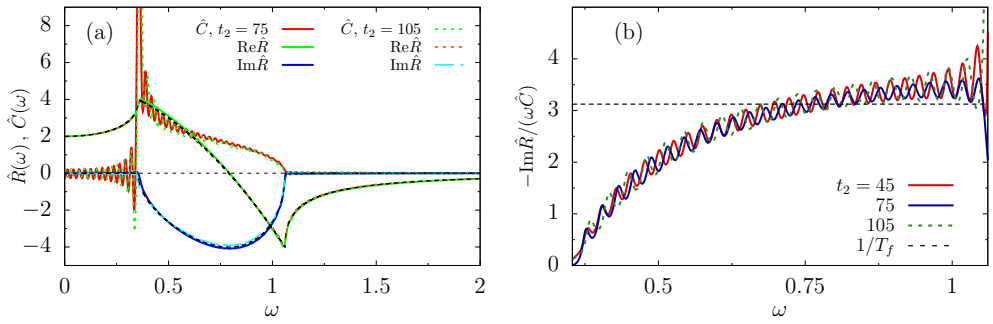

Figure 4.19: **Sector IV. Large energy injection on a condensed state.** The data shown is for the quench dynamics corresponding to the choice $T'/J_0 = 0.50$ and $J/J_0 = 0.25$. (a) Fourier transforms of the time-delayed autocorrelation and linear response functions, for two t_2 indicated in the key. The black dashed lines are the analytical predictions for the real and imaginary part of the Fourier transform of the linear response function, given by Eq. (4.108b) when taking $z_f = T' + J^2/T'$. (b) The ratio $-\mathrm{Im}\hat{R}(\omega, t_2)/(\omega\hat{C}(\omega, t_2))$, for two values of t_2. The dashed line is at $1/T_f$, with the temperature T_f given by Eq. (4.124). We recall that $\mathrm{Im}\hat{R}$ is non-vanishing only in the interval $[\omega_-, \omega_+]$, with $m\omega_\pm^2 = z_f \pm 2J$, z_f being the asymptotic value of $z(t)$.

by the behaviour of the ratio $\beta_{\rm eff}(\omega, t_2) = -\mathrm{Im}\hat{R}(\omega, t_2)/(\omega\hat{C}(\omega, t_2))$, shown in Fig. 4.19-(b). The behaviour is non-trivial and we observe that $\beta_{\rm eff}(\omega, t_2) \to 0$ as $\omega \to \omega_- = \sqrt{(z_f - 2J)/m}$, meaning that the modes associated with the largest eigenvalues of the post-quench interaction matrix aquire a diverging effective temperature. However, we must admit that our numerical estimate of the Fourier transform of the time-delayed autocorrelation, $\hat{C}(\omega, t_2)$, is affected significantly by the truncation error, in the time-window that our numerical solver is able to explore, for all quenches in Sector IV. Since $C(t_2 + \tau, t_2)$ does not have a fast relaxation to zero, we have a very poor accuracy of the result for small frequencies. In particular, we are not entirely sure whether the value of $\hat{C}(\omega)$ is supposed to diverge as $\omega \to \omega_-$, or remain finite. Nevertheless, the effective inverse temperature obtained for the $N \to +\infty$ agrees pretty well with the result of the finite-N calculation for large N, as shown in Fig. 4.20. In this figure, we compare $\beta_{\rm eff}(\omega)$ (averaged over different values of t_2 to get rid of the undesired noise due to numerical errors) to the mode temperatures of the finite N system, for $N = 1024$, obtained by time-averaging the kinetic mode energies. We see that both these estimates are different from the prediction given in Eq. (4.168) stemming from the independent harmonic oscillators approximation.

4.6 Integrals of motion

As we have seen in the previous Section, the post-quench Hamiltonian dynamics of the 2-spin interaction spherical spin glass model, with initial condition taken from equilibrium, almost never leads, in the long-time limit, to an equilibrium state with Gibbs-Boltzmann measure. This was somehow expected since the finite-N model is equivalent to a classical integrable model, namely, the Neumann model. In App. D.2 we recall the definition of the Neumann model and its main properties, and we establish the relation with the $p = 2$ spherical

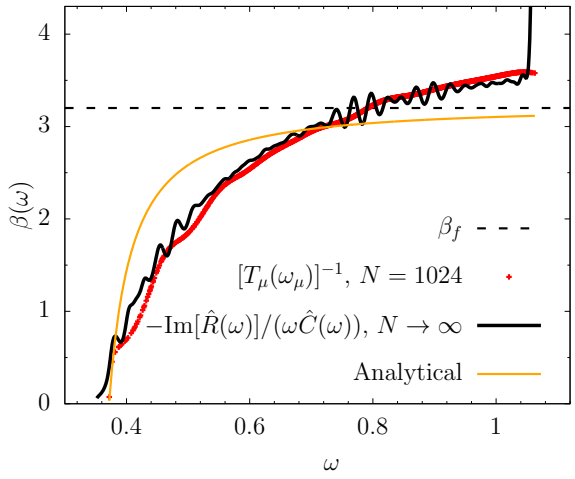

Figure 4.20: **Sector IV. Large energy injection on a condensed state.** Same choice of parameters as in Fig. 4.18 and 4.19. Comparison between the mode inverse temperatures for a finite-size system (red), the effective inverse temperature $\beta_{\rm eff} = -\mathrm{Im}\hat{R}(\omega, t_2)/(\omega\hat{C}(\omega, t_2))$, for the $N \to +\infty$ limit, averaged over a few values of t_2 (black curve) , and the analytical expression for the mode inverse temperatures obtained in the case of independent harmonic oscillators (yellow curve), *i.e.* Eq. (4.168) evaluated with $z_f = T' + J^2/T'$.

spin glass model. In this Section we will present some results concerning the behaviour of the integrals of motion. A key issue we address here is how these influence the statistical properties in the post-quench steady state.

The integrals of motion, derived from the equivalence with the Neumann model, are given by

$$I_\mu(\{s_k, p_k\}) = s_\mu^2 + \frac{1}{mN} \sum_{\nu(\neq\mu)} \frac{s_\mu^2 p_\nu^2 + s_\nu^2 p_\mu^2 - 2 s_\mu p_\nu s_\nu p_\mu}{\lambda_\nu - \lambda_\mu} \,, \tag{4.180}$$

where s_μ is the projection of the spin vector onto the direction of the eigenvector $\boldsymbol{v}_\mu$, corresponding to the eigenvalue λ_μ of the interaction matrix, while $p_\mu = m\dot{s}_\mu$ is its associated canonical momentum. They satisfy the following properties

$$\sum_{\mu=1}^N I_\mu = N \,, \qquad \sum_{\mu=1}^N \lambda_\mu I_\mu = H = \frac{1}{2m} \sum_{\mu=1}^N p_\mu^2 - \sum_{\mu=1}^N \lambda_\mu s_\mu^2 \tag{4.181}$$

(see Ref. [94]). These I_μs are conserved quantities for the single trajectories of the dynamics. However, in our case, we considered the dynamics of the $p = 2$ spherical model under a more complicated setting: the initial condition is taken at random from the Gibbs-Boltzmann equilibrium distribution with respect to the pre-quench potential energy, $H^0_{\rm pot}(\{s_\mu\}) = -\sum_\mu \lambda^0_\mu s^2_\mu$ (with λ^0_μ the eigeinvalues of the pre-quench interaction matrix, having variance J_0^2/N), and the system is let evolve with Hamiltonian dynamics with the modified potential $H_{\rm pot}(\{s_\mu\}) = -\sum_\mu \lambda_\mu s^2_\mu$, obtained by the uniform quench $J^0_{ij} \mapsto J_{ij} = (J/J_0)\, J^0_{ij}$. The results that we have shown so far corresponds to an average over the initial conditions. Therefore, we need to consider the average of the integrals of motion I_μ over the initial conditions $\{s_\mu(0), p_\mu(0)\}$,

that is

$$\langle I_\mu(t)\rangle = \langle s_\mu(t)^2\rangle + \frac{1}{mN}\sum_{\nu(\neq\mu)} \frac{\langle s_\mu(t)^2 p_\nu(t)^2\rangle + \langle s_\nu(t)^2 p_\mu(t)^2\rangle - 2\langle s_\mu(t)p_\nu(t)s_\nu(t)p_\mu(t)\rangle}{\lambda_\nu - \lambda_\mu} \,, \tag{4.182}$$

with the brackets $\langle\ \cdot\ \rangle$ indicating the average. These average quantities are conserved during the time evolution, that is, $\langle I_\mu(t)\rangle = \langle I_\mu(0)\rangle$ for all $t > 0$. They can be used to determine what are the conditions under which the system reaches asymptotically a Gibbs-Boltzmann equilibrium state. Indeed, one can compute $\langle I_\mu(+\infty)\rangle$ under the assumption that all modes have equilibrated at the same temperature T_f, and then impose $\langle I_\mu(+\infty)\rangle = \langle I_\mu(0)\rangle$.

Let us first compute the averages right after the instantaneous quench. We notice that the post-quench averages $\langle s_\mu^2(0^+)\rangle$ and $\langle p_\mu^2(0^+)\rangle$ coincide with those right before the quench, $\langle s_\mu^2(0^-)\rangle$ and $\langle p_\mu^2(0^-)\rangle$, respectively. Owing to the fact that the initial conditions are drawn from an equilibrium probability density with quadratic Hamiltonian, we have $\langle s_\mu^2(0^+)p_\nu^2(0^+)\rangle = \langle s_\mu^2(0^+)\rangle \cdot \langle p_\nu^2(0^+)\rangle$ and $\langle s_\mu(0^+)s_\nu(0^+)p_\mu(0^+)p_\nu(0^+)\rangle = \langle s_\mu(0^+)s_\nu(0^+)\rangle \cdot \langle p_\mu(0^+)p_\nu(0^+)\rangle$, for all $\mu,\nu = 1,\ldots,N$. Moreover, $\langle p_\mu(0^+)p_\nu(0^+)\rangle = \langle s_\mu(0^+)s_\nu(0^+)\rangle = 0$ for $\mu \neq \nu$. The average of the integrals of motion at $t = 0^+$ are then given by

$$\langle I_\mu(0^+)\rangle = \langle s_\mu^2(0^+)\rangle + \frac{1}{mN}\sum_{\nu(\neq\mu)} \frac{\langle s_\mu^2(0^+)\rangle\langle p_\nu^2(0^+)\rangle + \langle s_\nu^2(0^+)\rangle\langle p_\mu^2(0^+)\rangle}{\lambda_\nu - \lambda_\mu} \,. \tag{4.183}$$

In the cases in which $y = T'/J_0 < 1$, the initial state is condensed and the integrals of motion of the modes $\mu \neq N$ and $\mu = N$ scale very differently with N. For the modes in the bulk ($\mu < N$) we get

$$\begin{aligned}\langle I_\mu(0^+)\rangle \;\; = \;\; & \frac{T'}{z_0 - \lambda_\mu^0} + \frac{T'}{N}\frac{\langle s_N(0^-)^2\rangle}{\lambda_N - \lambda_\mu} + \frac{T'^2}{N}\sum_{\nu(\neq\mu,N)} \frac{1}{(z_0 - \lambda_\nu^0)\,(\lambda_\nu - \lambda_\mu)} + \\ & + \frac{T'^2}{N}\frac{1}{z_0 - \lambda_\mu^0}\sum_{\nu(\neq\mu)} \frac{1}{\lambda_\nu - \lambda_\mu} \,. \end{aligned} \tag{4.184}$$

where we used $\langle s_\nu(0^-)^2\rangle = \frac{T'}{z(0^-) - \lambda_\nu^0}$ for $\nu < N$, $\langle p_\nu(0^-)^2\rangle = m\ T'$ for all ν, we used the notation $z_0 = z(0^-)$, and we have isolated the contribution proportional to $\langle s_N(0^-)^2\rangle$ from the rest of the sum. In fact, in the condensed state, the spin vector has a macroscopic projection onto the direction of the eigenvector associated with the largest eigenvalue, *i.e.* $\langle s_N(0^-)^2\rangle \propto N$. Notice that, since we are dealing, for the moment, with N finite, z_0 is dependent on the particular disorder realization through Eq. (4.150). The above expression can be rewritten in the following form,

$$\begin{aligned}\langle I_\mu(0^+)\rangle \;\; = \;\; & \frac{T'}{z_0 - \lambda_\mu^0} + \frac{T'}{N}\,\frac{\langle s_N(0^-)^2\rangle}{\lambda_N^0 - \lambda_\mu^0}\frac{J}{J_0} + \\ & + \frac{T'^2}{z_0 - \lambda_\mu^0}\,\frac{J_0}{J}\,\left[\frac{1}{N}\sum_{\nu(\neq\mu,N)}\frac{1}{z_0 - \lambda_\nu^0} + \,\frac{2}{J_0}\,S_\mu - \frac{1}{N}(\lambda_N^0 - \lambda_\mu^0)^{-1}\right] \end{aligned} \tag{4.185}$$

where we define

$$S_\mu \equiv \frac{J_0}{N}\sum_{\nu(\neq\mu)}\frac{1}{\lambda_\nu^0 - \lambda_\mu^0} \,. \tag{4.186}$$

The term $\frac{1}{N}(\lambda_N^0 - \lambda_\mu^0)^{-1}$ can be neglected in the limit $N \to +\infty$. In fact, the distance between the largest eigenvalue and the second largest one, $\lambda_N - \lambda_{N-1}$, scale as $N^{-2/3}$ as $N \to +\infty$ [99], thus the quantity $\frac{1}{N}(\lambda_N^0 - \lambda_\mu^0)^{-1}$ can be at most $N^{-1/3}$ for all $\mu < N$, and vanishes as $N \to +\infty$. For N large we can approximate the sums of the form $\frac{1}{N}\sum_\mu g(\lambda_\mu)$ with the integral $\int \mathrm{d}\lambda\ \rho(\lambda) g(\lambda)$, where $\rho(\lambda)$ is the density of the distribution of the eigenvalues in the thermodynamic limit, that is to say, the Wigner semi-circle law (see Eq. (4.12)). Moreover, $z_0 \to 2J_0$ as $N \to +\infty$ for equilibrium in the condensed phase, thus we can make the replacement

$$\frac{1}{N} \sum_{\nu(\neq\mu,N)} \frac{1}{z_0 - \lambda_\nu^0} \to \int \mathrm{d}\lambda\, \rho(\lambda)(2J_0 - \lambda)^{-1} \tag{4.187}$$

(assuming that the contributions from the terms $(z_0 - \lambda_\mu)^{-1}$ and $(z_0 - \lambda_N)^{-1}$ are negligible). Taking $\rho(\lambda) = \frac{1}{2\pi J_0^2}\sqrt{(2J_0)^2 - \lambda^2}\ \Theta(2J_0 - |\lambda|)$, with J_0 the pre-quench disorder strength, one easily finds that the above integral equals $1/J_0$. In the limit $N \to +\infty$, we also have $\lambda_N^0 \to 2J_0$ and $\langle s_N(0^-)^2\rangle \to q_{\rm in} N = N(1 - T'/J_0)$. Then, the large N behaviour of $\langle I_\mu(0^+)\rangle$ for $\mu \neq N$ is given by

$$\langle I_\mu(0^+)\rangle \ \simeq\ \frac{T'}{2J_0 - \lambda_\mu^0}\left[1 + \frac{J_0}{J} + \frac{2T'}{J}\ S_\mu\right] . \tag{4.188}$$

Instead, in the case of the largest mode ($\mu = N$) one obtains, in the large N limit,

$$\langle I_N(0^+)\rangle \ =\ q_{\rm in} N\left(1 + \frac{T'}{J}\ S_N\right) + \frac{1}{J}\frac{T'^2}{z_0 - \lambda_N^0}(1 + S_N) . \tag{4.189}$$

Notice that $S_N \simeq -\frac{J_0}{N}\sum_\nu (2J_0 - \lambda_\nu^0)^{-1} \to -1$ as $N \to +\infty$, since $\lambda_N^0 \to 2J_0$ in the same limit, which means that the term $1 + S_N$ vanishes. However, we need to consider also that $z_0 \to 2J_0$ as $N \to +\infty$, thus the denominator of the second term in Eq. (4.189) vanishes too. The result of numerical calculation of $\langle I_N(0^+)\rangle$ directly through the expression given by Eq. (4.183) (with finite-N initial conditions), for given realisations of the random interaction matrix and for large N, suggests that the second term is negligible with respect to the first one, see Fig. 4.21-(a). Thus, approximately we have

$$\langle I_N(0^+)\rangle \ \simeq\ q_{\rm in} N\left(1 + \frac{T'}{J}\ S_N\right) \simeq \left(1 - \frac{T'}{J_0}\right)\left(1 - \frac{T'}{J}\right) N . \tag{4.190}$$

In the case in which the system is initially prepared in a paramagnetic equilibrium state ($y = T'/J_0 > 1$), we do not have to worry about any mode aquiring a macroscopic weight. However, we need to consider the fact that $z_0 = z(0^+) \to T' + J_0^2/T'$ and $N^{-1}\ \sum_{\nu(\neq\mu)}(z_0 - \lambda_\nu^0)^{-1} \to 1/T'$ (see Eq. (4.20)), in the limit $N \to +\infty$. The expression for the $\langle I_\mu(0^+)\rangle$ is thus given by

$$\langle I_\mu(0^+)\rangle \ \simeq\ \frac{T'}{z_0 - \lambda_\mu^0}\left(1 + \frac{J_0}{J} + \frac{2T'}{J} S_\mu\right) , \tag{4.191}$$

for large N, for all μ. Notice that this expression is the same as that in Eq. (4.188), with the only difference being in the value of z_0. Despite not being able to compute the limit $N \to +\infty$ of S_μ for $\mu \neq N$, we checked numerically that the expressions of both Eq. (4.188) and Eq. (4.191) are of order $\mathcal{O}(1)$ with respect to N, for all $\mu < N$. For the case $\mu = N$, the numerical estimate for $T'/J_0 > 1$ is displayed in Fig. 4.21-(b). The weak N-dependence

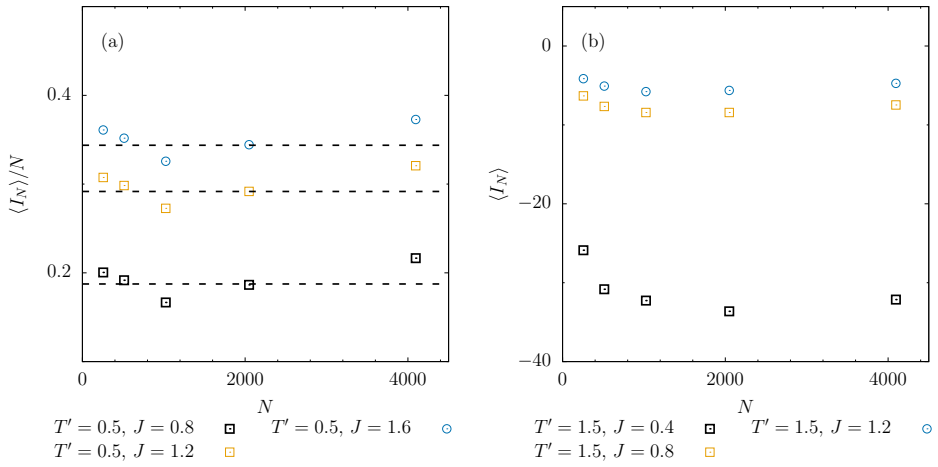

Figure 4.21: **Neumann integrals of motion** We show $\langle I_N(0^+) \rangle$, the average, over the initial equilibrium state, of the integral of motion associated with the largest eigenvalue of the interaction matrix. In (a) $\langle I_N(0^+) \rangle$ is plotted against N for three quenches with $T'/J_0 < 1$, while in (b) for three quenches with $T'/J_0 > 1$. In panel (a), the dashed lines correspond to constants $(1 - T'/J_0)(1 - T'/J)$.

is most likely due to the fluctuations in the realisation of the eigenvalues, which the above expressions do not take into account because we have evaluated all the summations on the discrete spectrum $\{\lambda_\mu\}$ by using the $N \to +\infty$ continous distribution $\rho(\lambda)$.

Concerning the time-evolution of the $\langle I_\mu(t) \rangle$, we have verified by integrating numerically the finite-N equations of motion that each of them are conserved (not shown), *i.e.* $\langle I_\mu(0^+) \rangle = \langle I_\mu(t) \rangle$ for all μ, and that they satisfy the two constraints $\sum_\mu \langle I_\mu(t) \rangle = N$ and $\sum_\mu \lambda_\mu \langle I_\mu(t) \rangle = -2e_{\rm tot}N$ for all $t > 0$, with $e_{\rm tot}$ the total energy density.

Fig. 4.22 shows the μ-dependence of the $\langle I_\mu \rangle$ together with the mode kinetic temperatures $T_\mu^{\rm kin} = 2\overline{e_\mu^{\rm kin}}$ (with $\overline{e_\mu^{\rm kin}}$ the time-averaged mode kinetic energies) obtained via the numerical solution of the finite-N system, for examples of quenches in the four sectors of the phase diagram. Note that the data shown correspond to a single realisation of the disorder. As one can see, in the case of the quenches in Sector III and IV, the values of $J\langle I_\mu \rangle$ are distributed very tightly around the corresponding mode temperatures $T_\mu^{\rm kin}$ for $\mu \ll N$: these are the so-called "fast" modes. The behaviour $J\langle I_\mu \rangle \simeq T_\mu^{\rm kin}$ suggests that these modes are very close to relaxing to a thermal equilibrium state. For μ close to the right edge of the spectrum, instead, the $\langle I_\mu \rangle$ diverge with N, as found in the calculations above. These are the modes that are dominant in the long-time regime and most responsible for the out-of-equilibrium behaviour. However, one must not confuse the fluctuations seen in the profile of the $\langle I_\mu \rangle$ with an evidence of the lack of thermalization, as for example in the case of the data relative to the quenches in Sectors I and II in Fig. 4.22. In fact, in order for the system to reach thermal equilibrium *à la* Gibbs-Boltzmann it is necessary that all modes have the same temperature $T_\mu^{\rm kin} = T_\mu^{\rm pot}$, but it is not required that all the $\langle I_\mu \rangle$ have the same value. In general, there is no simple relation between the $\langle I_\mu \rangle$s and the average mode energies $\overline{e_\mu^{\rm kin}}$ in the stationary regime.

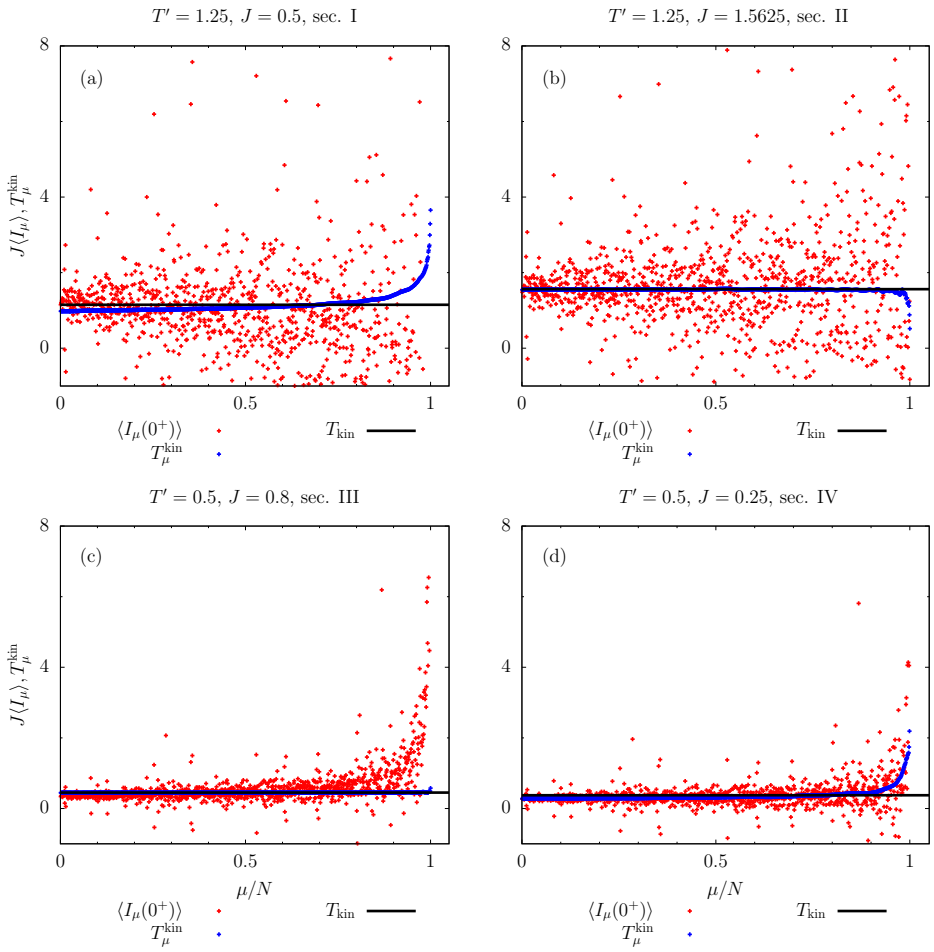

Figure 4.22: Comparison between the average integrals of motion $J\langle I_\mu\rangle$ (red data points) and the mode temperatures $T_\mu^{\rm kin} = 2\overline{e_\mu^{\rm kin}}$ (blue data points) for each mode, in the four sectors of the phase diagram (we have checked that $2\overline{\epsilon_\mu^{\rm pot}}$ yield equivalent results). We used the same vertical scale in all plots, leaving aside the values of $\langle I_\mu\rangle$ close to the edge in (c) for which, in particular, $\langle I_N\rangle \simeq 180$. There is no such divergence at the edge of the spectrum in the other panels. The black horizontal lines represent the global temperature $T_{\rm kin}$ predicted by assuming Gibbs-Boltzmann equilibrium.

4.6.1 Gibbs-Boltzmann equilibrium assumption

The analysis of the constants of motion should shed light on the "distance" from complete equilibration to a Gibbs-Boltzmann probability density. In particular, we are interested to quenches in Sector III of the parameter space ($y < 1$ and $y < x$), where the solutions obtained from integrating the Schwinger-Dyson equations suggest proximity to an equilibrium behaviour.

Thus, let us suppose that the system is able to reach an equilibrium state *à la* Gibbs-Boltzmann at the temperature T_f in the post-quench dynamics, and that $z(t) \to z_f = 2J$ as $t \to +\infty$, in the large N limit. We recall that this last condition is actually realised for quenches with parameters $y < x$. Moreover, let us assume that the final equilibrium state

is of condensed type, that is to say, $\langle s_N(+\infty)^2\rangle \propto N$, with s_N the projection of the spin vector over the eigenvector associated with the largest eigenvalue, while $\langle s_\mu(+\infty)^2\rangle = \frac{T_f}{z_f-\lambda_\mu}$ for $\mu < N$. In this state, the average $\langle I_\mu\rangle$ for $\mu < N$ is given by

$$\langle I_\mu\rangle_{T_f} = \frac{T_f}{z_f-\lambda_\mu}\left[1+\frac{2T_f}{J}S_\mu+\frac{T_f}{N}\sum_{\nu(\neq\mu,N)}(z_f-\lambda_\nu)^{-1}\right]+\frac{T_f}{\lambda_N-\lambda_\mu}\frac{\langle s_N^2\rangle}{N}\ . \quad (4.192)$$

In the limit $N\to+\infty$, we have $z_f\to 2J$, $\lambda_N\to 2J$, $\langle s_N^2\rangle\to qN$ with $q=1-T_f/J$ (the Edwards-Anderson order paramater at equilibrium) and we use

$$\frac{1}{N}\sum_{\nu(\neq\mu,N)}(z_f-\lambda_\nu)^{-1}\simeq 1/J \quad (4.193)$$

(by exploiting again the $N\to+\infty$ limit of the eigenvalue distribution) and thus Eq. (4.192) reduces to

$$\langle I_\mu\rangle_{T_f} = \frac{2T_f}{2J-\lambda_\mu}\left(1+\frac{T_f}{J}S_\mu\right)\ . \quad (4.194)$$

We wish to compare this expression to that in Eq. (4.188), that corresponds to the system being initially in equilibrium in a condensed state. After some rearrangements, one finds that the difference $\Delta I_\mu = \langle I_\mu\rangle_{T_f} - \langle I_\mu(0^+)\rangle$ is given by

$$\Delta I_\mu = \frac{1}{2J-\lambda_\mu}\left[T'\left(1+\frac{J}{J_0}\right)-2T_f-2\left(\frac{T'^2}{J_0}-\frac{T_f^2}{J}\right)S_\mu\right]\ . \quad (4.195)$$

Since we supposed that the "final" equilibrium state is also a condensed state, then the temperature T_f is given by $T_f = T'\left(1+J/J_0\right)/2$, according to the analysis done in Sec. 4.3.2.1 (see Eq. (4.127)). Substituting it into the above equation, we finally get

$$\Delta I_\mu = -\frac{T'^2}{2J\ (2J-\lambda_\mu)}\left(\frac{J}{J_0}-1\right)^2 S_\mu\ . \quad (4.196)$$

For the N-th mode we have instead

$$\langle I_N\rangle_{T_f} \simeq q\left(1+\frac{T_f}{J}S_N\right)N+\frac{T_f^2}{J(z_f-\lambda_N)}\left(1+S_N\right)\ , \quad (4.197)$$

and thus the difference from the average in the initial state is given by

$$\begin{aligned}\Delta I_N &= \langle I_N\rangle_{T_f}-\langle I_N(0^+\rangle = \left(\frac{1+S_N}{z_f-\lambda_N}\right)\frac{T'^2}{4J^2}\left(\frac{J}{J_0}-1\right)^2+\\ &+N\left\{\frac{T'}{2J_0}\left(1-\frac{J_0}{J}\right)+S_N\left[\frac{T'}{2J_0}\left(1-\frac{J_0}{J}\right)+\frac{T'^2}{4J^2}\left(\frac{J}{J_0}-1\right)^2\right]\right\}=\\ &\simeq \left(\frac{1+S_N}{z_f-\lambda_N}-N\right)\frac{T'^2}{4J^2}\left(\frac{J}{J_0}-1\right)^2\ . \end{aligned} \quad (4.198)$$

where we used the explicit expression of T_f given above and, in the last passage, we used the $N\to+\infty$ limit $S_N\to-1$ to simplify the term proportional to N. Notice that the first term

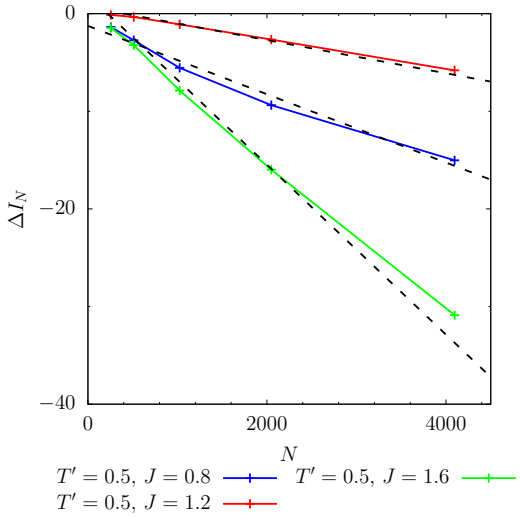

Figure 4.23: **Scaling of ΔI_N in sector III**. We show the N dependence of $\Delta I_N = \langle I_N \rangle_{T_f} - \langle I_N(0^+) \rangle$, with $\langle I_N \rangle_{T_f} - \langle I_N(0^+) \rangle$ estimated numerically, for three different choices of the quench parameters with $T'/J_0 < 1$. The dashed black lines correspond to the large N limit given by Eq. (4.198).

contains the factor $(1 + S_N)/(z_f - \lambda_N)$, which is of the form $0/0$ in the $N \to +\infty$, since both z_f and λ_N converge to $2J$. However, as explained above in the case of the average at the initial condition, we checked numerically that this term is of order at most $\mathcal{O}(1)$ with respect to N, see Fig. 4.23.

Quite clearly, ΔI_μ, for any μ, does not vanish for any choice of the quench parameters T'/J_0 and J/J_0, apart from the trivial one $J = J_0$, that corresponds to having no quench. This fact confirms, then, the lack of equilibration to a Gibbs-Boltzmann measure with a single T_f in Sector III of the parameter space.

We have seen that, on the curve $y = \sqrt{x}$, for $y > 1$, the asymptotic analysis for $N \to \infty$ predicts thermalization at temperature $T_f = J$. The numerical analysis of the Schwinger-Dyson equations confirms this prediction as the correlation and linear response are linked by FDT with respect to the temperature $T_f = J$. Let us check if this fact is confirmed by the conservation of the averages $\langle I_\mu \rangle$. In the case of these particular quenches, the initial state is paramagnetic, while the one reached in the long-time regime after the quench is also of paramagnetic kind but right at the (static) critical point, $T_f = J$, thus $z(t) \to z_f = 2J$ as $t \to +\infty$. For all μ, the difference ΔI_μ is given by

$$\Delta I_\mu \;=\; \frac{J}{2J - \lambda_\mu}\left(1 + \frac{J}{T'} + 2S_\mu\right) - \frac{J_0}{z_0 - \lambda_\mu^0}\left(\frac{J_0}{T'} + \frac{J}{T'} + 2S_\mu\right)\,, \tag{4.199}$$

and imposing the condition $\Delta I_\mu = 0$ leads to the equation

$$\frac{\lambda_\mu}{J}(1 - y) + 2S_\mu\, y\left(y(1 + y^2) - 2\right) + (y^2(1 + y) - 2)(1 + y^2) = 0\,, \tag{4.200}$$

in terms of the parameter $y = T'/J_0$, which is satisfied independently of the λ_μ only in the case $y = 1$, *i.e.* in the "no-quench" case ($J = J_0$).

We observe, however, that $\Delta I_\mu \simeq 0$ if J is close to J_0. Numerically, we find that, in the special case $T' = 1.25\ J_0$ and $J = 1.5625\ J_0$, the ΔI_μ is approximately of order 10^{-2}, for

all μ. We conclude that even in this case, in which the asymptotic analysis predicts that the global, mode-averaged quantities, behave as in equilibrium, a prediction that seems to be confirmed by the numerics, the constants of motion are not exactly the same in the initial state and in the thermal state the system would reach under the assumption of Gibbs-Boltzmann equilibrium.

In order to properly interpret these results, it is important to keep in mind that, strictly speaking, the conserved energy dynamics of an isolated (finite size) system should keep memory of the initial conditions, even if the system is non-integrable. In our problem, we see this information encoded in the I_μs. More so, not even in the $N \to \infty$ limit this memory is erased as the ΔI_μs do not vanish.

4.6.2 Fluctuations of the integrals of motion in the equal energy hypersurface

The fact that the system reaches a state that is very close to thermal equilibrium in Sector III, the sector with the lowest total energy in the phase diagram, allows us to infer some properties of the phase space structure of the model. In order for the system to reach a thermal equilibrium state, it needs to visit all configurations with the same energy in the course of its dynamical evolution. An integrable model can not achieve this goal since it is bound to wander in a region of the phase space compatible with the values that the integrals of motion (IOM) take on the initial configuration. The dynamics is constrained inside the phase space region composed by configurations which have the same values of the $I_\mu s$ for each μ. Such regions can be labeled with the values of the I_μs (which also define the energy of the group of configurations since $-\sum \lambda_\mu I_\mu = 2H$), and we shall call them iso-IOM-regions in the following.

A close-to-thermalised dynamics in an integrable system should be indicative of a substantial overlap between the constant energy manifold and the equal IOMs region in phase space. This claim is, however, highly non-trivial since the iso-energy manifold is $2N-1$ dimensional while the iso-IOM-region has only $2N - N = N$ dimensions. In the large N limit, the iso-energy manifold is huge with respect to the equal IOMs one.

Our hypothesis is that, for quenches in Sector III of the phase diagram with $x = J/J_0$ close to 1, the constant energy manifolds have a substantial overlap with any iso-IOMs-region that include a configuration with the given energy. In order to test this guess, we studied the following quantity:

$$\sigma_\mu^2(e) = \int \prod_{i=1}^{N} \mathrm{d}s_i \, \mathrm{d}p_i \, \delta(H[s_i, p_i]/N - e)(I_\mu[s_i, p_i] - \langle I_\mu[s_i, p_i]\rangle)^2 \,, \tag{4.201}$$

where the average is a microcanonical one given by

$$\langle I_\mu[s_i, p_i]\rangle = \int \prod_{i=1}^{N} \mathrm{d}s_i \, \mathrm{d}p_i \, \delta(H[s_i, p_i]/N - e) I_\mu[s_i, p_i] \,. \tag{4.202}$$

The quantity $\sigma_\mu^2(e)$ measures how large are the fluctuations in the value of a given IOM I_μ in the set of configurations with the same energy e. According to the discussion at the beginning of this Section, if, for a given energy, we observe a small value in $\sigma_\mu(e)$, this indicates a tendency of the integrable system to thermalise. In order to perform the averages over equal energy configurations, we replace the microcanonical average by a canonical one, introducing a Lagrange multiplier β and a measure $\exp(-\beta H)/Z$, fixing the average energy

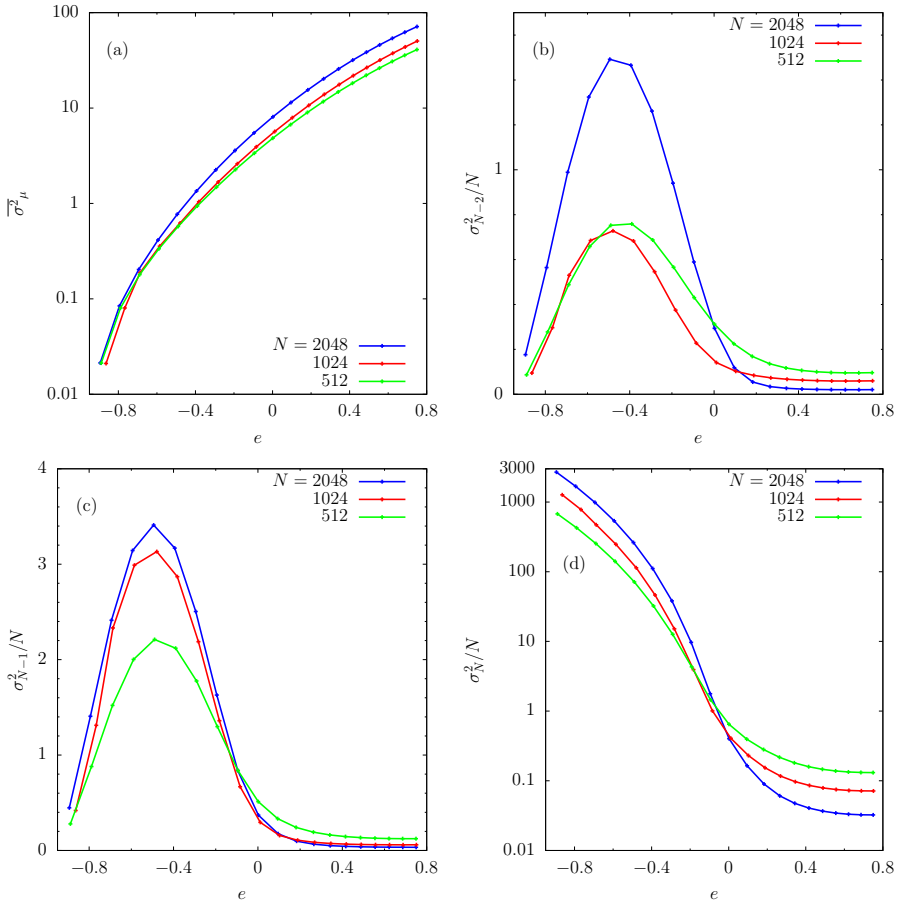

Figure 4.24: **Variance $\sigma_\mu^2(e)$ for different system sizes.** (a) Behaviour of the average of $\sigma_\mu^2(e)$ over the first three-fourths of the spectrum, see definition in Eq. (4.203). In (b) and (c) we show σ_μ^2/N for modes near the edge of the spectrum, specifically $\mu = N-2$ and $\mu = N-1$, respectively. In (d) we show σ_N^2/N. Note the logarithmic scale in the vertical axis in panels (a) and (d).

density of the ensemble. For large N, the fluctuations of the energy average are small and we get a good approximation to the microcanonical mean. The advantage of the canonical measure is that the $\langle I_\mu \rangle$s are expressed in terms of canonical averages of the same kind as those which we were using in the previous Sections to describe the initial state of the dynamics. Moreover, once z is fixed, the Hamiltonian is quadratic, and this allows one to express the higher order average $\langle I_\mu^2 \rangle$, which includes products of 4, 6 and 8 phase space variables, in terms of quadratic averages $\langle s_i^2 \rangle$ and $\langle p_i^2 \rangle$. A straightforward numerical calculation of $\sigma_\mu^2(e)$ is then possible. We show numerical results in Fig. 4.24. In panel (a) we plot $\overline{\sigma_\mu^2}$, the average of $\sigma_\mu^2(e)$ in the first three-fourths of the spectrum, namely

$$\overline{\sigma_\mu^2} = \frac{4}{3N} \sum_{\mu=1}^{3N/4} \sigma_\mu^2(e) \; . \tag{4.203}$$

We can clearly observe that it is very small for low energies and that it increases by several

orders of magnitude as we increase the energy density of the system. Such is the behaviour of $\sigma^2_\mu(e)$ for the great majority of the modes. In panels (b) and (c) we show the behaviour of $\sigma^2_\mu(e)$ for μ close to N, the edge of the spectrum. We observe that $\sigma^2_\mu(e)$ exhibits a maximum at low energies. Finally, in Fig. 4.24-(d) we plot $\sigma^2_N(e)$, the variance associated with the largest mode. For $e < 0$, $\sigma^2_N(e)$ is very large and it seems to diverge with N. Instead, for $e > 0$ we observe that $\sigma^2_N(e)$ approaches a plateau, and in particular we find that $\lim_{(e/J)\to 1} \sigma^2_N(e) \propto N^{-1}$.

Summarising, we observe that, far from the right edge of the spectrum ($\lambda_\mu \ll \lambda_N$), the fluctuations in the IOMs are very small for sufficiently low energies. This means that the low-energy configurations of the model have very similar values of the I_μs, at least for $\mu \ll N$. For modes close or at the edge of the spectrum fluctuations instead can be very large.

4.7 Conclusions

In this Chapter, we studied the two-spin interaction spherical spin glass model subject to Hamiltonian dynamics after an istantaneous (uniform) quench of the strength of the disorder, represented by the random couplings $\{J_{ij}\}$. The model is, at first look, quadratic in its degrees of freedom, but an effective interaction between the normal modes of the (random) interaction matrix is introduced dynamically by the spherical constraint.

The dynamics was studied both in $N \to \infty$ limit, through the Schwinger-Dyson equations describing the time-evolution of the two-time autocorrelation and linear response functions, and in the case of N finite, with N the number of spin degrees of freedom, by directly integrating their equations of motion. In each case, we consider a situation in which the system is initially prepared in an equilibrium state, at a given temperature, be it in the paramagnetic phase or in the condensed phase. The quench consists in a uniform rescaling of the random couplings, that is to say, $J^0_{ij} \to J^0_{ij} = (J/J_0)J_{ij}$, and the system is let evolve with the quenched potential energy through Hamiltonian dynamics. The goal was to determine whether the system is able to approach asymptotically in time a new equilibrium state *à la* Gibbs-Boltzmann, marked by the usual fluctuation dissipation relation between correlations and associated response functions.

We were motivated by a similar study performed on the p-spin spherical model with $p \geq 3$ [83]. In particular, in the $p = 3$ strongly interacting case, it was found that all quenches reach an asymptotic stationary regime in which either FDT with a single temperature is satisfied or a two-step non-equilibrium relaxation behaviour arises. For certain choices of the parameters controlling the quench, and for initial conditions in the PM phase, the system is able to equilibrate to a paramagnetic state with a proper temperature. For other choices instead it remains confined in a metastable state with restricted Gibbs-Boltzmann equilibrium at a single temperature, or a third possibility can happen. It consists in the system ageing indefinitely, *i.e.* the dynamics is characterised by two distinct regimes: a first one, occuring at short time delays, in which stationarity and FDT are satisfied, and a second one, occuring at long time delays, in which instead stationarity is violated, similarly to what happens in the purely dissipative case [98, 127, 126, 111, 84]. In the ageing scenario, the two temperatures T_f and T_{eff} depend on the pre and post-quench parameters in ways that were determined in [83].

The $p = 2$ model is in a certain way much easier to treat, thanks to the fact that the interaction term appearing in the potential energy is quadratic in the spin degrees of freedom. Indeed, one can argue that, in the long-time limit, the system enters in a stationary

regime where the Lagrange multiplier that is used to impose the spherical constraint becomes constant and, at that point, the problem can be reduced to that of a collection of decoupled harmonic oscillators. For some choices of the parameters controlling the quench, indeed we observe the system aquire this behaviour. More generally, the post-quench Hamiltonian dynamics is quite different both from the purely dissipative one [113, 114, 115, 116, 117] and the correspective in the case $p = 3$. This is due to its quasi-integrability, made explicit by its relation to the Neumann integrable model.

We outlined the dynamic phase diagram according to the asymptotic behaviour of the static susceptibility, the Lagrange multiplier, and the long time-delay limit of the two-time correlation function. In the analysis of the Schwinger-Dyson equations, we distinguished four sectors in the phase diagram depending on the initial state (being condensed or not) and the final value of the static susceptibility. We reduced these four sectors to three distinct dynamical phases. Basically, they are distinguished by two "order parameters", $\chi_{\rm st}$ and q, the static susceptibility and the asymptotic value of the two-time correlation.

In none of the phases the system equilibrates to a Gibbs-Boltzmann measure. Accordingly, there is no single temperature characterising the values taken by different observables in the long time limits, not even after being averaged over long time intervals. However, for cases in which the system is initially prepared in a condensed equilibrium state, and subject to quenches in which energy is extracted or injected in small amounts, the asymptotic values of the *global* observables, those averaged over all normal modes, are *close* to those predicted by assuming equilibrium at a given temperature T_f. Nevertheless, a closer look into the particular mode dynamics reveals that the modes are, in fact, not equilibrated amongst themselves, as expected. This is clearly seen for deep quenches in sector III of the parameter space. Another special case is provided by quenches with $T' > J_0$ and $T'^2 = JJ_0$. On this special curve, surprisingly, the global observables satisfy thermal equilibrium properties at $T_f = J$.

As already mentioned, the $p = 2$ spherical model turns out to be equivalent to the Neumann integrable model of classical mechanics. We stress the fact that in the field of classical integrable systems, the model of Neumann was usually defined and studied having only a few degrees of freedom. Here, as we are interested in searching for a statistical description of the post-quench dynamics, we dealt with the limit of large, and even diverging, number of degrees of freedom. Moreover, in the case of the Neumann model, the spherical constraint is imposed on the single trajectory, while, in our case, we relaxed this prescription by requiring that the spherical constraint is enforced on average over the initial conditions.

The $N - 1$ integrals motion of the Neumann model have been identified by K. Uhlenbeck [92, 94]. After a trivial extension that allows us to deal with the large N limit, we studied their scaling properties with system size. In cases in which the initial state is condensed, the integrals of motion associated to the edge of the spectrum also scale with N. The distance between their values and the ones they would have taken in equilibrium at a single temperature T_f gave us a rough measure of distance from Gibbs-Boltzmann equilibrium. Importantly enough, in the particular case in which the global correlation and linear response behave as in thermal equilibrium at $T_f = J$, that is to say, parameters on the curve $T'^2 = JJ_0$ in sector II, the integrals of motion are not identical to the ones expected in equilibrium. This proves that not even in this case the system is able to fully thermalize.

Appendices

Appendix A

A.1 Finite-temperature effects for KIM evolving with Glauber dynamics

It is interesting to study what are the effects of a (subcritical) finite-temperature quench on the percolation phenomena that have been discussed in Chap. 1.

Intuitively, one can expect that the coarsening process occuring in the case of a quench to $T > 0$, in terms of the geometrical and statistical properties of the spin clusters, is similar to that produced by the $T = 0$ quench in the early stages of the dynamics, as long as T is not too close to the Ising critical temperature, T_c. Indeed, thermal fluctuations are essentially responsible for two effects. On one hand they generate domains with the equilibrium properties (at the target temperature of the quench) on length scales shorter than ℓ_d. On the other hand, they cause the roughening of the domain walls thus opposing and slowing down their curvature-driven motion which constitutes the main mechanism producing the domain growth in the late stages of the NCOP dynamics. These effects do not undermine, in principle, the existence of a critical-percolation-like dynamical scaling regime since this one manifests only on length scales longer than $\ell_d(t)$.

Moreover, renormalization group treatments of domain growth dynamics [137, 18, 138, 139] suggest that the $T = 0$ equilibrium fixed point controls the domain growth for all $T < T_c$, *i.e.*, that thermal fluctuations are irrelevant to the asymptotic relaxation dynamics, with their contribution being limited primarily to the renormalization of temperature-dependent prefactors. In particular, for all $T < T_c$ the asymptotic behaviour of the dynamical length ℓ_d is given by

$$\ell_d(t;\ T) \simeq [\lambda_d(T)\ t]^{1/z_d} \tag{A.1}$$

with $z_d = 2$ and the factor $\lambda_d(T)$ encoding all the temperature dependence. In particular, it is known that, in the case of the IM evolving with Glauber dynamics, $\lambda_d(T) \to$ const. $\simeq 2.1$ as $T \to 0$, while $\lambda_d(T) \sim (T_c - T)^a$ as $T \to T_c$, with $a \simeq 0.15$ [11].

Nevertheless, thermal fluctuations start to play a major role in the evolution of the domain pattern in the late stages of the coarsening dynamics, for times of the order of magnitude of the equilibration time $t_{\rm eq} \sim L^{z_d}$. In the case of the zero-temperature Glauber dynamics, we have seen that percolating domain walls become topologically stable at a sufficiently long time, due to the curvature-driven motion mechanism. These walls eventually become flat, blocking the system in a metastable state. However, when spin-flip events that increase the energy of the system are allowed, the coarsening dynamics always leads to an equilibrium state, even though the typical time that is required to do so might not scale with the system size as expected. The reason why this happens is that, although percolating domain walls are not anymore topologically protected from the microscopic dynamics, they are still very long-lived.

As an example, let us consider a very simple situation: a spin configuration with just two domain walls (separating two large domains of opposite spin alignment) that are percolating along a certain direction of the lattice (think about a spin system on a finite lattice with PBC) and are nearly flat. Most of the spin-flip events that involve sites on the domain walls are energy-conserving and thus fully reversible, while very few spin flips increase the energy of the system thus going against the curvature-driven mechanism. The result is that these two domain walls fluctuate around a metastable position for a very long time. Only when they collide, and break into one or more non-percolating domain walls, the system can rapidly achieve the equilibrium state consisting in just one large spin cluster percolating along both directions of the lattice with small domains of opposite phase embedded in it. However, this process of domain wall collision requires that many energy increasing spin flip events occur in a sequence. In other words, in terms of free energy, the stochastic dynamics has to overcome a very high energy barrier.

Thus, states with two or more spin clusters percolating in the same direction, the so-called "stripe" states, are metastable and very long-lived for the subcritical Glauber dynamics. For finite systems, the presence of these metastable states make the late stages of the relaxation dynamics more complicated. In fact, it is observed that, for the Glauber dynamics at a finite but very small working temperature ($0 < T \ll T_c$), the typical time which the system takes to reach full equilibration is not the expected one $t_{\text{eq}} \sim L^2$, but $t_{\text{eq}} \sim L^{z_{\text{eq}}}$ with $z_{\text{eq}} > 2$ [9].

Note that, in general, the types of spin configurations that can act as metastable states depend on the particular lattice geometry and on the boundary conditions. For example, for the zero-temperature Glauber dynamics on the square lattice with PBC, spin configurations with any number of flat domain walls separated by at least two lattice spacings between each other, represent the only type of *frozen* states. Wrapping domain walls with the so-called "diagonal" topology (also called staircase domain walls [8]) have very long life, but eventually they annihilate each other. Instead, in the case of the zero-temperature Glauber dynamics on the honeycomb lattice, frozen spin configurations with non-percolating domains are possible, see App. A.2.

In the following we present some measurements from numerical simulations that support the fact that critical percolation phenomena are still emerging in the Glauber dynamics at finite temperature, and highlight some of the effects produced by the existence of these metastable states.

In Fig. A.1 we show the average magnetisation density, $m(t, L)$, for the Glauber dynamics on a square lattice with FBC and linear size L, plotted against the rescaled time t/L^2, for different values of L. The initial configuration is always taken from equilibrium at infinite temperature, and the working temperatures are $T = 0$, $T_c/4$, $T_c/2$, T_c on the different panels. In the case of the $T = 0$ quench (panel (a)), the magnetisation density converges approximately to 0.7332 (dotted line) asymptotically in time. This value can be understood by the following simple argument. As shown by Barros et al. [8], the probability that the system, at a certain point in the dynamics, develops a spin configuration with a cluster percolating in both directions, and that will evolve to a state with magnetisation density 1, is given by the corresponding probability in $2d$ critical percolation, $\pi_{\text{hv}}^{\text{FBC}}|_{\text{cp}} \simeq 0.6442$ [25, 26]. The complementary probability $\pi_{\text{stripe}} = 1 - \pi_{\text{hv}}^{\text{FBC}}|_{\text{cp}}$ is the probability that the system ends up frozen in a stripe state, that is to say, a spin configuration with flat domain walls that are percolating vertically or horizontally. These stripe states have magnetisation $m_{\text{stripe}} \simeq 1/4$ on average. Then the magnetisation density in the final state is expected to be given by $m_\infty^{\text{FBC}} \simeq \pi_{\text{hv}}^{\text{FBC}}|_{\text{cp}} + \frac{1}{4}(1 - \pi_{\text{hv}}^{\text{FBC}}|_{\text{cp}}) \simeq 0.7332$. We also notice that for $t/L^2 < 1$, the data

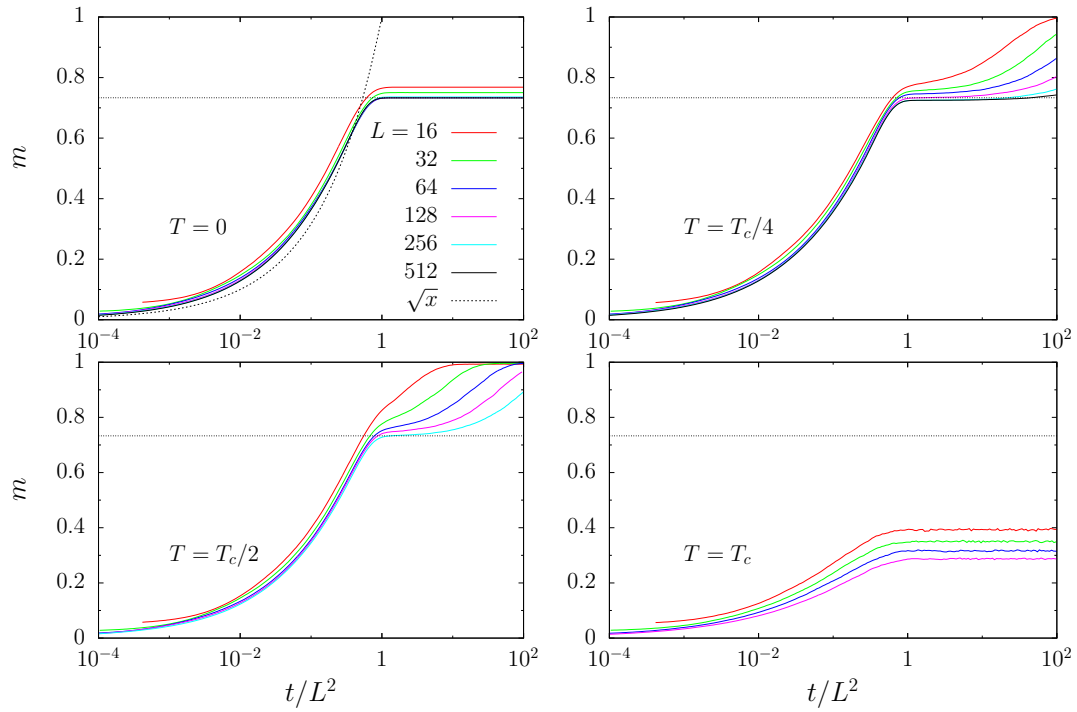

Figure A.1: Ising model on a finite square lattice with FBC, evolving with Glauber dynamics. We show the average magnetisation density, m, against rescaled time t/L^2, for various system sizes L given in the key of the first panel and various "target" temperatures T. The dotted horizontal line is the infinite time limit of the magnetisation density after a $T = 0$ quench, $m_\infty \simeq 0.7332$. We notice that at $T = 0$ and for $t/L^2 < 1$, the master curve can be roughly approximated by the power law $x^{1/2}$, indicated with a dotted line.

collapse approximately on the same master curve that is roughly given by the power law $x^{1/2}$ (indicated with a dotted line in Fig. A.1-(a)).

For $0 < T < T_c$ we see that the behaviour of $m(t)$ is similar to that of the case $T = 0$ up to times t such that $t/L^2 \simeq 1$. In particular, we observe that, for $t/L^2 > 1$, m tends to collapse on the constant value $m_\infty^{\mathrm{FBC}} \simeq 0.7332$ as L increases. This plateau corresponds to the fact that the system, during this stage of the coarsening dynamics, is getting "attracted" by the metastable states that have been described above and whose probability of occurence can be determined by using the corresponding critical percolation probabilities. It requires a certain amount of time, which increases with L, for the system to escape these metastable states and finally reach equilibrium. Notice that the transient between the metastable state reached at times $t \sim L^2$ and the final equilibrium state becomes shorter as the temperature increases, reflecting the fact that thermal fluctuations becomes more effective at destroying long percolating domain walls. For the relaxation dynamics corresponding to a quench to the critical point (panel (d)), we clearly see that the magnetisation reaches a plateau in the characteristic time $t_{\mathrm{eq}}(L) \sim L^2$, but its value is decreasing with L, as expected, since at $T = T_c$ the equilibrium magnetisation density vanishes in the thermodynamic limit.

In Fig. A.2 we show the time evolution of π_{hv}, the probability that the spin configuration has just one percolating spin cluster that has the "cross" topology, *i.e.*, percolating along both lattice principal directions, for the Glauber dynamics on a square lattice with FBC, at various target temperatures $T \leq T_c$ and various L, as in Fig. A.1. In all cases, π_{hv} is plotted

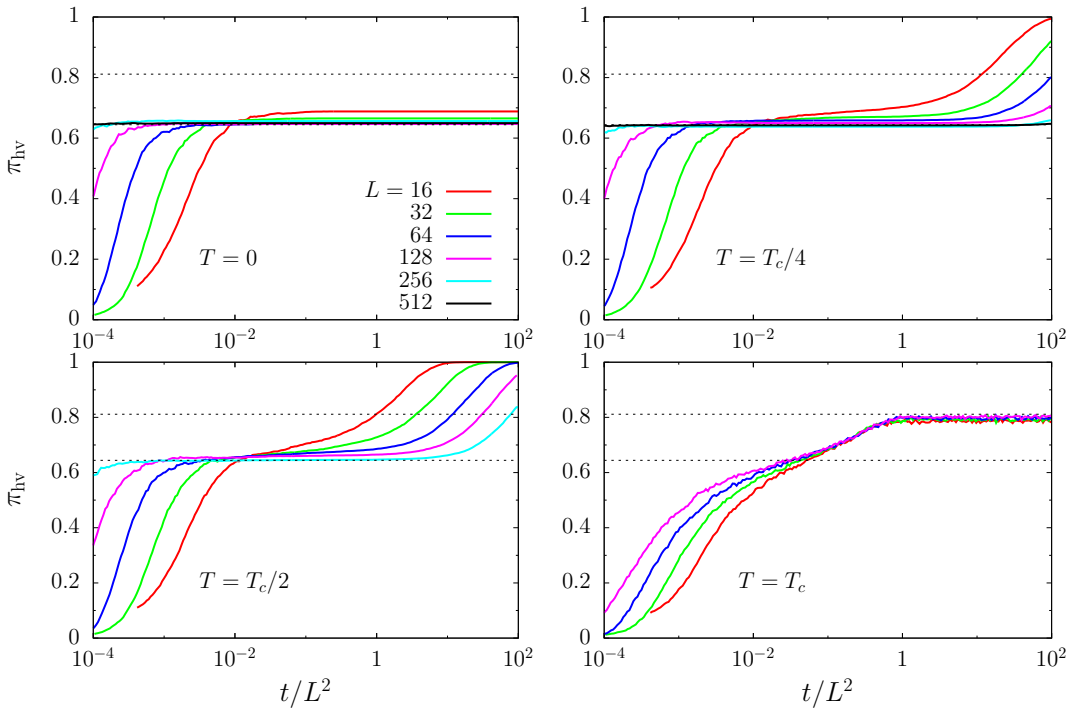

Figure A.2: Ising model on a finite square lattice with FBC, evolving with Glauber dynamics at various temperatures $T \leq T_c$. We show the probability $\pi_{\rm hv}$ that a spin cluster percolates across the lattice along both directions (in the so-called "cross" topology), against the rescaled time t/L^2, for different values of L. The colour code for the different sizes L is the same as in Fig A.1. The dotted horizontal lines are at $\pi_{\rm hv}^{\rm FBC}|_{\rm cp} \simeq 0.6442$ and $\pi_{\rm hv}^{\rm FBC}|_{T_c} \simeq 0.8113$ the probabilities of having a cluster that percolates along both horizontal and vertical directions at critical percolation, and at the Ising critical temperature, respectively.

against the rescaled time t/L^2. Two horizontal dotted lines are also shown, corresponding to $\pi_{\rm hv}^{\rm FBC}|_{\rm cp} = 0.6442$ and $\pi_{\rm hv}^{\rm FBC}|_{T_c} = 0.8113$, the latter being the probability of having a spin cluster percolating in both directions at the Ising critical point [140] (this state can be reached asymptotically by the dynamics following a quench to T_c).

There is a clear correspondence with the evolution of the magnetisation density. In fact, we observe that, for $0 < T < T_c$, $\pi_{\rm hv}$ develops a plateau that coincides approximately with $\pi_{\rm hv}^{\rm FBC}|_{\rm cp}$ whose duration increases as the system size L increases, while it becomes shorter as T increases. For $t/L^2 \gg 1$, $\pi_{\rm hv}$ "escapes" from this plateau and converges asymptotically to 1 (even though, for the larger values of L, we are not able to observe it due to the limited time accessible by the numerical simulations). This happens because, for $T < T_c$, the coarsening dynamics always leads the system to an equilibrium state, and such state is one with a unique percolating spin cluster. At $T = T_c$ there is no plateau at $\pi_{\rm hv}^{\rm FBC}|_{\rm cp} = 0.6442$. Instead, the probability $\pi_{\rm hv}$ saturates at the value $\pi_{\rm hv}^{\rm FBC}|_{T_c}$, as expected.

In all the cases corresponding to $T < T_c$ the time that the probability $\pi_{\rm hv}$ takes to reach the critical percolation value, that is to say, the typical time t_p, scales as $t_p \sim L^{z_p}$ with an exponent z_p smaller than $z_d = 2$. In order to obtain the L-dependence of t_p, we use the finite-size scaling argument adopted in Sec. 1.5.2, *i.e.*, we assume that $\pi_{\rm hv}$ depend on t and L only through the ratio $\ell_p(t)/L$, with the characteristic length $\ell_p(t) \sim \ell_d(t) t^{1/\zeta}$. The exponent

ζ is then determined by looking at the value that gives the best collapse of the data in the prepercolation regime, which corresponds to t such that $\ell_p(t)/L < 1$. In the case of the zero-temperature Glauber dynamics on the square lattice, we found $\zeta \simeq 0.5$, see Sec. 1.5.2. It turns out that the exponent ζ is not greatly affected by the working temperature, as long as it is not too close to T_c. In Fig. A.3 one can see the result of this scaling, for the same cases displayed in Fig. A.2. In these figures, $\pi_{\rm hv}$ is plotted against the rescaled time $t/[L/\ell_G(t)]^\zeta$ (which is equivalent to $[t^{1/\zeta}\ell_G(t)/L]^\zeta = [\ell_p(t)/L]^\zeta$) with $\zeta = 0.5$ for all T, where again the excess-energy growing length $\ell_G(t)$ has been taken as a measure of $\ell_d(t)$.

As one can see, the collapse of the data corresponding to different L works in the limit $L \to \infty$ (in the region $t/[L/\ell_G(t)]^\zeta < 1$), for $T < T_c$. Instead, it completely fails for $T = T_c$. Notice also that the plateau corresponding to the critical percolation value is reached for t_p such that $t_p/[L/\ell_G(t)]^\zeta \simeq 1$, for all $T < T_c$, as it was already observed for the $T = 0$ case.

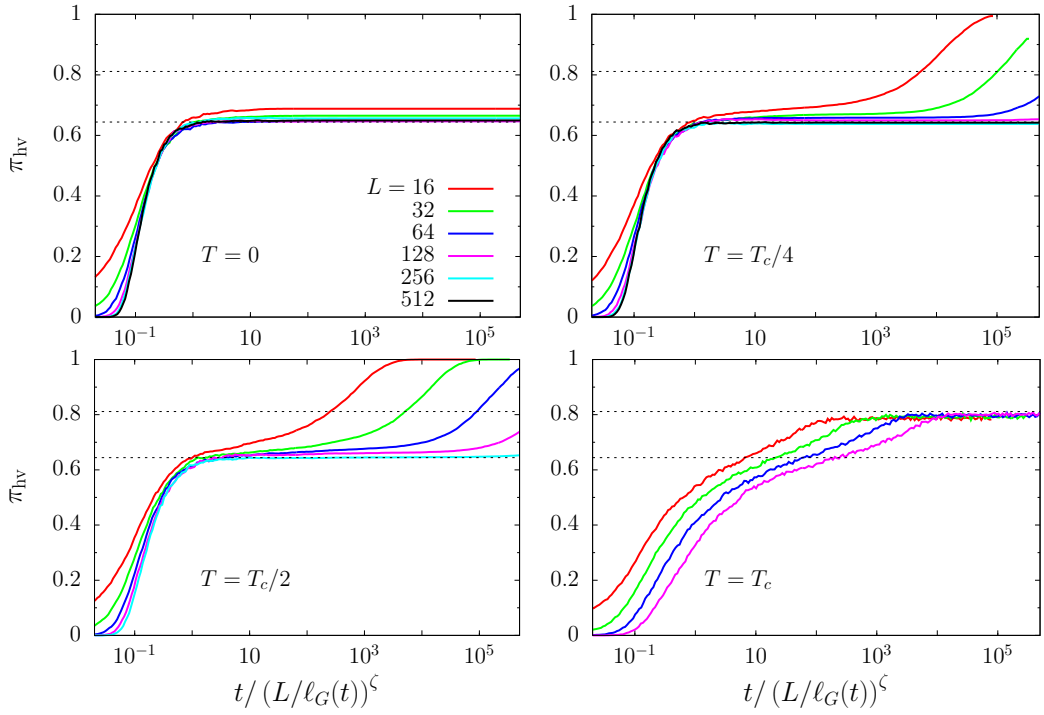

Figure A.3: Ising model on a finite square lattice with FBC, evolving with Glauber dynamics at various temperatures $T \leq T_c$. We show the probability $\pi_{\rm hv}$ that a spin cluster percolates across the lattice along both directions (in the so-called "cross" topology), against the rescaled time $t/\left(L/\ell_G(t)\right)^\zeta$, with $\zeta = 0.5$. The characteristic length scale $\ell_G(t)$ is the numerical value obtained as the inverse of the excess energy, in all cases. The colour code for the different sizes L is the same as in Fig. A.2. As in Fig. A.2, the dotted horizontal lines are at $\pi_{\rm hv}^{\rm FBC}|_{\rm cp} \simeq 0.6442$ and $\pi_{\rm hv}^{\rm FBC}|_{T_c} \simeq 0.8113$, the probabilities of having a cluster that percolates on both horizontal and vertical directions at critical percolation, and at the Ising critical temperature, respectively.

In conclusion, the data shown here suggest that a critical-percolation-like scaling regime appears also in the KIM evolving with Glauber dynamics at a finite subcritical temperature. In a certain sense, the $T = 0$ equilibrium fixed point acts as an attractive fixed point also for the relaxation dynamics at $T < T_c$. On the other hand, we clearly see that the phenomena associated to critical percolation disappear as $T \to T_c$.

A.2 Ising model evolving with Glauber dynamics on a honeycomb lattice

In what follows, we outline the main aspects of the percolation phenomena that emerge in the domain growth for a KIM evolving with Glauber dynamics (at a subcritical target temperature) on a honeycomb lattice. We show how the choice of the particular lattice geometry can affect greatly the typical times scales associated to the approach to the critical-percolation-like scaling regime studied in Chap. 1.

Before discussing these results, we need to clarify an important technical aspect, namely, the way we implemented the honeycomb lattice in our numerical simulations. Essentially, we implemented a mesh of honeycomb lattice with size $L \times L$ by taking a mesh of square lattice with the same linear size and then removing some of the lattice bonds. More precisely, we always represented the system by means of a $L \times L$ square grid. The particular lattice geometry is given by the rules that define the nearest-neighbours of each grid vertex. For the square lattice, each site (i, j), (with $1 \leq i, j \leq L$, i and j representing the row and column indices on the square grid, respectively) has links with the sites $(i, j+1)$, $(i+1, j)$, $(i, j-1)$ and $(i-1, j)$ (with additional constraints to take into account boundary conditions). For the honeycomb lattice, each site (i, j) such that $i + j$ is an even integer has only links with the sites $(i, j+1)$, $(i+1, j)$ and $(i, j-1)$, while each site (i, j) such that $i + j$ is odd has only links with the sites $(i, j+1)$, $(i, j-1)$ and $(i-1, j)$, which amounts essentially to removing some of the vertical links from the square lattice. The consequence of this construction is that the honeycomb lattice mesh used in our simulations has an aspect ratio different from 1. Precisely, the ratio between the longer side and the shorter one is $\sqrt{3}$.

We have seen that, in the case of the zero-temperature Glauber dynamics on a square lattice with PBC, the system can get blocked in a spin configuration in which only flat domain walls are present, and that these so-called "striped" spin configurations are the only possible *absorbing* states. In general, on most regular lattices, non-percolating spin clusters are unstable with respect to the single spin-flip zero-temperature dynamics. In the case of the $T = 0$ Glauber dynamics on the honeycomb lattice, however, there are many more possible ways of constructing spin clusters that are *frozen*, that is to say, spin clusters that can not be broken unless energy-increasing spin flips are allowed. In Fig. A.4 we give an example of a frozen spin configuration.

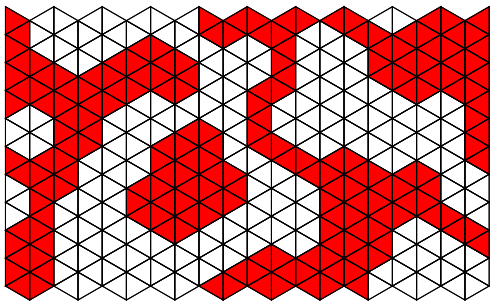

Figure A.4: Example of a *frozen* configuration for the zero-temperature Glauber dynamics on a honeycomb lattice of size 20×20 with PBC. Each lattice site is represented by a triangular cell, with the color (red or white) indicating the spin orientation.

Notice that non-percolating domain walls can be stable with respect to the zero-temperature

Glauber dynamics and, in general, stable domain walls can have a very complicated geometry compared to those generated in the case of the dynamics on the square lattice (or the triangular lattice) which, instead, can only be flat. The number of such metastable states is exponentially large in $N = L^2$ [141], the number of lattice sites, and each one corresponds to a valley in the energy landscape of the model, in a certain way, very similar to that of spin glass models [142]. It is no surprise, then, that the zero-temperature relaxation dynamics, starting from an infinite temperature condition, gets easily trapped in one of these metastable states and very rarely the system is actually led to one of the two ground states.

These aspects are reflected in the time evolution of the typical domain radius. In the left panel of Fig. A.5 we show the excess-energy growing length, ℓ_G, plotted against time t, for the zero-temperature Glauber dynamics on a honeycomb lattice with PBC, for various values of L. As already stated before, this observable measures approximately (or it is proportional to) the average radius of spin clusters, or equivalently, the average distance between two neighbouring domain walls. As one can see, ℓ_G saturates to the value $\ell_{\rm sat} \simeq 4$ very soon in the dynamics, precisely around $t_{\rm sat} \simeq 10$, independently of the system size.

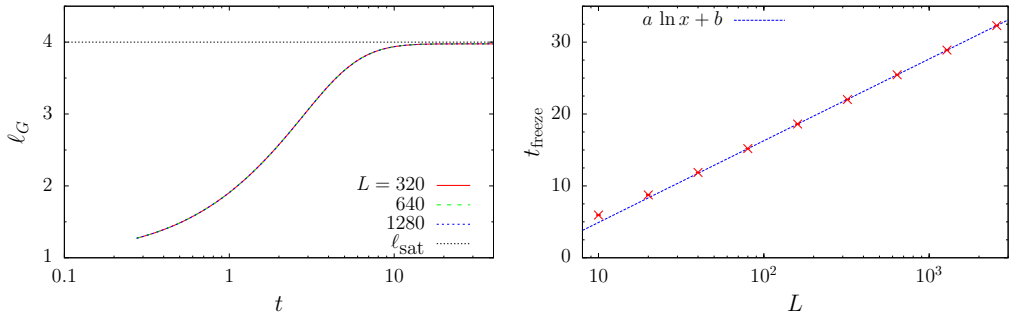

Figure A.5: In the left panel, the excess-energy growing length, ℓ_G, for the zero-temperature Glauber dynamics on a finite honeycomb lattice with PBC, as a function of time, for lattice sizes $L = 320,\ 640$ and 1280. ℓ_G saturates at $\ell_{\rm sat} \simeq 4$ at a time $\simeq 10$ independently of L. In the right panel, the average freezing time, $t_{\rm freeze}$, as a function of size L (red data points) and the best fit, $t_{\rm freeze} \simeq 4.95 \ln L - 6.47$ (keeping only data with $L > 40$), indicated by the dashed blue line.

The behaviour of $\ell_G(t)$ is totally different from what it is observed in the case of the zero-temperature Glauber dynamics on a finite square lattice, see Sec. 1.5.1 and Fig. 1.10. In fact, for the latter, ℓ_G takes the form $\ell_G(t) \sim t^{\frac{1}{2}}$ for very large times, thus agreeing with the NCOP coarsening theory according to which the typical domain radius should grow, asymptotically in time, as $\ell_d(t) \sim t^{1/z_d}$ with $z_d = 2$. Instead, in the case of the dynamics on the honeycomb lattice, after an initial fast transient, the growing length ℓ_G seems to saturate to $\ell_{\rm sat} \simeq 4$. To be more precise, if one zooms at the data at times $t \sim t_{\rm sat} \sim 10$, one can see that ℓ_G actually does not get immediately fixated at the saturation value, but it continues to grow very slowly, approaching this value from below only asymptotically in time (not shown in the plot). This fact suggests that, around time $t_{\rm sat} \simeq 10$, a realization of the dynamics has typically already reached a spin configuration which is very close to be frozen, that is to say, one in which the location of each domain wall in the future frozen configuration has already been established, apart from a few spin flips that are not going to alter significantly the morphology of the domain pattern. In particular, if in the frozen configuration there are percolating domain walls, they have been already established at the time $t_{\rm sat}$, and the further evolution is not going to change their topology.

To help the reader understand this qualitative description, we show some snapshots of a KIM evolving under zero-temperature Glauber dynamics, on a finite honeycomb lattice with PBC, in Fig. A.6.

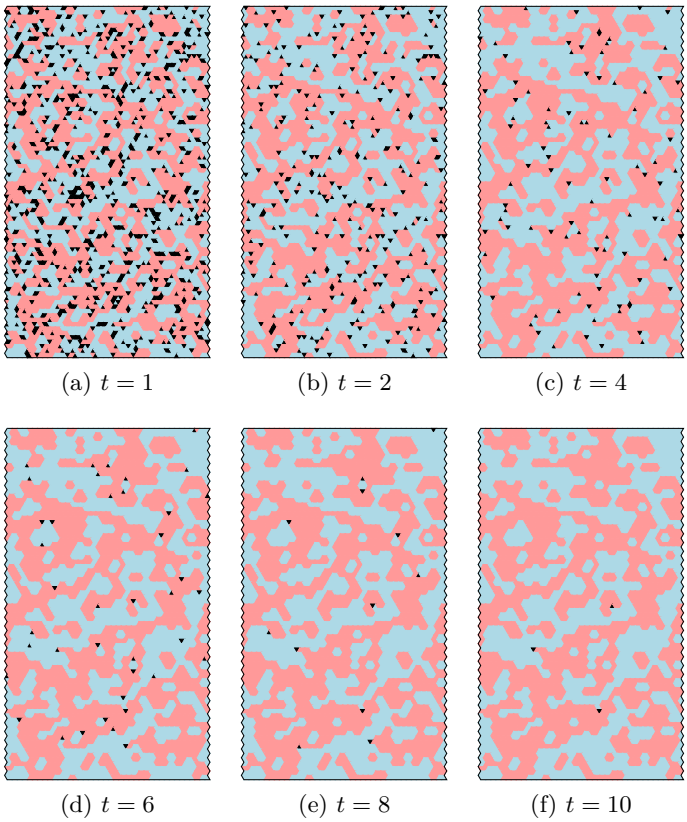

(a) $t = 1$ (b) $t = 2$ (c) $t = 4$

(d) $t = 6$ (e) $t = 8$ (f) $t = 10$

Figure A.6: Some snapshots of the evolution of a spin configuration under zero-temperature Glauber dynamics on a honeycomb lattice with linear size $L = 80$ and PBC. Each site of the lattice is represented by a triangular cell, as in Fig. A.4. The spins that are *frozen* at a given time, (*i.e.* those that can not be flipped without an energy cost) are represented with light colours, red for $+1$ spins and blue for -1 spins. The black cells represent spins belonging to the two phases that can still be flipped.

From these snapshots we see that, at late times, the sites whose spin can still be flipped are not very numerous and are far apart in the system. When one of these sites has its spin flipped the local effective field associated with each one of the remaining "flippable" spins, which determines their probability of flipping, is not changed. By using this observation we can attempt to estimate t_{freeze}, the average time at which the system freezes.

Let us assume that, at a sufficiently long time t, there is a population of $N_f(t)$ spins that can be flipped and that the act of flipping each one of these spins is independent from the others, as supported by the statement above. If λ is the probability of flipping a spin per unit time (or equivalently, $\tau = 1/\lambda$ the average time between two consecutive spin flips), then $N_f(t)$ decays with a "radioactive" law, $N_f(t) = N_f(t_0)\, e^{-\lambda(t-t_0)}$, with $N_f(t_0)$ the number of flippable spins at a reference time $t_0 < t$. We can fix t_0 to be t_{sat}, the time at which ℓ_G reaches saturation and thus the time at which the very few spins that can be flipped are located at a very large distance between each other, so that they can be considered

independent. Suppose $N_f(t_0) = \rho N$ with $N = L^2$ the number of lattice sites and $\rho \in (0, 1)$. The average time at which the system freezes can be associated with the time at which $N_f = 1$, implying $\lambda\,(t_{\text{freeze}} - t_0) \simeq \ln(\rho N)$. Then, assuming t_0 does not depend on the system size, for $t_{\text{freeze}} \gg t_0$ we obtain $t_{\text{freeze}} \simeq (2/\lambda) \ln L + C$, with C some constant.

This approximate law is actually confirmed by the measurements of t_{freeze} by means of numerical simulations. In the right panel of Fig. A.5 we show the average freezing time, t_{freeze}, for the zero-temperature Glauber dynamics on a finite honeycomb lattice, plotted against the system linear size L. By fitting the function $a \ln L + b$ to the data we find $t_{\text{freeze}} \simeq 4.95 \ln L - 6.47$.

A.2.1 Percolation phenomena

In the case of the zero-temperature Glauber dynamics on the honeycomb lattice, as we have already explained above, the system gets blocked in a spin configuration with a highly complex domain pattern at a relatively short time. The domain pattern of these so-called frozen configurations is richer in structure than that of the long-lived stripe states occurring in the late stages of the same coarsening dynamics on the square lattice. Nevertheless we can still observe a transition from the initial fully disordered spin configuration to a critical-percolation-like scaling regime. However, since the time required by the system to freeze depends logarithmically on the system linear size L, $t_{\text{freeze}}(L) \sim \ln L$, the typical time t_p needed to reach the critical-percolation-like scaling regime can not be a power law L^{z_p}, as conjectured in the case of the dynamics on the square lattice. Instead, we expect $t_p(L) \sim \ln L$.

First of all, a clear evidence of the existence of a dynamical scaling regime in which the spin clusters have the geometrical properties associated with $2d$ critical percolation is given by the measurements of the variance of the winding angle relative to the domain walls, the observable denoted by $\langle \theta^2 \rangle$ that we defined in Sec. 1.3.

In Fig. A.7, we show measurements of $\langle \theta^2 \rangle$ obtained from numerical simulations in the case of the zero-temperature Glauber dynamics on a honeycomb lattice with PBC and $L = 1280$. In this case $\langle \theta^2 \rangle$ was measured on the external hull of the largest spin cluster. As one can see, $\langle \theta^2 \rangle$, as a function of the curvilinear distance x, develops the expected behaviour $\langle \theta^2 \rangle \simeq a + b \ln x$ very soon in the course of the dynamics, and contrary to what happens in the case of the same dynamics on the square lattice, a short length scale region corresponding to equilibration, that is to say, smooth domain walls, is not present. This is due to the fact that, most of the times, the system is getting blocked in a spin configuration with domain walls that retain their fractal nature even at short length scales.

The behaviour of $\langle \theta^2 \rangle$ as function of $\ln x$ still conforms to that expected from critical percolation hulls. A fit of the function $f(x) = a + \frac{4\kappa}{(8+\kappa)} \ln x$ (also shown in the plot) to the data at $t \simeq 2.5$, in the whole range of x over which $\langle \theta^2 \rangle$ was measured, yields $\kappa \simeq 6.02(1)$. Even if a crossover between different length scales is not present, we can still collapse the data corresponding to different times t by rescaling the curvilinear coordinate x by $\ell_d(t)$, as it is shown in the inset in the same panel.

In Fig. A.8 we show the time evolution of the wrapping probabilities. Notice that, because of the way we implemented the honeycomb lattice in the numerical simulations, as explained above, the probabilities π_{h} and π_{v} are not equal. Precisely, the lattice mesh has aspect ratio $\sqrt{3}$, thus we need to compare our measurements to the values of the corresponding wrapping probabilities for $2d$ critical percolation on a lattice of aspect ratio $\sqrt{3}$. These can be computed [8, 57, 58] and are given by $\pi_{\text{hv}}^{(p)} \simeq 0.5120$, $\pi_{\text{h}}^{(p)} \simeq 0.4221$, $\pi_{\text{v}}^{(p)} \simeq 0.0408$ and

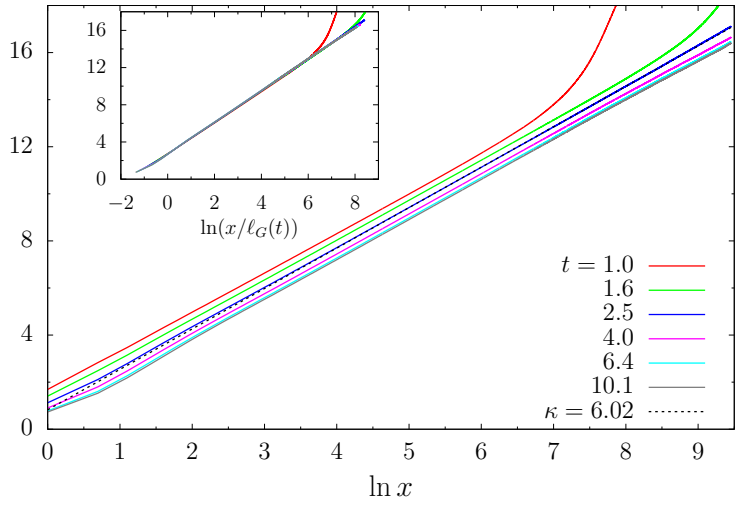

Figure A.7: KIM evolving with zero-temperature Glauber dynamics on a honeycomb lattice. We show the average squared winding angle, $\langle\theta^2(x,t)\rangle$, against $\ln x$ with x being the curvilinear distance along a hull. The data are relative to the dynamics on a honeycomb lattice with PBC and $L = 1280$, and $\langle\theta^2\rangle$ was measured on the external hull of the largest spin cluster (which exists only if the cluster is not wrapping). The straight dashed line represents a fit of the function $f(x) = a + 4\kappa/(8+\kappa)\ln x$ to the data in the "linear" region. The fit yields $\kappa = 6.02$. The inset contains the same observable plotted against $\ln[x/\ell_G(t)]$ with $\ell_G(t)$ the characteristic length obtained as the inverse of the excess energy.

$\pi^{(p)}_{\text{diag}} \simeq 0.0250$ (for us the vertical side will be the longer one). As already done in the case of the zero-temperature Glauber dynamics on the square lattice, we try to rescale time by a L-dependent characteristic time $t_p(L)$ in order to make the data corresponding to different values of L collapse in the so-called pre-percolation region. We expect $t_p \sim \ln L$ since this characteristic time scale can not increase faster than the average freezing time t_{freeze} with the system size. However, we find that a better collapse of the data is achieved by using the rescaled time $t/\ln[L/\ell_G(t)]$, with $\ell_G(t)$ the excess-energy growing length.

As one can see from Fig. A.8, the wrapping probabilities approach the corresponding values for $2d$ critical percolation around a time t such that $t/\ln[L/\ell_G(t)] \sim 1$, and then remain fixated at these values for the rest of the evolution of the system. An estimate of t_p is then given by the relation $t_p/\ln[L/\ell_G(t_p)] \simeq 1$, which entails $t_p + \ln(\ell_G(t_p)) \simeq \ln L$. This last relation is not explicit in t_p and, in particular, it does not coincide with the scaling behaviour $t_p \sim \ln L$. However, as seen previously, the growing length $\ell_G(t)$ reaches almost saturation very early in the course of the dynamics, thus we can assume that, for times t close to t_p, $\ln(\ell_G(t))$ grows much slower than t. Then we can use the approximation $t_p \simeq \ln L + C$, with C some constant.

The same characteristic time scale is extracted from the analysis of the time evolution of the largest spin cluster. We have seen in Sec. 1.5.4 that, when the system enters in the so-called critical-percolation-like dynamical scaling regime, (that is, for $t > t_p$), the size of the largest cluster, A_c, satisfies the scaling relation $A_c/\ell_d(t)^2 \sim (L/\ell_d(t))^{D_A}$ with $D_A = 91/48$ the fractal dimension of the incipient percolating cluster in $2d$ critical percolation. Analogously, the length of the domain walls that belong to its interface have the scaling behaviour $l_c/\ell_d(t) \sim (L/\ell_d(t))^{D_\ell}$ with $D_\ell = 7/4$ the fractal dimension of infinite domain

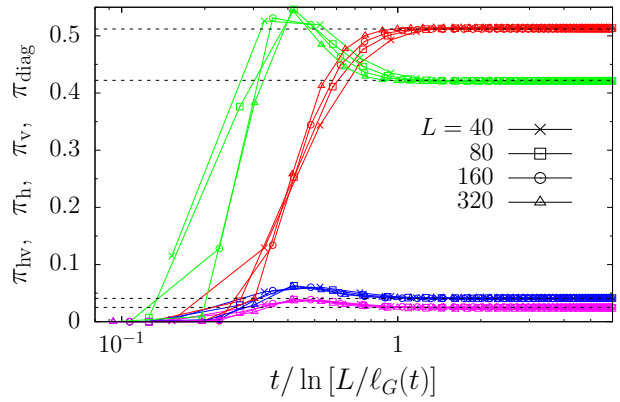

Figure A.8: Ising model on a finite honeycomb lattice with PBC, evolving under $T = 0$ Glauber dynamics. We show the probabilities $\pi_{\rm hv}$ (red), $\pi_{\rm h}$ (green), $\pi_{\rm v}$ (blue), $\pi_{\rm diag}$ (purple), for different lattice sizes L. The horizontal dashed lines correspond to the expected values at critical percolation for a rectangular sheet with aspect ratio $\sqrt{3}$: 0.5120, 0.4221, 0.0408 and 0.0250, respectively. Data are plotted against the scaling variable $t/\ln[L/\ell_G(t)]$, with $\ell_G(t)$ the excess energy growing length, taken as a measure of $\ell_d(t)$.

walls in $2d$ critical percolation. The presence of such scaling regime is confirmed by our measurements, as one can see in Fig. A.9. Again, we consider two different contributions to the measurement of l_c: on one hand, the length of the external hull of the largest spin cluster, which is present only when the cluster is not percolating; on the other hand, the length of one of the two wrapping hulls, which are present when the cluster is percolating.

The data corresponding to different values of L, the system linear size, can be collapsed by rescaling time as $t/\ln[L/\ell_G(t)]$. The onset of the critical percolation scaling regime (corresponding to the point where the rescaled data become constant) again occurs at a time t such that $t/\ln[L/\ell_G(t)] \sim 1$, approximately.

From the analysis of the wrapping probabilities and the scaling behaviour of the geometric properties of the largest spin cluster, we can conclude that, in the case of zero-temperature Glauber dynamics on a finite honeycomb lattice, the typical time scale t_p that the system needs to reach the critical-percolation-like scaling regime satisfies the relation $t_p + \ln(\ell_G(t_p)) \simeq \ln L$, with L the system linear size. In analogy with what was done in the case of the same dynamics on the square lattice, we introduce a characteristic length scale $\ell_p(t)$ that, for $t < t_p$, represents the length scale up to which it is possible to observe critical percolation features in the geometry and statistics of the spin clusters, with t_p satisfying $\ell_p(t_p) = L$. We assume that ℓ_p has the following form

$$\ell_p(t) \simeq \ell_G(t)\ \mathrm{e}^{\alpha t} \quad , \tag{A.2}$$

with α an exponent to be determined. This form of ℓ_p implies $t_p \simeq \frac{1}{\alpha}(\ln L - \ln(\ell_G(t_p)))$.

In order to test the validity of this assumption, we studied the time evolution of the number density of domain areas. In Fig. A.10 we report the measurements of $\mathcal{N}(A,t)$ for the zero-temperature Glauber dynamics on a finite honeycomb lattice with PBC and size $L = 1280$, as function of the domain area A, for several times t. We observe that the approach to a critical-percolation-like distribution, namely, an algebraic decay of the form $\mathcal{N}(A,t) \simeq C(t)A^{-\tau_A}$ with $\tau_A = 187/91$, occurs very early in the coarsening process. In particular, if we fit the function $f(A) = 2c\,A^{-\tau}$ to the data corresponding to time $t \simeq 10$ (which corresponds approximately to the time at which $\ell_G(t)$ has reached almost saturation),

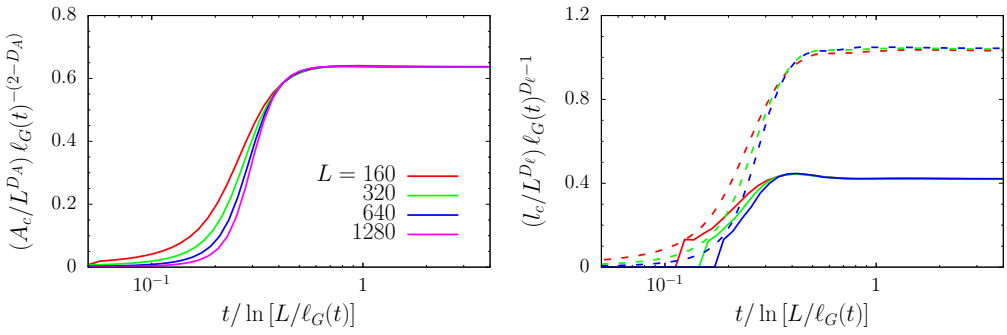

Figure A.9: Analysis of the geometric properties of the largest spin cluster in the case of the IM on a finite honeycomb lattice with PBC, evolving under $T = 0$ Glauber dynamics, for different values of L. On the left we show $A_c/L^{D_A}\ \ell_G(t)^{-(2-D_A)}$, while on the right $(l_c/L^{D_\ell})\ \ell_G(t)^{D_\ell-1}$ both plotted against the rescaled time $t/\ln[L/\ell_G(t)]$ where $\ell_G(t)$ is the characteristic length obtained as the inverse of the excess energy. In the right panel, the continuous lines represent the contribution to l_c due to wrapping domain walls, while the dashed ones the contribution from the external hull (when the largest cluster is not wrapping). The colour code is the same in both panels.

we obtain $c = 0.028(1)$ and $\tau = 2.035(5)$, values that are very close to the expected $c_d \simeq 0.0289$ and $\tau_A = 187/91 \simeq 2.0549$ for $2d$ critical percolation.

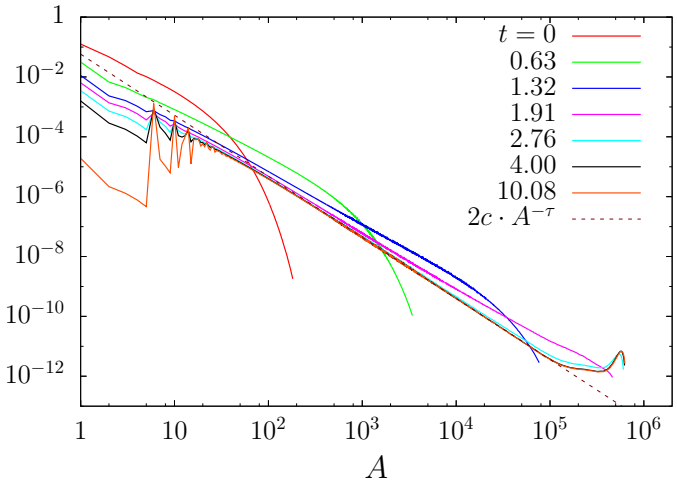

Figure A.10: Time evolution of the number density of domain areas for the zero-temperature Glauber dynamics on a honeycomb lattice with PBC and linear size $L = 1280$. We show the domain area distribution $\mathcal{N}(A,t)$ vs. A at various times t given in the key. The function $f(A) = 2c\,A^{-\tau}$ has been fitted to the data corresponding to time $t = 10.08$ in the range $[10^3, 5\times10^4]$ (the curve is represented by a dashed line). The fit yields the estimates $c = 0.028(1)$ and $\tau = 2.035(5)$ that are close to the expected $c_d \simeq 0.0289$ and $\tau_A = 187/91 \simeq 2.0549$.

In the left panel of Fig. A.11 we show the rescaled number density, $A^{\tau_A}\,\ell_G(t)^{2(2-\tau_A)}\,\mathcal{N}(A,t)$, plotted against $A/\ell_G(t)^{2-D_A}$ (with τ_A and D_A the Fisher exponent and fractal dimension of domains, respectively, in $2d$ critical percolation). As explained in Sec. 1.5.5, the reason why we rescale the domain area A as $A/\ell_G(t)^{2-D_A}$ is that this allows us to collapse the "bump"

appearing for very large A. From the plot we can see that a region where $\mathcal{N}(A,t)$ behaves as in $2d$ critical percolation is already established at $t \simeq 4$, corresponding to a plateau in the rescaled number density.

To highlight the existence of the additional length scale $\ell_p(t)$ we perform the same type of scaling analysis as in Sec. 1.5.5.2 in the case of the zero-temperature Glauber dynamics on the square lattice. We assume that

$$\mathcal{N}(A,t) \sim 2c_d^{\rm eff}(t)\, A^{-\tau_A}\, \Phi\left(\frac{A/\ell_d(t)^2}{[\ell_p(t)/\ell_d(t)]^{D_A}}\right) \quad , \tag{A.3}$$

where Φ is the corrective factor that takes into account the fact that, at a given time t, on scales A such that $\frac{A}{\ell_d(t)^2} > \left[\frac{\ell_p(t)}{\ell_d(t)}\right]^{D_A}$ the critical-percolation-like behaviour is not observed. In the right panel of Fig. A.11 we show the result of this scaling: we plot the rescaled number density $A^{\tau_A}\,\ell_G(t)^{2(2-\tau_A)}\,\mathcal{N}(A,t)$ against the rescaled area $(A/\ell_G(t)^{2-D_A})/\ell_p^{D_A}(t)$, where again $\ell_G(t)$ is taken as a measure of $\ell_d(t)$ and we used $\ell_p(t) = \ell_G(t)\,\mathrm{e}^{\alpha t}$. The constant α was estimated by looking at the value which yields the best collapse of the data after rescaling. Apart from deviations at small areas and in the region where the contribution from percolating clusters becomes significant (the steep peaks appearing for $t \geq 2.3$), the data for different t can be collapsed optimally if $\alpha \simeq 2.65$. As in the case of the data relative to the dynamics on the square lattice, in the region corresponding to the pre-percolation regime, that is for $A/[\ell_G^{2-D_A}(t)\ell_p^{D_A}(t)] \geq 1$ and before finite-size effects take over, the rescaled cluster size distribution can be described by a power law $C\cdot x^a$ in the scaling variable $x = A/[\ell_G^{2-D_A}(t)\ell_p^{D_A}(t)]$. The best fit of the function $f(x) = C\cdot x^a$ to the rescaled data $A^{\tau_A}\,\ell_G(t)^{2(2-\tau_A)}\,\mathcal{N}$ at time $t = 1$ in the interval $[0.1, 10]$ of $x = A/[\ell_G^{2-D_A}(t)\ell_p^{D_A}(t)]$ gives $a = 0.332(1)$, a value which is close to that found in the case of the dynamics on the square lattice.

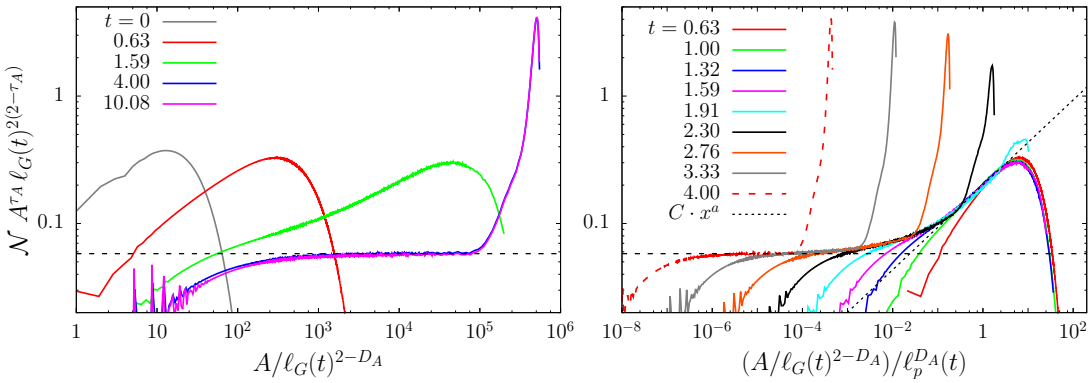

Figure A.11: Ising model on a honeycomb lattice with PBC and $L = 1280$, evolving under $T = 0$ Glauber dynamics. We show the pre-percolation scaling of the number density of domain areas. The quantity $A^{\tau_A}\,\ell_G(t)^{2(2-\tau_A)}\,\mathcal{N}(A,t,L)$ is plotted against $A/\ell_G(t)^{2-D_A}$ in the left panel and against $\left(A/\ell_G(t)^{2-D_A}\right)/\ell_p^{D_A}(t)$ in the right panel, with $\ell_G(t)$ the characteristic length obtained as the inverse of the excess energy, and $\ell_p(t) = \ell_G(t)\,\mathrm{e}^{\alpha\, t}$ with $\alpha \simeq 2.6$ yielding the best collapse. The constant $2c_d \simeq 0.0579$ is represented by a horizontal dashed line. In the right panel, the function $\Phi(x) = C\,x^a$ has been fitted to the data at time $t = 1$ in the region of the scaling variable corresponding to the pre-percolating regime (approximately, the interval $[0.1, 1]$), yielding $a = 0.332(1)$, and it is represented by the dotted line.

Finally, in Fig. A.12, we show the time evolution of the size distribution of the largest

spin cluster, denoted by N_p. In this figure the quantity $L^{2+D_A} N_p(A,t,L)$ is plotted against the rescaled area A/L^{D_A}, for different values of the linear size L and at different times. At short t, the overall shape of the distribution depends strongly on the size of the lattice and time, while at sufficiently long t it seems to approach a stationary form that depends only on A and L through A/L^{D_A}. As expected, for $t > t_p$ the system is in the so-called critical percolation dynamical scaling regime, and thus N_p should obey the finite-size scaling ansatz $N_p(A,t,L) \sim n_p\left(\frac{A}{L^{D_A}}, t\right)$, where n_p is a proper scaling function (with the t-dependence left unspecified), since we know that the average size of the largest cluster, A_c, scales with the system linear size as $A_c \sim L^{D_A}$. We also note a very particular scaling behaviour as both t and L vary, in the pre-percolating regime: the curves for $L = 40$ and $L = 160$ at $t = 1$ are replaced by the curves for $L = 160$ and $L = 640$, respectively, at $t = 1.5$. The same is true when passing from $t = 1.5$ to $t = 2$: the curves for $L = 160$, 640 and 2560 replace the ones for $L = 40$, 160 and 640, in this order, and so on. From this observation we can deduce that the typical time scale associated to the approach to percolation, t_p, roughly satisfies the rule $t_p(4L) = t_p(L) + C$ with $C \simeq 0.5$, which implies $t_p(L) \simeq (0.5/\ln 4)\ln L \simeq 0.36 \ln L$. This result supports our claim that $t_p(L) \sim \ln L$.

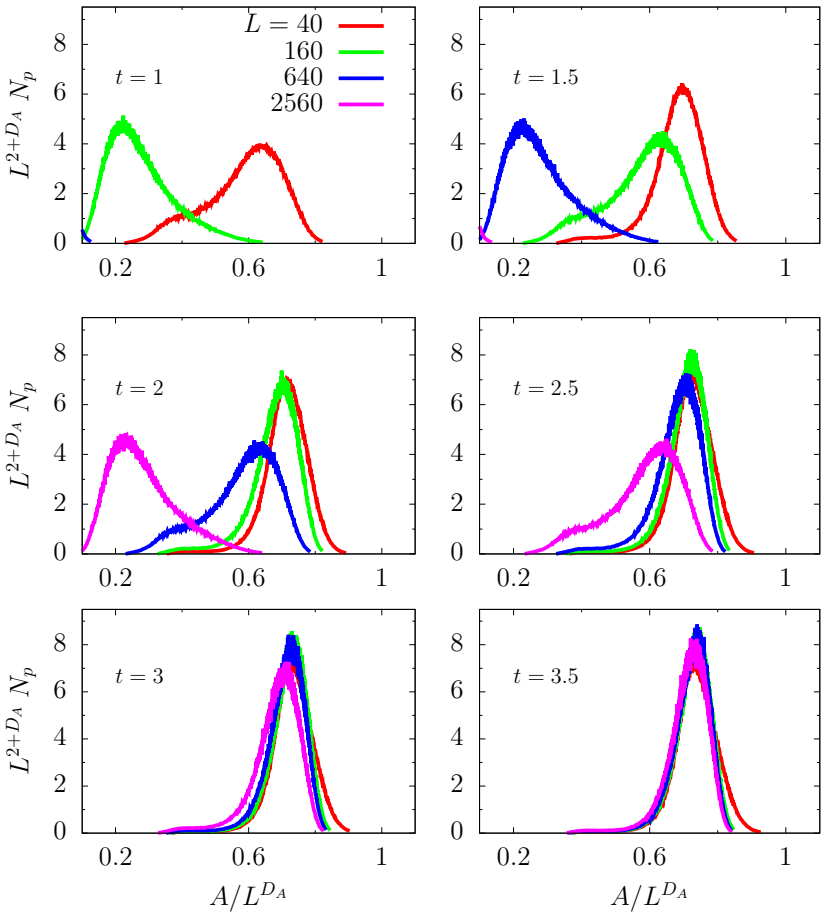

Figure A.12: Time evolution of the size distribution of the largest spin cluster, N_p, for the zero-temperature Glauber dynamics on a honeycomb lattice, for various values of L, the system linear size, as indicated in the key. The quantity $L^{2+D_A}\, N_p$ is plotted against A/L^{D_A} with A the cluster area and $D_A = 91/48$ the fractal dimension of the largest cluster in $2d$ critical percolation. Each panel corresponds to a different time t in the evolution of the system.

Appendix B

B.1 Ising model evolving with nonlocal Kawasaki dynamics

We consider here the nonlocal version of the spin-exchange dynamics studied in Chap. 2. The spin-exchange transition rates are the same as those of Kawasaki rule (Eq. (2.5)), but without the restriction that the lattice sites involved must be nearest-neighbours, that is

$$w_{i,j}(s) = \min\{\ 1,\ \exp\left[-\beta \Delta E_{i,j}(s)\right]\} \quad , \tag{B.1}$$

with

$$\Delta E_{i,j}(s) = J\left(s_i - s_j\right)\left(\sum_{k\in\mathcal{N}(i)\setminus\{j\}} s_k - \sum_{h\in\mathcal{N}(j)\setminus\{i\}} s_h\right) \tag{B.2}$$

where the lattice sites i and j can be chosen anywhere in the lattice. We refer to this (stochastic) spin update rule as nonlocal Kawasaki spin-exchange dynamics. We checked that this *a priori* artificial globally conserved order parameter (GCOP) relaxation dynamics, can be used to sample correctly the equilibrium distribution of the $2d$ Ising model asymptotically in time through Monte Carlo method, and is able to capture the thermodynamic instability at the critical temperature T_c, in the limit $L \to +\infty$.

For our purposes, the initial spin configuration is always chosen in the following way: half of the lattice sites, chosen at random, takes spin $+1$, while the other half takes spin -1. As in the case of the local version of the dynamics, we observed that an unbalanced concentration of the two species do not produce the same percolation phenomena, and, in particular, do not yield a critical percolation domain pattern in the limit of large system size.

The total magnetisation of the system is conserved by the dynamics but, on small scales, the coarsening process looks very similar to that produced by the single spin-flip dynamics. This similariy is somehow expected since, on average, the frequency of spin-exchange events that involve two distant lattice sites is larger than the frequency of spin exchanges between nearest-neighbour sites. Thus, most of the times, a transition of the spin configuration can be thought as made by two *almost* independent spin flips happening simultaneously at two distant points in the system.

The renormalisation group arguments exposed in [143, 137] suggest that, asymptotically, the global conservation law should become irrelevant and the dynamics be controlled by the $\ell_d(t) \simeq t^{1/2}$ growth law, as for NCOP dynamics. Studies of the phase ordering kinetics of coarse-grained field theories with the total magnetisation imposed (on average) through a time-dependent external magnetic field also suggest $\ell_d(t) \simeq t^{1/2}$ at finite temperature [144]. A simple argument exposed by Rutenberg in [145] signals a difference between the dynamics at $T = 0$, where he claimed that the locally conserved order parameter (LCOP) results should be found, $\ell_d(t) \simeq t^{1/3}$, and the dynamics at $T > 0$, where instead $\ell_d(t) \simeq t^{1/2}$. Numerical simulations [146, 147, 143, 148, 149, 144, 145] have only explored relatively short time scales,

$t < 10^4$, and, for this reason, they were not decisive for the determination of the precise value of the dynamical exponent z_d for this type of coarsening dynamics. An experiment using a $2d$ chiral liquid crystal, whose relaxation dynamics can be shown to belong to the GCOP universality class, was consistent with $\ell_d(t) \simeq t^{1/2}$ [150].

In the following we show that also in the more general case of nonlocal spin-exchange dynamics the domain growth process reaches a critical-percolation-like dynamical scaling regime in which several observables, in particular those related to the geometrical features of the spin clusters, satisfy dynamical scaling relations with scaling functions and scaling dimensions from $2d$ critical percolation universality class. Again, the approach to the critical-percolation-like scaling regime is described by a characteristic length $\ell_p(t)$ which we find to have the time dependence $\ell_p(t) \sim \ell_d(t) t^{1/\zeta}$, with the exponent ζ estimated numerically.

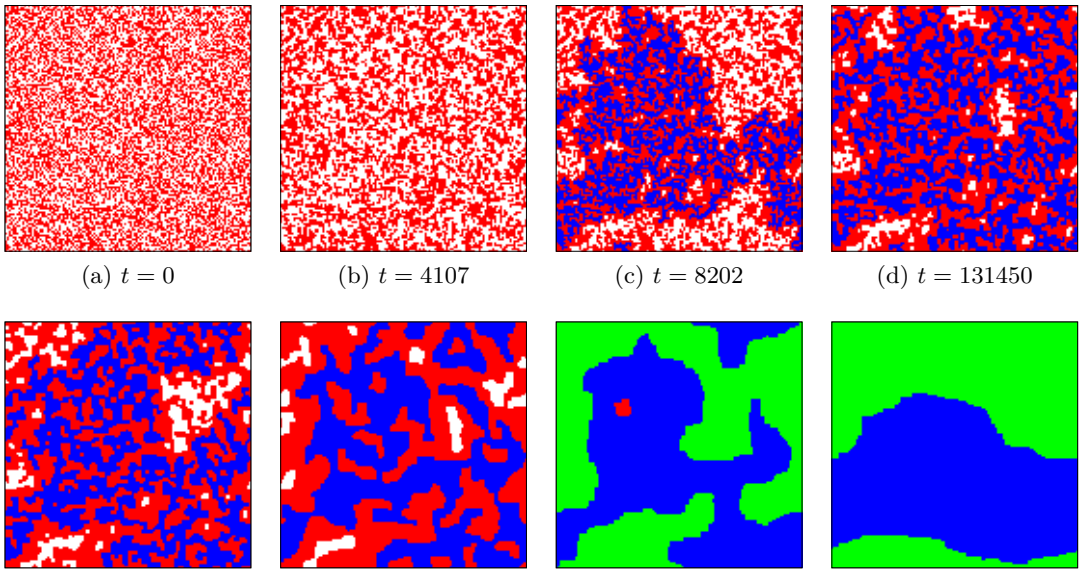

(a) $t = 0$ (b) $t = 4107$ (c) $t = 8202$ (d) $t = 131450$

(e) $t = 4.2 \times 10^6$ (f) $t = 1.3 \times 10^8$ (g) $t = 4.3 \times 10^9$ (h) $t = 1.4 \times 10^{11}$

Figure B.1: Snapshots of a spin configuration on a square lattice with PBC and size 128×128, evolving with nonlocal Kawasaki dynamics at target temperature $T = T_c/4$, starting from an infinite temperature initial condition. The concentration of the two species of spins is the same. Spins $s_i = -1$ are shown as red points while spins $s_i = +1$ are shown as white points. Percolating clusters of spins $s_i = -1$ are shown in green and percolating clusters of spins $s_i = +1$ in blue. The times at which the snapshots are taken are indicated below each panel.

Before delving into the analysis of the results obtained through the numerical simulations, let us show an example of spin configuration evolving under nonlocal Kawasaki dynamics. In Fig. B.1 we present a series of snapshots of the Ising model, on a finite square lattice with PBC, evolving under nonlocal Kawasaki dynamics at temperature $T_c/4$. Also in this case we observe the presence of percolating structures. Apart from the absolute time values, that are definitely much longer than those explored using local Kawasaki spin-exchange updates for the same lattice size (see Fig. 2.3), we do not see much of a difference in the overall morphology of the spin clusters. In particular, when the system is still far from reaching equilibrium, the domain walls display a fractal structure. As one can see, at a certain point, there are two large percolating spin clusters, of opposite spin, that are occupying most of the

system. As the coarsening process goes on, these two large clusters "absorb" all the remaining non-percolating domains, until the system is left in the situation of panel (h): only two long percolating domain walls survive, apart from some small ones produced by very rare thermal fluctuations. At this stage of the dynamics, the system is practically equilibrated (under the constraint of conserved total magnetisation).

B.1.1 The growing length

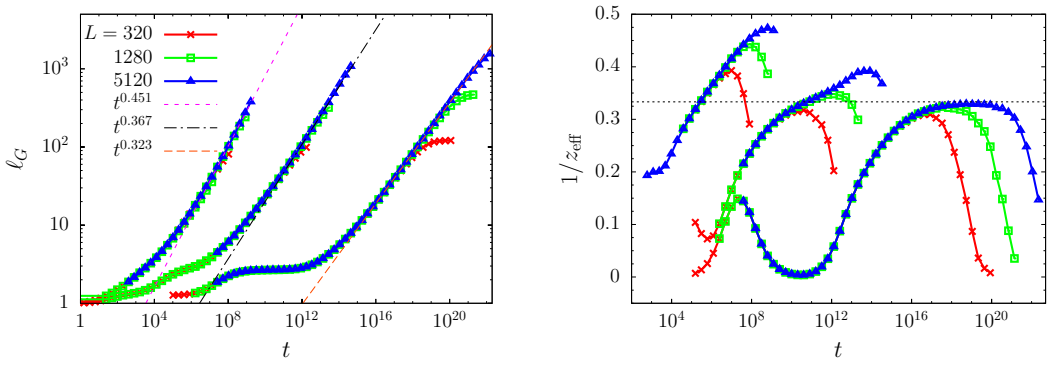

Figure B.2: Left: the excess-energy growing length ℓ_G as a function of time t for the nonlocal Kawasaki dynamics on a square lattice with PBC at temperatures $T = T_c/2$ (data on the left), $T = T_c/4$ (data in the middle) and $T = T_c/8$ (data on the right). For each temperature, we show the data for three different values of L, the lattice linear size. A power law $a\,t^b$ has been fitted to the data corresponding to $L = 5120$ in the intermediate region (between the initial transient region and the final saturation one) and is represented by the straight dashed lines (see the key for the fitted exponents). Right panel: corresponding effective growth exponents. They increase weakly with the linear size L of the lattice. The dotted horizontal line corresponds to 1/3.

In the left part of Fig. B.2 we show $\ell_G(t)$ for the nonlocal Kawasaki dynamics on a square lattice with PBC, with linear sizes $L = 320$, 1280, 5120. The leftmost curves correspond to the dynamics at temperature $T = T_c/2$, the ones in the middle to $T = T_c/4$, and the ones on the right to $T = T_c/8$. Note that $\ell_G(t)$ can be at most $L/2$ because of the global conservation of the number of spins of each species which makes sure that the spin configuration corresponding to minimal energy is the one with just two domains separated by a straight interface. In each case, we observe the presence of an initial transient regime and a final saturation (which is clearly visible only for the smaller L) and in both regimes the behaviour of $\ell_G(t)$ cannot be described by a simple power law. Between these two regimes, $\ell_G(t)$ can be approximated by a power law. Moreover, we notice the presence of a *plateau* in the transient regime which becomes longer as T decreases with the effect of delaying the point at which the power law behaviour sets in.

In the left panel we display a fit of the function $f(t) = C\,t^{1/z}$ to the data relative to $L = 5120$ in the intermediate region, for each temperature. For the dynamics at $T = T_c/2$ we obtain $1/z \simeq 0.442$, a value which is close to the expected asymptotic result for GCOP dynamics, $1/z_d = 1/2$; for the dynamics at $T = T_c/4$ we obtain $1/z \simeq 0.367$; and, for the one at $T = T_c/8$ we find $1/z \simeq 0.322$, close to the value $1/z_d = 1/3$ expected for the dynamics at

$T = 0$, according to Rutenberg [145].

In the right panel in Fig. B.2 we show the effective growth exponent z_{eff}^{-1}, defined as the logarithmic derivative of $\ell_G(t)$, for each one of the cases present in the left panel. At $T_c/2$, the effective exponent z_{eff}^{-1} seems to converge towards $1/2$ as L increases, as expected. At $T_c/8$ it spends approximately three time decades around $1/3$. At $T_c/4$, we observe an intermediate result. At each temperature, the effective exponent reaches a maximum and then starts to fall off due to the final saturation of $\ell_G(t)$. Note that, for fixed T, the larger is L the larger is the maximum value reached by z_{eff}^{-1} and longer is the period of time that z_{eff}^{-1} stays at this value. These observations confirm that the expected value $z_{\text{eff}} = 2$ at finite temperature is reached for not too low temperature (for example, $T = T_c/2$), as $L \to \infty$. Instead, for sufficiently low temperature (*e.g.* $T = T_c/8$), the zero-temperature predicted result $z_{\text{eff}} = 3$, corresponding to COP coarsening universality class, is instead observed in the large L limit.

B.1.2 Critical percolation phenomena

B.1.2.1 *Average squared winding angle*

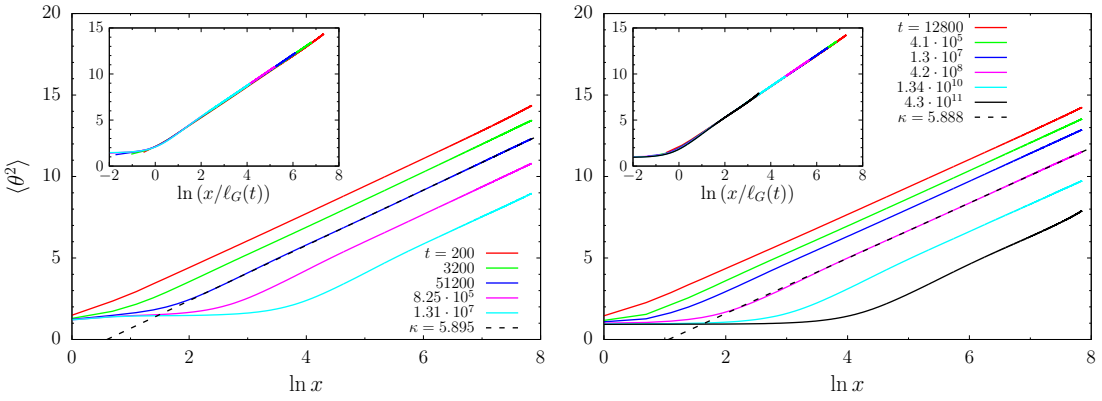

Figure B.3: Average squared winding angle, $\langle\theta^2\rangle$, against $\ln x$ with x the curvilinear distance along a hull, for closed hulls (nonzero total winding angle). The data is for the Ising model on a square lattice with PBC and $L = 1280$, evolving under nonlocal Kawasaki dynamics at temperatures $T = T_c/2$ (left panel) and $T = T_c/4$ (right panel). In the insets, the length x is rescaled by $\ell_G(t)$, the characteristic length obtained as the inverse of the excess energy. The black dashed lines are fits of the function $f(x) = \text{cst.} + 4\kappa/(8+\kappa)\ln x$ to the numerical data in the "linear" region. The fits yield $\kappa \simeq 5.895$ and $\kappa \simeq 5.888$ for the quench to $T_c/2$ and that to $T_c/4$, respectively. The times shown are the same in the main plots and the insets and are indicated in the keys.

A signature of the presence of the critical-percolation-like scaling regime in the coarsening process can be seen in the time evolution of the variance of the winding angle relative to the domain walls, the observable that we denoted by $\langle\theta^2\rangle$. As explained in Sec. 1.3, this observable allows us to easily determine the type of criticality, or SLE family, that the domain walls generated by the particular microscopic dynamics belong to. We remind the reader that, for conformally invariant planar curves generated by SLE, $\langle\theta^2\rangle$, as a function of the curvilinear distance x along a domain wall, takes the form $\langle\theta^2(x)\rangle \simeq \text{const.} + 4\kappa/(8+\kappa)\ln x$, with the parameter κ indicating the universality class that the critical model belongs to. For the

domain walls in $2d$ critical percolation, $\kappa = 6$.

In Fig. B.3 we show $\langle \theta^2(x,t) \rangle$ as a function of the logarithm of the curvilinear distance x, measured for closed hulls (*i.e.*, hulls that have nonzero total winding angle) for a KIM evolving with nonlocal Kawasaki dynamics at a finite working temperature, on a square lattice with PBC. A very similar behavior is obtained for the measurements of $\langle \theta^2 \rangle$ on the wrapping hulls (*i.e.*, hulls that have zero total winding angle), so we do not show these results. The left panel displays data for the dynamics at working temperature $T_c/2$, while the right panel for $T_c/4$. A fit of the function $f(x) = \text{const.} + 4\kappa/(8+\kappa) \ln x$ to the data in the region where the dependence of $\langle \theta^2 \rangle$ on $\ln x$ is linear, gives us an estimate of the SLE parameter: $\kappa \simeq 5.895$ for the dynamics at $T = T_c/2$ and $\kappa \simeq 5.888$ for the dynamics at $T = T_c/4$, results that are close to the expected value $\kappa = 6$ for critical percolation hulls. A similar analysis for the nonlocal Kawasaki dynamics on the honeycomb and triangular lattices at $T_c/2$ is shown in Fig. B.4.

As in the case of the local Kawasaki dynamics, we observe that the fractal properties ascribed to critical percolation can be observed only on length scales $x > \ell_d(t)$, with $\ell_d(t)$ the usual dynamical length. On smaller length scales, spin clusters display instead the properties of equilibrium at the target temperature, that is to say, their walls appear smooth. To highlight this behaviour, we also included in each figure an inset where we present the same data but plotted against $\ln(x/\ell_G(t))$, with $\ell_G(t)$ being the excess-energy growing length taken as a measured of $\ell_d(t)$. As one can see, a crossover between the critical-percolation-like region and the "equilibrium" region occurs for $x/\ell_G(t) \sim 1$.

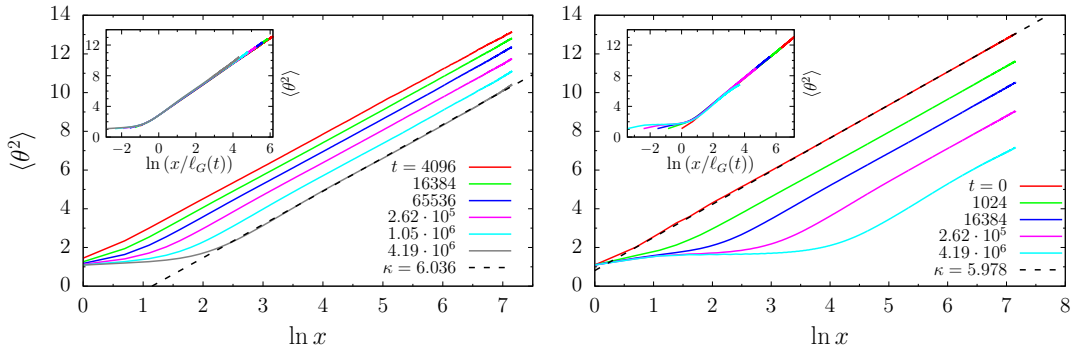

Figure B.4: Ising model evolving under nonlocal Kawasaki dynamics at target temperature $T_c/2$, on a honeycomb lattice (left panel) and on a triangular lattice (right panel), in both cases with PBC and $L = 640$. We show the average squared winding angle, $\langle \theta^2 \rangle$, against $\ln x$ with x the curvilinear distance along a cluster hull, for wrapping hulls (zero total winding angle). As in Fig. B.3, the black dashed lines represent a fit of the function $f(x) = \text{cst.} + 4\kappa/(8+\kappa) \ln x$ to the data in the "linear" region, yielding $\kappa \simeq 6.036$ (honeycomb lattice) and $\kappa \simeq 5.978$ (triangular lattice). In the insets we report $\langle \theta^2 \rangle$ against $\ln(x/\ell_G(t))$, with $\ell_G(t)$ the excess-energy growing length. The times shown are the same in the main plots and the corresponding insets.

B.1.2.2 *Wrapping probabilities*

In Fig. B.5 we display the wrapping probabilities for the nonlocal Kawasaki dynamics on a square lattice (in the left panel) and on a honeycomb lattice (in the right panel), for different values of L, and at temperature $T_c/4$ in both cases. Notice that for the honeycomb lattice the probabilities π_{h} and π_{v} are shown separately, since our construction of this lattice does

not have unit aspect ratio, as explained before. As for the local version of the dynamics, the πs are plotted against the rescaled time $t/(L/\ell_d(t))^\zeta$, with $\ell_d(t)$ taken to be the excess-energy growing length $\ell_G(t)$, and the exponent ζ determined numerically by data collapse. This is achieved with $\zeta \simeq 1.15$ for the dynamics on both the square and honeycomb lattices.

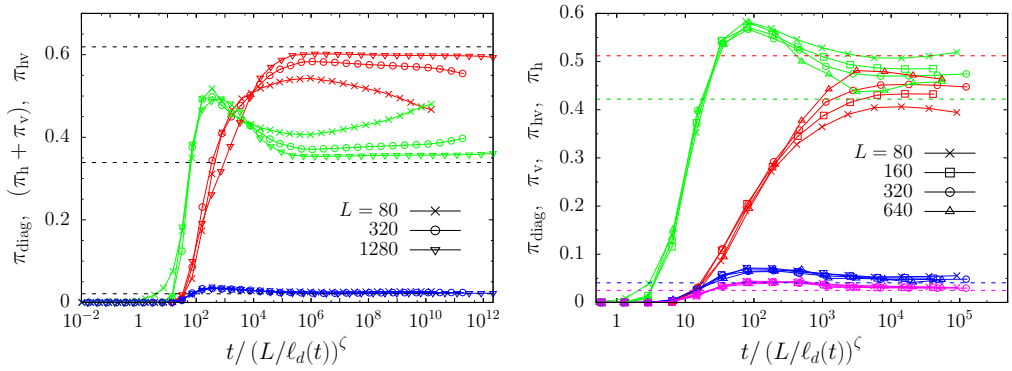

Figure B.5: Ising model evolving under nonlocal Kawasaki dynamics at target temperature $T = T_c/4$. In the left panel we show the probability of having a cluster wrapping in both directions (red curves), $\pi_{\rm hv}$, either horizontally or vertically (green curves), $(\pi_{\rm h}+\pi_{\rm v})$, and diagonally (blue curves), $\pi_{\rm diag}$, in the case of the dynamics on a square lattice with PBC, for different values of L. The data are plotted against the rescaled time $t/(L/\ell_d(t))^\zeta$, where $\ell_d(t)$ is taken to be the inverse of the excess energy, $\ell_G(t)$, and the value of the exponent ζ is chosen to obtain the best data collapse, $\zeta \simeq 1.15$. The horizontal dashed lines are the wrapping probabilities in critical percolation on a torus with unit aspect ratio. In the right panel, the same wrapping probabilities but for the model defined on a finite honeycomb lattice with PBC, with aspect ratio $\sqrt{3}$. We show $\pi_{\rm hv}$ in red, $\pi_{\rm h}$ in green, $\pi_{\rm v}$ in blue and $\pi_{\rm diag}$ in purple. The best data collapse is achieved with $\zeta \simeq 1.15$ also in this case. The dashed horizontal lines are the exact values of $\pi_{\rm hv}$, $\pi_{\rm h}$, $\pi_{\rm v}$ and $\pi_{\rm diag}$ at critical percolation on a lattice with aspect ratio $\sqrt{3}$.

As the system size increases, the data approach asymptotic values that are very close to those of $2d$ critical percolation on the corresponding lattice, shown with dashed horizontal lines. Note that very large system sizes are needed to see the approach to these values (the curves for $L = 1280$ are still a bit away from them). Another feature is that, at sufficiently long times, $\pi_{\rm hv}$ tends to decrease while $\pi_{\rm h} + \pi_{\rm v}$ increases. This behaviour is expected since the system evolves under the constraint of conserved total magnetisation, hence configurations consisting of two large spin clusters of opposite phase both percolating along the same direction of the lattice become more and more likely (this should be true independently of the lattice geometry), while spin configurations that are characterised by the presence of just one spin cluster percolating along both directions in the so-called "cross" topology become less and less likely. On the other hand, we do not observe, in the time window explored by our simulations, the disappearance of the "diagonally" percolating spin clusters, as it happens instead in the case of the single spin-flip dynamics.

By using the criterium $t_p/(L/\ell_d(t_p))^\zeta \simeq 10^4$ for the nonlocal Kawasaki dynamics at $T = T_c/4$ on the square lattice, and $t_p/(L/\ell_d(t_p))^\zeta \simeq 10^3$ for the same dynamics on the honeycomb lattice (that corresponds, approximately, to the value of the scaling variable $t/(L/\ell_d(t))^\zeta$ at which the wrapping probabilities get close to the critical percolation ones) we are able to find estimates of t_p, namely $t_p \simeq 4.91\cdot 10^5,\ 2.11\cdot 10^6,\ 8.46\cdot 10^6$ for $L = 80,\ 320,\ 1280$, respectively, for the case of the square lattice, and $t_p \simeq 3.32 \cdot 10^4,\ 6.36 \cdot 10^4,\ 1.20 \cdot 10^5,\ 2.23 \cdot 10^5$ for

$L = 80,\ 160,\ 320,\ 640$, respectively, for the case of the honeycomb lattice.

B.1.2.3 *Largest cluster scaling*

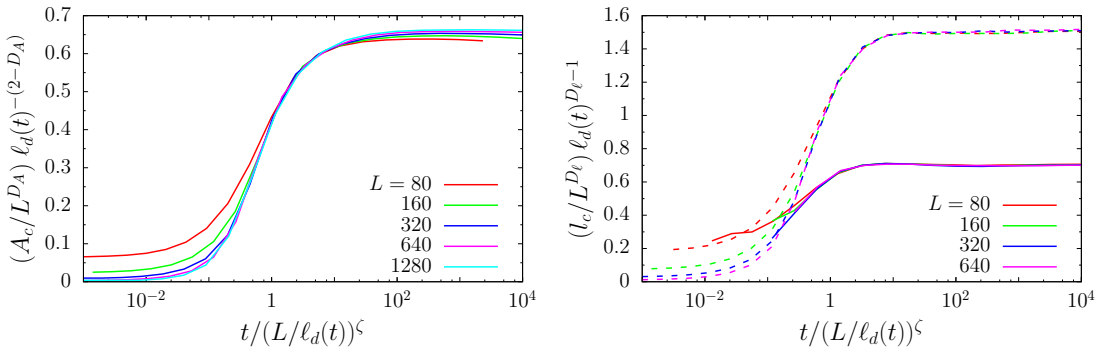

Figure B.6: Ising model on a finite square lattice with PBC, evolving with nonlocal Kawasaki dynamics at target temperature $T_c/2$. In the left panel we show the quantity $\left(A_c/L^{D_A}\right)\ell_d(t)^{-(2-D_A)}$, with A_c the largest cluster size, while in the right panel the quantity $\left(l_c/L^{D_\ell}\right)\ell_d(t)^{-(1-D_\ell)}$, with l_c the length of the largest cluster interface, for different values of L. We took $\ell_d(t) = \ell_G(t)$, with $\ell_G(t)$ the excess-energy growing length. Regarding l_c, we have separated the contribution of the wrapping hulls shown with continuous lines, from that of the enclosing (non-wrapping) hull shown with dashed lines. All the quantities are plotted against the rescaled time $t/(L/\ell_d(t))^{\zeta}$ with $\zeta \simeq 1.16$ giving the best collapse for both A_c and l_c.

We now discuss the scaling properties of the size of the largest spin cluster, A_c, and the length of its interface, l_c. The data shown correspond to nonlocal Kawasaki dynamics at temperature $T_c/2$ on a square lattice (Fig. B.6) and on a honeycomb lattice (Fig. B.7). We present the two main contributions to the average length of the largest cluster interface, l_c, the one coming from wrapping hulls (that exist only if the cluster is wrapping) and the one coming from the enclosing hull (which exists only if the cluster is not wrapping), as two separate quantities.

We rescale A_c as $(A_c(t,L)/L^{D_A})\,\ell_d(t)^{-(2-D_A)}$, while l_c as $(l_c(t,L)/L^{D_\ell})\,\ell_d(t)^{-(1-D_\ell)}$, with $\ell_d(t)$ taken to be the excess-energy growing length $\ell_G(t)$ and $D_A = 91/48$ and $D_\ell = 7/4$ the fractal dimensions of the largest cluster and the percolating hulls in $2d$ critical percolation, respectively. Both quantities are plotted against the rescaled time $t/\left(L/\ell_d(t)\right)^{\zeta}$. Again, the value of the exponent ζ is determined by looking for the best collapse of the datasets corresponding to different L. For the dynamics on the square lattice we find $\zeta \simeq 1.16$, while on the honeycomb lattice $\zeta \simeq 1.17$, both values being compatible, within numerical accuracy, with the ones obtained studying the scaling of the wrapping probabilities.

B.1.2.4 *Number density of domain areas*

We now focus on the analysis of the number density of domain areas.

First of all, we expect that for $t > t_p$, that is to say, when the system is in the so-called critical-percolation-like dynamical scaling regime, $\mathcal{N}(A,t)$ satisfies the dynamical scaling relation given by Eq. (1.25) This behaviour is confirmed by our measurements of $\mathcal{N}(A,t)$ from

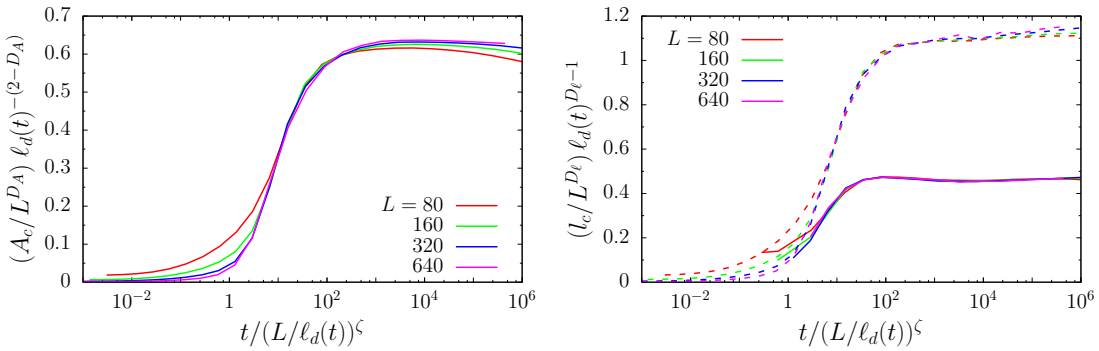

Figure B.7: Ising model on a finite honeycomb lattice with PBC, evolving under nonlocal Kawasaki dynamics at target temperature $T_c/2$. In the left panel we show the quantity $\left(A_c/L^{D_A}\right)\ \ell_d(t)^{-(2-D_A)}$, with A_c the largest cluster size, while in the right panel $\left(l_c/L^{D_\ell}\right)\ \ell_d(t)^{-(1-D_\ell)}$, with l_c the length of the largest cluster interface, separating the contribution due to wrapping hulls from that due to the external hull (when the cluster is not wrapping). The former is indicated with continuous lines, while the latter with dashed lines. We took $\ell_d(t) = \ell_G(t)$, with $\ell_G(t)$ the characteristic length from the inverse of the excess-energy. All the quantities are plotted against $t/(L/\ell_d(t))^{\zeta}$, where $\zeta \simeq 1.17$ gives the best collapse for all cases.

numerical simulations, as one can see from Fig. B.8. In this figure we show the rescaled number density, $\mathcal{N}(A,t)\,\ell_d(t)^4$ against the rescaled domain area $A/\ell_d(t)^2$, for the nonlocal Kawasaki dynamics on a triangular lattice with PBC and $L = 640$, at working temperature $T = T_c/2$. Here the estimate of the characteristic length $\ell_d(t)$ is given, as usual, by $\ell_G(t)$, the excess-energy growing length. In the plot we also included the two curves $f(x) = 2\,c_d\,(1+x)^{-\tau_A}$ and $g(x) = 2\,c_d\,x^{1/2}\left(1+x^{3/2}\right)^{-(2\,\tau_A+1)/3}$, with $\tau_A = 187/91$ and $c_d \simeq 0.0289$, corresponding to the scaling functions for the number density of domain areas in the case of NCOP dynamics and LCOP dynamics, respectively (see Eq. (1.26)). Notice that these functions differ significantly only at small values of the scaling variable x, yielding $f(x) \sim 2c_d$ and $g(x) \sim 2c_d\ x^{1/2}$, respectively. Both represent very well the rescaled data for sufficiently large values of $A/\ell_d(t)^2$, in particular, for $A/\ell_d(t)^2 \gtrsim 1$. However, one clearly sees that, in the small-area region, the NCOP scaling function is the one that matches the data better. A similar result was found in the experiments in [150]. These observations confirm the fact that, for sufficiently high temperature (but way below T_c), the domain growth process caused by nonlocal spin-exchange dynamics falls in the universality class of NCOP coarsening.

From the time evolution of the number density of domain areas we can also extract informations about the characteristic length $\ell_p(t)$, that is associated to the so-called pre-percolation regime. We remind the reader that $\ell_p(t)$ is defined as the length up to which one can observe critical percolation properties in the domain pattern, at time t, and we conjecture that $\ell_p(t) \sim \ell_d(t)t^{1/\zeta}$, with the exponent ζ to be determined. In the case in which the initial state of the system is not already at the percolation critical point, the scaling form of $\mathcal{N}$ must be corrected with a term that takes into account areas A such that $\frac{A}{\ell_d(t)^2} > \left[\frac{\ell_p(t)}{\ell_d(t)}\right]^{D_A}$, as discussed in Sec. 1.5.5.2.

The presence of this pre-percolation regime is observed in our measurements of $\mathcal{N}$ for the nonlocal Kawasaki dynamics on the square and honeycomb lattices. In Fig. B.9 we display

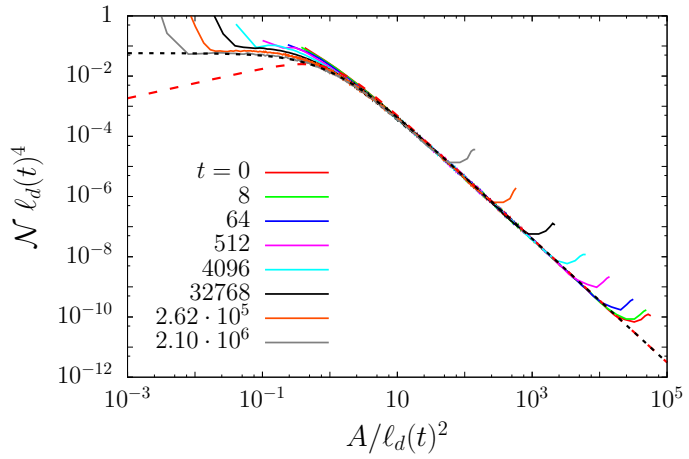

Figure B.8: Scaling of the time-dependent number density of spin cluster areas for the Ising model on a triangular lattice with PBC and $L = 640$, evolving with nonlocal Kawasaki dynamics at temperature $T_c/2$, starting from a fully disordered configuration with equal concentration of up and down spins. Here $\ell_G(t)$, the excess-energy growing length, is taken as the estimate of the dynamical length $\ell_d(t)$. The curves $f(x) = 2\,c_d\,(1+x)^{-\tau_A}$ and $g(x) = 2\,c_d\,x^{1/2}\,\left(1+x^{3/2}\right)^{-(2\,\tau_A+1)/3}$ are represented by dashed lines. The NCOP scaling function $f(x)$ matches accurately the data for $t = 2.10 \cdot 10^6$ in the small-area region, $A/\ell_d(t)^2 < 1$.

the number density of domain areas, $\mathcal{N}(A,t,L)$, rescaled as $A^{\tau_A}\ \ell_d(t)^{2(2-\tau_A)}\ \mathcal{N}(A,t)$, plotted against A in the left panel, and against the rescaled area $\left(A/\ell_d(t)^{2-D_A}\right)/\ell_p(t)^{D_A}$ in the right panel, for the nonlocal Kawasaki dynamics on a square lattice with $L = 1280$, at $T = T_c/2$. Here again $\ell_G(t)$, the excess-energy growing length, is taken as the estimate of the dynamical length $\ell_d(t)$, and $\ell_p(t) = \ell_d(t)t^{1/\zeta}$. We see that the onset of the critical-percolation-like scaling regime occurs for $t \simeq 5 \cdot 10^4$, that corresponds approximately to the time at which the rescaled number density develops a plateau corresponding to the constant $2c_d \approx 0.0580$ for sufficiently large areas.

For shorter times, the data can be collapsed in the region corresponding to large domain areas that have not aquired yet the critical percolation statistical behaviour, by rescaling A as $\left(A/\ell_d(t)^{2-D_A}\right)/\ell_p(t)^{D_A}$ with $\ell_p(t) = \ell_d(t)t^{1/\zeta}$ and $\zeta \simeq 1.20$, as seen in the right panel of Fig. B.9. The value of exponent ζ was fixed by looking for the value that produces the best collapse. Although this value is not coincident with the one obtained through the scaling of the other observables, it is not very far from it, taking into account that the method that we used is very rough. Moreover, in the pre-percolation scaling regime the rescaled distribution can be fitted to $\Phi(x) = C\,x^a$ with $a \approx 0.333$ (indicated by a black dashed line in the right panel of Fig. B.9), a value that is very close to the one found for the other types of spin dynamics already studied.

A similar behaviour is observed on the honeycomb lattice. In Fig. B.10 we show the rescaled number density, $A^{\tau_A}\ \ell_d(t)^{2(2-\tau_A)}\ \mathcal{N}(A,t)$, for the nonlocal Kawasaki dynamics on a honeycomb lattice with linear size $L = 640$, at $T = T_c/2$. As in Fig. B.9, in the left panel the rescaled distribution is plotted against A, while in the right one, against the rescaled area $\left(A/\ell_d(t)^{2-D_A}\right)/\ell_p(t)^{D_A}$. Here again $\ell_p(t) = \ell_d(t)\,t^{1/\zeta}$. The best collapse of the data in the pre-percolation region is achieved by using $\zeta \simeq 1.18$. The function $\Phi(x) = C\,x^a$ was also fitted to the data at $t = 1024$ in an interval inside the pre-percolating scaling region yielding

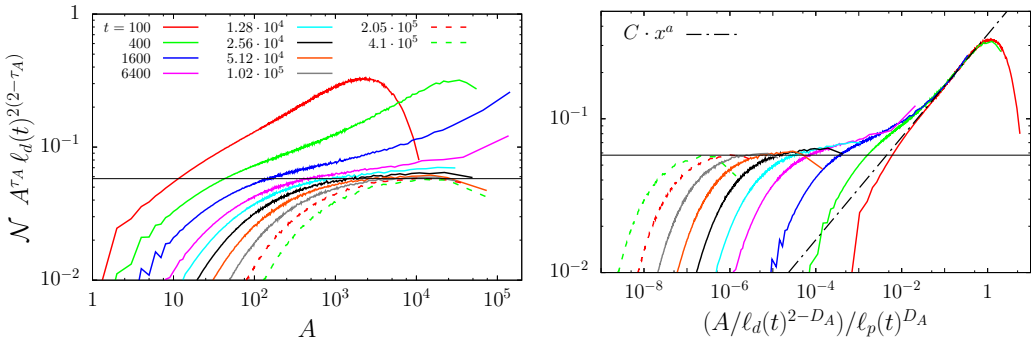

Figure B.9: Ising model on a square lattice with PBC and $L = 1280$, evolving under nonlocal Kawasaki dynamics at target temperature $T_c/2$, starting from a fully disordered configuration with equal concentration of up and down spins. In the left panel we plot the quantity $\mathcal{N}(A, t, L)\, A^{\tau_A}\ \ell_d(t)^{2(2-\tau_A)}$ against A, where the estimate of $\ell_d(t)$ is given by $\ell_G(t)$. The constant $2c_d \approx 0.0580$ is indicated by the black horizontal line. In the right panel, the same quantity is plotted against the rescaled area $\left(A/\ell_d(t)^{2-D_A}\right)/\ell_p(t)^{D_A}$, with $\ell_p(t) = \ell_d(t)\, t^{1/\zeta}$ and $\zeta \simeq 1.20$ giving the best collapse. The function $\Phi(x) = C\, x^a$ has been fitted to the rescaled data at $t = 100$ in the interval $[0.01, 1]$ yielding $a \simeq 0.333$, see the dashed straight line in the right panel.

$a \simeq 0.332$.

B.1.3 Summary

We conclude by stating that the results obtained for the nonlocal version of the spin-exchange dynamics do not change significantly the global picture that we are building. As in the case of the local Kawasaki dynamics, we observe that a critical-percolation-like dynamical scaling regime sets in at a certain time t_p. When the system is in this regime the statistical and geometrical properties of the spin clusters are the same as in $2d$ critical percolation (after a proper rescaling of all lengths by $\ell_d(t)$) over length scales $R > \ell_d(t)$, with $\ell_d(t)$ the dynamical length describing the growth of domains equilibrated at the target temperature of the relaxation dynamics. The main evidence for the existence of this regime is given by the variance of the winding angle measured on the domain walls, which let us identify with great precision the type of criticality (or universality class) that generates the fractal properties of the same domain walls. We observe that the critical behaviour of the domain walls, again over length scales $R > \ell_d(t)$, is exactly the one of $2d$ percolation.

The transient between the initial completely disordered state and this critical-percolation-like scaling regime is governed by a characteristic length scale $\ell_p(t)$, which grows faster than $\ell_d(t)$, as already observed for NCOP and LCOP dynamics. The scaling analysis of the wrapping probabilities, of the geometrical properties of the largest spin cluster and of the number density of domain areas, indicates that

$$\ell_p(t) \sim \ell_d(t)\, t^{1/\zeta}\ , \qquad \text{with} \quad \zeta \in [1.15, 1.20] \tag{B.3}$$

in the case of the dynamics on the square and honeycomb lattices.

The fact that the exponent ζ takes approximately the same value for these two cases suggests that the nonlocality of the spin update rule is such that the characteristic length $\ell_p(t)$ is not affected much (apart from the factor $\ell_d(t)$ in the early time regime) by the

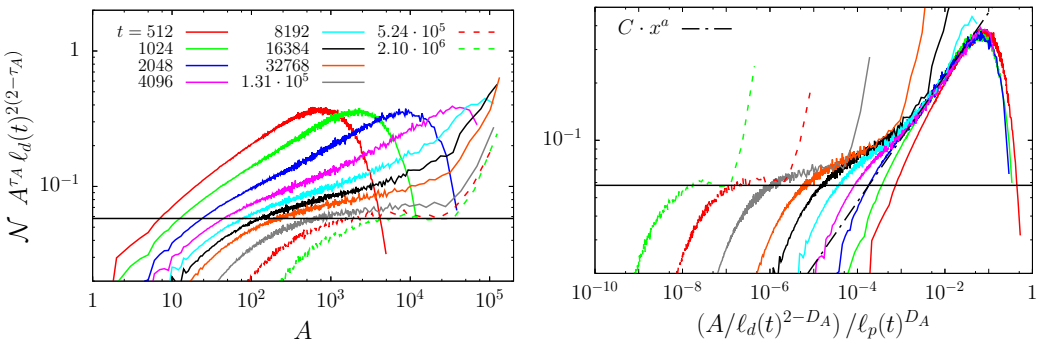

Figure B.10: Ising model on a square lattice with PBC and $L = 1280$, evolving under nonlocal Kawasaki dynamics at target temperature $T_c/2$, starting from a fully disordered configuration with equal concentration of up and down spins. In the left panel we show $\mathcal{N}(A,t,L)\,A^{\tau_A}\,\ell_d(t)^{2(2-\tau_A)}$ against A, where the estimate of $\ell_d(t)$ is given by $\ell_G(t)$. The constant $2c_d \approx 0.058$ is indicated by the black horizontal line. In the right panel, the same quantity against the rescaled area $\left(A/\ell_d(t)^{2-D_A}\right)/\ell_p(t)^{D_A}$, with $\ell_p(t) = \ell_d(t)\,t^{1/\zeta}$ and $\zeta \simeq 1.18$ giving the best collapse. The function $\Phi(x) = C\,x^a$ has been fitted to the data at $t = 1024$ in the interval $[10^{-3}, 10^{-2}]$ yielding $a \simeq 0.332$, see the dashed straight line in the right panel.

particular geometry of the lattice, in contrast to what happens for the local version of the dynamics and the NCOP dynamics, where different values of ζ are found.

Appendix C

C.1 Generalized $2d$ KIM

In the following we define a class of $2d$ kinetic Ising models evolving with single spin-flip stochastic dynamics whose transition rates are dependent on two temperature-like parameters. We show how the Glauber dynamics and the voter model can be recovered as two particular instances in this general class.

First, we consider a stochastic Ising spin system defined on a square lattice, represented by $\mathbb{Z}^2$, with single spin-flip transitions. We assume that the spin-flip rate for site i, given that the system is in the configuration $s = \{s_k\}_{k\in\mathbb{Z}^2}$, denoted by $w_i(s)$, depends on s only through the quantity $h_i(s) = s_i \sum_{j\in\mathcal{N}(i)} s_j$, where again $\mathcal{N}(i)$ is the set of nearest-neighbours to site i. We also assume that $w_i(s)$ has the following form [69, 74]

$$w_i(s) = \frac{1}{2}\left[1 + f(h_i(s))\right] \tag{C.1}$$

with the function f satisfying $f(-h) = -f(h)$ and $|f(h)| \leq 1$. With this choice, the spin-flip rate $w_i(s)$ respects the up-down spin symmetry and is a local and spatially symmetric function of the spin configuration s. The quantity $h_i(s) = s_i \sum_{j\in\mathcal{N}(i)} s_j$ can only take integer values in a discrete set, namely $h_i \in \{0, \pm 2, \pm 4\}$ (since the Ising spin system is defined on the square lattice). Thus, in order to define completely the stochastic process which is determined by the spin-flip rates $w_i(s)$ in Eq. (C.1), it is sufficient to know the value of the function f on this discrete set. Notice that, because of the properties imposed on f, $f(0) = \frac{1}{2}$, $f(-2) = -f(2)$ and $f(-4) = -f(4)$, so that we only require the knowledge of the two parameters

$$p_1 = \frac{1}{2}(1 + f(2)), \quad p_2 = \frac{1}{2}(1 + f(4))\,. \tag{C.2}$$

We can rewrite these two parameters in the following form

$$p_1 = \frac{1}{2}\left[1 - \tanh\left(2\beta_1\right)\right], \quad p_2 = \frac{1}{2}\left[1 - \tanh\left(4\beta_2\right)\right]\ , \tag{C.3}$$

and introduce the two effective temperatures $T_1 = \beta_1^{-1}$ and $T_2 = \beta_2^{-1}$, thus establishing a formal connection with the spin-flip rates that define the Glauber dynamics.

T_1 and T_2 can be interpreted as the two temperatures associated to *interfacial* noise and *bulk* noise, respectively. A very simple way of understanding this association is given in the following. Consider, for example, an initial spin configuration where the system is divided in half by a flat interface: all the lattice sites that are located on one side of the interface have spin $+1$, while all the sites on the other side have spin -1. All the sites that are in the bulk of the half-planes have local field $h = 4$, while those ones that are located along the interface have local field $h = 2$. Then, if $T_1 = T_2 = 0$ (meaning $\beta_1, \beta_2 \to +\infty$), *i.e.* $p_1 = p_2 = 0$, the

spin configuration is frozen in time, since no spin flip is allowed, neither in the bulk of two half-planes, nor on the interface. However, if $T_2 = 0$ (that is $p_2 = 0$) but $T_1 > 0$, then sites on the interface can flip their spin, while those in the bulk can not. On the other hand, if $T_1 = 0$ (that is $p_1 = 0$) but $T_2 > 0$, sites that are in the bulk can flip their spin, while those ones on the interface can not (even though they may become "flippable" in the subsequent steps of the process when the bulk fluctuations reach the flat interface). Notice that for a site with local field $h = 0$, that is to say, a site surrounded by equal numbers of spins up and spins down, the spin-flip probability (per unit time) is always $p_0 = 1/2$. This means that a spin configuration consisting of just two infinite domains separated by a curved interface is always going to evolve, even if $T_1 = T_2 = 0$.

In order to better analyse this class of models it is useful to introduce the coordinate system

$$t_1 = \tanh(2\beta_1), \quad t_2 = \tanh(2\beta_2) \ , \tag{C.4}$$

with $0 \leq t_1, t_2 \leq 1$, in terms of which the parameters p_1 and p_2 can be expressed as

$$p_1 = \frac{1}{2}(1 - t_1), \quad p_2 = \frac{1}{2}\left(1 - \frac{2t_2}{1 + t_2^2}\right) \tag{C.5}$$

with $0 \leq p_1, p_2 \leq 1/2$. Notice that we have implicitly assumed that $\beta_1, \beta_2 \geq 0$.

Each point in the parameter plane $(p_1,\ p_2)$, or alternatively in the "temperature" plane $(t_1,\ t_2)$, corresponds to a particular model. As an example, the ferromagnetic IM on a square lattice, evolving with Glauber dynamics, is obtained by setting $\beta_1 = \beta_2 = \beta$, *i.e.* it corresponds to the choice $p_1 = (1 + \tanh(2\beta))/2$ and $p_2 = (1 + \tanh(4\beta))/2$ or $t_1 = t_2 = \tanh(2\beta)$, with β the usual inverse temperature associated to Gibbs-Boltzmann equilibrium. In the $(p_1,\ p_2)$ plane this model corresponds to the line defined by $p_2 = \frac{p_1^2}{1-2p_1+2p_1^2}$ when β varies. In particular, the zero-temperature Glauber dynamics corresponds to $p_1 = p_2 = 0$ $(t_1 = t_2 = 1)$, while the dynamics at the critical Ising point is obtained for $\beta = \beta_c = \ln(1 + \sqrt{2})/2$, or alternatively $t_1 = t_2 = 1/\sqrt{2}$ (corresponding to $p_1 = (2 - \sqrt{2})/4 \approx 0.1464$ and $p_2 = (3 - 2\sqrt{2})/6) \approx 0.0286$).

The spin-flip rate that defines the voter model is given by $w_i(s) = \frac{1}{2}[1 - h_i(s)/4]$, for given site i and spin configuration s, that is to say, $f(h) = -h/4$. This choice corresponds to $p_1 = 1/4$ and $p_2 = 0$, or alternatively to $t_1 = 1/2$ and $t_2 = 1$. It is then clear that, for this model, the bulk noise is zero while the interfacial one is not, *i.e.* $T_1 > 0$ and $T_2 = 0$. A slight generalization of the voter model dynamics is given by the so-called *noisy* voter model. In this model, every time that a spin needs to be updated, it is aligned with a probability γ with one of its nearest-neighbours, chosen at random. The spin-flip probability (per unit time step) for such a process is given by

$$w_i(s) = \frac{1}{2}\left[1 - \gamma\frac{h_i(s)}{4}\right] \tag{C.6}$$

for given lattice site i ans spin configuration s. Hence $f(h) = -\gamma h/4$ with $\gamma \in [0, 1]$. In terms of the parameters p_1, p_2 the noisy voter model corresponds to the line $p_2 = 2p_1 - \frac{1}{2}$ with p_1 varying in the interval $[1/4,\ 1/2]$, or the line $t_1 = \frac{t_2}{1+t_2^2}$ in the (t_1, t_2) plane, with $t_2 \in [0, 1]$.

Finally, let us introduce an other interesting family of models belonging to this class of generalized KIM on the square lattice, the so-called majority voter models [151]. The spin-flip rule for a majority voter model consists in the following: at each time step, a lattice site is chosen at random and its spin is aligned with the local field produced by the nearest-neighbour sites (*i.e.* with the spin of the majority of neighbours) with a given probability.

The spin-flip rate for site i, given that the system is in the spin configuration s, is given by

$$w_i(s) = \frac{1}{2}\left[1 - \gamma\ \mathrm{sign}(h_i(s))\right]\ , \quad (0 \leq \gamma \leq 1)\ . \tag{C.7}$$

meaning that $f(h) = -\gamma\ \mathrm{sign}(h)$ (for $h_i = 0$ we assume $w_i = 1/2$, so the function $\mathrm{sign}(h)$ is supported with the value at $h = 0$ as $\mathrm{sign}(0) = 0$). If the majority of the sites that are neighbours to site i have antiparallel spin to that of i, then s_i flips with probability (per unit time) $w_i = (1+\gamma)/2$; on the other hand, if the majority of the neighbouring sites "agree" with site i, s_i can flip with probability (per unit time) $w_i = (1-\gamma)/2$. The noise-free majority voter model is obtained for $\gamma = 1$ and coincides with the $T = 0$ Glauber dynamics. In terms of the parameters p_1 and p_2, the majority voter model corresponds to $p_1 = p_2 = (1-\gamma)/2$. Alternatively, it corresponds to the line defined by $t_1 = \frac{2t_2}{1+t_2^2}$ in the $(t_1,\ t_2)$ plane, when $t_1 = \gamma$ varies from 0 to 1.

In Fig. C.1 we present a depiction of the generalized KIM on the square lattice on the plane $(t_1,\ t_2)$, with lines corresponding to the Ising model evolving with Glauber dynamics, the noisy (linear) voter model and the majority voter model. We also highlight some special points in the diagram: the noise-free (linear) voter model, the $T = 0$ Glauber dynamics and the critical Glauber dynamics. The line $t_2 = 1$ (that is $\beta_2 \to \infty$, or $p_2 = 0$) corresponds to models without bulk noise. On the other hand, the line $t_1 = 1$ (that is $\beta_1 \to \infty$, or $p_1 = 0$) corresponds to models without interfacial noise. Notice that, in both these cases, curved domain walls can still evolve since the spin-flip rate for $h = 0$ is always $1/2$. Amongst all these models, the family of KIMs evolving with Glauber dynamics is the only one whose spin-flip rates satisfy the detailed balance condition with the Gibbs-Boltzmann equilibrium distribution. In fact, if we impose the detailed balance condition (see Eq. (2.2)) based on the equilibrium distribution of the IM, $P_{\mathrm{eq}}(s) \propto \exp\left[-\beta\mathcal{H}(s)\right]$ with $\mathcal{H}(s) = -\frac{1}{2}\sum_i s_i \sum_{j\in\mathcal{N}(i)} s_j$ (setting the coupling $J = 1$), we get the following equation for the function $f(h)$,

$$1 + f(h) = (1 - f(h))\mathrm{e}^{-2\beta h} \tag{C.8}$$

which solves to $f(h) = -\tanh(\beta h)$.

It is also observed, based on numerical simulations and mean-field approximations [74], that the diagram presented in Fig. C.1 is divided in two regions: a "high-temperature" region where spin clusters grow up to a maximum length scale (corresponding to the equilibrium correlation length), and a "low-temperature" region where, instead, spin clusters grow indefinitely (*i.e.* the system display coarsening phenomena). These two phases, that we denote as paramagnetic phase and ferromagnetic phase as for a usual magnetic system in equilibrium, are separated by a critical line. The exact location of this line is not known, but it is known that it passes by the critical Glauber dynamics point $(t_1 = 1/\sqrt{2}\ , t_2 = 1/\sqrt{2})$ and the noise-free (linear) voter model point $(t_1 = 1/2\ , t_2 = 1)$. The qualitative behaviour of this critical line is traced in Fig. C.1.

C.2 Some analytic results for the voter model

In the present Section, we show some known analytical results in regards to the voter model. We consider the (linear and noise-free) voter model on the d-dimensional hypercubic lattice, that is to say, $\mathbb{Z}^d$. We assign to each site $\boldsymbol{x} \in \mathbb{Z}^d$ a spin variable $s_{\boldsymbol{x}} = \pm 1$ and, as usual, the spin configuration of the system is indicated by $s = \{s_{\boldsymbol{x}}\}_{\boldsymbol{x}\in\mathbb{Z}^d}$. The spin-flip rate

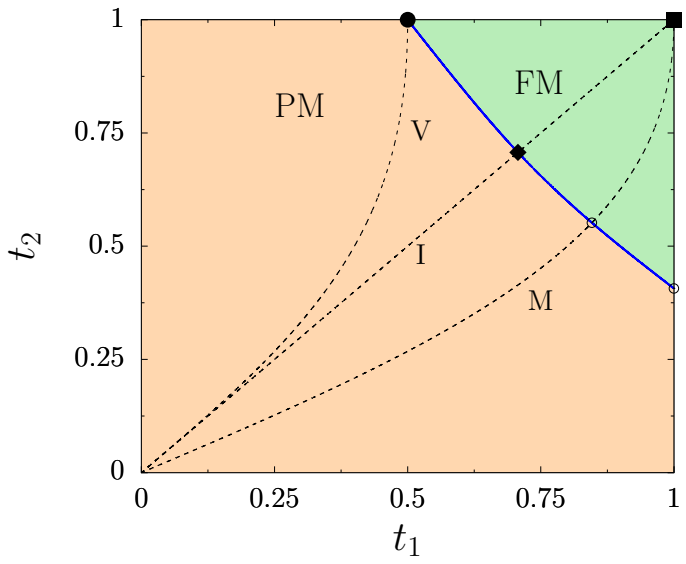

Figure C.1: The phase diagram of the generalized KIM on the square lattice, in terms of the parameters $t_1,\ t_2$, with $0 \leq t_1, t_2 \leq 1$. Dashed lines correspond to the (linear) voter model (V), Ising model evolving with Glauber dynamics (I) and majority voter model (M). Three special points are highlighted: the noise-free (linear) voter model (●), the Ising model evolving with zero-temperature Glauber dynamics (■), and the Ising model evolving with Glauber dynamics at the critical temperature (◆). The continous blue line represents approximately the critical line separating the high-temperature phase (PM) from the low-temperature one (FM).

for the site $\boldsymbol{x}$, given that the system is in configuration s, is

$$w_{\boldsymbol{x}}(s) = \frac{1}{2}\left(1 - \frac{1}{2d}\, s_{\boldsymbol{x}} \sum_{\boldsymbol{y}\in\mathcal{N}(\boldsymbol{x})} s_{\boldsymbol{y}}\right) , \tag{C.9}$$

where $\mathcal{N}(\boldsymbol{x})$ is the set of nearest-neighbours to site $\boldsymbol{x}$, d the number of dimensions.

We have already stated that this spin model has no bulk noise, *i.e.*, if a site 'agrees' with all its nearest-neighbours, its spin-flip rate vanishes. The consequence is that the 'consensus' states, *i.e.*, the states in which all sites have the same opinion-spin, are absorbing states. However, this does not mean that, for the infinite system, the asymptotic steady state must be one of full consensus. In fact, it turns out that the coarsening process is not always effective in bringing the system towards a single-domain state, and whether it does or not depends on the dimensionality of the lattice. For $d \leq 2$ the system coarsens until ultimately reaching a single domain state, while for $d > 2$ there is an infinite family of non-completely-ordered steady states [71, 152]. The discrepancy in the asymptotic regime reached above and below $d = 2$ will be further discussed in this section.

The time-dependent probability distribution of the stochastic process in the spin configuration space $\{-1, +1\}^{\mathbb{Z}^d}$ satisfies the master equation

$$\frac{\mathrm{d}}{\mathrm{d}t}P(s,t) = \sum_{\boldsymbol{x}} \Big(w_{\boldsymbol{x}}(s^{\boldsymbol{x}})P(s^{\boldsymbol{x}},t) - w_{\boldsymbol{x}}(s)P(s,t)\Big) , \tag{C.10}$$

where $P(s,t)$ denotes the probability for the system to be in the spin configuration s at the time t and $s^{\boldsymbol{x}}$ denotes the spin configuration obtained from s by flipping the spin at site $\boldsymbol{x}$.

Since the spin-flip rates $w_{\boldsymbol{x}}(s)$ have a linear dependence on s, the differential equations for the general n-point correlation function are closed, that is to say, correlation functions of different orders are completely independent. This fact allows, in principle, for the solution in closed form of any n-point correlation function. As an example, the single-point correlation function (or average site magnetisation) satisfies [64, 153]

$$\frac{\mathrm{d}}{\mathrm{d}t}\langle s_{\boldsymbol{x}}\rangle_t = -2\langle s_{\boldsymbol{x}} w_{\boldsymbol{x}}(s)\rangle_t = \frac{1}{2d}\Delta_{\boldsymbol{x}}\langle s_{\boldsymbol{x}}\rangle_t \ , \tag{C.11}$$

where $\Delta_{\boldsymbol{x}}$ denotes the discrete Laplace operator, defined by

$$\Delta_{\boldsymbol{x}} f_{\boldsymbol{x}} \equiv -2d\ f_{\boldsymbol{x}} + \sum_{i=1}^{d}\left(f_{\boldsymbol{x}+\mathbf{e}_i} + f_{\boldsymbol{x}-\mathbf{e}_i}\right) \ , \tag{C.12}$$

for a generic function f of $\mathbb{Z}^d$ and with $\{\mathbf{e}_i\}_{i=1,\ldots,d}$ the canonical orthonormal basis of $\mathbb{Z}^d$. The brackets $\langle\cdot\rangle_t$ denote the average over the probability distribution at time t. For a given observable $O(s)$, $\langle O\rangle_t = \sum_{s\in\{-1,+1\}^{\mathbb{Z}^2}} O(s)P(s,t)$.

By summing both sides of Eq. (C.11) over all lattice sites, one finds that $\frac{\mathrm{d}}{\mathrm{d}t}\sum_{\boldsymbol{x}}\langle s_{\boldsymbol{x}}\rangle_t = 0$, that is to say, the average total magnetisation of the system, $\langle\sum_{\boldsymbol{x}} s_{\boldsymbol{x}}\rangle_t$, is a constant. Notice however that, while the total magnetisation averaged over all possible trajectories of the dynamics is a conserved quantity (if one fixes the total magnetisation at $t = 0$), $\sum_{\boldsymbol{x}} s_{\boldsymbol{x}}$ is not a conserved quantity for a single realization of the VM dynamics. In this sense, the VM belongs to the family of NCOP coarsening systems. We can also define a magnetisation density, $m(t)$, as

$$m(t) = \lim_{L\to+\infty} L^{-d}\left\langle \sum_{\boldsymbol{x}\in\Lambda_L} s_{\boldsymbol{x}} \right\rangle_t \tag{C.13}$$

where we denote by Λ_L the finite box of linear size L centered at the origin of the lattice. Then $m(t)$ is a constant and equal to the initial magnetisation density of the system, $m_0 = m(t=0)$. Suppose now that the initial spin configuration is chosen by fixing the fraction ρ of sites with spin $+1$, *i.e.*, for each $\boldsymbol{x}$, $s_{\boldsymbol{x}} = +1$ at $t = 0$ with probability ρ (independently from the value of the spin on all other sites), so that the initial magnetisation density is $m_0 = 2\rho - 1$. Then let $p_+(\rho)$ be the probability for the system to reach the absorbing state with all spins $+1$, given that the dynamics gets blocked in one of the two absorbing states. Since $m(t) = m_0$ for all $t \geq 0$, one has $2\rho - 1 = 2p_+(\rho) - 1$, hence $p_+(\rho) = \rho$.

Concerning again Eq. (C.11), by using the discrete Fourier transform of $\langle s_{\boldsymbol{x}}\rangle$, one can prove that the general solution has the following form [64, 153]

$$\langle s_{\boldsymbol{x}}\rangle_t = \mathrm{e}^{-t}\sum_{\boldsymbol{y}\in\mathbb{Z}^d}\sigma_{\boldsymbol{y}}\,\mathcal{J}_{\boldsymbol{x}-\boldsymbol{y}}\left(\frac{t}{d}\right) \tag{C.14}$$

where we denote by $\sigma_{\boldsymbol{x}} = \langle s_{\boldsymbol{x}}\rangle_{t=0}$ the average magnetisation of site $\boldsymbol{x}$ in the initial configuration and $\mathcal{J}_{\boldsymbol{x}}$ is a shorthand notation for the multi-index modified Bessel functions, namely

$$\mathcal{J}_{\boldsymbol{x}}(u) = \prod_{i=1}^{d}\mathcal{I}_{x_i}(u) \tag{C.15}$$

for given $\boldsymbol{x} = (x_1, x_2, \ldots, x_d) \in \mathbb{Z}^d$, with $\mathcal{I}_\alpha$ the modified Bessel function of the first kind, of order α [154]. If the initial configuration is such that a single $+1$ "voter" sits at the origin

and is surrounded by a "sea" of undecided voters, *i.e.* $s_{\boldsymbol{x}}(t=0) = \pm 1$ with probability $1/2$ for all $\boldsymbol{x} \neq \boldsymbol{0}$ and $s_{\boldsymbol{0}}(t=0) = 1$ (meaning $\sigma_{\boldsymbol{x}} = \delta_{\boldsymbol{x},\boldsymbol{0}}$), then the solution to Eq. (C.14) reduces to

$$m_{\boldsymbol{x}}(t) \equiv \langle s_{\boldsymbol{x}} \rangle_t = \mathrm{e}^{-t} \mathcal{J}_{\boldsymbol{x}}(t/d) \quad . \tag{C.16}$$

By using now the asymptotic relation $\mathcal{I}_\alpha(z) \sim \mathrm{e}^z / \sqrt{2\pi z}$ as $z \to +\infty$, valid for any real α, one finds that the asymptotic behaviour of the average site magnetisation is $m_{\boldsymbol{x}}(t) \sim [2\pi t/d]^{-d/2}$ for all $\boldsymbol{x}$. Thus, as expected, a single voter relaxes to the average undecided opinion of the rest of the population.

The last result is exact, but does not provide meaningful information on how the steady state of the system is reached. In this sense, a more interesting quantity is the two-point correlation function, $\langle s_{\boldsymbol{x}} s_{\boldsymbol{y}} \rangle_t$. The two-point correlation function satisfies the following equation [64, 153]

$$\frac{\mathrm{d}}{\mathrm{d}t} \langle s_{\boldsymbol{x}} s_{\boldsymbol{y}} \rangle_t = -2 \Big\langle s_{\boldsymbol{x}} s_{\boldsymbol{y}} \Big(w_{\boldsymbol{x}}(s) + w_{\boldsymbol{y}}(s) \Big) \Big\rangle_t = \frac{1}{2d} \Big(\Delta_{\boldsymbol{x}} + \Delta_{\boldsymbol{y}} \Big) \langle s_{\boldsymbol{x}} s_{\boldsymbol{y}} \rangle_t \; . \tag{C.17}$$

In order to solve this equation [64] one makes the assumption that the initial configuration of the system is translationally invariant (on average over the initial ensemble), and thus that it is translationally invariant also at each time $t > 0$, so that $\langle s_{\boldsymbol{x}} s_{\boldsymbol{y}} \rangle_t$ depends on the lattice vectors $\boldsymbol{x}$ and $\boldsymbol{y}$ only through their difference $\boldsymbol{n} = \boldsymbol{x} - \boldsymbol{y}$. Then, by denoting $\mathrm{G}_{\boldsymbol{n}}(t) = \langle s_{\boldsymbol{x}} s_{\boldsymbol{x}+\boldsymbol{n}} \rangle_t$, Eq. (C.17) simplifies to

$$\frac{\mathrm{d}}{\mathrm{d}t} \mathrm{G}_{\boldsymbol{n}}(t) = \frac{1}{d} \, \Delta_{\boldsymbol{n}} \mathrm{G}_{\boldsymbol{n}}(t) \tag{C.18}$$

which should be solved with the boundary condition $\mathrm{G}_{\boldsymbol{0}}(t) = \langle s_{\boldsymbol{x}}^2 \rangle_t = 1$, for any t. In addition, it is natural to choose the initial condition $\mathrm{G}_{\boldsymbol{n}}(0) = \delta_{\boldsymbol{n},\boldsymbol{0}}$, that corresponds to a completely uncorrelated initial state. Since Eq (C.18) is basically identical to Eq. (C.11) apart from numerical factors, one would be tempted to consider a solution of the form $\widetilde{\mathrm{G}}_{\boldsymbol{n}}(t) = \mathrm{e}^{-2t} \mathcal{J}_{\boldsymbol{n}}(2t/d)$. However, with this solution, $\widetilde{\mathrm{G}}_{\boldsymbol{0}}(t)$ does not satisfy the boundary condition. In order to maintain $\mathrm{G}_{\boldsymbol{0}}(t) = 1$ throughout the evolution, one can reformulate the problem posed by Eq. (C.18) as the equivalent lattice diffusion problem with a constant localised source at the origin, and look for a solution of the form

$$\mathrm{G}_{\boldsymbol{n}}(t) = \mathrm{e}^{-2t} \; \mathcal{J}_{\boldsymbol{n}} \left(\frac{2t}{d} \right) + \int_0^t \mathrm{d}t' \, S_d(t-t') \, \mathrm{e}^{-2t'} \; \mathcal{J}_{\boldsymbol{n}} \left(\frac{2t'}{d} \right) \tag{C.19}$$

with $S_d(t)$ the "strength" of the source. From a physical point of view, this solution corresponds to placing a particle source $\mathrm{G}_{\boldsymbol{0}} = 1$ at $t = 0$ in the origin and supplement it by an amount $S_d(t)dt$ during the time interval $(t, t+dt)$ in order to keep the overall value unchanged. Equation (C.19) evaluated at the origin ($\boldsymbol{n} = \boldsymbol{0}$) becomes

$$1 = \left[\mathrm{e}^{-\frac{2t}{d}} \; \mathcal{I}_0 \left(\frac{2t}{d} \right) \right]^d + \int_0^t \mathrm{d}t' \, S_d(t-t') \left[\mathrm{e}^{-\frac{2t'}{d}} \; \mathcal{I}_0 \left(\frac{2t'}{d} \right) \right]^d \; . \tag{C.20}$$

If we denote by $\hat{S}_d(\lambda)$ the Laplace transform of the function $S_d(t)$, $\hat{S}_d(\lambda) = \int_0^{+\infty} \mathrm{d}t \, S_d(t) \mathrm{e}^{-\lambda t}$, and by $\hat{T}_d(\lambda)$ the Laplace transform of the function $T_d(t) = \left[\mathcal{I}_0(t) \mathrm{e}^{-t} \right]^d$, one obtains from Eq. (C.20) the following relation between the two

$$\hat{S}_d(\lambda) = -1 + \frac{2}{d} \Big[\lambda \, \hat{T}_d \left(\frac{d}{2} \lambda \right) \Big]^{-1} \; . \tag{C.21}$$

Using now the integral representation of the modified Bessel function $\mathcal{I}_0$, namely $\mathcal{I}_0(x) = \frac{1}{2\pi}\int_0^{2\pi} \mathrm{d}q\, \mathrm{e}^{x\cos(q)}$, it is possible to express $\hat{T}_d$ in terms of the so-called Watson integrals,

$$\hat{T}_d(\lambda) = \frac{1}{(2\pi)^d}\int_0^{2\pi}\cdots\int_0^{2\pi} \mathrm{d}q_1\cdots\mathrm{d}q_d\, \frac{1}{\lambda + d - \sum_{i=1}^d \cos q_i}\ , \tag{C.22}$$

and find an expression for $\hat{S}_d(\lambda)$. For example, in the case $d = 1$, $\hat{S}_1(\lambda) = \sqrt{(\lambda+2)/\lambda}$. More complicated expressions arise when d is larger and ultimately there is no closed-form for them. Nevertheless, we are just interested in the asymptotic behaviour of the source strength S_d, which in turn is given by the low-λ limit of its Laplace transform [64],

$$\hat{S}_d(\lambda) \sim \begin{cases} (\lambda/2)^{-\frac{1}{2}} & \text{if } d = 1 \\ -\lambda^{-1}/\ln\lambda & \text{if } d = 2 \\ (d\lambda/2)^{-1} & \text{if } d > 2 \end{cases} \ , \text{ as } \lambda \to 0 \tag{C.23}$$

and thus

$$S_d(t) \sim \begin{cases} 1/\sqrt{2t} & \text{if } d = 1 \\ 1/\ln t & \text{if } d = 2 \\ \text{const.} & \text{if } d > 2 \end{cases} \ , \text{ as } t \to +\infty\,. \tag{C.24}$$

We are particularly interested in the case $d = 2$ since it seems to sit at the border between two very different behaviours. Using the asymptotic relations for $\mathcal{I}_\alpha$, and calling $\boldsymbol{n} = (n_1, n_2) \in \mathbb{Z}^2$, for $d = 2$ Eq. (C.19) implies

$$\mathrm{G}_{\boldsymbol{n}}(t) \simeq \frac{1}{2\pi t} + \frac{c}{\ln t}\int_0^t \mathrm{d}t'\, \mathrm{e}^{-2t'}\ \mathcal{I}_{n_1}(t')\,\mathcal{I}_{n_2}(t') \tag{C.25}$$

as $t \to +\infty$ dropping corrections $\mathcal{O}(t^{-2})$, with c a numerical factor to be determined. Using the integral representation of the modified Bessel function $\mathcal{I}_n$ for integer values of n, that is $\mathcal{I}_n(t) = (2\pi)^{-1}\int_{-\pi}^{\pi}\mathrm{d}k\, \exp\left[t\cos k - i\, n\, k\right]$, Eq. (C.25) reduces to

$$\mathrm{G}_{\boldsymbol{n}}(t) \simeq \frac{c}{\ln t}\frac{1}{(2\pi)^2}\int_{-\pi}^{\pi}\mathrm{d}k_1\ \int_{-\pi}^{\pi}\mathrm{d}k_2\, \mathrm{e}^{-i\boldsymbol{n}\cdot\boldsymbol{k}}\,\hat{g}\,(\boldsymbol{k},t)\ + \mathcal{O}\left(\frac{1}{t}\right) \tag{C.26}$$

where $\boldsymbol{k} = (k_1, k_2)$ and the function $\hat{g}\,(\boldsymbol{k},t)$ is given by

$$\hat{g}\,(\boldsymbol{k},t) = \frac{1 - \mathrm{e}^{-t(2-\cos k_1 - \cos k_2)}}{2 - \cos k_1 - \cos k_2}\ . \tag{C.27}$$

Apart from a time-dependent prefactor $1/\ln t$, one can recognise in $\hat{g}$ the dynamical structure factor of the system, which is defined as the lattice Fourier Transform of the two-point correlation function,

$$S(\boldsymbol{k},t)\ \equiv\ \sum_{\boldsymbol{n}\in\mathbb{Z}^2}\mathrm{G}_{\boldsymbol{n}}(t)\,\mathrm{e}^{i\boldsymbol{n}\cdot\boldsymbol{k}}\ \sim\ \frac{1}{\ln t}\,\hat{g}\,(\boldsymbol{k},t)\ . \tag{C.28}$$

In the limit $|\boldsymbol{k}| \to 0$, $\hat{g}$ can be approximated as $\hat{g}\,(\boldsymbol{k},t) \simeq 2\ k^{-2}(1 - \mathrm{e}^{-\frac{1}{2}tk^2})$, where $k = |\boldsymbol{k}|$, *i.e.* it becomes isotropic in k-space. Then the large-distance behaviour of the correlation function is characterized by the scaling form

$$\mathrm{G}_{\boldsymbol{n}}(t)\ \sim\ \frac{1}{\ln t}\,\mathcal{G}\left(\frac{|\boldsymbol{n}|}{\sqrt{t}}\right) \tag{C.29}$$

where the scaling function $\mathcal{G}$ is obtained by taking the inverse Fourier Transform of $\hat{g}$. Eq. (C.29) clearly displays the emergence of a dynamical characteristic length $\ell_d(t)$ which scales as $\sqrt{t}$, but also a logarithmic violation of the usual dynamic scaling law.

An interesting quantity that can be extracted from the two-point correlation function is the density of interfaces ρ_{int}, defined as the average value of the fraction of unsatisfied bonds or, equivalently, the fraction of pairs of neighbouring sites with antiparallel spin. This quantity is linked to the correlation function through the relation

$$\rho_{\text{int}}(t) = -\frac{1}{4d}\Delta_{\mathbf{0}}\mathrm{G}_{\mathbf{0}}(t) = \frac{1}{2}\left(1 - \frac{1}{2d}\sum_{i=1}^{d}\left[\mathrm{G}_{\mathbf{e}_i}(t) + \mathrm{G}_{-\mathbf{e}_i}(t)\right]\right) \quad , \tag{C.30}$$

where $\mathbf{e}_i$ are the lattice unit vectors. Note that the sum over the nearest-neighbours can be lifted since the dynamics is isotropic along the d principal directions of the lattice. From Eq. (C.19) evaluated at $\boldsymbol{n} = (1, 0, ..., 0)$ and the fact that $\mathrm{G}_{\mathbf{0}} \equiv 1$, one obtains

$$\begin{aligned}\rho_{\text{int}}(t) = {} & \frac{1}{2}\,\mathrm{e}^{-2t}\,\mathcal{I}_0^{d-1}\left(\frac{2t}{d}\right)\left[\mathcal{I}_0\left(\frac{2t}{d}\right) - \mathcal{I}_1\left(\frac{2t}{d}\right)\right] \\ & + \frac{1}{2}\int_0^t \mathrm{d}u\, S_d(t-u)\,\mathrm{e}^{-2u}\,\mathcal{I}_0^{d-1}\left(\frac{2u}{d}\right)\left[\mathcal{I}_0\left(\frac{2u}{d}\right) - \mathcal{I}_1\left(\frac{2u}{d}\right)\right].\end{aligned} \tag{C.31}$$

Combining the latter equation with Eq. (C.24) and the asymptotic relations $\mathcal{I}_0(z) \simeq \mathcal{I}_1(z) \simeq e^z\left[1/\sqrt{2\pi z} + \mathcal{O}(z^{-3/2})\right]$ and $\mathcal{I}_0(z) - \mathcal{I}_1(z) \simeq e^z\left[1/\sqrt{8\pi z^3} + \mathcal{O}(z^{-5/2})\right]$, the asymptotic behaviour of the density of interfaces is found to be [64, 68]

$$\rho_{\text{int}}(t) \sim \begin{cases} t^{-\frac{1}{2}} & \text{if } d = 1 \\ 1/\ln t & \text{if } d = 2 \\ a - bt^{-d/2} & \text{if } d > 2 \end{cases} \quad , \quad \text{as } t \to +\infty \tag{C.32}$$

These results allow us to establish some conclusions on the coarsening process in the voter model: in $d \leq 2$ the probability that two lattice sites at a given separation had opposite spin vanishes asymptotically in time, no matter how much distant they are, and coarsening eventually leads to a single-domain final state. In $d > 2$, an infinite system reaches a dynamic frustrated state, where opposite-spin domains can coexist and continually evolve in such a way that the average concentration of each species remains fixed. Dimension $d = 2$ is particular since it lies at the border between the two cases. There is a coarsening process which brings the system towards the single-domain state, but it is very slow since the density of interfaces vanishes only as $1/\ln t$.

As a last effort, we derive the two-time autocorrelation function, defined as

$$A_{\boldsymbol{x}}(t, t_0) = \langle s_{\boldsymbol{x}}\; m_{\boldsymbol{x}}(t|s, t_0)\rangle_{t_0} \tag{C.33}$$

where $m_{\boldsymbol{x}}(t|s, t_0)$ is the average magnetisation of site $\boldsymbol{x}$ at time t given that the system is in the spin configuration s at the time $t_0 < t$, and the brackets $\langle\cdot\rangle_{t_0}$ denotes the average over the ensemble of configurations at time t_0. Notice that, for any $\boldsymbol{x} \in \mathbb{Z}^d$ and for fixed spin configuration s and time t_0, the quantity $M_{\boldsymbol{x}}(\tau) = m_{\boldsymbol{x}}(t_0 + \tau|s, t_0)$ (seen as just a function of the time delay τ) satisfies Eq. (C.11) with an initial condition $M_{\boldsymbol{x}}(0) = s_{\boldsymbol{x}}$. Then one obtains

$$A_{\boldsymbol{x}}(t, t_0) = \left\langle s_{\boldsymbol{x}}\mathrm{e}^{-(t-t_0)}\sum_{\boldsymbol{y}\in\mathbb{Z}^d} s_{\boldsymbol{y}}\,\mathcal{J}_{\boldsymbol{x}-\boldsymbol{y}}\left(\frac{t-t_0}{d}\right)\right\rangle_{t_0} = \mathrm{e}^{-(t-t_0)}\sum_{\boldsymbol{y}\in\mathbb{Z}^d}\langle s_{\boldsymbol{x}}s_{\boldsymbol{y}}\rangle_{t_0}\,\mathcal{J}_{\boldsymbol{x}-\boldsymbol{y}}\left((t-t_0)/d\right) \tag{C.34}$$

Then, assuming that at each time the state of the system is (statistically) translationally invariant (in space) one gets

$$A(t,t_0) \;=\; \mathrm{e}^{-(t-t_0)} \sum_{\boldsymbol{n}\in\mathbb{Z}^d} \mathrm{G}_{\boldsymbol{n}}(t_0)\; \mathcal{J}_{\boldsymbol{n}}\left(\frac{t-t_0}{d}\right)\;, \tag{C.35}$$

where $\mathrm{G}_{\boldsymbol{n}}$ is the two-point correlation function (notice that we have dropped the $\boldsymbol{x}$-dependence in the notation for $A(t,t_0)$). As a simple check we verify that setting $t=t_0$ in Eq. (C.35) we find $A(t_0,t_0)=\mathrm{G}_{\boldsymbol{0}}(t_0)=1$. Indeed, using $\mathcal{J}_{\boldsymbol{n}}(0)=\prod_{i=1}^d \mathcal{I}_{x_i}(0)=0$ for all $\boldsymbol{n}\neq\boldsymbol{0}$ and $\mathcal{J}_{\boldsymbol{0}}(0)=\prod_{i=1}^d \mathcal{I}_{x_i=0}(0)=1$ this fact is verified.

In the particular case $t_0=0$, if the initial configuration is completely uncorrelated, *i.e.* $\mathrm{G}_{\boldsymbol{n}}(0)=\delta_{\boldsymbol{n},\boldsymbol{0}}$, the solution reduces to

$$A_0(t)\equiv A(t,t_0=0)=\mathrm{e}^{-t}\left[\mathcal{I}_0\left(\frac{t}{d}\right)\right]^d \tag{C.36}$$

with asymptotic behaviour $A_0(t)\sim[2\pi t/d]^{-d/2}$. In the limit $t\gg t_0$ one can use the asymptotic expansion $\mathcal{J}_{\boldsymbol{n}}(u)=\prod_{i=1}^d \mathcal{I}_{x_i}(u)\simeq[\mathrm{e}^u/\sqrt{2\pi u}]^d$ for $u\gg 1$ and, therefore,

$$\lim_{t\gg t_0} A(t,t_0) \;=\; [2\pi(t-t_0)/d]^{-d/2} \sum_{\boldsymbol{n}\in\mathbb{Z}^d} \mathrm{G}_{\boldsymbol{n}}(t_0)\;. \tag{C.37}$$

Let us derive the asymptotic behaviour of $A(t,t_0)$ for large $t-t_0$ and t_0, in the particular case $d=2$. The t_0-dependent factor $S(\boldsymbol{0},t_0)=\sum_{\boldsymbol{n}}\mathrm{G}_{\boldsymbol{n}}(t_0)$ can be estimated for large t_0 by using the expression of Eq. (C.29) and using a continuum space approximation for the evaluation of the sum,

$$S^{(d=2)}(\boldsymbol{0},t_0)\equiv \sum_{n_1,n_2\in\mathbb{Z}} \mathrm{G}_{(n_1,n_2)}(t_0) \sim \frac{1}{\ln t_0}\int \mathrm{d}^2x\; \mathcal{G}\left(\frac{|\boldsymbol{x}|}{\sqrt{t_0}}\right) = \tag{C.38}$$

$$= \frac{2\pi t_0}{\ln t_0}\int_0^{+\infty} \mathrm{d}r\, r\mathcal{G}(r) \quad , \tag{C.39}$$

assuming that the quantity $\int_0^{+\infty}\mathrm{d}r\, r\mathcal{G}(r)$ is finite. Going back to Eq. (C.37) this implies

$$\lim_{t\gg t_0,\; t_0\gg 1} A(t,t_0) \propto \frac{t_0}{\ln t_0}\;(t-t_0)^{-1}\;. \tag{C.40}$$

Further details on how to obtain the analytical results sketched in this section can be found in [64, 68, 153, 155].

Appendix D

D.1 Equilibrium measure for the simple harmonic oscillator after a quench

Consider, as an example, a simple harmonic oscillator. The dynamics of the system is given by the familiar Newton equation

$$m\ddot{x} + m\omega^2 x = 0 \,, \tag{D.1}$$

given certain initial conditions $x(0) = x_0$ and $p(0) = m\dot{s}(0) = p_0$.

Let us take the initial conditions in canonical equilibrium with respect to the Hamiltonian $H_0 = \frac{p_0^2}{2m} + V_0(x_0)$, with $V_0(x_0)$ the initial potential energy given by $V_0(x_0) = \frac{1}{2}\omega_0^2\, x_0^2$. The probability distribution of (x_0, p_0) is given by

$$P_0(x_0, p_0) = Z_0^{-1}\, e^{-\beta' H_0} = Z_0^{-1}\, e^{-\beta'[\frac{p_0^2}{2m} + V_0(x_0)]} \tag{D.2}$$

with $\beta' = 1/T'$ the inverse temperature (using the same notation adopted in Chap. 4 for the initial temperature). The average kinetic energy of the ensemble of initial states sampled with this probability distribution is

$$\frac{1}{2m}\langle p_0^2 \rangle = \frac{T'}{2} \,, \tag{D.3}$$

which corresponds to the so-called equipartition of energy. Here the angular brackets indicate average over the initial conditions sampled with the equilibrium distribution P_0.

Let us now consider an istantaneous quench in the potential energy term of the form

$$V_0(x) \mapsto V(x) \,, \quad \text{with } V(x) = \frac{1}{2}\, \omega^2 x^2 \,, \tag{D.4}$$

where $\omega \neq \omega_0$, and then let the system evolve with the new Hamiltonian $H = \frac{p^2}{2m} + V(x)$. By performing this abrupt change one injects or extracts a finite amount of energy,

$$\Delta E = H(x_0, p_0) - H_0(x_0, p_0) = V(x_0) - V_0(x_0) \,. \tag{D.5}$$

The iso-energy surface on which the dynamics takes place for $t > 0$ is the one corresponding to the post-quench energy $E(0^+) = p_0^2/(2m) + V(x_0)$. The time evolution of the initial configuration (x_0, p_0) is given by

$$\begin{aligned} x(t) &= x_0 \cos\omega t + \frac{p_0}{m\omega} \sin\omega t \,, \\ p(t) &= -m\omega x_0 \sin\omega t + p_0 \cos\omega t \,. \end{aligned} \tag{D.6}$$

For ease of notation, let us call $y = x(t)$ and $z = p(t)$ the position and momentum at a time t. The probability density of (y, z) is given by

$$P(y,z,t) = \int dx_0 \int dp_0 \; P_0(x_0,p_0) \; \delta\left(y - x_0\cos\omega t - \frac{p_0}{m\omega}\sin\omega t\right) \times \\ \times \; \delta\left(z + m\omega x_0 \sin\omega t - p_0\cos\omega t\right) \; .$$

We use the second δ function to integrate over p_0, obtaining

$$P(y,z,t) = \int dx_0 \; P_0\left(x_0, \frac{z}{\cos\omega t} + m\omega x_0 \tan\omega t\right) \frac{1}{\cos\omega t} \times \\ \times \; \delta\left(y - x_0\cos\omega t - \frac{z + mx_0\omega\sin\omega t}{m\omega\cos\omega t}\sin\omega t\right) \; .$$

The remaining δ function implies

$$y - \frac{z}{m\omega}\tan\omega t - x_0\left(\cos\omega t + \tan\omega t\sin\omega t\right) = y - \frac{z}{m\omega}\tan\omega t - x_0\frac{1}{\cos\omega t} = 0 \; , \tag{D.7}$$

and we use it to integrate over x_0. Indeed, replacing $x_0 = y\cos\omega t - \frac{z}{m\omega}\sin\omega t$ and taking care of the Jacobian one easily finds

$$P(y,z,t) = P_0\left(y\cos\omega t - \frac{z}{m\omega}\sin\omega t,\; z\cos\omega t + m\omega y\sin\omega t\right) \; . \tag{D.8}$$

The above implies

$$\ln Z_0 + \ln P(y,z,t) = -\frac{\beta'}{2m}\left(z\cos\omega t + m\omega y\sin\omega t\right)^2 - \frac{\beta'}{2}m\omega_0^2\left(y\cos\omega t - \frac{z}{m\omega}\sin\omega t\right)^2 \; ,$$

and after some rearrangements, one gets

$$\ln Z_0 + \ln P(y,z,t) = -\frac{\beta'}{2}\left[\left(\cos^2\omega t + \frac{\omega_0^2}{\omega^2}\sin^2\omega t\right)\frac{z^2}{m} + m\omega^2\left(\sin^2\omega t + \frac{\omega_0^2}{\omega^2}\cos^2\omega t\right)y^2 \right. \\ \left. + 2m\omega\left(1 + \frac{\omega_0^2}{\omega^2}\right)\cos\omega t\;\sin\omega t\;yz\right] \; .$$

Although the measure P is still Gaussian, it does not have the same covariance as the initial P_0. The mean values and the variances of the position and momentum can be computed directly from the solutions to the equations of motion. The mean values vanish, while for the variances one finds

$$\begin{aligned} \sigma_x^2(t) &= \langle x^2(t)\rangle = \langle x_0^2\rangle\cos^2\omega t + \langle p_0^2\rangle\;\frac{1}{m^2\omega^2}\sin^2\omega t \; , \\ \sigma_p^2(t) &= \langle p^2(t)\rangle = \langle x_0^2\rangle\; m^2\omega^2\sin^2\omega t + \langle p_0^2\rangle\cos^2\omega t \; . \end{aligned} \tag{D.9}$$

Replacing now the averages of the initial values $\langle p_0^2\rangle/m = m\omega_0^2\langle x_0^2\rangle = T'$, one gets

$$\begin{aligned} m\omega^2\sigma_x^2(t) &= m\omega^2\langle x^2(t)\rangle = T'\left(\frac{\omega^2}{\omega_0^2}\cos^2\omega t + \sin^2\omega t\right) , \\ \tfrac{1}{m}\sigma_p^2(t) &= \frac{1}{m}\langle p^2(t)\rangle = T'\left(\cos^2\omega t + \frac{\omega^2}{\omega_0^2}\sin^2\omega t\right) . \end{aligned} \tag{D.10}$$

One readily verifies that, as expected, the average total energy is conserved

$$\langle E(t)\rangle = m\omega^2\sigma_x^2(t) + \frac{1}{m}\sigma_p^2(t) = T'\left(1+\frac{\omega^2}{\omega_0^2}\right) = \langle E(0^+)\rangle\ , \qquad \text{for} \quad t>0 \tag{D.11}$$

since each single trajectory does conserve its initial energy.

The time-average of an observable $A(x(t),p(t))$ is defined as

$$\overline{A} = \lim_{\tau\to+\infty}\frac{1}{\tau}\int_{t_0}^{t_0+\tau} \mathrm{d}t\ A(x(t),p(t)) \tag{D.12}$$

for any $t_0>0$. Ultimately $\overline{A}$ should not depend on the reference time t_0 if the system is able to reach a stationary state in the post-quench dynamics. In the case of the simple harmonic oscillator, the trajectory of the system is periodic and thus one can compute a time average over an interval which is a multiple of the period. If computed in this way, the time-averaged values of the variances are given by:

$$m\omega^2\overline{\sigma_x^2(t)} = \frac{T'}{2}\left(\frac{\omega^2}{\omega_0^2}+1\right)\ , \tag{D.13}$$

$$\frac{1}{m}\overline{\sigma_p^2(t)} = \frac{T'}{2}\left(\frac{\omega^2}{\omega_0^2}+1\right)\ , \tag{D.14}$$

$$\overline{x(t)p(t)} = 0 \tag{D.15}$$

and from these one can identify the "final" temperature as

$$T_f \equiv 2\overline{E_{\rm pot}} = m\omega^2\overline{\sigma_x^2(t)} = \frac{T'}{2}\left(\frac{\omega^2}{\omega_0^2}+1\right)\ . \tag{D.16}$$

D.2 Neumann's model, integrability and equilibration

In this Appendix we explain the relation between the Hamiltonian dynamics of the $p=2$ spherical spin glass model and the integrable model of Neumann [91]. We start by recalling some basic properties of classical integrable systems in the sense of Liouville [156, 157]. We then recall the definition of Neumann's model and we introduce the corresponding integrals of motion in the $p=2$ spherical model. We also provide a brief description of the Generalised Gibbs Ensemble.

Integrable systems

In classical mechanics, systems are said to be Liouville integrable if there exist sufficiently many well-behaved first integrals or constant of motions in *involution* such that the problem can be solved by quadratures [156, 157], in other words, the solution can be reduced to a finite number of algebraic operations and integrations. In more concrete terms, an integrable dynamical system with $2N$ degrees of freedom (N coordinates and N canonical momenta) consists of a $2N$-dimensional phase space Γ together with N independent functions[1] $O_1,\dots,O_N$: $\Gamma\to\mathbb{R}$, such that the mutual Poisson brackets vanish,

$$\{O_j,O_l\} = 0 \qquad \text{for all}\ \ j,l\ . \tag{D.17}$$

[1] In the sense that the gradients $\vec{\nabla}O_i$ are linearly independent vectors on the tangent space to any point in Γ

We will assume henceforth that the O_i do not depend explicitly on time and that $dO_i/dt = 0$ is equivalent to $\{H, O_i\} = 0$, with H the Hamiltonian of the system. The Hamiltonian H is itself an integral of motion and the energy is the first constant of motion one can think of.

The dynamics can be seen as the motion in a manifold of dimension $2N - N = N$ in which all the trajectories share the initial values of all the conserved quantities $O_i(t) = O_i(0)$. Under these conditions the Hamilton equations of motion are solvable by performing a canonical transformation into so-called *action-angle* variables (I_i, ϕ_i) with $i = 1, \ldots, N$ such that the Hamiltonian is rewritten as $\tilde{H}(\{I_i\})$ and

$$I_k(t) = I_k(0) \ , \qquad \phi_k(t) = \phi_k(0) + t \ \frac{\partial \tilde{H}(\{I_i\})}{\partial I_k} = \phi_k(0) + t \ \omega_k(\{I_i\}) \ , \tag{D.18}$$

for all $k = 1, \ldots, N$ and $t \geq 0$, where we define $\omega_k(\{I_i\}) = \frac{\partial \tilde{H}(\{I_i\})}{\partial I_k}$. The remaining evolution is given by N circular motions with constant angular velocities, that is to say, the N-dimensional manifold $\Gamma(O_1, \ldots, O_N)$ corresponding to the trajectories that have same values for the constant of motions O_i, is transformed into a N-dimensional torus under the canonical transformation to the action-angle variables. Both deciding whether a system is integrable and finding the canonical transformation that leads to the pairs (I_i, ϕ_i) are in practice very difficult tasks. Whenever the system is integrable, and one knows the action-angle pairs, the statement in Eq. (D.18) is part of the Liouville-Arnold theorem [158].

Neumann's model and its integrals of motion

The model proposed by Neumann in 1850 describes the dynamics of a particle constrained to move on the $(N-1)$-dimensional sphere under the effect of harmonic forces [91]. The Hamiltonian is given by

$$H = \frac{1}{4N} \sum_{k \neq l} L_{kl}^2 + \frac{1}{2} \sum_k a_k x_k^2 \tag{D.19}$$

where the L_{kl} are the elements of an angular momentum anti-symmetric matrix

$$\sqrt{m} \, L_{kl} = x_k p_l - p_k x_l \ , \tag{D.20}$$

and p_k and x_k are phase space variables with canonical Poisson brackets $\{x_k, p_l\} = \delta_{kl}$. The global spherical constraint

$$\sum_{k=1}^{N} x_k^2 = N \tag{D.21}$$

ensures that the motion takes place on S_{N-1}, the $(N-1)$-sphere. Using the fact that $L_{kk} = 0$ to rewrite the double sum in the first term in H as an unconstrained sum, and replacing L_{kl} by its explicit form in terms of x_k and p_k, one derives

$$m \sum_{k \neq l} L_{kl}^2 = m \sum_{k,l} L_{kl}^2 = 2 \sum_k x_k^2 \sum_l p_l^2 - 2 \sum_k x_k p_k \sum_l x_l p_l \ . \tag{D.22}$$

Imposing next the spherical constraint, that also implies $\sum_k x_k p_k = 0$, the above sum reduces to

$$m \sum_{k \neq l} L_{kl}^2 = 2N \ \sum_k p_k^2 \ . \tag{D.23}$$

Note that we added a factor $1/N$ in front of the kinetic energy in Eq. (D.19) in order to ensure that the two terms are extensive and the thermodynamic limit is non-trivial.

It is quite clear that Neumann's model is therefore identical to the Hamiltonian $p = 2$ spherical spin glass model (with a strict spherical constraint) once the latter is written in the basis of eigenvectors of the interaction matrix J_{ij}, with the correspondence $a_k \mapsto -\lambda_k$, where λ_k are the eigenvalues of J_{ij}.

The $N-1$ integrals of motion were constructed by K. Uhlenbeck [92] and more recently rederived by Babelon & Talon [94] with a separation of variables method. In a notation that is convenient for our application they read

$$I_k = x_k^2 + \frac{1}{N}\sum_{l(\neq k)} \frac{L_{kl}^2}{a_k - a_l} = x_k^2 + \frac{1}{mN}\sum_{l(\neq k)} \frac{x_k^2 p_l^2 + x_l^2 p_k^2 - 2x_k p_l x_l p_k}{a_k - a_l} \tag{D.24}$$

and satisfy $\sum_k I_k = N$ and $\frac{1}{2}\sum_k a_k I_k = H$. After a trivial translation to the variables of the $p = 2$ spherical model we have

$$I_\mu(\{s_k, p_k\}) = s_\mu^2 + \frac{1}{mN}\sum_{\nu(\neq\mu)} \frac{s_\mu^2 p_\nu^2 + s_\nu^2 p_\mu^2 - 2s_\mu p_\nu s_\nu p_\mu}{\lambda_\nu - \lambda_\mu}\,, \tag{D.25}$$

where s_μ represents the projection of the spin vector onto the direction of the eigenvector of the interaction matrix associated with the eigenvalue λ_μ, and $p_\mu = m\dot{s}_\mu$ its momentum.

Statistical measures for integrable systems

Let $\vec{X} = (x_1, p_1, \ldots, x_N, p_N)$ be a generic point in phase space. One readily constructs a microcanonical measure

$$\rho_{\mathrm{GME}}(\vec{X}) = Z_{\mathrm{GME}}^{-1} \prod_{j=1}^{N} \delta(I_j(\vec{X}) - c_j) \tag{D.26}$$

with the normalisation $Z_{\mathrm{GME}}(\{c_i\}) = \int d\vec{X} \ \prod_{j=1}^N \delta(I_j(\vec{X}) - c_j)$, where c_k is the constant value taken by the integral of motion I_k, for $k = 1, \ldots, N$. The Liouville-Arnold theorem [158] ensures that this measure is sampled asymptotically if the frequencies $\omega_k = \frac{\partial H}{\partial I_k}$ of the periodic motion on the torus are independent, that is to say, if the equation $\sum_k z_k\omega_k = 0$, with z_k integer numbers, has the unique solution $z_k = 0$ for all k. One can call this ensemble the Generalized Microcanonical Ensemble (GME).

In principle, the Generalized Canonical Ensemble, commonly called Generalized Gibbs Ensemble (GGE), can now be constructed from the Generalized Microcanonical Ensemble following the usual steps. The idea is to look for the joint probability measure $P(c_1, \ldots, c_N)\mathrm{d}c_1 \ldots \mathrm{d}c_N$ of N extensive (as for the Hamiltonian, in the usual case) constants of motion of a subsystem. As in cases with just one conserved quantity, it is convenient to interpret P as a probability over position and momenta variables, and write

$$P_{\mathrm{GGE}}(\vec{X}) = Z_{\mathrm{GGE}}^{-1}(\zeta_1, \ldots, \zeta_N) \ \exp\left(-\sum_j \zeta_j I_j(\vec{X})\right)\,, \tag{D.27}$$

where the parameter ζ_k is the equivalent of an inverse temperature for the k-th integral of motion I_k, and Z_{GGE} is the normalisation factor. This form can be derived under the same kind of assumptions used in the derivation of the canonical measure from the microcanonical one. Let the system be divided into two disjoint parts, subsystem A and subsystem B, with

A much smaller than B, and denote by $I_1^{(A)}, \ldots, I_N^{(A)}$ the conserved quantities for subsystem A, while by $I_1^{(B)}, \ldots, I_N^{(B)}$ those for subsystem B. One can constructs a GGE measure for subsystem A under the following assumptions:

(i) additivity of the conserved quantities, that is to say, $I_k = I_k^{(A)} + I_k^{(B)}$, for all k;

(ii) independence of the chosen subsystem with respect to the rest of the system, in other words, the factorisation of the density of states,

$$g\left(I_1, \ldots, I_N\right) = g_A\left(I_1^{(A)}, \ldots, I_N^{(A)}\right)\ g_B\left(I_1^{(B)}, \ldots, I_N^{(B)}\right)\ ;$$

(iii) constant inverse "temperatures" given by

$$\zeta_k \equiv \frac{\partial}{\partial I_k^{(B)}} S_B\left(I_1^{(B)}, \ldots, I_N^{(B)}\right) = \frac{\partial}{\partial I_k^{(B)}} \ln g_B\left(I_1^{(B)}, \ldots, I_N^{(B)}\right)\ ,$$

with $S_B = \ln g_B$ the microcanonical entropy of subsystem B.

An inspiring discussion along these lines appeared in [159]. The conditions just listed imply a locality requirement on the I_ks. This is similar to the requirement of having short-range interactions to derive the equivalence between the canonical and microcanonical ensembles in standard statistical mechanics.

In the case of the Neumann model, or the $p = 2$ spherical spin glass model, the set of conserved quantities are the I_μ defined in Eq. (D.25). We note that if, under some special conditions, the Lagrange multipliers ζ_k became equal to $-\lambda_k\beta/2$, with $\{\lambda_\mu\}$ the eigenvalues of the interaction matrix and β some constant, then the GGE measure would be

$$P_{\rm GGE}(\vec{X}) = Z_{\rm GGE}^{-1}\ e^{-\beta\left(-\frac{1}{2}\sum_\mu \lambda_\mu I_\mu(\vec{X})\right)} = Z_{\rm GGE}^{-1}\ e^{-\beta H(\vec{X})} = P_{\rm GB}(\vec{X}, \beta)\ , \tag{D.28}$$

with $P_{\rm GB}(\vec{X}, \beta)$ the Gibbs-Boltzmann measure at inverse temperature β, having used $H = -\frac{1}{2}\sum_\mu \lambda_\mu I_\mu$.

Bibliography

[1] A. Tartaglia, L. F. Cugliandolo & M. Picco; «Percolation and coarsening in the bidimensional voter model»; Phys. Rev. E **92**, p. 042 109 (2015). VII, 69

[2] T. Blanchard, L. F. Cugliandolo, M. Picco & A. Tartaglia; «Critical percolation in the dynamics of the bidimensional ferromagnetic Ising model»; Journal of Statistical Mechanics: Theory and Experiment **2017**, p. 113 201 (2017). VIII

[3] A. Tartaglia, L. F. Cugliandolo & M. Picco; «Phase separation and critical percolation in bidimensional spin-exchange models»; EPL (Europhysics Letters) **116**, p. 26 001 (2016). VIII, 20, 46

[4] A. Tartaglia, L. F. Cugliandolo & M. Picco; «Coarsening and percolation in the kinetic 2d Ising model with spin-exchange updates and the voter model»; (2018); arXiv:1805.05775. VIII

[5] L. F. Cugliandolo, G. S. Lozano, N. Nessi, M. Picco & A. Tartaglia; «Quenched dynamics of classical isolated systems: the spherical spin model with two-body random interactions or the Neumann integrable model»; Journal of Statistical Mechanics: Theory and Experiment **2018**, p. 063 206 (2018). IX

[6] V. Spirin, P. L. Krapivsky & S. Redner; «Fate of zero-temperature Ising ferromagnets»; Phys. Rev. E **63**, p. 036 118 (2001). 3, 5, 23, 30

[7] V. Spirin, P. Krapivsky & S. Redner; «Freezing in Ising ferromagnets»; Phys. Rev. E **65**, p. 016 119 (2002). 3, 5, 23

[8] K. Barros, P. L. Krapivsky & S. Redner; «Freezing into stripe states in two-dimensional ferromagnets and crossing probabilities in critical percolation»; Phys. Rev. E **80**, p. 040 101 (2009). 3, 5, 31, 54, 164, 171

[9] J. Olejarz, P. L. Krapivsky & S. Redner; «Fate of 2D Kinetic Ferromagnets and Critical Percolation Crossing Probabilities»; Phys. Rev. Lett. **109**, p. 195 702 (2012). 3, 5, 30, 31, 164

[10] J. J. Arenzon, A. J. Bray, L. F. Cugliandolo & A. Sicilia; «Exact results for curvature-driven coarsening in two dimensions»; Phys. Rev. Lett. **98**, p. 145 701 (2007). 3, 4, 8, 9, 15, 35, 36, 81

[11] A. Sicilia, J. J. Arenzon, A. J. Bray & L. F. Cugliandolo; «Domain growth morphology in curvature driven two dimensional coarsening»; Phys. Rev. E **76**, p. 061 116 (2007). 3, 4, 15, 35, 36, 81, 163

[12] A. Sicilia, J. J. Arenzon, A. J. Bray & L. F. Cugliandolo; «Geometric properties of two-dimensional coarsening with weak disorder»; Europhys. Lett. **82**, p. 10 001 (2008). 3, 4

[13] A. Sicilia, Y. Sarrazin, J. J. Arenzon, A. J. Bray & L. F. Cugliandolo; «Geometry of phase separation»; Phys. Rev. E **80**, p. 031 121 (2009). 4, 15, 48

[14] T. Blanchard, F. Corberi, L. F. Cugliandolo & M. Picco; «How soon after a zero-temperature quench is the fate of the Ising model sealed?»; EPL **106**, p. 66 001 (2014). 4, 20, 23, 24

[15] R. J. Glauber; «Time-dependent Statistics of the Ising Model»; J. Math. Phys. **4**, p. 294 (1963). 7

[16] G. T. Barkema & M. E. J. Newman; *Monte Carlo methods in statistical physics* (Oxford University Press, Oxford) (1999). 7, 8

[17] A. B. Bortz, M. H. Kalos & J. L. Lebowitz; «A new algorithm for Monte Carlo simulation of Ising spin systems»; J. Comp. Phys. **17**, p. 10 (1975). 7

[18] A. J. Bray, K. Humayun & T. J. Newman; «Kinetics of ordering for correlated initial conditions»; Phys. Rev. B **43**, p. 3699–3702 (1991). 8, 163

[19] S. Chakraborty & S. K. Das; «Role of initial correlation in coarsening of a ferromagnet»; Eur. Phys. J. B **88**, p. 160 (2015). 8

[20] F. Corberi & R. Villavicencio-Sanchez; «Role of initial state and final quench temperature on aging properties in phase-ordering kinetics»; Phys. Rev. E **93**, p. 052 105 (2016). 8

[21] M. Henkel & M. Pleimling; *Non-Equilibrium Phase Transitions: ageing and Dynamical Scaling Far from Equilibrium* (Springer-Verlag) (2010). 9

[22] A. J. Bray & K. Humayun; «Non-equilibrium dynamics of the Ising model for $T \leq T_c$»; J. Phys. A **24**, p. L1185 (1991). 9

[23] A. J. Bray; «Theory of phase ordering kinetics»; Adv. Phys. **43**, p. 357 (1994). 11, 98

[24] H. Pinson; «Critical percolation on the torus»; J. Stat. Phys. **75**, p. 1167 (1994). 13, 54

[25] J. Cardy; «Critical Percolation in Finite Geometries»; J. Phys. A **25**, p. L201 (1992). 13, 164

[26] G. M. T. Watts; «A crossing probability for critical percolation in two dimensions»; J. Phys. A: Math. Gen. **29**, p. 363 (1996). 13, 164

[27] H. Saleur & B. Duplantier; «Exact determination of the percolation Hull exponent in two dimensions»; Phys. Rev. Lett. **58**, p. 2325–2328 (1987). 13, 16

[28] S. Smirnov; «Critical percolation in the plane: conformal invariance, Cardy's formula, scaling limits»; C. R. Acad. Sci. Paris I **333**, p. 239 (2001). 14, 15

[29] D. Stauffer & A. Aharony; *Introduction To Percolation Theory* (Taylor and Francis, London) (1994). 14, 17

[30] O. Schramm; «Scaling limits of loop-erased random walks and uniform spanning trees»; arXiv:math/9904022v2. 15

[31] I. Benjamini & O. Häggström (rédacteurs); *Conformally invariant scaling limits: an overview and a collection of problems*; p. 1161–1191 (Springer New York, New York, NY) (2011). 15

[32] G. F. Lawler; «Schramm-Loewner Evolution»; arXiv:0712.3256v1. 15

[33] F. Camia & C. M. Newman; «Two-Dimensional Critical Percolation: The Full Scaling Limit»; Communications in Mathematical Physics **268**, p. 1–38 (2006). 15

[34] R. Langlands, P. Pouliot & Y. Saint-Aubin; «Conformal invariance in two-dimensional percolation»; Bull. Am. Math. Soc. **30**, p. 1 (1994). 15

[35] B. Wieland & D. B. Wilson; «Winding angle variance of Fortuin-Kasteleyn contours»; Phys. Rev. E **68**, p. 056 101 (2003). 16

[36] K. Christensen & N. R. Moloney; *Complexity and Criticality* (Imperial College Press) (2005). 17

[37] A. A. Saberi; «Recent advances in percolation theory and its applications»; Phys. Rep. **578**, p. 1 (2015). 17

[38] F. Corberi, L. F. Cugliandolo, F. Insalata & M. Picco; «Coarsening and percolation in a disordered ferromagnet»; Phys. Rev. E **95**, p. 022 101 (2017). 20, 26

[39] S. M. Allen & J. W. Cahn; «A microscopic theory for antiphase boundary motion and its application to antiphase domain coarsening»; Acta Metall. **27**, p. 1085 (1979). 28, 36

[40] H. Takeuchi; «Domain Size Distribution in Segregating Binary Superfluids»; J. of Low Temp. Phys. **183**, p. 169 (2016). 46

[41] J. Hofmann, S. S. Natu & S. D. Sarma; «Coarsening Dynamics of Binary Bose Condensates»; Phys. Rev. Lett. **113**, p. 095 702 (2014). 47

[42] D. Reith, K. Bucior, L. Yelash, P. Virnau & K. Binder; «Spinodal decomposition of polymer solutions: molecular dynamics simulations of the two-dimensional case»; J. Phys.: Condens. Matter **24**, p. 115 102 (2012). 47, 48

[43] K. Kawasaki; «Diffusion Constants near the Critical Point for Time-Dependent Ising Models. I»; Phys. Rev. **145**, p. 224 (1966). 47, 48

[44] K. Kawasaki; «Diffusion Constants near the Critical Point for Time-Dependent Ising Models. II»; Phys. Rev. **148**, p. 375 (1966). 47, 48

[45] A. J. Bray; «Coarsening dynamics of phase-separating systems»; Phil. Trans. Roy. Soc. Lond. **361**, p. 781 (2003). 48

[46] I. M. Lifshitz & V. V. Slyozov; «The kinetics of precipitation from supersaturated solid solutions»; J. Phys. Chem. Solids **19**, p. 35–50 (1961). 48

[47] C. Wagner; «Theory of precipitate change by redissolution»; Z. Elektrochem. **65**, p. 581 (1961). 48

[48] D. A. Huse; «Corrections to late-stage behavior in spinodal decomposition: Lifshitz-Slyozov scaling and Monte Carlo simulations»; Phys. Rev. B **34**, p. 7845 (1986). 48, 53

[49] J. G. Amar, F. E. Sullivan & R. D. Mountain; «Monte Carlo study of growth in the two-dimensional spin-exchange Kinetic Ising Model»; Phys. Rev. B **37**, p. 196 (1988). 48, 53

[50] T. M. Rogers, K. R. Elder & R. C. Desai; «Numerical study of the late stages of spinodal decomposition»; Phys. Rev. B **37**, p. 9638 (1988). 48, 53

[51] C. Godrèche, F. Krzakała & F. Ricci-Tersenghi; «Non-equilibrium critical dynamics of the ferromagnetic Ising model with Kawasaki dynamics»; J. Stat. Mech. **2004**, p. P04 007 (2004). 48

[52] F. Krzakała; «Glassy Properties of the Kawasaki Dynamics of Two-Dimensional Ferromagnets»; Phys. Rev. Lett. **94**, p. 077 204 (2005). 48

[53] H. Takeuchi, Y. Mizuno & K. Dehara; «Phase-ordering percolation and an infinite domain wall in segregating binary Bose-Einstein condensates»; Phys. Rev. A **92**, p. 043 608 (2015). 48, 55

[54] G. F. Mazenko; «Growth kinetics for a system with a conserved order parameter»; Phys. Rev. E **50**, p. 3485–3501 (1994). 50

[55] J. F. Marko & G. T. Barkema; «Phase ordering in the Ising model with conserved spin»; Phys. Rev. E **52**, p. 2522–2534 (1995). 50

[56] S. Puri, A. J. Bray & J. L. Lebowitz; «Phase-separation kinetics in a model with order-parameter-dependent mobility»; Phys. Rev. E **56**, p. 758–765 (1997). 50

[57] G. Pruessner & N. R. Moloney; «Winding Clusters in Percolation on the Torus and the Möbius Strip»; J. Stat. Phys. **115**, p. 839 (2004). 54, 171

[58] T. Blanchard; «Wrapping probabilities for Ising spin clusters on a torus»; Journal of Physics A: Mathematical and Theoretical **47**, p. 342 002 (2014). 54, 171

[59] P. Clifford & A. Sudbury; «Model for spatial conflict»; Biometrika **60**, p. 581 (1973). 69

[60] R. A. Holley & T. M. Liggett; «Ergodic theorems for weakly interacting infinite systems and voter model»; Annals of Probability **3**, p. 643 (1975). 69

[61] T. M. Liggett; *Stochastic interacting systems: contact, voter and exclusion processes* (Springer, Berlin) (1999). 69

[62] P. L. Krapivsky; «Kinetics of monomer-monomer surface catalytic reactions»; Phys. Rev. A **45**, p. 1067 (1992). 69

[63] P. L. Krapivsky; «Kinetics of a monomer-monomer model of heterogeneous catalysis»; J. Phys. A **25**, p. 5831 (1992). 69

[64] L. Frachebourg & P. L. Krapivsky; «Exact results for kinetics of catalytic reactions»; Phys. Rev. E **53**, p. R3009 (1996). 69, 195, 196, 197, 198, 199

[65] F. Vazquez, P. L. Krapivsky & S. Redner; «Constrained opinion dynamics: freezing and slow evolution»; J. Phys. A **36**, p. L61 (2003). 69

[66] J. Fernández-Gracia, K. Suchecki, J. J. Ramasco, M. S. Miguel & V. M. Eguiluz; «Is the voter model a model for voters?»; Phys. Rev. Lett. **112**, p. 158 701 (2014). 69

[67] K. S. Korolev, M. Avlund, O. Hallatschek & D. R. Nelson; «Genetic demixing and evolution in linear stepping stone models»; Rev. Mod. Phys. **82**, p. 1691–1718 (2010). 69

[68] M. J. de Olivieira; «Linear Glauber model»; Phys. Rev. E **67**, p. 066 101 (2003). 71, 198, 199

[69] J.-M. Drouffe & C. Godrèche; «Coarsening and persistence in a class of stochastic processes interpolating between the Ising and voter models»; J. Phys. A **32**, p. 249 (1999). 71, 74, 191

[70] C. Castellano, S. Fortunato & V. Loreto; «Statistical physics of social dynamics»; Rev. Mod. Phys. **81**, p. 591 (2009). 71

[71] M. Scheucher & H. Spohn; «A soluble kinetic model for spinodal decomposition»; J. Stat. Phys **53**, p. 279 (1988). 71, 194

[72] T. Blanchard, L. F. Cugliandolo & M. Picco; «A morphological study of cluster dynamics between critical points»; J. Stat. Mech. p. P05026 (2012). 73

[73] H. Ricateau, L. F. Cugliandolo & M. Picco; «Critical percolation in the slow cooling of the bi-dimensional ferromagnetic Ising model»; Journal of Statistical Mechanics: Theory and Experiment **2018**, p. 013 201 (2018). 74

[74] M. J. de Oliveira, J. F. F. Mendes & M. A. Santos; «Nonequilibrium spin models with Ising universal behaviour»; J. Phys. A: Math. Gen. **26**, p. 2317 (1993). 74, 191, 193

[75] A. Polkovnikov, K. Sengupta, A. Silva & M. Vengalattore; «Nonequilibrium dynamics of isolated interacting quantum systems»; Rev. Mod. Phys. **83**, p. 863 (2011). 89, 90

[76] I. Bloch, J. Dalibard & W. Zwerger; «Many-body physics with ultracold gases»; Rev. Mod. Phys. **80**, p. 885 (2008). 89

[77] D. M. Basko, I. L. Aleiner & B. L. Altshuler; «Metal-insulator transition in a weakly interacting many-electron system with localized single-particle states»; Ann. Phys. **321**, p. 1126 (2006). 89

[78] P. Calabrese, F. H. L. Essler & G. Mussardo; «Introduction to Quantum Integrability in Out of Equilibrium Systems»; Journal of Statistical Mechanics: Theory and Experiment **2016**, p. 064 001 (2016). 89

[79] M. Rigol, V. Dunjko, V. Yurovsky & M. Olshanii; «Relaxation in a completely integrable many-body quantum system: An *ab initio* study of the dynamics of the highly excited states of 1D lattice hard-core bosons»; Phys. Rev. Lett. **98**, p. 050 405 (2007). 90

[80] M. Rigol, V. Dunjko & M. Olshanii; «Thermalization and its mechanism for generic isolated quantum systems»; Nature **452**, p. 854 (2008). 90

[81] P. Calabrese; «Quantum integrability in out-of-equilibrium systems»; J. Stat. Mech. p. 064001 (2016). 90

[82] C. Gogolin & J. Eisert; «Equilibration, thermalisation, and the emergence of statistical mechanics in closed quantum systems»; Rep. Prog. Phys. **79**, p. 056 001 (2016). 90

[83] L. F. Cugliandolo, G. S. Lozano & N. Nessi; «Non equilibrium dynamics of isolated disordered systems: the classical Hamiltonian p-spin model»; J. Stat. Mech p. P083301 (2017). 90, 107, 125, 140, 158

[84] L. F. Cugliandolo; «Dynamics of glassy systems»; dans J. L. Barrat, M. V. Feigel'man, J. Kurchan & J. Dalibard (rédacteurs), «Slow Relaxations and Nonequilibrium Dynamics in Condensed Matter», Les Houches LXXVII (Springer-Verlag) (2003); arXiv:cond-mat/0210312. 90, 94, 158

[85] A. Cavagna; «Supercooled liquids for pedestrians»; Phys. Rep. **476**, p. 51 (2009). 90

[86] L. Berthier & G. Biroli; «Theoretical perspective on the glass transition and amorphous materials»; Rev. Mod. Phys. **83**, p. 587 (2011). 90

[87] A. Engel; «Replica symmetry breaking in zero dimension»; Nucl. Phys. B **410**, p. 617–646 (1993). 90, 92

[88] S. Franz & M. Mézard; «Off-Equilibrium Glassy Dynamics: A Simple Case»; EPL **26**, p. 209 (1994). 90, 92

[89] L. F. Cugliandolo & P. Le Doussal; «Large time nonequilibrium dynamics of a particle in a random potential»; Phys. Rev. E **53**, p. 152 (1996). 90, 92

[90] T. Scaffidi & E. Altman; «Semiclassical Theory of Many-Body Quantum Chaos and its Bound»; arXiv:1711.04768. 90

[91] C. Neumann; «De problemate quodam mechanico, quod ad primam integralium ultraellipticorum classem revocatur»; Crelle Journal **56**, p. 46 (1850). 90, 203, 204

[92] K. K. Uhlenbeck; «Equivariant harmonic maps into spheres»; Springer Lecture Notes in Mathematics **49**, p. 146 (1982). 90, 159, 205

[93] J. Avan & M. Talon; «Poisson Structure and Integrability of the Neumann-Moser-Uhlenbeck Model»; Int. J. Mod. Phys. A **05**, p. 4477–4488 (1990). 90

[94] O. Babelon & M. Talon; «Separation of variables for the classical and quantum Neumann model»; Nucl. Phys. B **379**, p. 321 (1992). 90, 149, 159, 205

[95] J. M. Kosterlitz, D. J. Thouless & R. C. Jones; «Spherical Model of a Spin-Glass»; Phys. Rev. Lett **36**, p. 1217 (1976). 91, 94, 106

[96] D. Sherrington & S. Kirkpatrick; «Solvable Model of a Spin-Glass»; Phys. Rev. Lett. **35**, p. 1792–1796 (1975). 91

[97] A. Crisanti & H.-J. Sommers; «The spherical p-spin interaction spin glass model: the statics»; Zeitschrift für Physik B Condensed Matter **87**, p. 341 (1992). 92

[98] L. F. Cugliandolo & J. Kurchan; «Analytical solution of the off-equilibrium dynamics of a long-range spin-glass model»; Phys. Rev. Lett. **71**, p. 173 (1993). 92, 99, 100, 101, 158

[99] M. L. Mehta; *Random matrices* (Elsevier, Amsterdam) (2004). 93, 123, 151

[100] Y. V. Fyodorov; «High-Dimensional Random Fields and Random Matrix Theory»; Markov Proc. and Rel. Fields **21**, p. 483 (2015). 93, 94

[101] A. B. de Monvel, L. Pastur & M. Shcherbina; «On the statistical mechanics approach in the random matrix theory: Integrated density of states»; Journal of Statistical Physics **79**, p. 585–611 (1995). 93

[102] R. A. Adler; *The Geometry of Random Fields* (J. Wiley and Sons, New York) (1981). 94

[103] A. J. Bray & D. S. Dean; «Statistics of critical points of Gaussian fields on large-dimensional spaces»; Phys. Rev. Lett. **98**, p. 150 201 (2007). 94

[104] G. B. Arous, L. Sagun, V. U. Guney & Y. LeCun; «Explorations on high dimensional landscapes»; International Conference on learning representations, ICLR 2015; arXiv:1412.6615. 94

[105] D. J. Wales; *Energy Landscapes: With Applications to Clusters, Biomolecules and Glasses* (Cambridge University Press, Cambridge, U.K.) (2004). 94

[106] M. Mueller & M. Wyart; «Marginal Stability in Structural, Spin, and Electron Glasses»; Ann. Rev. Cond. Matt. Phys. **6**, p. 177 (2015). 94, 98

[107] L. Susskind; «The Anthropic Landscape of String Theory»; arXiv:hep-th/0302219. 94

[108] M. R. Douglas, B. Shiffman & S. Zelditch; «Critical Points and Supersymmetric Vacua I»; Commun. Math. Phys. **252**, p. 325–358 (2004). 94

[109] Y. V. Fyodorov & B. A. Khoruzhenko; «Nonlinear analogue of the May-Wigner instability transition»; Proc. Nat. Ac. Sc. **113**, p. 6827 (2016). 94

[110] K. H. Fischer & J. A. Hertz; *Spin glasses* (Cambridge University Press, Cambridge) (1991). 94

[111] T. Castellani & A. Cavagna; «Spin-glass theory for pedestrians»; J. Stat. Mech. p. P05012 (2005). 94, 100, 101, 158

[112] M. Mézard, G. Parisi & M. A. Virasoro; *Spin Glass Theory and Beyond: An Introduction to the Replica Method and Its Applications* (World Scientific, Singapore) (1986). 96

[113] P. Shukla & S. Singh; «Spin glass dynamics in the spherical model»; J. Phys. C: Solid State Physics **14**, p. L81 (1981). 97, 159

[114] S. Ciuchi & F. di Pasquale; «Nonlinear relaxation and ergodicity breakdown in random anisotropy spin glasses»; Nucl. Phys. B **300**, p. 31–60 (1988). 97, 159

[115] L. F. Cugliandolo & D. S. Dean; «Full dynamical solution for a spherical spin-glass model»; J. Phys. A: Math. Gen. **28**, p. 4213 (1995). 97, 98, 99, 140, 159

[116] L. F. Cugliandolo & D. S. Dean; «On the dynamics of a spherical spin-glass in a magnetic field»; J. Phys. A: Math. Gen. **28**, p. L453 (1995). 97, 159

[117] Y. V. Fyodorov, A. Perret & G. Schehr; «Large time zero temperature dynamics of the spherical $p = 2$ spin glass model of finite size»; J. Stat. Mech. p. P11017 (2015). 97, 159

[118] A. Onuki; *Phase transition dynamics* (Cambridge University Press) (2004). 98

[119] S. Puri & V. Wadhawan (rédacteurs); *Kinetics of phase transitions* (Taylor and Francis Group) (2009). 98

[120] F. Corberi & P. Politi; «Coarsening Dynamics»; Comptes Rendus de Physique **16**, p. 255 (2015). 98

[121] A. Barrat, S. Franz & G. Parisi; «Temperature evolution and bifurcations of metastable states in mean-field spin glasses, with connections with structural glasses»; J. Phys. A **30**, p. 5593 (1997). 98

[122] L. F. Cugliandolo, J. Kurchan & L. Peliti; «Energy flow, partial equilibration, and effective temperatures in systems with slow dynamics»; Phys. Rev. E **55**, p. 3898 (1997). 99

[123] L. F. Cugliandolo; «The effective temperature»; J. Phys. A **44**, p. 483 001 (2011). 99

[124] D. Boyanovsky, C. Destri & H. J. de Vega; «Approach to thermalization in the classical ϕ^4 theory in $1 + 1$ dimensions: Energy cascades and universal scaling»; Phys. Rev. D **69**, p. 045 003 (2004). 100

[125] A. Houghton, S. Jain & A. P. Young; «Role of initial conditions in the mean-field theory of spin-glass dynamics»; Phys. Rev. B **28**, p. 2630 (1983). 100, 101, 104

[126] A. Barrat; «The p-spin spherical spin glass model»; (1997); arXiv:cond-mat/9701031. 101, 158

[127] L. F. Cugliandolo & J. Kurchan; «Weak Ergodicity Breaking in Mean-Field Spin-Glass Models»; Phil. Mag. B **71**, p. 501 (1995). 101, 158

[128] S. Franz & G. Parisi; «Recipes for Metastable States in Spin Glasses»; J. Phys. I France **5**, p. 1401–1415 (1995). 101, 107

[129] A. Barrat, R. Burioni & M. Mézard; «Dynamics within metastable states in a mean-field spin glass»; J. Phys. A: Math. Gen. **29**, p. L81 (1996). 101, 107

[130] H. Sompolinsky & A. Zippelius; «Relaxational dynamics of the Edwards-Anderson model and the mean-field theory of spin-glasses»; Phys. Rev. B **25**, p. 6860–6875 (1982). 104

[131] K. B. Blagoev, F. Cooper, J. F. Dawson & B. Mihaila; «Schwinger-Dyson approach to nonequilibrium classical field theory»; Phys. Rev. D **64**, p. 125 003 (2001). 108

[132] W. Milne; «The Numerical Determination of Characteristic Numbers»; Phys. Rev. **35**, p. 863 (1930). 117

[133] E. Pinney; «The nonlinear differential equation $y'' + p(x)y + cy^{-3} = 0$»; . 117

[134] S. Sotiriadis & J. Cardy; «Quantum quench in interacting field theory: A self-consistent approximation»; Phys. Rev. B **81**, p. 134 305 (2010). 117, 118

[135] A. Khinchin; *Mathematical foundations of statistical mechanics* (Dover, New York) (1949). 123

[136] C. Aron, G. Biroli & L. F. Cugliandolo; «Symmetries of generating functionals of Langevin processes with colored multiplicative noise»; J. Stat. Mech. **2010**, p. P11 018 (2010). 129

[137] A. J. Bray; «Renormalization-group approach to domain-growth scaling»; Phys. Rev. B **41**, p. 6724 (1990). 163, 179

[138] M. Grant & J. D. Gunton; «Temperature dependence of the dynamics of random interfaces»; Phys. Rev. B **28**, p. 5496 (1983). 163

[139] M.-D. Lacasse, M. Grant & J. Viñals; «Temperature dependence of the amplitude of power-law growth in the spin-flip kinetic Ising model»; Phys. Rev. B **48**, p. 3661–3665 (1993). 163

[140] T. Blanchard & M. Picco; «Frozen into stripes: fate of the critical Ising model after a quench»; Phys. Rev. E **88**, p. 032 131 (2013). 166

[141] S. Masui, T. Li, B. W. Southern & A. E. Jacobs; «Metastable states of Ising models on the honeycomb lattice»; Phys. Rev. B **40**, p. 7096–7100 (1989). 169

[142] A. E. Jacobs & C. M. Coram; «Ferromagnetic random-bond Ising model: Metastable states and complexity of the energy surface»; Phys. Rev. B **36**, p. 3844–3850 (1987). 169

[143] A. J. Bray; «Comment on "Critical dynamics and global conservation laws"»; Phys. Rev. Lett. **66**, p. 2048 (1991). 179

[144] C. Sire & S. N. Majumdar; «Coarsening in the q-state Potts model and the Ising model with globally conserved magnetization»; Phys. Rev. E **52**, p. 244 (1995). 179

[145] A. D. Rutenberg; «Nonequilibrium phase ordering with a global conservation law»; Phys. Rev. E **54**, p. 972 (1996). 179, 182

[146] P. Tamayo & W. Klein; «Critical dynamics and global conservation laws»; Phys. Rev. Lett. **63**, p. 2757 (1989). 179

[147] P. Tamayo & W. Klein; «Critical dynamics and global conservation laws. Reply»; Phys. Rev. Lett. **66**, p. 2049 (1991). 179

[148] J. F. Annett & J. R. Banavar; «Critical dynamics, spinodal decomposition, and conservation laws»; Phys. Rev. Lett. **68**, p. 2941 (1992). 179

[149] L. Moseley, P. W. Gibbs & N. Jan; «Kawasaki dynamics with infinite-range spin exchange»; J. Stat. Phys. **67**, p. 813 (1992). 179

[150] A. Sicilia, J. J. Arenzon, I. Dierking, A. J. Bray, L. F. Cugliandolo, J. Martinez-Perdiguero, I. Alonso & I. C. Pintre; «Experimental test of curvature-driven dynamics in the phase ordering of a two dimensional liquid crystal»; Phys. Rev. Lett. **101**, p. 197 801 (2008). 180, 186

[151] M. J. de Oliveira; «Isotropic majority-voter model on a square lattice»; J. Stat. Phys. **66**, p. 273–281 (1992). 192

[152] J. T. Cox & D. Griffeath; «Diffusive clustering in the two-dimensional voter model»; Ann. Prob. **14**, p. 347 (1986). 194

[153] E. Ben-Naim, L. Frachebourg & P. Krapivski; «Coarsening and Persistence in the Voter Model»; Phys. Rev. E **53**, p. 3078 (1996). 195, 196, 199

[154] M. Abramowitz; *Handbook of Mathematical Functions* (Dover Publications, USA) (1965). 195

[155] F. Sastre, I. Dornic & H. Chaté; «Bona Fide Thermodynamic Temperature in Nonequilibrium Kinetic Ising Models»; Phys. Rev. Lett. **91**, p. 267 205 (2003). 199

[156] O. Babelon, D. Bernard & M. Talon; *Introduction to Classical Integrable Systems* (Cambridge University Press) (2009). 203

[157] M. Dunajski; *Integrable systems* (Cambridge University Lectures) (2012). 203

[158] V. I. Arnold; *Mathematical Methods of Classical Mechanics* (Springer-Verlag, Berlin) (1978). 204, 205

[159] E. Yuzbashyan; «Generalized microcanonical and Gibbs ensembles in classical and quantum integrable dynamics»; Annals of Physics **367**, p. 288 (2016). 206